NANOPARTICLE THERANOSTICS TARGETING CLEC14A ON TUMOUR VASCULATURE

By Jack Goddard Pearce

A thesis submitted to the University of Birmingham for the degree

DOCTOR OF PHILOSOPHY

School of Chemistry

Physical Sciences of Imaging in the Biomedical Sciences

The University of Birmingham

2019

Abstract

This thesis studies the development of a method to knockdown CLEC14A *in-vivo*. CLEC14A has been shown to have strong pro-angiogenic signalling properties and its knockdown *in-vitro* has been shown to decrease wound healing and tube formation. Additionally, CLEC14A knockout mice showed a decreased rate of tumour growth in implanted Lewis Lung Carcinoma tumours. siRNA is a common tool used to knockdown genes but needs protection from degrading enzymes found in serum. To this end, a chitosan-based nanoparticle was developed to deliver siRNA. A 60% knockdown of CLEC14A was achieved *in-vitro* using untargeted chitosan nanoparticles. Microarray analysis of HUVEC cells treated with siRNA entrapped nanoparticles showed that CLEC14A was not knocked down at an mRNA level but that endothelial genes related to blood flow were affected in a similar manner to an increase in laminar blood flow, suggesting that CLEC14A has a regulatory role in endothelial gene expression. Conjugating antibodies to the surface of the chitosan nanoparticles may increase cellular uptake and improve knockdown of CLEC14A. Antibody targeting of the nanoparticles did not improve knockdown, and in fact, decreased efficiency at higher concentrations. Bio-distribution studies were performed with untargeted nanoparticles and showed localisation to tumour vascular endothelium. Nanoparticles were found in the liver and kidneys as well as the tumour.

An anti-angiogenic, CLEC14A based, vaccine was developed to be delivered by the chitosan nanoparticles. A CLEC14A-Tetanus FrC fusion protein was produced in HEK293 cells but failed to fold correctly and be excreted at a sufficient concentration. A CLEC14A-VLRB fusion was created and cloned into a bacterial plasmid. Two fragments of CLEC14A were created to fuse to

VLRB with the small fragment being successfully synthesised and purified ready for *in-vivo* immunisation studies.

Acknowledgments

I wish to express sincere appreciation to Professor Roy Bicknell for his assistance throughout my PhD. In addition, special thanks to Dr. Victoria Heath and the rest of the Bicknell group for their support and advice. I thank Elliot Brown and all the students I supervised for being eager to learn and enthusiastic about their projects. Finally, I would like to thank my Wife who supported me in countless ways and whose council I will forever seek.

Table of Contents

<u>Glossary</u>

Bp – Base Pairs (DNA)

BSA – bovine serum albumin

cDNA – complementary DNA

ChNP – Chitosan Nanoparticles

ChNP-siRNA – Chitosan nanoparticles with siRNA entrapped inside

ChGlutNP – Chitosan glutamate nanoparticles

ChGlutNP-siRNA – Chitosan glutamate nanoparticles with siRNA entrapped inside

CRT4 – CLEC14A Antibody Cancer Research Type 4

DAPI – (4', 6-damidino-2-phenylindole)

dH$_2$O – distilled water

DMSO – Dimethyl sulfoxide

E. coli – Escherichia coli

EDTA – Ethylene-diamine-tetra-acetic acid

EGF – epidermal growth factor

FC – Fragment crystallisable

FCS – Foetal Calf Serum

HIS-Tag – Polyhistidine tag

HRP – Horse Radish Peroxidase

IgG – immunoglobulin G

IPTG – Isopropyl β-D-1-thiogalactopyranoside

kDa – Kilo Dalton

NaCl – Sodium Chloride

NP-Antibody-1 – Antibody conjugation adapted from (Lee et al., 2012)

NP-Antibody-2 – Antibody conjugation adapted from (Zhu et al., 2015)

PBS – Phosphate Buffered Saline

PEI - Polyethylenimine

PVDF – Polyvinylidene difluoride

Rpm – Revolutions per minute

SDS – Sodium dodecyl sulphate

siRNA – Small interfering ribonucleic acid

VEGF – Vascular endothelial growth factor

Chapter I.

Introduction

CLEC14A:

C-type lectin family 14 member A (CLEC14A) is a trans-membrane, endothelial cell specific, glycoprotein (Figure 1.1); first discovered through microarray analysis (Ho et al., 2003). The identification as a novel endothelial specific gene was further validated through *in silico* analysis (Herbert et al., 2008). Identification of CLEC14A as a potential tumour endothelial marker was achieved through immunohistochemical staining of tumour vs healthy tissue. The strong staining of vessels in the tumour compared to the near absence in healthy tissue confirmed the upregulation and high expression of CLEC14A in tumour blood vessel tissue (Mura et al., 2012). It has been shown that CLEC14A is upregulated on the messenger RNA level in non-small cell lung cancer when compared to healthy tissue (Pircher et al., 2013). Two separate, pancreatic and ovarian, spontaneous mouse tumour models have shown that up-regulation of CLEC14A at the tumour level is correlated with tumour progression (Zanivan et al., 2013). Bevacizumab has been shown to down-regulate CLEC14A as well as CD93, further suggesting an angiogenic role for CLEC14A (Bais, 2011). Meta-analysis of 959 breast cancer, 170 renal cancers and 212 head and neck cancers lead to CLEC14A being labelled a "tumour angiogenesis signature". The potential for CLEC14A as a prognostic tool was further made a possibility by the detection of CLEC14A in the urine of patients with low grade bladder cancer (Ambrose et al., 2015). It

13

has also been proposed as a marker for circulating endothelial cells from blood cancer patients (Mancuso et al., 2014). CLEC14A can be shed from the membrane of endothelial cells by serine protease rhomboid-like 2 (RHBDL2), cleaving close to the transmembrane domain. The shedding of the extracellular domain of CLEC14A allows for the regulation of sprouting angiogenesis *in-vivo*.

Figure 1.1
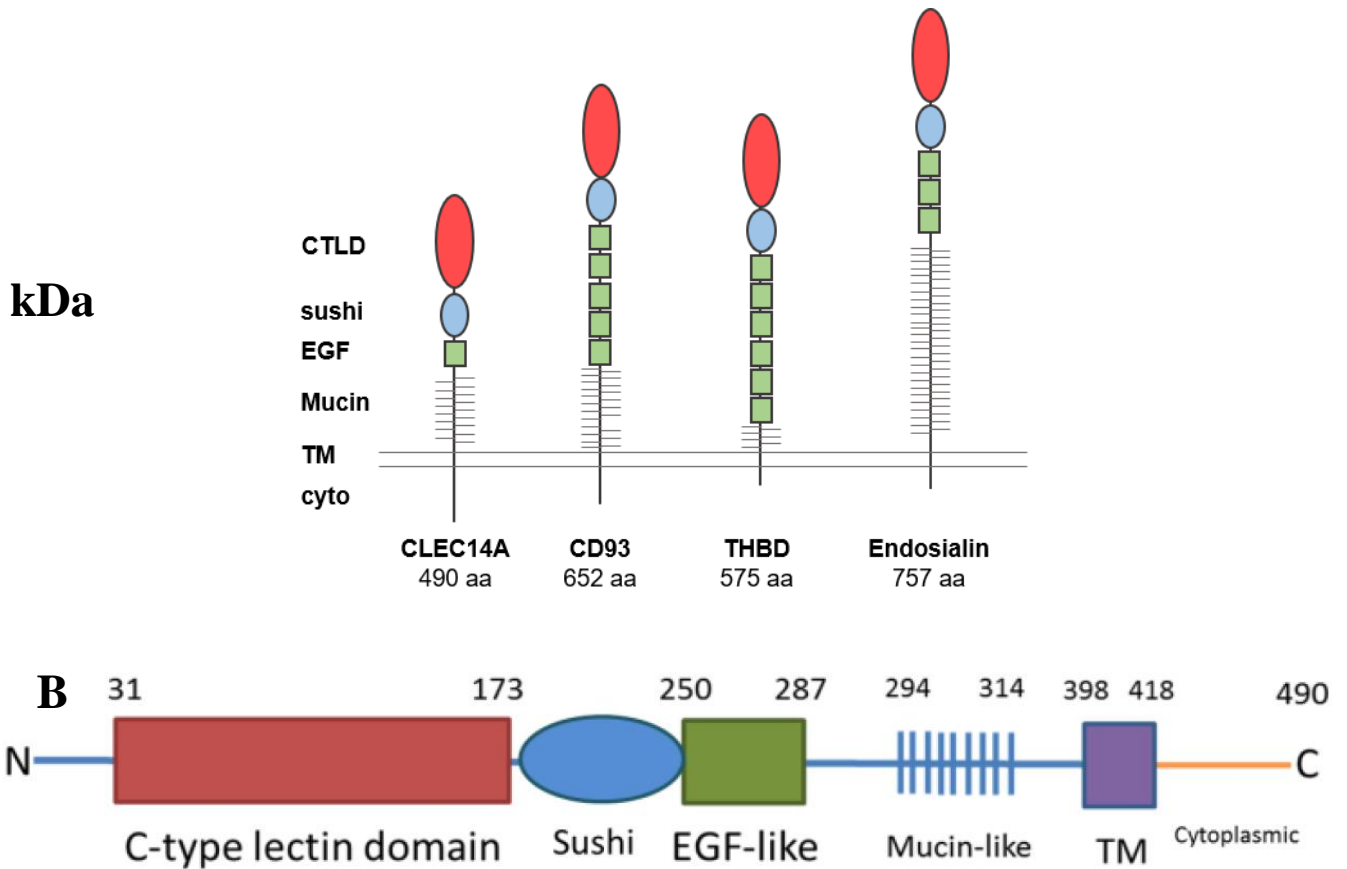
Figure 1.1 | C-Type-Lectin Family and CLEC14A

(A) From left to right, CLEC14A, CD93, thrombomodulin and endosialin. The multiple domains of the C-type lectin domain group 14 family proteins can be seen. C-type Lectin Domain (Red), Sushi Domain (Blue), Epidermal Growth Factor-like Domain (Green), Mucin-like Region, Transmembrane domain and cytoplasmic domain.
(B) the structure of CLEC14A can be more clearly seen with each domain mapped to its amino acid numbers, for example, the C-type lectin domain on the N terminus of the extracellular portion of the protein is made up from amino acids 32 to 173.

CLEC14A Expression and Function:

Low shear stress has been shown to up-regulate CLEC14A (Mura et al., 2012). A gene expression study during zebra fish embryo development showed that CLEC14A expression decreased as the heart began beating due to the increase in sheer stress from blood flow (Mura et al., 2012). 2 Pa of laminar shear flow applied to HUVEC in culture is enough to reduce CLEC14A expression by over 90%. Data showing high expression of CLEC14A in tumour blood vessels seems to corroborate with the disordered nature of tumour blood vessels and lack of shear flow from blood (Wragg et al., 2014). Apart from tumour vasculature, atherosclerosis is another area showing increased CLEC14A expression. Microarray analysis of atherosclerotic vessels show an up-regulation of CLEC14A proportional to stenosis (Hagg et al., 2009). A previous study also suggested that shear stress is lower in atherosclerotic vessels compared to healthy tissue (Gnasso et al., 1997). The Sp1 transcription factor binding site found on CLEC14A could be a method by which this shear stress is translated to a cell signal. Sp1 has been shown to be phosphorylated in response to shear stress resulting in the inhibition of MT1-MMP cell migration mechanics (Yun et al., 2002).

A morpholino knockdown of CLEC14A at 24 hours post fertilization has been shown to have strong anti-angiogenic during development resulting in deformed vasculature in zebrafish embryos (Mura et al., 2012). The introduction of human mRNA to the

knockdown embryos reverted the vasculature morphology to normal, showing the conserved nature of the CLEC14A gene.

The study of mouse embryos has shown expression of CLEC14A in the intersomitic vessels and vessels within the brain at day 10.5 as well as the vessels of the retina day 12 (Rho et al., 2011, Maeng et al., 2009).

A study that reinforced the role of CLEC14A in angiogenesis looked at a homozygous knockout in mice (Noy et al., 2015). The mice were viable and showed no defects during development. Lewis lung carcinomas (LLC) were introduced and it was shown that tumour growth and angiogenesis were reduced compared to wild type mice. Subcutaneous sponge implants also showed FGF2-induced angiogenesis to be reduced.

CLEC14A Interactions:

The intracellular domain of CLEC14A currently has no known protein interactions but global phosphoproteomic analysis of HUVEC show the potential of up to five serine phosphorylation sites (Meijer et al., 2013, van den Biggelaar et al., 2014). Scratch assays have been used to assess the requirement of CLEC14A in angiogenesis. siRNA mediated knockdown of CLEC14A reduced the ability of HUVEC to form tubes or close wounds formed on cell monolayers (Mura et al., 2012, Rho et al., 2011). Spheroid assays, with siRNA knockdown, demonstrated a reduction in sprout formation and showed cells with a lack of CLEC14A expression were likely to be found on the tip of sprouts (Noy et al., 2015). A final study in the involvement of CLEC14A in filopodia formation induced

ectopic expression of CLEC14A in cells that normally do not resulting in the formation of filopodia-like protrusions (Mura et al., 2012). All of this shows the importance of CLEC14A and its involvement in angiogenesis.

As well as filopodia formation, CLEC14A has been implicated in cell-cell interactions. Over expression of CLEC14A in HEK293 cells results in the formation of clumps which disperse upon addition of antibodies targeted at the CTLD of CLEC14A. (Ki et al., 2013). Antibodies targeted at the CTLD also resulted in a down-regulation of CLEC14A on the surface of HUVEC due to internalization of the protein. This down-regulation of CLEC14A resulted in decreased cell migration and tube formation in *in vitro* analysis.

Angiogenesis:

Angiogenesis is a word derived from the Greek words *Angeion* meaning vessel and *Genesis* meaning birth. Angiogenesis is the birth or generation of new blood vessels from pre-existing vessels. Perturbation of normal angiogenesis is the basis for many serious diseases including inflammatory diseases, retinal disorders and tumour formation and regenerative medicine (Carmeliet, 2003).

Tumour growth is limited to around 1-2 mm^3 without the growth of new, invasive, vessels to supply the growing tumour with extra oxygen and nutrients. Autopsies from deceased patients, that did not die from cancer, proved this through the discovery of many small, non-malignant, tumours (Naumov et al., 2008). Preventing this invasion of new blood

vessels or destroying existing vessels that supply the tumour present exciting aims for anti-cancer therapies and cancer preventions.

Many growth factors and cell signalling pathways regulate angiogenesis during development and in healthy tissue. A balance is maintained in quiescent endothelial cells. When this balance shifts in favour of pro-antigenic signals then it is said to turn on the "angiogenic switch" (Hanahan and Folkman, 1996).

Many different forms of angiogenesis exist but the main method of new vessel formation is sprouting angiogenesis, first elucidated in 1977 (Ausprunk and Folkman, 1977). Later in 1984 Folkman worked with Haudenschild to show that human endothelial cells placed on dishes coated in a thin layer of extracellular matrix organised into tube like structures (Folkman and Haudenschild, 1980). In 1991 Grant et al., used electron microscopy to confirm that these tubes acted like capillary networks with lumens and cell specialization much like blood vessels found in *in-vivo* models (Grant et al., 1991). Figure 1.2 describes sprouting angiogenesis with its main stages and functional cells. Figure 1.3 shows other variations of angiogenesis that can be used by a tumour to develop its own blood supply.

1: Activation of quiescent endothelial cells by pro-angiogenic growth factor stimuli such as vascular endothelial growth factor (VEGF).
2: Extracellular matrix (ECM) is degraded by matrix metalloproteinases (MMPs) as perivascular cells detach from the vessel.

3: The sprout forms a tip with "tip cells" generating filopodia to migrate towards the pro-angiogenic stimulus.

4: Proliferation of stalk cells causes the lengthening of the sprout and the formation of a lumen just behind the tip.

5: Sprouts join and form new vessels via anastomosis and perivascular cells are recruited through the secretion of platelet derived growth factor-B (PDGFB). Perivascular cells promote maturation of the newly formed vessel (Bjarnegard et al., 2004).

This sprouting tip is highly regulated by complex signalling pathways; however, its elucidation gave rise to some of the first anti-angiogenic therapies targeting VEGF stimulation. It was shown that, upon binding of VEGF to its receptor, tip cells develop filopodia and begin migratory processes. The tip cells begin to express high levels of VEGF receptor-2, Dll-4, PDGF-b and other proteins (Hellstrom et al., 2007). Low levels of Notch signalling also begins. The filopodia are numerous and guide the new sprout towards the angiogenic stimulus, up the chemical concentration gradient. The tip cells divide only minimally but cells with fewer filopodia divide more rapidly to form lumens, branches and basement membranes. Nearing the end of vessel formation endothelial cells adopt a phalanx structure. This phalanx of immobile endothelial cells promotes vessel integrity, increases cell adhesion and dampens the response to VEGF resulting in a halt to vessel growth (Jakobsson et al., 2010).

Figure 1.2
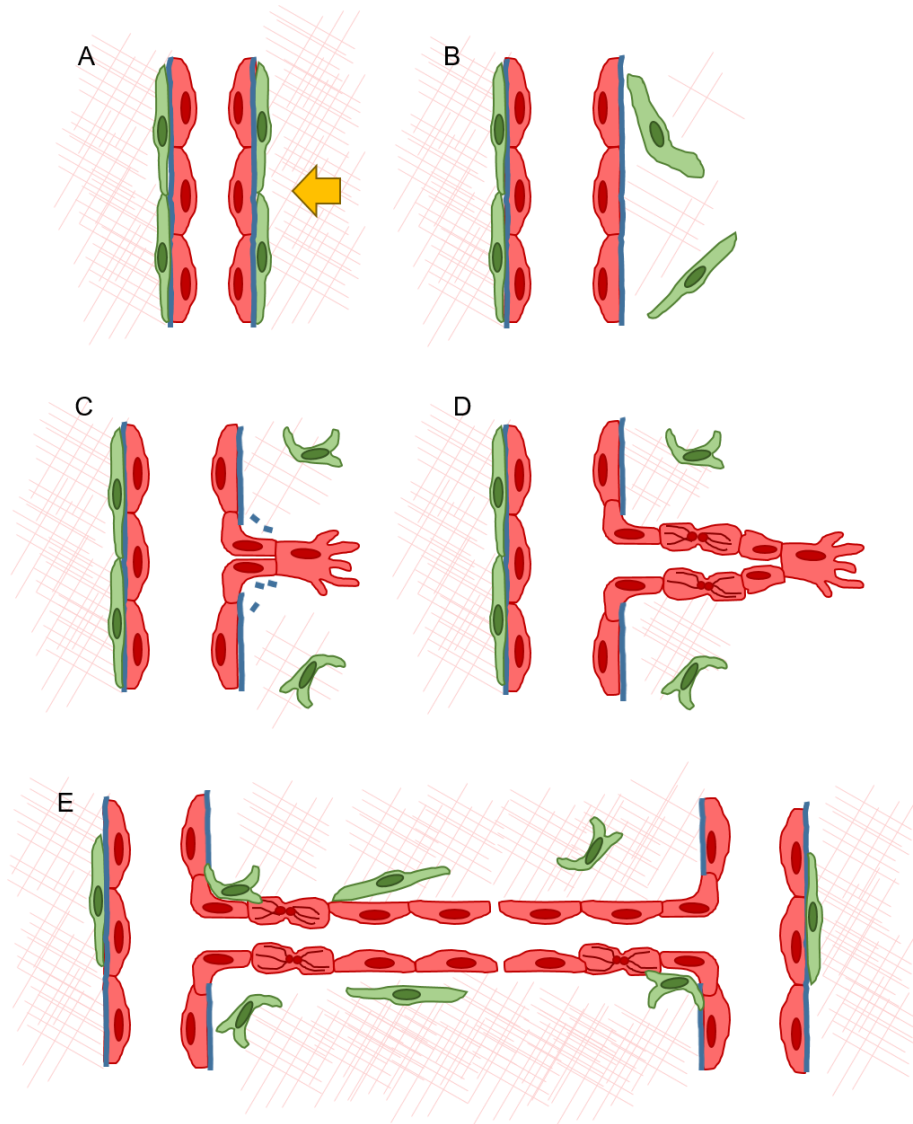
Figure 1.2 | Sprouting Angiogenesis
(A) Endothelial cells (pink) are stimulated by a pro angiogenic signal represented by the yellow arrow. (B) the perivascular cells, detailed in green, detach from the extracellular matrix (cross hatch mesh), resulting in degradation of the matrix. (C) stimulated endothelial cells form tip or stalk cells that digest and migrate through the basement membrane (Blue lines). (D) the growing sprout elongates through proliferation of the stalk cells. (E) The new vessel sprout tip comes into contact with a secondary sprout resulting in fusion of the two branches to form one single vessel. The (green) perivascular cells are recruited to mature the vessel. (Diagram Adapted from (Bergers and Benjamin 2003).

Figure 1.3
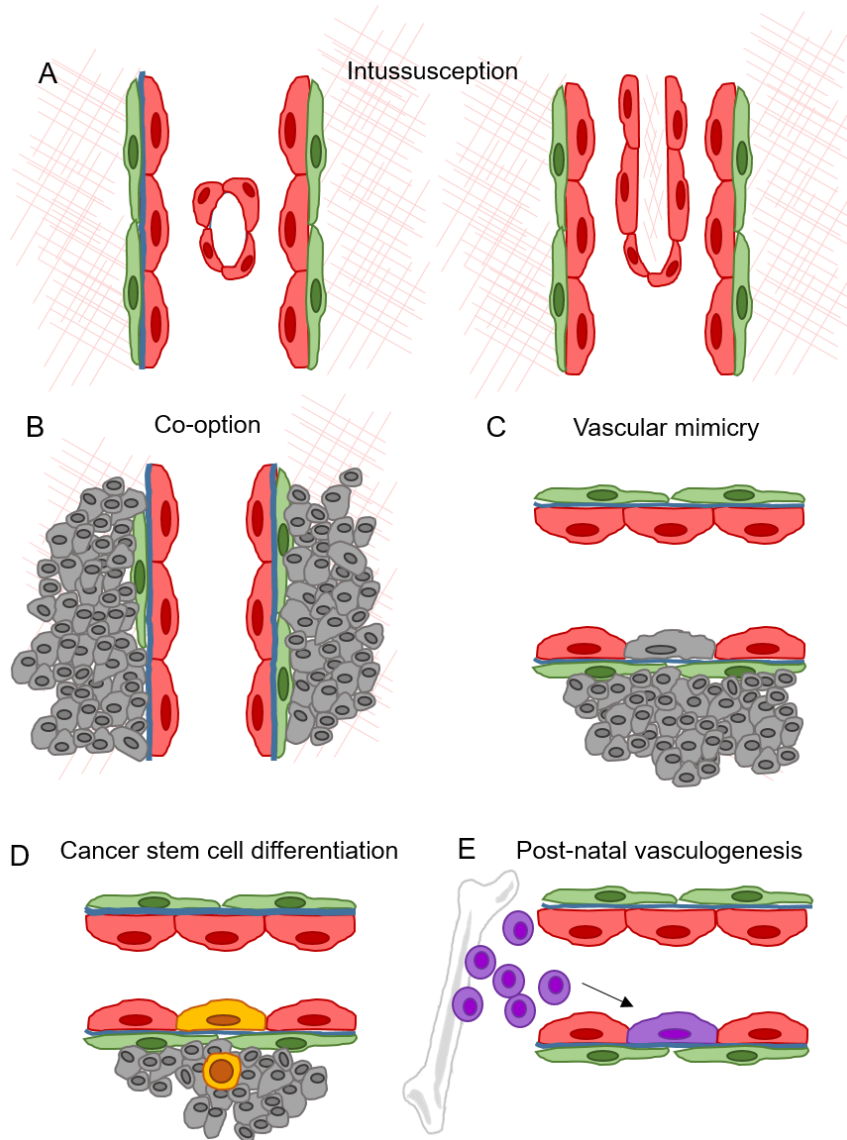
Figure 1.3 | Less common variations of vessel formation

The less common variants of vessel formation: (A) shows the splitting of an existing vessel into two separate vessels. This is called intussusception. (B) cancer cells (grey) co-opt or "hijack" the existing vasculature structure. (C) cancer cells mimic endothelial cells and exhibit endothelial like characteristics and functions. (D) The differentiation of cancer stem cells (yellow) into endothelial like cells to form a vascular structure. (E) endothelial progenitor cells (purple) are recruited from the bone marrow through post-natal vasculogenesis. These progenitor cells differentiate into endothelial cells that line the vessel. (Diagram Adapted from Bergers and Benjamin 2003).

Figure 1.4
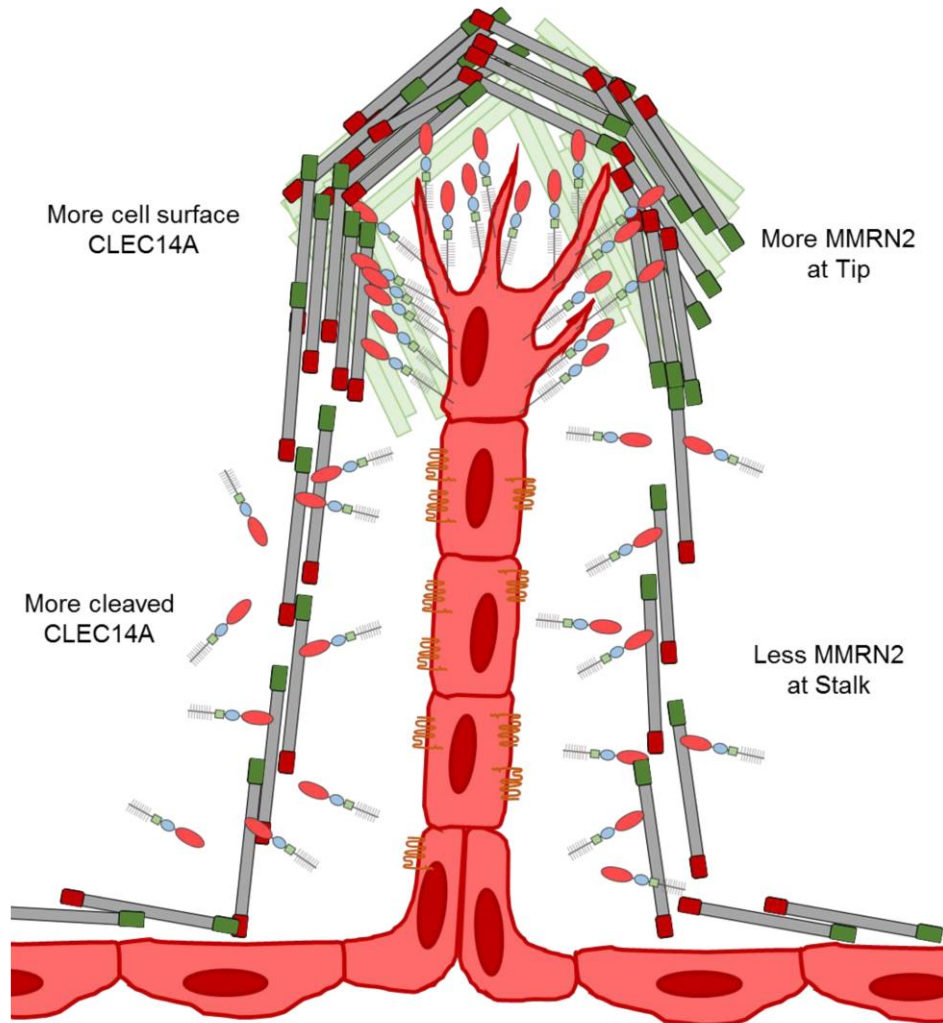
Figure 1.4 | Sprouting Angiogenesis and CLEC14A

A blood vessel sprout forms a tip that protrudes out from an existing vessel. CLEC14A expression is extremely high on the tip cell, resulting in more recruitment of Multimerin 2 (MMRN2) and increased CLEC14A signalling. Cells further down from the tip cell shed their CLEC14A thereby resulting in the sprouting vessel being 'led' by the tip cell with new cells being generated at the base of the sprout. (Diagram Adapted from Bergers and Benjamin 2003).

CLEC14A plays an integral role in sprouting angiogenesis as its high expression on tip cells drive filopodia formation and cell migration to move the new vessel towards its target (Figure 1.4).

There are other processes for the development of new blood vessels such as intussusception (Figure 1.2). Intussusception involves the splitting of existing blood vessels thereby increasing the complexity of the existing network (Burri et al., 2004). Other processes for tumours to increase their vascularization include hijacking existing vasculature by the invasion of cancer cells that adapt to perform endothelial-like functions. This method of cancer cell hijacking is also known as co-option. Cancer stem cells have also been known to differentiate into endothelial like cells and perform vascular mimicry. It has also been suggested that endothelial progenitor cells can be sequester from the bone marrow and differentiated to form new vessels. This "sequestering" is a form of post-natal vasculogenesis and is a controversial mechanism (Carmeliet and Jain, 2011). There is also some evidence for a tumour promoting nature in endothelial cells that goes past simple vessel formation. Endothelial cells have been shown to produce angiocrine factors in the liver and pancreas during low blood flow. It is hypothesised that these factors aid in tissue regeneration and could potentially contribute to tumour progression or recurrence after anti-cancer therapy (Lammert et al., 2001). It must not go unsaid that blood vessel invasion is also a major contributor to metastasis.

Anti-angiogenic therapies

The Hallmarks of Cancer was a landmark paper that laid out six "hallmarks" that every cancer cell possesses (Hanahan and Weinberg, 2000). Invasion and metastasis was one of these original 6 hallmarks and a large amount of focus was put on elucidating the mechanisms that allow this. In 2011 The Hallmarks of Cancer: The Next Generation established inducing angiogenesis as a hallmark in its own right (Hanahan and Weinberg, 2011). Inhibiting unwanted angiogenesis quickly became a focus in the fight on cancer. Attempting to disrupt tumour blood vessels as a viable therapy was not considered until well into the late 1960's early 1970s by Folkman and his team who did much of the ground work in understanding angiogenesis at the beginning of the field. The team assumed that there must exist natural inhibitors to angiogenesis that could tip the equilibrium of pro vs anti-angiogenic signals towards the negative and block tumour angiogenesis (Folkman, 1971).

At present the most successful and commonly used methods to prevent tumour angiogenesis are through blocking vascular endothelial growth factor (VEGF), a pro angiogenic protein. Bevacizumab is an anti-VEGFA antibody that gained FDA approval in 2004 for use on colorectal cancer (Hurwitz et al., 2004). Small molecule tyrosine kinase inhibitors such as sunitinib and sorafenib, which target the intracellular kinase domain of several types of receptors, have also been approved (Roskoski, 2007, Wilhelm et al., 2008). The birth of anti-angiogenic therapies promised highly effective drugs that would significantly aid in the fight against cancer. Most modern anti-angiogenics are able to

prolong survival but only for a few months and this early optimism was most likely due to the results garnered from early mouse model experiments (Kerbel, 2008).

Drug resistance is a major obstacle in many anti-cancer therapies, but it seems to play a particularly large role in anti-angiogenics. Most anti-VEGF therapies are extremely effective at blocking the signalling produced by VEGF and its associated receptors but the highly adaptive nature of the tumour microenvironment simply results in a switch to the production of other growth factors such as angiopoietin-2 (Ang2) or fibroblast growth factor-2 (FGF2) (Casanovas et al., 2005). Apart from the issue of resistance, anti-VEGF therapies have also been shown to increase the invasive and metastatic phenotypes in multiple cancer types (Ebos et al., 2009, Paez-Ribes et al., 2009).

Other growth and signalling factors can be targeted to prevent blood vessel growth in tumours. Blockage of platelet-derived growth factors (PDGFs) (Hellberg et al., 2010), integrins (Desgrosellier and Cheresh, 2010), regulator of G-Protein signalling 5 (Rgs5) (Hamzah et al., 2008) and epidermal growth factor receptor (EGFR) (Cerniglia et al., 2009) all present potential targets of inhibition.

Proteolytic enzymes have also been shown to have vascular normalization effects and trastuzumab has been shown to decrease the volume, diameter and permeability of tumour vessels (Izumi et al., 2002).

Tumour vasculature vaccines

Vaccination is yet another approach taken to prevent the growth of new vessels in tumours. There are many advantages to using a vaccine rather than a traditional therapy including lower cost and lower doses. Vaccines are generally recombinant proteins and so require far less complicated synthesis than an antibody or aptamer and induce a polyclonal antibody response rather than monoclonal like an antibody would.

An issue with cancer vaccines is that the nature of the patients often mean they have an already compromised immune system, either from some other pre-existing condition (resulting in a higher cancer of the development of cancer) or as a result of chemotherapy already administered. A 2014 study that looked at the combination of ipilimumab (a checkpoint inhibitor) and bevacizumab showed promising results (Hodi et al., 2014).

To produce a viable anti-cancer vaccination, several factors must be considered: The magnitude of the immune response induced, the type of immunity generated and how long the immune protection lasts. The correct antigens must be introduced to the appropriate dendritic cell groups thereby inducing differentiation of the DC cells into their immunostimulatory state. Activated on DC can be achieved either *in-vivo* or ex-vivo. This thesis will focus on *in-vivo* activation as the development of a vaccine involves inducing an immune response from within a host.

To induce an immune response via the *in-vivo* method involves injection of the target antigen in combination with an adjuvant. Adjuvants were used long before their function was understood. Antigens must be injected into the host and taken up by immature DCs thereby stimulating them to mature and activate an immune response. The likelihood of uptake by DC's is greatly improved by targeting of the antigen (Biragyn et al., 2001). Adjuvants are chemicals or molecules that strongly stimulate the immune system and if given in conjunction with a self-antigen may allow tolerance to be broken. Lipopolysaccharides (LPS) are a common adjuvant as they simulate the liposomes that often contain bacterial antigens and therefore induce a strong immunogenic response.

Adjuvants important in stimulating a strong immune response however only a small number of adjuvants have ever been licensed for human use due to concerns with toxicity and safety. Fusing an immunogenic protein fragment to the self-antigen before injection into the host may remove the need for toxic adjuvants (Herrin et al., 2008, Hirano et al., 2011, Kasahara and Sutoh, 2014). If an immunity against a particular antigen already exists, say through vaccination, then a strong immunogenic response will be mounted against the foreign part of the fusion protein.

A novel study was recently released that showed an effective immune response could be mounted against primary tumour masses and metastasis without the need to identify a tumour specific antigen (Sagiv-Barfi et al., 2018).

The covalent coupling of short 6-12 amino acids strings of non-self-antigen to self-antigens can induce a high antibody titre against the self-antigen. Unfortunately, it has been shown that this response is variable among individuals and it has been shown that using a larger non self-antigen in the fusion protein resulted in a more stable response but also correlated with a lower average immune response. This effect has been dubbed carrier suppression and has been noted by several other publications (Herzenberg and Tokuhisa, 1982, Herzenberg et al., 1982, Jegerlehner et al., 2010, McCluskie et al., 2016)

Robo4 and fibronectin (extra domain A and B) represent two examples of tumour endothelial markers used for vaccination (Zhuang et al., 2015, Huijbers et al., 2010, Femel et al., 2014)

Another way of improving immune response is improving the delivery of the antigen to the antigen presenting cells or providing a slow release of the antigen over a long period of time. Both methods were attempted through the use of nanoparticles.

Targeting anti-angiogenic therapies

The efficacy of most therapies can be increased through the targeting of said therapy to its desired tissue. Targeting of anti-angiogenics involves the identification of tumour endothelial markers. The endothelium presents as a desirable target due to its easy access using the blood vessels themselves. Another large advantage is the relative stability of endothelial cell genome. The issue with anti-VEGF therapies is that the tumour itself is

extremely genetically unstable. In somatic tissues the rate of mutation is approximately 1.62-9.0 mutations per cell division (Lynch, 2010). Genomic instability in cancer cells is likely to raise this number much higher. More rapid cell division (once every 3-4 days) sees the accumulated number of mutations drastically increase to several thousand over a life-time for individual cancer cells. The majority of these mutations remain present in only a small subset of cells. When looked at as a whole, the total accumulated individual mutations of the entire tumour can quickly reach into the hundreds of millions or potentially billions (Ling et al., 2015, Diaz et al., 2012). This rapid mutation allows the tumour to adapt and express other pro-angiogenic factors other than VEGF.

Targeting the endothelium of the blood vessels directly removes the risk of rapid adaptation away from a therapy. This is especially important when it comes to the targeting of a therapy. Highly targeted therapies have a high chance of the tumour mutating so that it down-regulates the target protein.

Antibody Conjugates:

It was not until 1993 that the first antibody drug conjugate was created to target tumour endothelium. To demonstrate complete necrosis of solid tumours the study conjugated ricin to antibodies raised against MHC class II proteins (Burrows and Thorpe, 1993). MHC class II proteins were expressed on tumour endothelium due to being induced by tumour cells releasing interferon-γ (IFN- γ). Antibody drug conjugates (ADCs) are typically used to increase the concentration, and specific distribution, of drugs in a tissue (Amani et al.,

2019). It is thought that internalization of the protein takes the antibody and linked drug with it inside the cell, however, recent evidence suggests that simply releasing the drug into the tumour microenvironment can still result in entry into endothelial cells (Perrino et al., 2014).

There has been positive pre-clinical data produced with the tumour endothelial marker Robo4. Antibodies against Robo4 were conjugated to neocarzinostatin resulting in the reduction of tumour growth and less negative side effects such as weight loss compared to anti-VEGFR2 conjugates (unpublished Data).

Fibronectin is one of the most widely studied tumour endothelial markers (specifically extra domain B). It represents a useful marker for tumour specific endothelium as it is only present during remodelling of the endothelium and so is highly expressed in a multitude of developing tumours (Neri and Bicknell, 2005). Antibodies conjugated with radioactive iodine (^{131}I) directed radiation therapy selectively at the tumour vasculature in glioma rat models (Spaeth et al., 2006).

Introduction to Nanoparticles:

The success of ADCs has prompted the study of how to most effectively target and deliver drugs and small molecules to specific tissues in a patient. Nanoparticles allow for the delivery of large numbers of drugs or molecules with many other benefits. The designing of "intelligent" particles that possess specific physiochemical properties such as size,

shape, surface chemistry, drug binding methods and drug release methods, can increase the efficacy and effectiveness of many anti-cancer therapies. By shielding small molecules like small interfering RNA (siRNA) from the highly reducing conditions inside an organism as well as endogenous nucleotide enzymes, nanoparticles are set to make DNA and RNA delivery a more viable possibility (Zhang et al., 2011).

The abnormal structure and growth of tumour vasculature results in a chaotic maze of vessels resultant from aberrant and imbalanced expression of angiogenic growth factors (Tredan et al., 2007). Healthy growth of vessels results in a hierarchical distribution from arteries to veins to capillaries. The structure of each individual vessel is also organized with endothelial cells aligned tightly together as monolayers with the basement membrane intact and pericyte intermediated close to the endothelial cells. To contrast this, tumour blood vessels are disorganized with a lack of regular monolayer structure to the endothelial cells (resulting in a lack of endothelial barrier, chaotic blood flow and leakiness). The basement membrane is discontinuous with large gaps left (some hundreds of nanometers in size (Hashizume et al., 2000)). These holes result in leakage from the tumour and vessels increasing the interstitial fluid pressure (IFP) and reducing blood supply resulting in hypoxia which stimulates angiogenesis and aids drug resistance (Rapisarda and Melillo, 2009).

Nano-therapies aim to circumvent or exploit these differences so as to normalize or destroy the tumour blood supply. Normalization aids in the effectiveness of other anti-cancer therapies. One approach taken is the prevention of binding of pro-angiogenic factors to their cell surface receptors. Antibodies, or other ligands, are raised against the desired receptor (such as VEGFR-2) and are conjugated to the surface of the nanoparticles. Upon

binding their pro-angiogenic growth factors these receptors can activate endothelial cells to release several proteases that degrade the basement membrane. Li et al., designed a nanoparticle to hold low molecular weight heparin and ursolic acid that would inhibit matrix metalloproteinase enzymes thereby disrupting the degrading of the basement membrane by pro-angiogenic growth factor signalling (Li et al., 2016b).

Different types of nanoparticles used for siRNA delivery

Nanoparticles and nanomaterials have gained greater interest due to their tuneable characteristics. Their physical, chemical, and biological interactions can be tailored to fit the required job. Three main factors differentiate nanoparticles: Their size, shape and composition. Generally, nanoparticles vary in size ranging from 10s of nanometers to hundreds.

Nanoparticles are becoming more important as modern drugs require precise dosage or protection due to the presence of proteins or nucleic acids (Vo et al., 2012). The efficiency of most existing drug delivery methods are directly related to their size. Smaller nanoparticle carriers present with higher bioavailability, can cross the blood brain barrier, enter the pulmonary system, be absorbed directly by cells or move through tight junctions of endothelial cells (Kohane, 2007).

Particles biodegradability level has also been an area of interest. Changing the bioactivity of the particle can change biodistribution and breakdown via endogenous enzymes (Zhang and Saltzman, 2013).

Before attempting to "design" the perfect nanoparticle vector for drug delivery, one must first understand how the body deals with these foreign nano-bodies.

Nanoparticles can be administered through three main routes, injection, inhalation or be taken orally. Once inside an organism, the first hurdle is nanoparticle-protein interactions to form protein coronas. (Mu et al., 2014, Prado-Gotor and Grueso, 2011). Protein coronas, if they last long enough, are said to potentially even out govern the particle own biochemistry (Lundqvist et al., 2011). These coronas evolve and equilibrate over time as the particles pass from one fluid to another.

After the nanoparticle-protein interactions the particles are absorbed from the blood vessels and distributed via the lymphatic system. If nanoparticles are recognized by lymph nodes as foreign bodies, then they will be engulfed by macrophages and cleared from the body. This makes nanoparticle delivery challenging but can be overcome through altering of size and surface characteristics of the particle.

Gold:

Gold nanoparticles (AuNPs) have attracted greater and greater interest as the study of nanomaterials progresses (Zhang et al., 2014b). AuNPs possess high X-ray absorption, are easy to synthesize, due to their inert nature their physiochemical properties are easy to control (Zhang et al., 2014a). They have strong affinity for thiols, amines and disulphides possess tuneable optical properties and also unique electronic characteristics (Y. Zhou, 1999, Zhang et al., 2014b, Zhang et al., 2013).

AuNPs can be divided into three groups:

One dimensional nanorods, wires, tubes and belts.

Two dimensional nanoplate stars, pentagons, squares, hexagons and dimpled nanoplates

Three dimensional nanotadpoles, dumbbells, nanodendrites and nanostars.

Spherical AuNPs are the structure that has received the most interest due to the ease of synthesis (S. Zeng, 2011, Zhang et al., 2014b).

AuNPs have potential use in therapeutics, detection biolabeling, drug delivery and diagnostics, imaging, photovoltaics and catalysis (Zhang et al., 2013, Youssef et al., 2014, Zhang et al., 2014b).

The high surface area of AuNPs, along with their nontoxicity, make them ideal for loading drugs to including siRNAs and other anti-cancer agents (Luo et al., 2011).

Liposome:

Liposome nanoparticles are known as soft or organic nanoparticles. The simplest method for integration of siRNA is to simply mix liposomes with siRNA at the correct ratio to form lipoplexes (Podesta and Kostarelos, 2009). These complexes are easily endocytosed by the cell and so represent fantastic delivery vehicles. Liposomes synthesized by mixing siRNA with glycosylated liposomes to knockdown a hepatic gene Ubc13 (Sato et al., 2007). Integration of PEG is vital to the protection from reticuloendothelial breakdown and increase circulation time in the vasculature (Ho et al., 2013). PEG modification improves the nanoparticles stability and half-life in the blood circulation however these still remain an issue for liposome nanoparticles, remaining at around 30 minutes (Santel et al., 2006, Aigner, 2007).

Silica:

Hom et al., developed mesoporous silica nanoparticles containing 2.5nm pores within the nanoparticle providing potential binding locations for siRNA molecules. Hom et al., showed that binding within a pore gives siRNA molecules more protection from nuclease enzymes and other degrading conditions like low pH and oxidising environments, increasing the lifetime of the siRNA in serum.

Chitosan:

Chitosan is a polymer, specifically a mucopolysaccharide which is close in relation to cellulose. Crustacean shells are the major source of chitin which is deacetylated to form chitosan. The deacetylation of chitosan was first described by Rouget in 1859 through the decolouring of chitin in potassium permanganate and then boiling in sodium hydroxide (van der Lubben et al., 2001)

The low toxicity of chitosan has been demonstrated in mice with the LD_{50} reaching above 16 g/kg (Paul W., 2000). Chitosan is digested by chitinases which are secreted by the intestinal microorganisms after oral administration. Chitosan is an umbrella term that can be separated into many groups, along with its physical structure, this makes chitosan readily biodegradable. The biodegradable nature, biocompatibility and FDA approval, chitosan provides a fantastic medium for nanoparticle synthesis (Lee K. Y., 1995, Muzarelli R. A. A., 1996, Dodane V.).

Chitosan is formally given as a name once the polymer chitin has its acetylglucosamine units decreased to below 50% creating N-acetyl-glucosamine (chitosan) the presence of a primer amine at the C-2 position of N-acetyl-glucosamine results in the unique structural properties that can be exploited for nanoparticle synthesis and other bio-fabrication aims (van der Lubben et al., 2001) (Figure 2.1).

Deacetylation is key to the properties of the chitosan polymer. Low deacetylation chitosan's have increased absorption qualities with dose dependent toxicity at high and low molecular weights. Highly deacetylated chitosan's show low toxicity at low molecular weights but that this may not be relating to absorption (Schipper N. G., 1996). Chitosan has a pKa of around 6.5 so a pH of less than about 6 results in protonation of its amines. For this reason, synthesis is kept at a pH of 5.5 to ensure chitosan's solubility in organic acid solutions.

Chitosan is ideal for the development of drug delivery through nanostructures (anything from 1 nm – 100s of nm) due to stability, low toxicity and simple preparation methods (Tiyaboonchai W., 2003) (Figure 2.1).

Figure 1.5
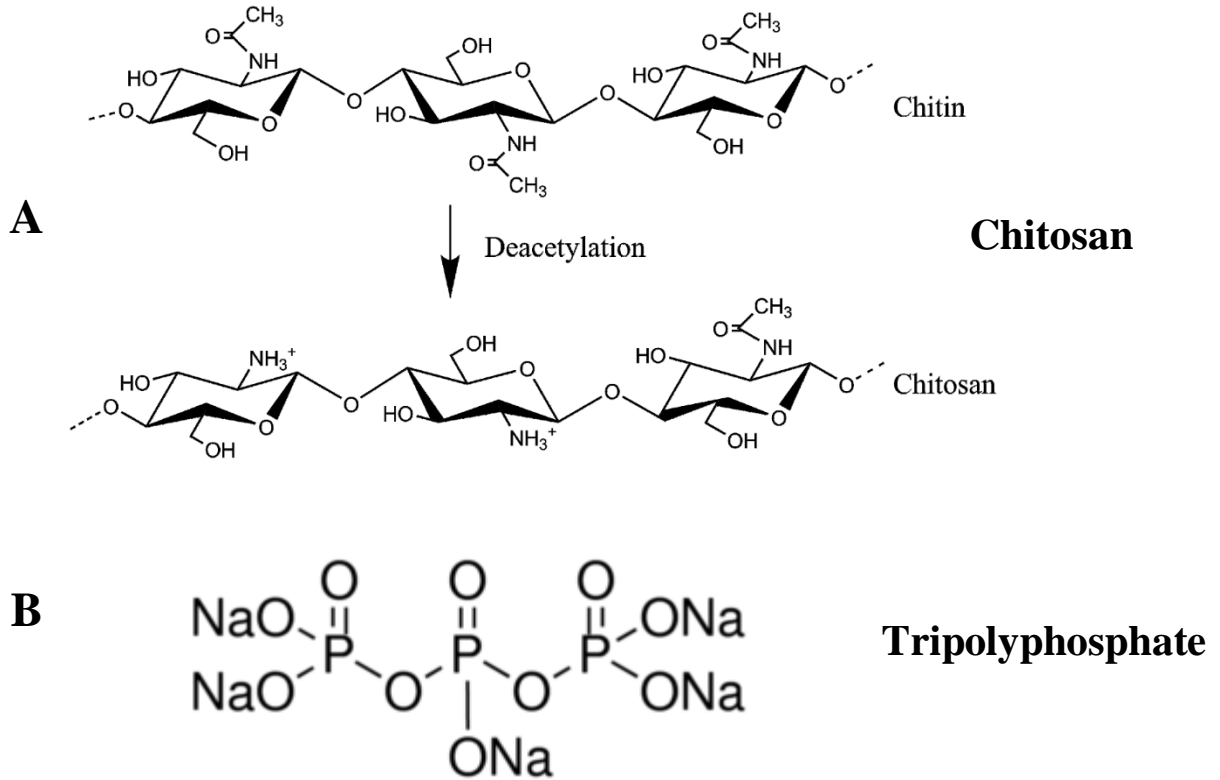
Figure 1.5 | Structure of Chitosan and Tripolyphosphate

(A) Chitosan is a polymer of β-(1→4)-linked D-glucosamine, created by the deacetylation of a N-acetyl-D-glucosamine polymer chain. The deacetylation percentage varies but must be above 50% to change chitin to chitosan.

(B) Tripolyphosphate is the crosslinking agent used to form the chitosan nanoparticle. Nanoparticle formation is achieved through electrostatic interaction between amine groups on the chitosan polymer and the negatively charged groups of TPP.

Figure 1.6
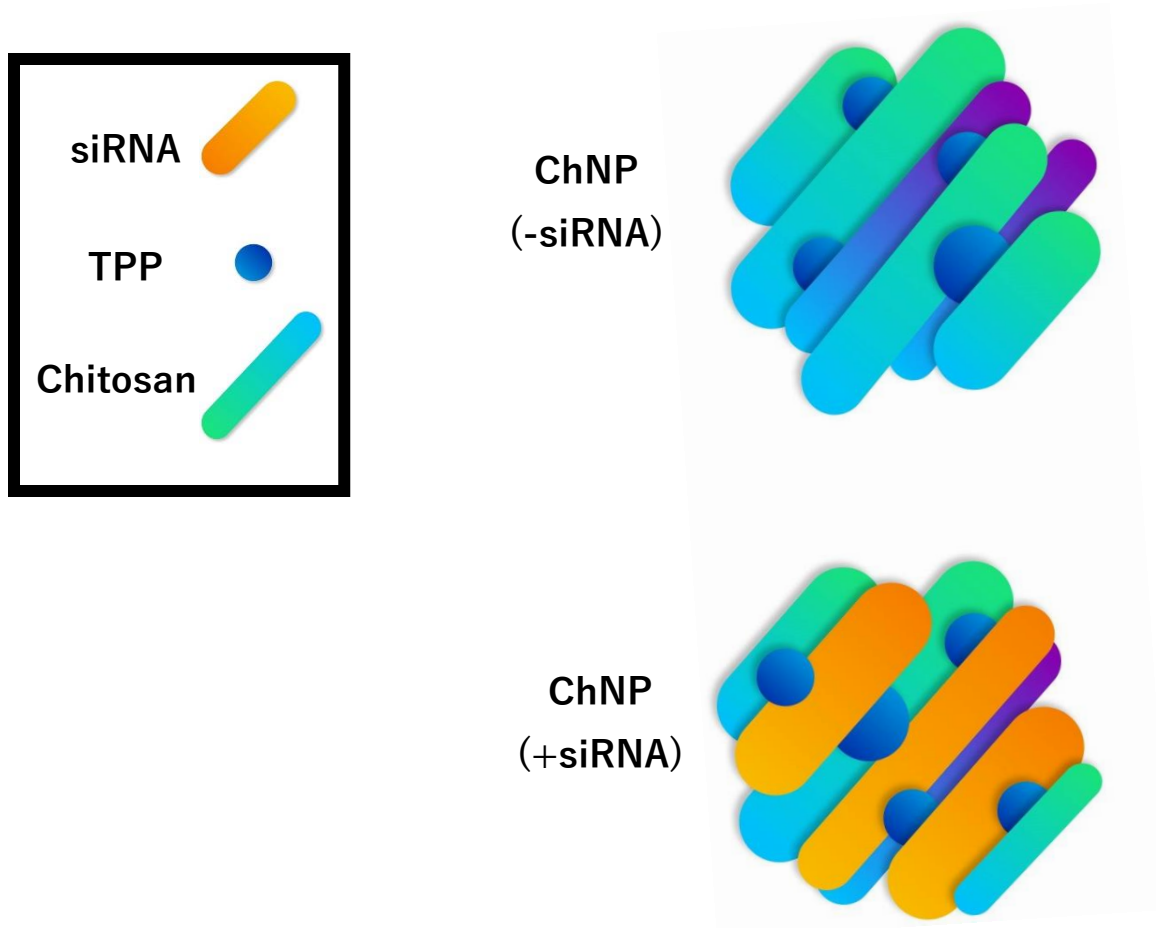
Figure 1.6 | Chitosan Nanoparticle Crosslinking and siRNA Entrapment

Figure 1.5 shows the crosslinking characteristics of TPP on chitosan and the ability of siRNA to become entrapped inside the chitosan-TPP mesh acting as a cross linker itself. The siRNA (orange) or the TPP (blue) are both negatively charged and so bind to the positive chains on the chitosan polymer (green) inducing polymerisation and formation of the nanoparticle.

As can be seen in ChNP (-siRNA), the TPP acts as a crosslinker, binding the different strands of chitosan together.

ChNP (+siRNA) Shows that siRNA also acts as a crosslinker, binding to the chitosan and becoming entrapped inside the chitosan-TPP crosslinked mesh.

Ionic gelation has been shown to be an extremely successful method for drug entrapment inside chitosan nanoparticles (Raja et al., 2015). Tripolyphosphate (TPP) represents a common polyanion used in chitosan-nanoparticle synthesis (Figure 1.5). Ionic gelation is based on the method of electrostatic interaction between carboxyl groups on the chitosan polymer with negatively charged groups of polyanions (Figure 1.6). The size of nanoparticles is directly affected by chitosan:TPP weight ratio and must be kept between 3:1 and 6:1. Increasing temperature has also been shown to decrease particle size (HueiChen, 2008a). Other methods of drug binding exist such as the microemulsion method in which free amino groups on the chitosan polymer conjugate with glutaraldehyde or the polyelectrolyte complex (PEC) method emulsification-crosslinking method, complex coacervation method, solvent evaporation method and coprecipitation method (Nagpal et al., 2010).

Nanoparticle Characteristics:

- **Size:**

The size and shape of any given nanoparticle defines how the body will interact with and affects biodistribution, toxicity, absorption and whether targeting moiety's can be attached (McMillan et al., 2011). It has been shown that 100 nm particles have a 2.5 times greater

cell uptake compared to 1000 nm nanoparticles and over a 6 times increase in uptake compared to 10 µm particles (Desai et al., 1997).

An obvious key role for any nanoparticle delivery system is the eventual release of its drug at the desired location. Size has a direct effect on drug release. Smaller particles have a larger surface area to volume ratio. If the drug in question is kept inside the particle then a larger volume to surface area will result in a more rapid release (Buzea et al., 2007). The size is one of the key factors in biodistribution, determining filtering by the lymph system and absorption by various tissues. It has been demonstrated that nanoparticles synthesized at greater than 200 nm are more likely to activate the lymphatic system and be removed from the vascular system sooner (Prokop and Davidson, 2008) In 2005 nanoparticle uptake in red blood cells was studied. Red blood cells were used to study passive uptake of particles due to their lack of a nucleus and other complex organelles. The study found that particles smaller than 200 nm we capable of passive cellular uptake (Geiser et al., 2005). Therefore, 200 nm represented an important limit due to filtration, immune activation and cellular uptake.

- **Surface Properties:**

It can now be seen that size has a large role to play in the effectiveness of any nanoparticle therapy, however, the surface characteristics of a nanoparticle also play a vital role in its interaction with cells and drug delivery (Bantz et al., 2014). Many factors must be taken into account for surface properties: targeting ligands, surface charge, stability and receptor binding (Khanbabaie and Jahanshahi, 2012). Clearance of nanoparticles from the system

is of obvious concern. Hydrophobic nanoparticles are more likely to trigger an immune response or be cleared by the lymphatic system through binding to other components of the blood (Kou L., 2013). Polyethylene glycol (PEG) can be used to diminish surface hydrophobicity and has been shown to decrease opsonization (Araujo et al., 1999).

Aggregation is also a real issue for any nanoparticle therapy. A nanoparticles particular chemistry and size are what define its interaction with any biological structure. Aggregation of smaller particles into a larger "clump" chances these characteristics and can have huge impacts on receptor binding and cellular uptake. Several methods have been developed to attempt to prevent aggregation of particles such as alteration of zeta potential or capping agents (Li and Kaner, 2006).

Binding moieties also play a role in nanoparticle therapies. Many particles store drugs inside the particle to protect them from the reducing conditions inside the vascular system. However, should it be better to have the drug on the outside or if targeting moieties/antibodies are to be attached then the surface chemistry of the nanoparticle is key in achieving these ends.

- **Drug Loading and Release:**

Perfecting the size and surface properties of a nanoparticle ensure that the drug is delivered to precisely where you want it without being cleared by the body's natural systems. However, there is no benefit to perfecting the chemistry of your particle if the drug cannot be released once it reaches the desired target. Many factors can go into stimulating drug

release e.g. pH, drug solubility, temperature, desorption of a surface bound drug, diffusion from inside the particle, dissolving of the particle matrix/polymer (Siepmann and Gopferich, 2001, Son G.H., 2017).

Two main types of nanoparticle are used for carrying drugs within the nanoparticle itself; Nanospheres and nanocapsules. Nanospheres are a homogeneous particle made from the introduction of surfactants and micelle formation during synthesis. Nanocapsules are heterogeneous and contain the drug inside a reservoir formed from a polymer (Mora-Huertas et al., 2010). Nanocapsules are formed through an ionic interaction between negatively charged and positively charged particles. Chitosan is one of the better-known materials used to create nanocapsule particles. An ionic interaction between negatively charged phospholipids and positively charged chitosan molecules forms the nanoparticle polymer mesh.

Nanospheres release their contents through erosion of the particle matrix until a rapid burst of drug is released in one go. Nanocapsules hold the drugs more dispersed throughout the particle mesh and require it to diffuse out. If there are ionic interactions between the drug and particle polymer strands, then other agents are required to induce release. For chitosan it is known that heparin induces rapid depolymerisation and release of ionicly bound molecules within the nanoparticle mesh due to its strong ionic interaction out competing other bound molecules (Raja et al., 2015).

- **Targeted Drug Delivery:**

43

Choosing the correct starting materials can improve the particles chances at reaching its desired target but to improve the specificity of any therapy, additional targeting moieties are required. Passive targeting is when a particle reaches its target without active methods via diffusion through large epithelial junctions for example (Varshosaz and Farzan, 2015). Active targeting involves conjugation of a specific ligand that is bound upon reaching its target. A perfect nanoparticle therapy can reach its target, recognize a specific ligand, bind to said ligand and deliver its payload to specific cells, tissues or pathogens. Targeting methods include peptides, antibodies and aptamers (Rihe Liu, 2009, Friedman et al., 2013). A wealth of literature already exists on antibody targeting of drug therapies (Padma, 2015) Small molecules predominate the nanoparticle targeting landscape due to their ease of synthesis and conjugation with the particles. Biotin (vitamin H) is a prime molecule in particle targeting due to its high affinity for streptavidin (Pramanik et al., 2016). Folic acids affinity for the folate receptor has also placed it as a valuable targeting moiety due to the high expression of the receptor on cancer cells (Zhao et al., 2008).

Han et al., studied a way to target chitosan nanoparticles at the tumour vasculature using an Arg-Gly-Asp (RGD) peptide which binds to $\alpha v \beta 3$-intagrin expressing cells. In this study Flow cytometry and fluorescence microscopy were used to assess the binding efficiency of the Arg, Gly, Asp-Chitosan-Nanoparticles (RGD-CH-NP). The RGD-CH-NP's were conjugated to an Alexa555 fluorophore and siRNA and were roughly 200nm in size. Han et al., used siRNA against periostin osteoblast specific factor (POSTN) was used to assess the knockdown efficiency of the siRNA conjugated RGD-CH-NP's. The RGD-CH-NP's were also tested *in-vivo*. Tissue sections from relevant locations were studied under x200

magnification to confirm αvβ3-intagrin mediated binding (Han et al., 2010). A2780ip2 (αvβ3 negative) and SKOV3ip1 (αvβ3-intagrin positive) breast cancer cell lines were used for the binding efficiency studies *in-vitro*. Comparison of binding efficiency of the CH-NP and RGD-CH-NP in each cell line showed the advantages of targeting αvβ3 with increased cellular uptake demonstrated by increased fluorescence in the given sections. Five concentrations were made of the RGD-CH-NP and tested in each cell line. Unsurprisingly, the five concentrations of NP had little effect on the A2780ip2 cells. In contrast, SKOV3ip1 cells showed a marked, concentration dependent, increase in binding. When comparing the binding efficiency of CH-NP and RGD-CH-NP using Alexa555 labelled nanoparticles, A2780ip2 cells show little increase in binding whereas SKOV3ip1 cells exhibit a threefold increase in binding efficiency with the addition of RGD (Han et al., 2010). This shows that the expression of αvβ3 is a viable target for RGD-CH-NP as it dramatically increases binding efficiency and offers a tumour vasculature specific target. Transmission electron microscopy (TEM) was also used to observe binding of RGD-CH-NP in tumour cells. TEM images confirmed the higher binding efficiency of SKOVip1 cells. Confocal microscopy was used to observe intracellular delivery of CH-NP and RGD-CH-NP. Alexa555 staining showed higher internalisation of siRNA/RGD-CH-NP in SKOV3ip1 cells compared to siRNA/CH-NP, again showing the increased efficacy gained by targeting αvβ3-intagrins. *In-vivo* studies for RGD-CH-NP's demonstrated similar increases in binding and targeting. A preliminary 48 h mouse study showed that the RGD-CH-NP's showed up in > 80% of areas examined with a 3-fold higher localisation in tumour tissues compared to CH-NP. This data from (Han et al., 2010), shows that chitosan nanoparticles with siRNA can induce a knockdown in tumour endothelial cell related genes and that targeting the particles to the

endothelial cells themselves can increase the localisation of the particles to the tumour vasculature.

Liposomes present another branch of active targeting. The similarity to the cell membrane allows liposomes to be tailored to incorporate the targeting ligands into their membrane. These membrane like properties allow for more natural release of the drugs upon reaching their target however liposomes come with their own drawbacks such as their fragility (Kelly et al., 2011, Singh and Lillard, 2009).

siRNA:

Fire and Mello discovered the revolutionary technology of small interference RNA molecules (siRNA) and their ability to induce sequence specific messenger RNA degradation (Fire et al., 1998). The mediators of this gene silencing are 21- and 22-nucleotide small interfering RNA duplexes. RNA duplexes are generated by cleaving longer double stranded RNA molecules with ribonuclease III. Gene silencing through double stranded RNA molecules had been shown to work previously in insects, however, had not been shown to be possible in mammalian cell lines. It was shown that high concentrations of double stranded RNA molecules induced an interferon response which would be associated with an inflammatory response in an organism. Sayda et al., showed that double stranded base paired 21- and 22-nucleotide siRNAs could induce degradation of specific mRNA targets within Drosophila embryos and so paved the way for mammalian siRNA technologies (Elbashir et al., 2001). Sequence specific degradation of messenger

RNA allows for targeted silencing of endogenous gene expression in many mammalian cells and has gained a lot of attention for its potential in cancer therapies.

Filleur et al., studied the potential of delivering VEGF siRNA to tumour endothelial cells to combat resistance to Thrombospondin-1 therapies. The strategy was to inhibit endothelial growth factor with siRNA thereby increasing the efficacy of any anti-VEGF therapy. The team implanted luciferase expressing cJ4-derived cells into nude mice and injected luciferase siRNA either into the tail vain or directly into the tumour (Filleur et al., 2003). For this study there was no attempt to target the naked siRNA. Interestingly, the direct tumour administration had no effect on luciferase activity whereas systemic administration showed a 50% knockdown of luciferase.

Schneider et al., uses bispecific VEGF-R2 antibodies to target anti CD31 (PECAM) siRNA to endothelial cells. MCF-7 xenograft cells which did not express CD31 were implanted in mice and did not express CD31 ensuring any knockdown was purely endothelial related (Schneider et al., 2012).

Double stranded RNA sequences pertaining to the target gene are transduced into the cells. Upon entering the cell, the RNA gets incorporated into a variety of proteins forming the RISC complex. The double stranded RNA is then cleaved into two separate strands and the less stable strand is retained within the complex. The complex now "scans" for complementary sequences, binds them and induces mRNA cleavage. mRNA coming from the nucleus is now bound and cut as it is recognised as foreign by the cell

resulting in a lack of translation from the target mRNA to its relevant protein, thus

silencing the gene (Figure 1.7).

Figure 1.7
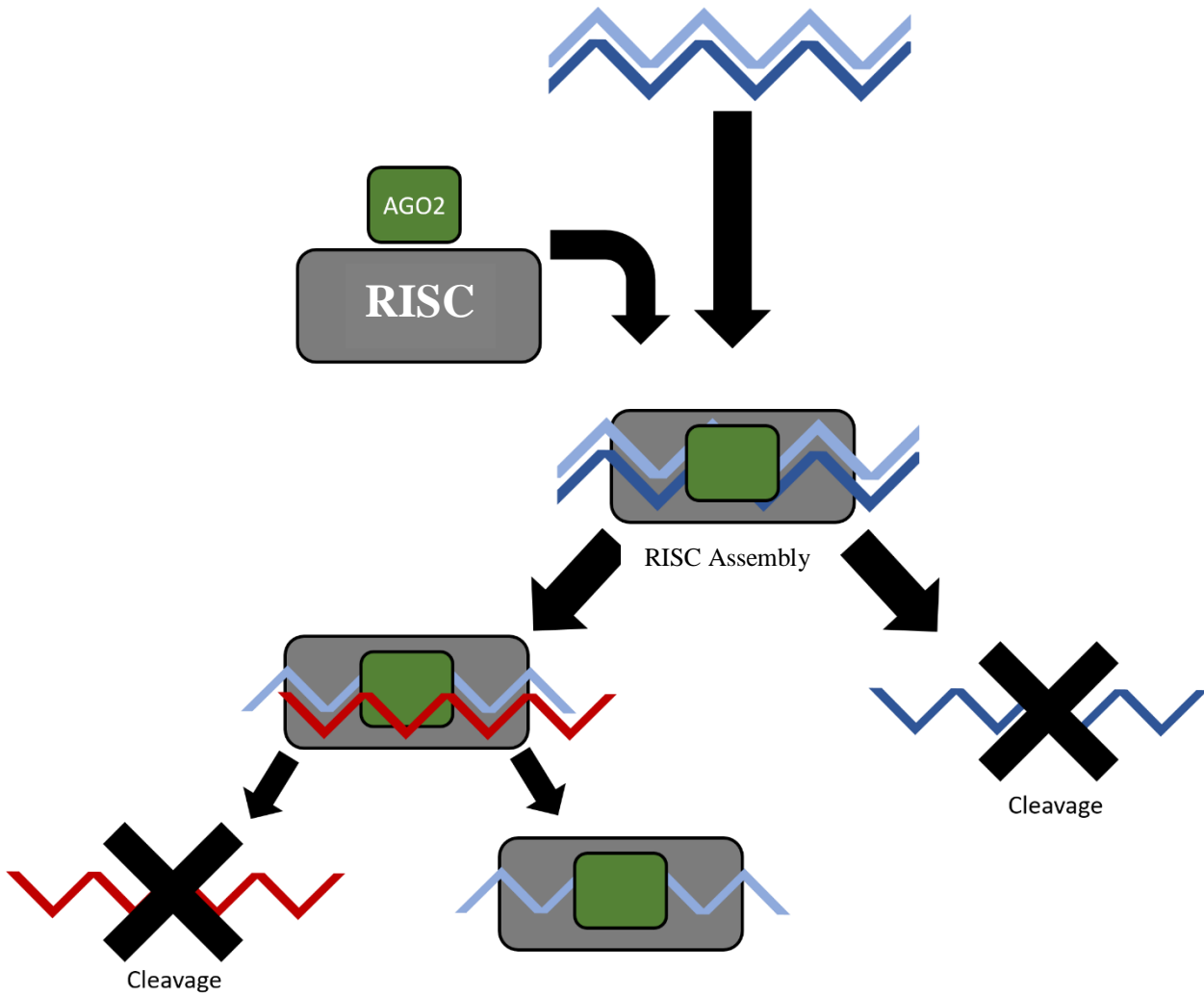
Figure 1.7 | siRNA and The RISC Complex

siRNA (blue) enters the cell inducing the formation of the RISC complex (grey). AGO2 (green) binds to the complex, trapping the double stranded RNA. The siRNA is trapped inside the complex and the double strands are separated. One strand is cleaved. The complex then diffuses around the cell interior, binding any complementary strands (red) which are then separated again, and the complimentary strand cleaved. The binding and cleaving of complimentary strands result in removal of any complimentary mRNA which effectively silences the relevant gene.

Nanoparticles and their use as siRNA carriers

Binding siRNA to a vector can improve delivery efficiency, targeting efficiency and offer protection for the siRNA from nucleases and other damaging conditions. When designing a vector to transport siRNA molecules to the tumour vasculature *in-vivo* the first, and potentially most important, decision must be the nature of that vector. Use of nanoparticles in cancer research has increased over the last 10 years. The potential for conjugation of large numbers of drugs or imaging probes offers novel opportunities for improving efficacy and resolution of treatments and research methods.

Though the material used as the basis for the nanoparticle structure is important, the next step must be to establish the most effective way to bind the siRNA. siRNA can be attached to nanoparticles through several methods. Table 1 column 2 lists the various methods for siRNA conjugation discussed here. Some methods such as electrostatic binding present with easy release of siRNA but do not retain siRNA under physiological conditions as effectively.

Though not targeting vascular endothelial cells, Katas and Alpar studied three methods for binding siRNA to chitosan nanoparticles; simple complexation and the two forms of ionic gelation, adsorption and entrapment (Katas et al., 2013). Varying forms of chitosan was

used in nanoparticle synthesis to assess the biological activity. Sodium tripolyphosphate (TPP) was added to the nanoparticle conjugate to increase the positive charge and aid in siRNA adsorption and entrapment. Chitosan glutamate showed the highest silencing of the pGL3 luciferase gene transfected into CHO K1 cells resulting in a 51% gene knockdown with simple siRNA complexation, 82% with TPP-entrapment and 63% with TPP-adsorption at 24 h after incubation. In CHO K1, cells the chitosan glutamate showed higher knockdown percentages than Lipofectamine. Interestingly, when used in HEK293T cells, the chitosan glutamate nanoparticles were 22%, 14% and 64% less efficient than the Lipofectamine for TPP-adsorbed, TPP-entrapped and chitosan-siRNA complex respectively (Katas et al., 2013). This discrepancy in knockdown efficiency shows the importance of choosing the siRNA binding method best suited for the chosen nanoparticle and for the chosen cell type. It is for this reason that targeting tumour vasculature appears to be a rational choice. Tumour vessel endothelium vary genetically and phenotypically far less than the tumour cells themselves. Designing a nanoparticle vector to transport siRNA to the tumour vasculature would require far less alteration between tumour types and patient variations.

MTT cell viability tests showed over 90% average cell survival for the chitosan-siRNA complex and naked siRNA. MTT viability assays test the reducing power of the mitochondria in the cell. If a chemical kills a cell, it will no longer be able to reduce the components of the MTT assay showing the cells to be non-viable. TPP-chitosan nanoparticles used for entrapment and adsorption had 18-40% loss in cell survival. Some

TPP-chitosan treated cells did recover 48 h after incubation; however, this does indicate transient stress when exposed to these TPP-chitosan nanoparticles.

Knockdown efficiency of the chitosan particles was represented by percentage knockdown and relative response ratio. Silencing percentages and ratios were calculated through a decrease in fluorescence due to gene silencing. The luminescent pRL-TK gene was used to account for cell death or off target effects. The method for attaining a comparison of luminescence were not mentioned and no images are provided. Gel electrophoresis and Western Blotting would have been a more accurate way to measure gene knockdown as it does not rely on selecting image slices if confocal imaging was used.

Varied cell response presents a large problem with assessing the effectiveness of nanoparticle siRNA delivery *in-vitro*. Some immortalised cells are extremely efficient in uptake and delivery of nanoparticles whereas some primary cell types take up foreign structures far less readily. Studies that knockdown exogenous genes transfected into immortalised cells must be looked at with caution. Immortalised cells that have been shown to be easily transfectable with exogenous genes are not representative of the cellular trafficking and filtering of healthy endothelial cells.

Aim of this thesis:

The overarching aim of this thesis is the development of a method for the delivery of therapeutics to perturbate the expression of CLEC14A in endothelial cells in-vivo. This will be attempted through two methods. First the development of a nanoparticle that can bind and retain CLEC14A siRNA to protect it from the reducing conditions and enzymatic breakdown within an organism's vasculature. The particle will be tested for siRNA binding, siRNA release, Cellular uptake of the nanoparticle, method for cellular uptake and knockdown of CLEC14A using only siRNA bound nanoparticles. Methods for improving the knockdown of the particles will be examined.

A CLEC14A fusion vaccine will be developed with the aim of breaking immune tolerance to CLEC14A so that an immune response can be mounted against CLEC14A expressing cells in tumour blood vessels. The nanoparticles created in the previous siRNA studies will be tested for binding and retaining proteins to better deliver the protein to antigen presenting cells.

Finally, in-vivo and gene array studies will be performed to look at the biodistribution of the nanoparticles in a mouse model as well as the impact of the nanoparticles on gene expression within endothelial cells.

Chapter II.

Materials and Methods

Materials:

Solution Name:	Components/Reagents:
Phosphate buffered saline (PBS)	140 mM NaCl, 10 mM Na_2HPO_4, 2.7 mM KCl and 1.76 mM KH_2PO_4, pH 7.4
Phosphate buffered saline TWEEN (PBS-T)	140 mM NaCl, 10 mM Na_2HPO_4, 2.7 mM KCl and 1.76 mM KH_2PO_4, pH 7.4, 0.1% (v/v) TWEEN
Tris-acetate-EDTA (TAE)	40 mM Tris, 20 mM acetic acid, 1 mM EDTA
6 x SDS-PAGE sample buffer (reducing)	375 mM Tris-HCl pH 6.8, 6% (w/v) SDS, 48% (v/v) glycerol, 0.03% (w/v) bromophenol blue, 9% (v/v) β-mercaptoethanol
6 x SDS-PAGE sample buffer (non-reducing)	375 mM Tris-HCl pH 6.8, 6% (w/v) SDS, 48% (v/v) glycerol, 0.03% (w/v) bromophenol blue
Resolving gel buffer	375 mM Tris-HCl pH 8.8, 0.1% (w/v) SDS
Stacking gel buffer	125 mM Tris-HCl pH 6.8, 0.1% (w/v) SDS
SDS-PAGE running buffer	25 mM Tris, 250 mM glycine, 0.1% (w/v) SDS. pH 8.3
Western blot transfer buffer	25 mM Tris, 187.2 mM glycine, 20% methanol
RIPA Buffer	150 mM NaCl, 1% (v/v) NP_4O, 0.5 % (v/v) DOC, 0.1 % (w/v) SDS, 50 mM Tris-HCl
Ni-NTA Agarose beads washing buffer	PBS, 0.5 M NaCl, 10 mM imidazole
Elution buffer for Ni-NTA Agarose beads	PBS, 0.5 M NaCl, 250 mM imidazole
Luria Broth (LB) media	In 1L of dH_2O, 10 g Tryptone, 5 g Yeast, 5 g NaCl

Table 2.1. Buffers and Solutions commonly used in experiments with concentrations of each chemical component.

Antibody Name:	Manufacturer:	Species:	Concentration used:
CLEC14A Polyclonal	R&D (#AF4968)	Sheep	WB (0.1 µg/mL)
CLEC14A monoclonal (Clone CRT4)	N/A – Produced in laboratory	Mouse	WB (0.1 µg/mL) NP Conjugation (30 µL/5 mL)

Table 2.2. Primary Antibodies:

Western Blot (WB), ELISA, Nanoparticle Conjugation.

Antibody Name:	Manufacturer:	Species :	Concentration used:
Anti-rabbit HRP	GE Healthcare (#NA9340V)	Donkey	WB (1:5000)
Anti-sheep HRP	R&D (#HAF016)	Donkey	WB (1:5000)
Anti-mouse HRP	Dako (#P0447)	Goat	WB (1:5000)
Anti-Mouse 12 nm Gold	Abcam (ab39619)	Goat	NP Conjugation (30 µL/5 mL)
Anti-mouse Alexafluor 488	Abcam (ABIN5624060)	Goat	NP Conjugation (30 µL/5 mL)

Table 2.3. Secondary antibodies with manufacturer and catalogue details, species raised in and application in the lab e.g. Western Blot (WesBlot), Nanoparticle Conjugation (NP Conjugation)

Protein:	Epitope tags:	Expression system:	Buffer:
Mouse CLEC14A-Fc	Human IgG1 Fc	HEK293T	PBS
Human CLEC14A-Fc	Human IgG1 Fc	HEK293T	PBS

Table 2.4. Recombinant proteins showing epitope tags, the system used for expression, for what application they were used and the buffer they were kept in. These were synthesised in the Bicknell Lab.

Name and Description:	Sequence:
mCLEC14a-FrC 629-648 bp F	CAGAGGTGAGTGCGATGTGT
mCLEC14A-FrC 1806-1825 bp R	TGTTGTTGTTGCAACGGTCC

Table 2.5 Oligonucleotide primers used for sequencing. The sequence is displayed 5'-3'. Created by Genescript.

Plasmid contents and name:	Restriction enzymes for digest:
CLEC-FrC (pWPI)	PstI-HF
FrC (pcDNA3)	HindIII , XhoI
L-VLRB (pET21a+)	NdeI , XhoI
F-VLRB (pET21a+)	NdeI , XhoI

Table 2.6. Plasmids used for protein production and restriction enzymes used to extract relevant fragments. FrC plasmids were created by the Kai Tolner group (University Birmingham) and the VLRB plasmids were synthesised by Genescript.

Cell Type:	Cell Source:	Medium:
HEK293-T	Human Embryonic Kidney Cells	DMEM
HUVEC	Human Umbilical Vein Endothelial Cells	M199/DMEM with additions
LLC	Mouse Lewis Lung Carcinoma	DMEM
HeLa	Human Cervical Cancer Cells	DMEM

Table 2.7. Cell Types The varying cell types used for experimentation. HEK293 for cell uptake and protein production. HUVEC for knockdown studies. LLC for mouse tumour implantation. HeLa for cell imaging.

Target Gene:	Sequence:	Supplier:
CLEC14A D1	GAACAAGACAAUUCAGUAA	Eurogentec (Custom)
CLEC14A D2	CAAUCAGGGUCGACGAGAA	Eurogentec (Custom)

Table 2.8. siRNA: The two duplexes of siRNA used to knockdown siRNA. It was found that Duplex 2 (D2) was more effective than D1 and so it was D2 that was used for the nanoparticle studies. Duplexes were synthesised by Source Bioscience.

Methods:

Polymerase Chain Reaction

Polymerase chain reaction (PCR) was performed on RNA extracted from cell lysis. RNA from the cell lysis was extracted via the RNeasy RNA extraction Kit (Qiagen) using the kits recommended protocol. The purified RNA was converted to complimentary DNA (cDNA) via the High-Capacity RNA-to-cDNA Kit™ (Thermo Scientific) using the provided protocol with the kit. PCR amplifications used forward and reverse oligonucleotide primers that were newly designed for the CLEC-FrC construct (Table Below).

The Phusion high fidelity DNA polymerase kit New England Biolabs (NEB) was used for the PCR protocol. Specially designed forward and reverse primers were designed for the CLEC-FrC construct (Genscript).

Template cDNA from HEK293 lysate	1 μL (500 ng)
5xPhusion HF buffer	5 μL
10mM dNTPs	0.5 μL
10μM Forward primer	1.25 μL
10μM Reverse primer	1.25 μL
DMSO	0.75 μL
Nuclease free dH2O	9.75 μL

PCR was carried out as follows, with annealing temperatures and protocol taken from

New England Biolabs and the NEB Phusion annealing temperature calculation program.

Initial denaturation 98°C 30 seconds
Denaturation 98°C 30 seconds
Annealing 55 °C 20 seconds 28 cycles
Extension 72°C 30 seconds/ kb
Final extension 72°C 7 minutes

Restriction Enzyme Digest:

All restriction enzymes were ordered from NEB and were used with the manufacturer's

suggested protocol. Enzyme digests were incubated at 37°C for 1 hour.

Digested plasmids were separated by agarose gel electrophoresis. 1% agarose gels were

made with 1 gram agarose (Bioline) in 100 ml of TAE buffer (table 1). The solution was

microwaved for 2-3 minutes until the agarose was completely dissolved and the resultant

liquid was boiling. The agarose solution was left to cool at room temperature. 10 µL of

SYBR safe DNA gel stain (Invitrogen) was added after a 2-3 minutes of cooling. 6x DNA

loading dye (Themo scientific) was added to the sample before loading onto the agarose

gel. A 1kb DNA ladder (Themo scientific) was added to the first well to assess size of the

DNA fragments.

The New England Biolab protocol was followed for all restriction enzyme digests.

DNA/RNA Agarose Gel Electrophoresis:

Molecular Biology grade agarose (Sigma) was used at varying concentrations.

Restriction enzyme Restriction enzyme digest, 1% (w/v)

siRNA dissociation 4% (w/v)

Streptavidin dissociation 5% (w/v)

All DNA agarose gels were made in 1 x TAE buffer with 1% SYBR safe DNA gel stain (Invitrogen). siRNA samples that contained a fluorophore did not require SYBR safe labelling. DNA/siRNA samples were mixed with 6x DNA loading dye (Thermo scientific). All DNA gels were run with Generuler 1kb DNA ladder unless specified otherwise (Them scientific).

Restriction enzyme digests were run at 100 V for 30 minutes visualized using the GeneSnap imaging system. siRNA gels were run at 110 V for 30 minutes and were visualized using the Odyssey® Fc Imaging System (Li-COR).

DNA and RNA gel electrophoresis followed the protocol laid out by Addgene.

Electrophoresis experiments involving nanoparticles were developed specifically for this thesis.

Bacterial Transformations:

Bacterial transformations were performed in competent gold efficiency DH5α *E. coli* (Bioline). Bacteria were kept in 20 µL aliquots which were thawed on ice and plasmid was added. The mix was incubated for 20 minutes on ice and then heat-shocked in a 42°C water bath for 90 seconds. The transformation mix was removed from the water bath and incubated for 2 minutes on ice. 200 µL SOC media was added and the mix was transferred to a shaking incubator at 37°C for 1 hour. After the hour incubation the mix was spread onto a pre-warmed LB agar plate, containing relevant antibiotic, and grown over night for isolated colonies.

Bacterial transformations were performed using the ThermoFisher suggested protocol.

Plasmid DNA Isolation:

A single colony of *E. coli* was selected from the transformation plates and introduced into 4 mL of LB media with the appropriate antibiotic (Ampicillin 100 µg/mL). Colonies were grown overnight in a shaking incubator at 37°C. The overnight cultures were pelleted by centrifugation (13,000 rpm) and plasmids isolated with GeneJET plasmid miniprep (Thermo scientific). DNA concentration was measured using a NanoDrop 1000 spectrophotometer (Thermo scientific).

The Thermo scientific protocol was followed for Plasmid DNA isolation.

Sequencing:

DNA was sequenced using the terminal nucleotide sequencing method and was performed by the functional genomics service (The University of Birmingham).

Gene Array:

The gene arrays were purchased for Source Biosciences. HUVEC cells were treated with siRNA containing chitosan nanoparticles and the RNA was extracted with RNeasy isolation kit (Qiagen 74104) (Full nanoparticle transfection protocol can be seen in: Nanoparticle Transfections section of materials and methods). RNA samples were sent to Source Biosciences to perform the gene array. Analysis of the data was aided by Dr Zsuzsanna Nagy (z.nagy@bham.ac.uk).

Cell Culture:

Cell culture experiments were performed in a laminar flow hood under sterile conditions. Immortalized cell lines (HEK293 and HeLa) were grown in Dulbecco's modified Eagle's serum (DMEM) (Sigman-Aldrich, Gillingham UK) with 10% foetal calf serum (FCS GIBCO Life technologies), 4mM L-glutamine (Life technologies), 100 µg/ml penicillin and 100 µg/ml streptomycin (Life technologies. Primary cells (HUVEC) were grown in Medium 199 10% FCS, 1% bovine brain extract (Maciag et al., 1979), 90 µg/ml heparin (Sigma Aldrich), 4 mM L-glutamine (Life technologies) 100 µg/ml penicillin and 100 µg/ml streptomycin (Life technologies).

This protocol was developed by the Bicknell Lab.

siRNA Transfections

All small interfering RNA (siRNA) duplexes were ordered from Eurogentec and made up to a stock concentration of 100 µM in RNase free water to be stored in aliquots at -80°C. The day before siRNA transfection, 175,000 cells were plated in antibiotic free media onto a gelatine coated 6 well plate. The next day, for each separate transfection, two mixes were made. The first contained 167.5 µL Optimem medium (Thermofisher 31985062) and 2.5 µL of 20 µM siRNA (resulting in a final concentration of 50 nM when added to the cell culture. The second mixes 27 µL Optimem with 3 µL RNAiMAX Lipofectamine (Invitrogen #13778-150) (resulting in a final concentration of 0.3%). Both of these mixtures were left at room temperature for 10 minutes. After 10 minutes the lipofectamine mix was added to the siRNA mix and this new mixture was again left for 10 minutes at room temperature. 800 µL Optimem was added to each well of the 6 well plate and after the 10 minute incubation, the 200 µL siRNA/lipofectamine mix was added to the cells as well. The cells were incubated at 37°C for 4 hours upon which the media is removed and replaced by media without antibiotics. The cells were left for the next day and on the 4th day were collected and lysed for analysis.

This protocol was developed by the Bicknell Lab.

Lentiviral Transduction:

Lentiviral transduction was performed in HEK293T cells. Plasmid transfection was achieved through the use of linear molecular weight 25000 Da polyethyleneimine (PEI) (Sigma-Aldrich #408727) using a 1:4 ratio of DNA:PEI. For 10 cm plates, HEK293T cells

were transfected with a pWPI plasmid containing the gene of interest (4.39 µg), psPax2 (3.29 µg) and pMD2G (1.32 µg). 5 HEK293T plates were transduced and left to generate lentiviral particles for 24 hours. The media from 5 plates was used to transduce 1 plate of fresh HEK293T cells and so media from the 5 was concentrated down using Corning Spin-X UF concentrators with 5 kDa molecular weight cut off (Sigma-Aldrich #CLS431487). Lentiviral constructs contain an internal ribosome entry site (IRES) followed by the GFP gene which results in the translation of both the gene of interest and GFP. GFP expression allows for microscope or flow cytometry analysis to asses transduction efficiency.

The specific lentivirus protocol used was developed by the Bicknell Lab.

Nanoparticle Transfection:

Nanoparticle transfection was achieved without PEI or lipofectamine. Simply: A nanoparticle stock was made up in 1 ml of the required cell medium. The stock contained 4.75 ng siRNA. 10 µL, 20 µL, 30 µL or 40 µL were taken from the stock and mixed with the cell medium to be incubated with the HUVEC. These volumes provided the 1x 2x 3x and 4x concentrations used for the knockdowns. 1x concentration of the nanoparticles contains 50 nM siRNA and each increasing volume contains more nanoparticles and thereby more siRNA. Nanoparticle stock was added to 900 µL media in a 6 well plate with 175,000 cells with more cell medium added to make the total volume to 1 mL.

This method was modified for this thesis from the standard siRNA transfection (laid out in (siRNA transfections) but replaced the lipofectamine and siRNA steps with addition of siRNA containing nanoparticles.

HUVEC Isolation:

Human umbilical cords were collected from Birmingham Women's Hospital with written consent from the mother. Upon return to the lab the cords were placed in a laminar flow hood, cleaned thoroughly with 70% ethanol (v/v) and checked for any damage. Olive cannulas were attached to the cord via two cable ties. Sterile PBS was flushed through the cannulas and cord to clear blood clots. The cannula at one end of the cord was closed and collagenase 1A (Sigma-Aldrich #C2674) was injected into the cord to fill it. The cord was incubated at 37°C for 20 minutes after which one of the cannulas was opened and the detached endothelial cells washed out with two rounds of 20 mL PBS into a 50 mL falcon tube. The cells were centrifuged at 1100 rpm for 5 minutes and the supernatant removed. The pellet was re-suspended in either M199 or DMEM 10 μg/mL gentamicin and 250 ng/mL amphotericin B (Thermo Scientific #R01510), then seeded onto gelatine coated cell culture plates. The medium was changed the next day and again 24 hours later. The cells were considered passage 1 when they were confluent enough to split from 1 10 cm dish to 3.

The specific HUVEC isolation from umbilical cords protocol used was developed by the Bicknell Lab. Licence 70/8704 held by Roy Bicknell

Cell Lysis

Cells were washed twice with PBS and removed from the cell culture dish via cell scraping or exposure to trypsin (for a 10 cm plate 2 ml of trypsin was added and incubated for two minutes at room temperature). For HEK293T cells 500 μL of lysis (RIPA) buffer was added to a 10 cm plate and cells were scraped from top to bottom as the plate was rotated around its axis. After collection, the cells were centrifuged at 1100 rpm for 5 minutes to

remove trypsin enzyme. Once centrifuged lysis buffer was added to the cells. After cell collection through cell scraping or trypsin digest and addition of lysis buffer, cells were vortexed for 1 minute. Large cell fragments were removed from the lysis through centrifugation at 15,000 rpm at 4°C for 30 minutes. The supernatant was removed and added to a fresh micro centrifuge tube to be stored at -20.

The Thermofisher cell lysis protocol was followed.

SDS PAGE Western Blotting

Proteins were separated using the chromatography method of sodium dodecyl sulphate polyacrylamide gel electrophoresis (SDS-PAGE). SDS-PAGE gels were set in disposable XCell SureLOCK mini gel Cassettes (Thermo Scientific). Once set the gels were loaded and run in XCell Surelock apparatus in an SDS running buffer at 80 mV through the stacking gel and 140 mV through the resolving gel. The resolving gel can be made in several different percentages usually ranging from 8-18% with the most common being 10%. A 10% gel was made using 97.5 mM Tris pH 8.8, 0.025% SDS, 0.001% ammonium persulphate, 0.001% TEMED with 10% polyacrylamide.

Stacking gel was made with 15.8 mM Tris pH 6.8, 0.013% SDS, 5% polyacrylamide, 0.001% ammonium persulphate and 0.001% TEMED. Once proteins were run on the SDS gel they were transferred to PVDF membranes using transfer buffer inside the XCell Surelock apparatus for 2 hours at 30 mV. After transfer, PVDF membranes were blocked

in 2% (w/v) milk in PBST for 1 hour at room temperature. After blocking, PVDF membranes were washed once in PBS-T and then incubated with Primary antibodies (concentrations found in table 2.2). PVDF membranes were incubated with the primary antibodies for 1 hour at room temperature or 4°C over night. Post primary antibody incubation, membranes were washed 5 times at 5 minutes per time in PBS-T. PVDF membranes were then incubated with HRP conjugated secondary antibodies for 1 hour at room temperature (concentration can be seen in table 2.3). Again, to remove non-specific binding after incubation with secondary antibodies the membrane was washed 5 times at 5 minutes per wash in PBS-T. HRP conjugated antibodies were detected using enhanced chemi-luminescence (ECL) via Amersham ECL western blotting detection reagent (GE Healthcare). The membrane was visualised either using Amersham Hyperfilm X-ray film (GE Healthcare) or Odyssey® Fc Imaging System (Li-COR).

Western Blot protocol was adapted from the Thermofisher protocol by the Bicknell Lab.

ELISAs

Enzyme-linked immunosorbent assays (ELISAs) were used to assess the binding efficacy of the antibody linked nanoparticles.

First, 100 µL of CLEC14A antigen (diluted 1 in 500 PBS) was added to each of the relevant wells in the 96 well Nunc MaxiSorp™ flat-bottom dish and incubated at 4ºC overnight. The next day, liquid was removed from the wells and 200 µL of blocking solution (10% milk w/v in PBS) was added. The plate was then incubated for a further 2 hours at room

temperature after which it was washed 5 times with 100 µL PBS-T. Next, 200 µL sonicated antibody labelled nanoparticles were added to each well including the controls. The nanoparticles were incubated on the plate for 1.5 hours at room temperature with constant agitation. After the incubation period, all wells were washed 5 times with 100 µL PBS-T. After the final wash the plates were imaged on the Odyssey® Fc Imaging System (Li-COR).

This ELISA method was developed for this thesis by adaptation of the standard ELISA method found in Engvall and Perlmann (Engvall and Perlmann, 1972).

Production of CLEC14A-FrC

The CLEC14A-FrC construct was cloned in the pWPI plasmid. The plasmid was acquired from the Kai Tollner group (University of Birmingham 4th floor IBR) and was amplified in gold efficiency DH5α *E. coli*. The concentration of amplified plasmid was calculated through spectrophotometry analysis with the NanoDrop 1000 spectrophotometer (Thermo scientific).

The protein was produced in HEK293-T cells. The gene was transfected into HEK293-T cells via lentiviral transduction (Lentivirus protocol can be seen in Lentiviral Transduction). Transduced cells were transferred to 10 cm cell culture dishes and grown to confluency in DMEM. The cell medium was replaced with Opti-MEM and left to produce and secrete the recombinant protein.

Protein was harvested through several methods including collection of the cell medium (Opti-MEM) and lysis buffer and sonication of cells using the Thermofisher protein harvesting protocol. The cell lysis was analysed for presence of the target protein through western blotting. No purification steps were performed.

Production and Purification of CLEC14A-VLRB

The L-VLRB plasmid was transduced into SHuffle® T7 Express lysY Competent *E. coli* (NEB #C3030J) using the heat shock method. Bacteria were grown over night at 30°C in 150 ml LB medium, ampicillin (100 µg/ml). To ensure bacteria were in the exponential growth phase, OD_{590} was measured and the culture was diluted down with LB broth to OD_{590} 0.3. The culture was then left to grow until it reached OD_{590} 0.5. At OD_{590} 1mM IPTG (ProMega #V395D) was added to all but two samples to induce protein production. 10 ml samples were removed at 0.5 hrs, 1 hr, 2 hr, 4 hr and 22 hrs and frozen. The samples were defrosted and centrifuged at 4000rpm for 20 mins. The pellets were washed three times in PBS and lysed using sonication. The resultant lysis was left on ice for 30 minutes. The lysis was centrifuged again for 15 minutes at 15,000 rpm and 4°C. The supernatant and the pellet were kept. The Bradford assay was used to measure protein concentration and ensure equal loading into the SDS-PAGE. The SDS-PAGE was washed in Coomassie Brilliant Blue Dye (Expedeon) to visualize the proteins.

Protein purification was achieved through Ni-NTA Agarose Beads (Qiagen) which bind to the HIS tag on the fusion protein. After sonication of the cells, urea was added to make a 5 M concentration (Saupe et al., 2017). The urea containing solution was then mixed with 20 µL Ni-NTA agarose beads and incubated over night at 4°C. Urea is used to prevent

multimerising of the protein which hinders binding to the Ni-NTA beads (Chowdhury et al., 2014). After incubation the beads were centrifuged and washed. The protein should remain bound to the beads, but the supernatant was kept for future analysis in case of a low protein yield. Protein was removed from the beads by boiling them at 100°C for 5 minutes after addition of 10 µL 6x SDS-PAGE reducing loading buffer. The loading buffer and high temperature disrupt the binding of the HIS tag to the Ni-NTA beads. The resultant slurry was run on an SDS-PAGE to visualize the proteins with an anti polyhistidine tag monoclonal antibody.

The yield was calculated through the growth of a 1 L culture of transformed SHuffle bacteria overnight. The culture was split into 4 250 mL samples and each centrifuged to produce a pellet. The pellet was again washed 3 times and re-suspended in 20 ml PBS. 10 ml from each 20 ml was extracted and sonicated after the addition of 5 M urea. The remaining 10 ml was sonicated without urea. 500 µL of each 10 mL sample was taken and centrifuged at 4000 rpm for 20 minutes. The supernatant was removed, and the pellet was re-suspended in 500 µL PBS. The remaining 9.5 mL was also centrifuged at the same speed for 20 minutes. The supernatant from the 9.5 mL samples was removed and 50 µL of Ni-NTA agarose beads (Qiagen) was added. The bead mixture was incubated at 4ºC overnight. After incubation the bead mixture was centrifuged at 12,000 rpm for 1 minute. The supernatant was discarded, and the beads were washed 5 times with agarose beads washing buffer. The protein was eluted from the beads by adding 100 µL elution buffer to 40 µL of beads and incubating at room temperature for 30 minutes. The beads were removed from the mixture via centrifugation at 12,000 rpm for 1 minute. The supernatant was removed

and tested for the presence of protein using the NanoDrop 1000 spectrophotometer (Thermo scientific). Yield was calculated through the use of BSA standards. After confirmation of the presence of protein the elutants were separated using reducing and non-reducing SDS-PAGE. L-VLRB is known to form multimers of varying numbers and so both reducing and non-reducing were used to maximize the possibility of seeing multimers and the individual monomer unit. BSA standards of 5 µg, 2 µg and 1 µg were also loaded onto the gel to provide a reference for calculating the yield. Proteins were visualised on the gel using Coomassie Brilliant Blue Dye (Expedeon). The gels were imaged using the Odyssey® Fc Imaging System (Li-COR).

This protocol was adapted from (Saupe et al., 2017)

Nanoparticle Synthesis:

Silica Nanoparticles Synthesis:

All chemicals for silica nanoparticle synthesis were purchased from Sigma-Aldrich. Mesoporous silica nanoparticle synthesis was achieved by dissolving 100 mg cetyltrimethylammonium bromide (95%) in 48 mL dH$_2$O and 350 µL sodium hydroxide (2M). The solution was heated to 80°C. Once at 80°C, 0.5 mL tetraethylorthosilicate (98%) was added. 127 µL 3-(trihydroxysilyl)propylmethylphosphonate (42%) was added 15 min later and was stirred for 2 hours. The synthesised particles were centrifuged at 15,000 rpm for 30 min and washed with methanol twice. The surfactants that enabled a porous surface

were removed by re-suspended and refluxing the particles in 20 mL methanol and 1 mL hydrochloric acid (12.1M) for 24 hours. The final particles were collected and washed through centrifugation with ethanol.

5 mg of the particles were re-suspended in a 2.5 mg polyethyleneimine – 1 mL absolute ethanol, solution under magnetic stirring for 30 min. Loading of siRNA onto the nanoparticles was achieved by incubating siRNA and nanoparticles together in serum free medium at a 1:25 mass ratio under agitation at 4°C. Particles were collected 24 hours after via centrifugation

The synthesis of silica nanoparticles followed the protocol in (Hom et al., 2010).

Chitosan Nanoparticles (ChNP):

Chitosan nanoparticles were synthesized using low molecular weight deacetylated (90%) chitosan and tripolyphosphate (TPP). Nanoparticle size is directly affected by chitosan concentration and inversely affected by TPP concentration. For ChNP: 1.3 ml 0.1% TPP (w/v) deionized water, was added dropwise to 3 ml 0.1% chitosan (w/v) glacial acetic acid under 15,000 rpm magnetic stirring. The solution was stirred magnetically at 15,000 rpm for 30 minutes then left at room temperature for a further 30 minutes. Finally, the particles were collected by centrifuging at 15,000 g for 30 minutes at 4°C. The supernatant was removed, and particles were re-suspended in desired solution.

The synthesis of chitosan nanoparticles adapted the protocol in (Katas et al., 2013). *It was found during experimentation for this project that increasing the rate of magnetic stirring resulted in more reliable nanoparticle size.*

Chitosan Glutamate Nanoparticles (ChGlutNP):

Chitosan glutamate (PROTASAN™ UP G 213) particles were synthesized in a very similar process to the normal chitosan particles. Chitosan glutamate particles resulted in an increased size for the same concentration of chitosan compared to the normal chitosan. To decrease the size of the particles the concentration of chitosan and TPP was reduced to 0.025% and 0.05% respectively as well as increasing the temperature of the solution to 45°C. These particles will be referred to as NP-Glut-siRNA and NP-Glut-Blank (For particles without siRNA).

PROTASAN™ UP G 213 is 75-90% deacetylated. Normal base chitosan is only ~50% deacetylated. The extra deacetylation is replaced by glutamate residues. The glutamate content is 30-50%. The molecular weight is 150,000-600,000 g/mol and contains ultra-low levels of endotoxins and proteins.

Viscosity [mPa*s]: 20-200

Appr. Mw [kDa]: 200-600

Deacetylation [%]: 75-90

Endotoxins [EU/g] : ≤ 100

This protocol was devised purely for this thesis and was an adaptation of the protocol used to synthesise the ChNP's.

Ionic Gelation

Ionic gelation is the process of "trapping" molecules inside the chitosan complex. To achieve ionic gelation, the molecule in question must be negatively charged and be added dropwise in the same manner as the crosslinker TPP. Ionic interactions occur during the dropwise addition of the crosslinking agent. Ionic interactions between the positively charged amino groups on chitosan and the negative groups of the polyanion (crosslinker) induce polymerisation of the chitosan strands into the nanoparticle structure.

The entrapment of siRNA inside of chitosan nanoparticles followed the protocol laid out in (Katas et al., 2013).

Antibody Conjugation to Nanoparticle Surface:

NP-Antibody-1:

Chitosan-Antibody conjugates were formed using the EDC sulfo-NHS reaction. 15 mg sulfo-NHS and 30 mg EDAC were added to 5 mL 0.1% chitosan glutamate in PBS (w/v). To this mixture 30 µL CRT4 antibody was added (0.67 mg/mL). The solution was agitated at room temperature for one hour. Nanoparticles were synthesised in exactly the same method as with the ChNP particles but using the 5 mL PBS-chitosan-antibody reaction mixture for the source of the 3 mL chitosan. The particles were collected through

centrifugation at 15,000 rpm for 30 minutes and washed with PBS twice to remove any unbound antibody. These particles will be referred to as NP-Antibody-1.

This the method for conjugation of antibodies to chitosan was taken from (Lee et al., 2012), *however the synthesis of the particles after conjugation of the antibodies was developed during this thesis.*

NP-Antibody-2:

The activated antibodies method involved synthesizing ChGlutNP first. Before synthesis of the nanoparticles, 30 µL antibody was mixed with 30 mg EDAC and 15 mg sulfo-NHS in 5 mL PBS. The EDC reaction activates the carboxyl groups on the antibodies and prepares them for coupling to the glutamate on the nanoparticle surface. The NP-Glut-siRNA were re-suspended in 800 µL PBS. With vigorous magnetic stirring, 375 µL activated antibody, EDAC, sulfo-NHS solution was added dropwise and left over night at room temperature. The next day the antibody conjugate nanoparticles were collected by centrifugation at 15,000 rpm for 30 minutes. These particles will be referred to as NP-Antibody-2.

For assessing the binding of the antibody to the nanoparticle, several methods were used. First, a fluorescently tagged (Alexafluor 488) antibody was activated and added to the NP-Glut-siRNA. The resultant conjugate particles were centrifuged at 15,000 rpm for 30 minutes and washed with PBS twice to remove any unbound antibodies. The conjugated particles as well as blank particles were added to separate wells on a 96 well plate. The

plate was imaged in the Odyssey® Fc Imaging System (Li-COR) to compare the fluorescence of blank vs antibody conjugated particles.

Conjugated nanoparticles with fluorescent antibodies were also run on an agarose gel to show   that the binding of the antibody was chemical and not electrostatic. A 1% gel was used so that nanoparticles would be prevented from moving and remain stuck in the wells but should allow un-bound antibody to move through the gel.

This method of antibody conjugation was adapted from (Zhu et al., 2015) who had used a similar technique for attaching antibodies to Hed-CS-NPs, however this method was developed and improved on during this thesis.

Techniques for Nanoparticle Sizing

Dynamic light scattering:

Samples were diluted to 5 ng/µL in 1 mL of deionized water. The samples were transferred to a plastic cuvette with a path length of 1 cm and placed into the Dynamic Light Scattering (DLS) machine (Malvern Panalytical ZetaSizer). Samples were measured multiple times to obtain statistical significance.

Transmission Electron Microscopy:

Transmission Electron Microscopy was used to image nanoparticles at up to 250,000 times magnification (Jeol 1200EX). Blank particles were synthesised, washed and re-suspended

in deionised water. 2 µL of nanoparticles were pipetted onto a carbon fibre film coated copper grid and left at room temperature for 30 minutes to evaporate. A 3% w/v Phosphotungstic acid deionised water solution was made. 2 µL of 3% phosphotungstic acid stain was pipetted onto the copper grid with the evaporated nanoparticles. The grid was left at room temperature for 5 minutes and then the stain was removed. The grids were placed inside the Jeol 1200EX and imaged by me at varying concentrations.

To test antibody binding, gold nanoparticle labelled antibodies were conjugated to the nanoparticles. The conjugates were evaporated onto the copper grids in the same way as previously, however, no stain was added to visualise the chitosan. The gold nanoparticles absorb electrons due to the density of gold and so show up as black dots on the TEM images giving a clear indication of antibodies bound to the surface of the nanoparticles. The lack of a negative stain will result in the chitosan particles being invisible, but a ring of black dots should clearly be seen, indicating the antibodies bound to the surface of the particles. *Using gold nanoparticle tagged antibodies for visualising antibodies conjugated to the surface of nanoparticles is completely novel and developed during this thesis.*

Live Cell Confocal Microscopy Imaging:

Nanoparticle Uptake:

Cell uptake studies were performed using the Nikon A1R Inverted Confocal/TIRF microscope. To assess cellular uptake of chitosan nanoparticles (NP-siRNA) 175,000

HEK/HeLa cells were plated onto Matek imaging dishes the night before imaging. The next morning, chitosan nanoparticles (NP-siRNA) with Alexafluor 488 tagged siRNA were synthesized. Two hours before imaging the nanoparticles were added to the cells at varying concentrations and left to incubate at 37°C. 10 minutes before imaging, 10 µL diluted Hoechst® 33342 stain was added, and the cells were incubated for a further 10 minutes at 37°C. (Hoechst® 33342 stock solution was diluted 1:2,000 in PBS). After the 10 minute incubation the cells were washed 3 times with PBS to remove any stain or nanoparticles not taken up by the cells. The cells were taken to the microscope and imaged at varying magnifications.

To assess the method of cell uptake of the nanoparticles an additional staining step was added. BacMam early endosome stain was added to the cells the night before imaging and left to incubate for a total of 16 hours. Again, the nanoparticles were added two hours before imaging and Hoechst® 33342, 10 minutes before. The cells were washed 3 times with PBS and imaged using the Nikon A1R Inverted Confocal/TIRF microscope at varying magnifications.

In-Vivo Work:

All animal work was performed in C57Bl.6 Mice. Mice were housed at the Birmingham Biomedical Services Unit (Birmingham, UK). All animal experimentation was carried out

in accordance with Home Office License number PPL I3FDCE112 and PPL 70/8704 held by Roy Bicknell.

Subcutaneous injection of LLC:

Exponentially growing LLC were treated with trypsin to remove them from the culture plate and were counted for concentration. The cells were centrifuged and washed with 5 mL sterile PBS. 1 million cells were resuspended in 200 µL sterile PBS and subcutaneously injected into the right flank of male C57BL/6 mice aged 15 days old.

Tumours were measured daily by callipers. After 15 days or when tumour size limit of 1200 mm3 was reached animals were culled, tumours and organs excised fixed in formaldehyde. The organs were set in paraffin wax and cut into 10 micron sections which were stained with H&E stain by the Tissue Bank (Queen Elisabeth Hospital). Sections were later imaged by me on the Nikon Eclipse E600.

Nanoparticle Localisation Study:

Fluorescently tagged siRNA loaded nanoparticles were synthesised the day of injection (see methods: Nanoparticle synthesis) (mice were 15 days old or tumour had reached 1 cm in size) and were re-suspended in 200 µL sterile PBS. The same mass of nanoparticles was injected as were found to be most effective in the cell culture knockdown experiments. The mouse work was a bio distribution study and so the siRNA concentration did not need to

be optimised. Nanoparticles were injected intravenously into the tail vein. The mice were culled either two hours later or 24 hours later and all organs and tumour removed and fixed in formalin. The formalin preserved organs and tumour were embedded in paraffin wax, cut into 10 µm sections and stained using the H&E stain by the Tissue Bank (Queen Elisabeth Hospital). Sections were later imaged by me on the Nikon Eclipse E600.

Chapter III.

Nanoparticle Development

<u>Introduction:</u>

It has been shown that knockdown of CLEC14A *in-vitro* results in decreased wound healing in scratch assays and decreased filopodia formation in spheroid assays (Mura et al., 2012, Rho et al., 2011, Noy et al., 2015). Homozygous CLEC14A knockout mice show no gross developmental defects and when implanted with Lewis Lung Carcinoma (LLC) tumour angiogenesis and growth were significantly reduced compared to wild type mice (Noy et al., 2015). Other studies have shown that subcutaneous sponge implants have decreased FGF2-induced angiogenesis compared to wildtype controls (Noy et al., 2015). This evidence for the importance of CLEC14A in angiogenesis *in-vitro* and *in-vivo* points towards the possibility for targeted gene therapy and silencing of CLEC14A in tumour endothelial cells.

The use of nanoparticles in the delivery of therapeutics has become an area of intense research. Specifically, their ability to deliver and protect small molecules including nucleotides such as siRNA make them ideal vectors for gene modulating therapies in cancer. The aim of this chapter was to synthesize a nanoparticle of the correct size (under 200 nm), that is able to bind CLEC14A siRNA (enough to deliver roughly 50 nM siRNA

in cell culture as this is the amount given in a lipofectamine knockdown), that can retain and protect the siRNA under simulated conditions, can enter cells in cell culture and induce a knockdown of CLEC14A comparable to other nanoparticles in the literature.

In-vitro studies silence a gene using small RNA molecules such as small interfering RNA (siRNA) transported into a cell via Lipofectamine RNAi-Max (Invitrogen #12778-150). Lipofectamine captures the siRNA in a lipid vesicle that then passes through the cell membrane. Lipid assisted cellular uptake works very efficiently (80-90% knockdown) *in-vitro* but cannot be used *in-vivo* due to the delicate nature of lipid vesicles. Solid nanoparticles present excellent alternatives for siRNA delivery vectors *in-vivo* as they can withstand the harsher environments of an organism's vascular system.

To deliver siRNA to a tumour *in-vivo* a more stable vector to protect the siRNA. Therefore, the development of a stable and reliable nanoparticle vector presents as an important step in the knockdown of CLEC14A in tumour blood vessels.

Mesoporous Silica Nanoparticles:

After searching the literature for the ideal nanoparticle for delivery of siRNA to the tumour vasculature, mesoporous silica nanoparticles (MSNs) were decided on as the particle to move ahead with. Hom et al., detailed a method for synthesizing mesoporous silica nanoparticles that contained "pores" an ideal size for siRNA to fit inside (Hom et al., 2010). The nanoparticles were relatively simple to synthesize but did require a full day of

synthesis. The average particle size was 130 nm with an average pore size of 2.5 nm. These particles were perfect for the aims of this thesis as they were below 200 nm and, most importantly, contained pores that would protect the siRNA from the reducing conditions and enzymes in the blood system. Degradation of siRNA is a large problem with nucleotide based therapies (Wang et al., 2010a). Silica particles were synthesized according to the protocol in Hom et al., Loading of siRNA onto the nanoparticles was achieved by incubating siRNA and nanoparticles together in serum free medium at a 1:25 mass ratio under agitation at 4°C. Particles were collected 24 hours after incubation with siRNA via centrifugation.

MSNs with and without siRNA attached were sized using dynamic light scattering (DLS) (Figure 3.1). As can be seen the particles were synthesized at the expected size of 130 nm and addition of the siRNA had no appreciable effect on particle size. It was expected that siRNA would have no effect on size due to them being present inside the pores of the particle. Next the amount of siRNA bound and retained was assessed. siRNA was mixed with the nanoparticles and measured on the nanodrop for absorption at 260. This will give the absorption for all of the siRNA added to the nanoparticles whether bound or not. The particles were then centrifuged at 15,000 rpm for 1 minute, the supernatant removed and measured for absorption at 260 (Figure 3.1 (A)). The two measurements (1: Nanoparticles and siRNA in suspension and 2: the supernatant after the nanoparticles were centrifuged for 15 minutes) showed that 90% of the siRNA bound to the nanoparticle and only 10% remained in the supernatant unbound. This showed a high level of binding and that excess siRNA was present, so binding was saturated.

Next, it has been suggested that physiological conditions can cause premature release of siRNA from the nanoparticles. Cellular uptake studies performed by other labs have shown that the nanoparticles can enter cells within 1-2 hours and so siRNA release studies were performed at time intervals between 0 and 1 hours (Geiser et al., 2005).

Figure 3.1

MSN siRNA Absorbance
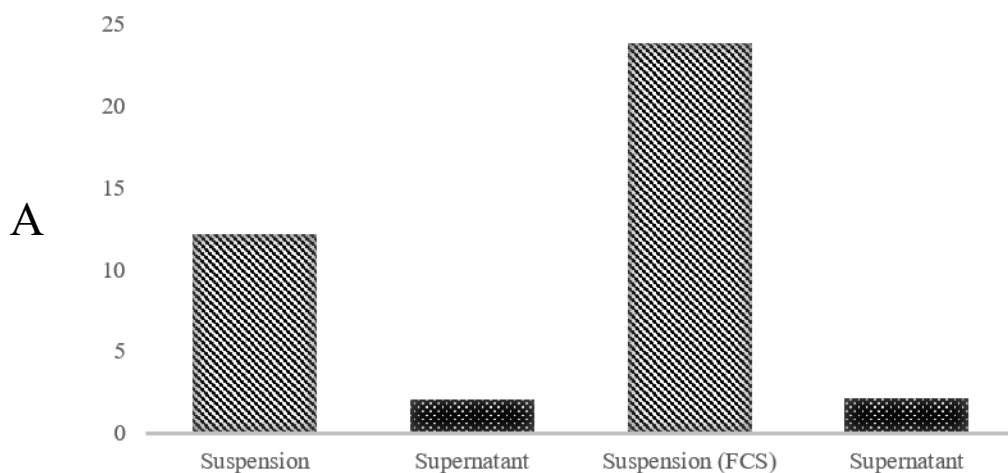
FCS Absorbance Increase: Silica Nanoparticles
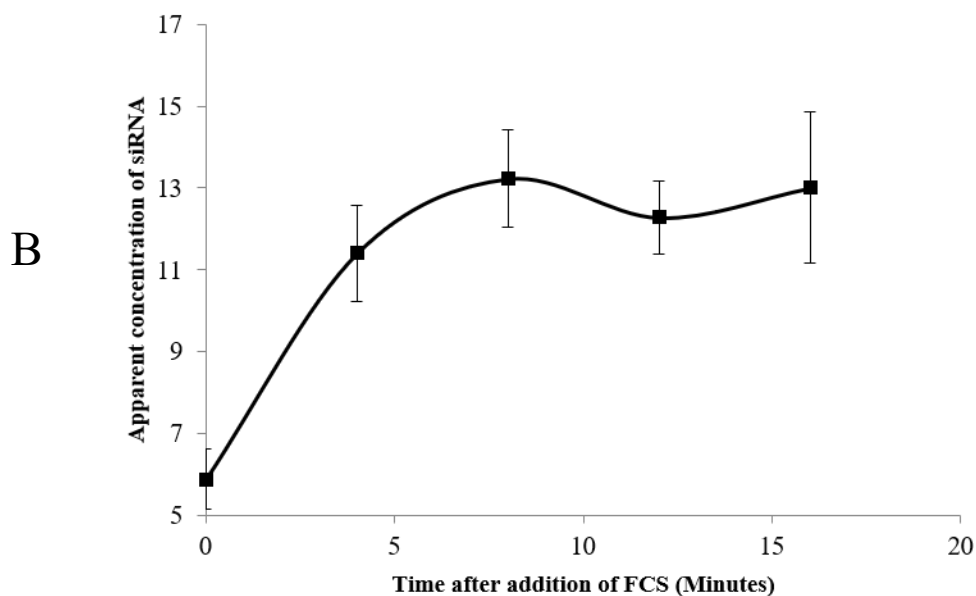
Figure 3.1 | Mesoporous Silica Nanoparticle siRNA absorption and retention (UV Absorption).

(A) Absorption study of MSNs to see siRNA binding and effect of serum on siRNA retention. Suspension: Nanoparticles with siRNA attached to surface in suspension. Supernatant: Nanoparticles centrifuged to pellet, and supernatant tested for presence of siRNA. Suspension (FCS): nanoparticles resuspended in 50% FCS and measured for absorption at 260 again. Supernatant: Nanoparticles left in 50% FCS for 1 hour are centrifuged for a last time and the supernatant measured for presence of siRNA.

(B) Increase in absorption of MSNs at 2-minute time points after the addition of FCS. It appeared that the addition of FCS affected the absorption of the nanoparticles in the 260 nm range, increasing in effect over time (up to 8 minutes).

To make sure the MSNs were retaining the siRNA, the particles were re-suspended in 10% FCS and the absorption measured at 260 nm. The particles were then centrifuged for 1 minute at 15,000 rpm and the supernatant measured for absorption at 260 nm. Confusingly it appeared as if the absorption increased from the first measurements (nanoparticles and siRNA in suspension). This first measurement should represent the highest absorption at 260 as it contains the largest amount of siRNA. The experiment was repeated several times at different time points after the addition of FCS and the change in absorption appeared to differ depending on the time point.

To assess what was causing this disparity FCS was added to siRNA containing MSNs and the absorption was measured every 4 minutes. Figure 3.1 (B) shows the increase in absorption over time with a plateau at 12 minutes. This shows that addition of FCS caused an increase in absorption over the first 12 minutes after addition.

As mentioned previously, protein coronas have a dramatic effect on nanoparticle surface chemistry. This time dependent change in absorption after addition of FCS suggests the formation of a protein coroner. Interestingly absorption was not affected in a similar way if siRNA was not added to the MSNs before FCS (data not shown). Something about the interaction between the siRNA, nanoparticles and proteins present in FCS resulted in an increase in absorption at 260 nm. It can also be seen that FCS in the supernatant did not affect the absorption at 260 showing it was a nanoparticle dependent effect.

To attempt to overcome issues of absorption a new method for testing siRNA retention in serum was devised. Previous studies have used gel electrophoresis to measure siRNA that has been removed from the surface of a nanoparticle after exposure to FCS to check for damage by endonucleases (Hom et al., 2010). This idea was taken and modified. 4% agarose gel is required to separate the short strands of siRNA. A 4% agarose gel will be too dense to allow migration of 130 nm MSNs. The MSNs will remain stuck in the wells of the gel and any siRNA that has been dissociated from the particles because of FCS will be pulled through the gel.

The MSNs were incubated in 50% FCS for 1 hour at room temperature. Samples were taken every 10 minutes and run on a 4% agarose gel along with fluorescently tagged siRNA bound MSNs and a release control (heparin induces 100% release of siRNA from the particle). Figure (3.2) shows the electrophoresis gel. It can be seen that there was no increase in release of siRNA. A majority of the siRNA was already released at time 0.

siRNA is only bound to the surface of the MSNs through adsorption. This weak electrostatic bond is easily overcome by the forces holding the siRNA to the surface.

Figure 3.2

B

A
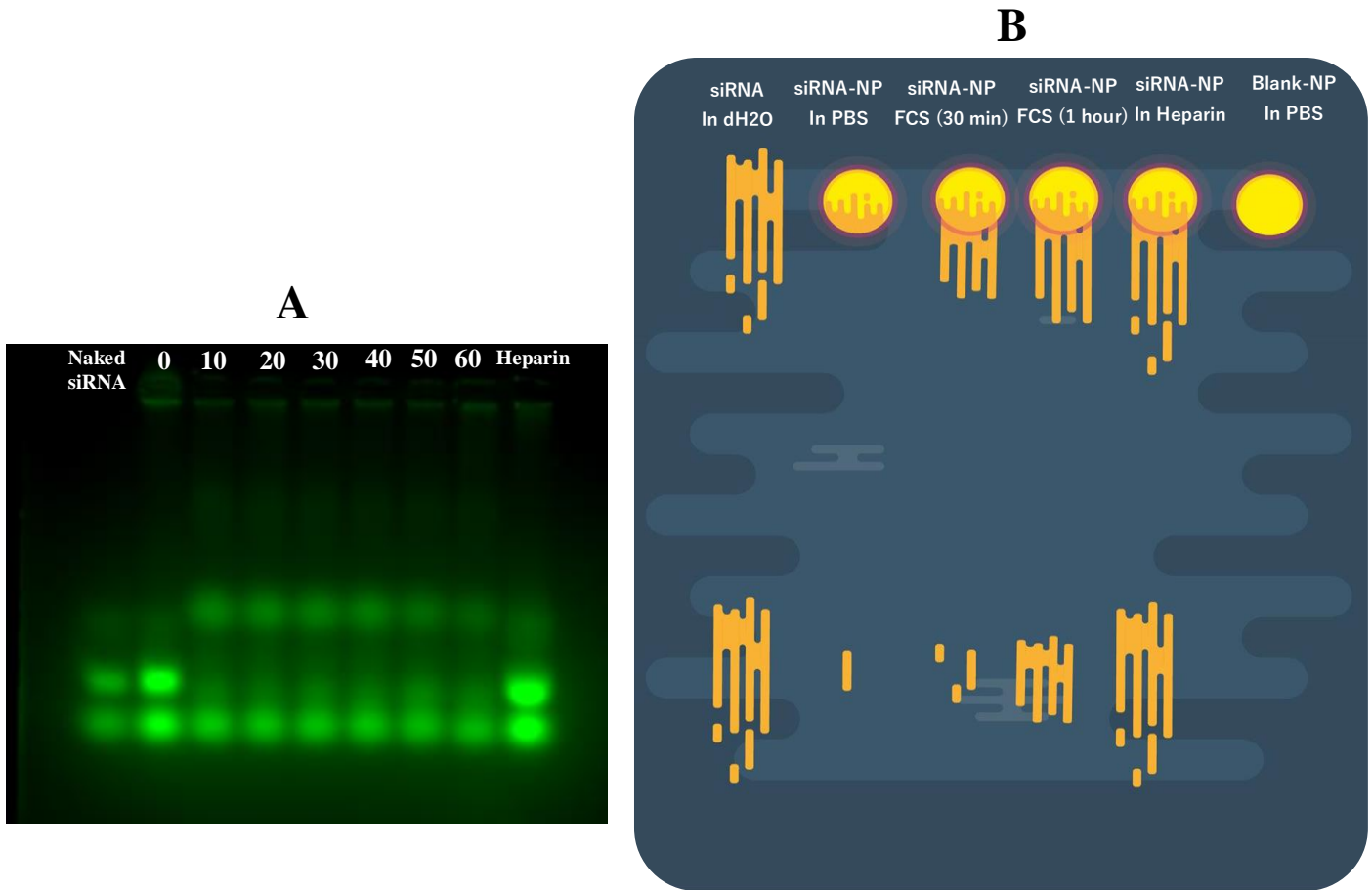
Figure 3.2 | Mesoporous Silica Nanoparticle siRNA absorption and retention (Gel Electrophoresis).

(A) MSN's with bound fluorescently tagged siRNA are incubated in FCS over an hour with samples removed and frozen at 10-minute intervals. The nanoparticles are defrosted and added to the wells of a 4% agarose gel along with DNA loading buffer and run for 20 min. Naked siRNA (siRNA not attached to a nanoparticle) and nanoparticles incubated with heparin are used as negative and positive controls respectively. As can be seen, all of the siRNA is pulled off the nanoparticles with very little fluorescence remaining in the wells. The nanoparticles remain trapped in the wells due to their size. Any siRNA further down the gel has dissociated from the particle. The only difference that can be seen in the FCS treated particles is an extra band higher up the gel, likely some of the serum proteins binding to the siRNA.

(B) This is a diagram shows the expected results from an siRNA retention and release study. The various conditions are shown at the top (nanoparticles yellow circle, siRNA yellow lines). The result of each condition can be seen at the bottom of the gel. It is expected that NP in PBS will leak little siRNA and NP in FCS will leak more siRNA as incubation time increases. Incubation with heparin should result in 100% siRNA release.

All the attempts to assess the effects of serum on the siRNA-MSN binding were unsuccessful in producing a clear result. The interactions between FCS and the siRNA bound MSNs provide doubt that they would be a good candidate for delivery of siRNA via the blood system. To this end it was decided that a different nanoparticle composition, that could hold onto siRNA with a stronger bond and withstand agarose gel analysis, should be researched.

Switch to Chitosan Nanoparticles:

Another literature search was performed to find a new candidate for delivery of siRNA. Chitosan nanoparticles represent the best solution as the synthesis is rapid (a few hours) and siRNA is trapped inside the nanoparticle mesh preventing premature siRNA release (Katas et al., 2013). Chitosan is also nontoxic, LD_{50} above 16 g/kg in mice (Paul W., 2000) and have already been widely used for siRNA knockdown studies (Lu et al., 2010, Masiero et al., 2013).

ChNP Sizing:

The same tests were performed on the ChNP as the MSNs. The particles were synthesized as described in them methods section. ChNPs were synthesized with and without siRNA attached. To confirm the sizing, DLS, and transmission electron microscopy were used

(Figure 3.3, Figure 3.4). Chitosan particles are made from biological material and so suffer from a higher polydispersity index (PDI) (Katas et al., 2013). High polydispersity is the presence of many particles at varying sizes where as low polydispersity is characterized by an all the particles existing in one or only a few different sizes. It can be seen from the DLS that the chitosan nanoparticles were synthesized at 127 nm with the siRNA containing nanoparticles being slightly smaller. This decrease in size is due to the crosslinking between the positively charged chitosan polymer and negatively charged siRNA. The TPP is already acting as a crosslinker but the addition of more negatively charged crosslinking agents holds the polymer strands closer together rather than increasing the size of the particle.

Secondly, for sizing, transmission electron microscopy gives the most detailed look at the particles, showing size, shape and polydispersity all in one image. To analyse the particles a Matlab script was written that picked out the particles from the image and measured their size in nanometers (Figure 3.4) for MatLab code see appendix 1. The TEM confirmed the nanoparticle size at around 130-140 nm, that they were spherical and that there was a range of sizes, but most were of the expected size.

The program analyses pixel values and plots a histogram to find a threshold value. A threshold pixel value is needed to define a "threshold" above which any pixel is made white and below which any pixel is made black. The plotting and analysis of the histogram allows for the ideal pixel value to be chosen to provide the clearest black and white image. The black and white image generated is not perfect and often has holes in the middle of particles

as well as rough edges due to differential staining. The program runs over the image several times filling in blank holes in the middle of particles and smoothing the edges to give a more photo realistic black and white mask. The program next measures any continuous objects in the image providing data such as the largest number of pixels in a row (effectively the largest diameter of an object measured in pixels) and the volume of each object etc. The program next compares the number of pixels in the 100 nm scale bar to the number of pixels that line up to make the longest diameter of the objects in the image. From this, it is known how many pixels make up 100 nm (from the scale bar) and the diameter (in nm) can be calculated of the nanoparticles in the image. The code for this program can be seen in the appendix.

Figure 3.3

Nanoparticle Type	Size (nm)	PDI
ChNP (No siRNA)	114.2	0.312
	119.9	0.403
	121.4	0.372
	131	0.386
	139.1	0.448
	135.7	0.339
	134.3	0.301
	135.4	0.297
	138.1	0.29
	116.6	0.294
	119.2	0.304
	121.5	0.302
Average	127.2	0.337

Nanoparticle Type	Size (nm)	PDI
ChNP-siRNA	146.8	0.301
	135.3	0.285
	144.5	0.408
	114.9	0.282
	119.9	0.296
	121.9	0.304
	105.9	0.345
	112.7	0.34
	128.5	0.312
	96.93	0.256
	120.7	0.206
	116.8	0.297
Average	122	0.30

Table 3.3 | Blank Nanoparticle and siRNA Entrapped Nanoparticle Sizes.

The table shows the DLS results for the sizes (nm) of different types of nanoparticle, NP-siRNA and NP-Blank

The Polydispersity Index (PDI) was also measured to show the range of particle size.

The graph below shows the average size of the ChNP compared to ChNP-siRNA. As can be seen there is no significant difference in the size of the particles after addition of siRNA.

n=13

93
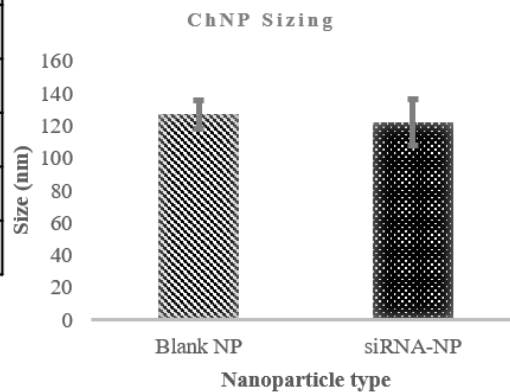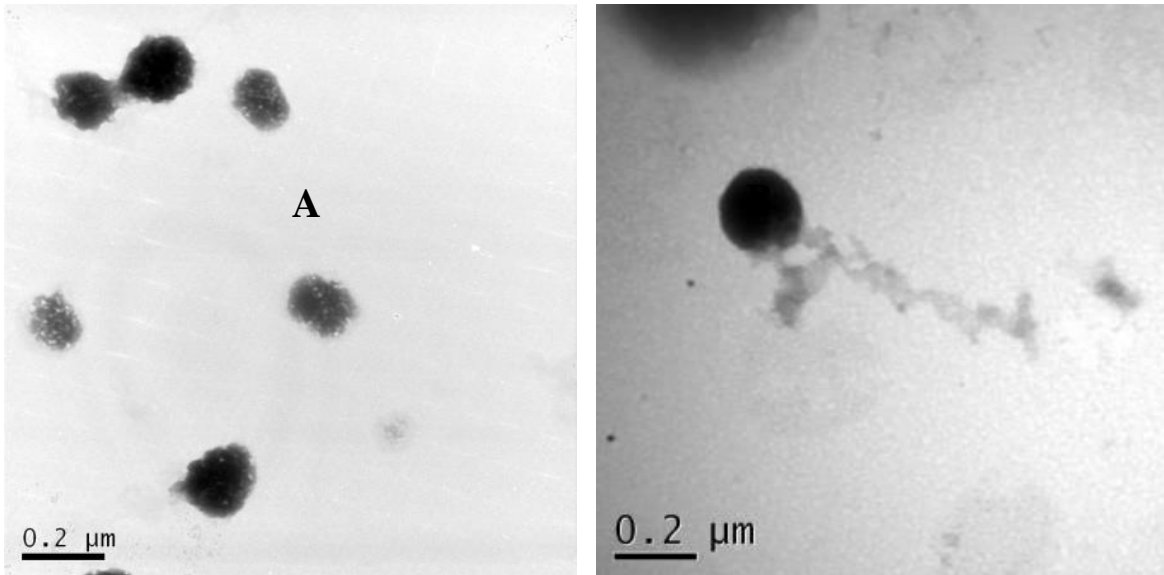
Figure 3.4

Figure 3.4 | Chitosan Nanoparticle Transmission Electron Microscope Images.
ChNP-siRNA were synthesised, washed and 2 µl added to a TEM copper grid. The nanoparticles were left to dry and were then stained with phosphotungstic acid. The images were taken with the JEOL 1200EX Transmission Electron Microscope. Phosphotungstic acid is a negative stain and is taken up into the chitosan polymer mesh, as a result the nanoparticles appear black. Particles appear spherical and around 200 nm in size. (A) and (B) show two examples of the ChNP.

Figure 3.5
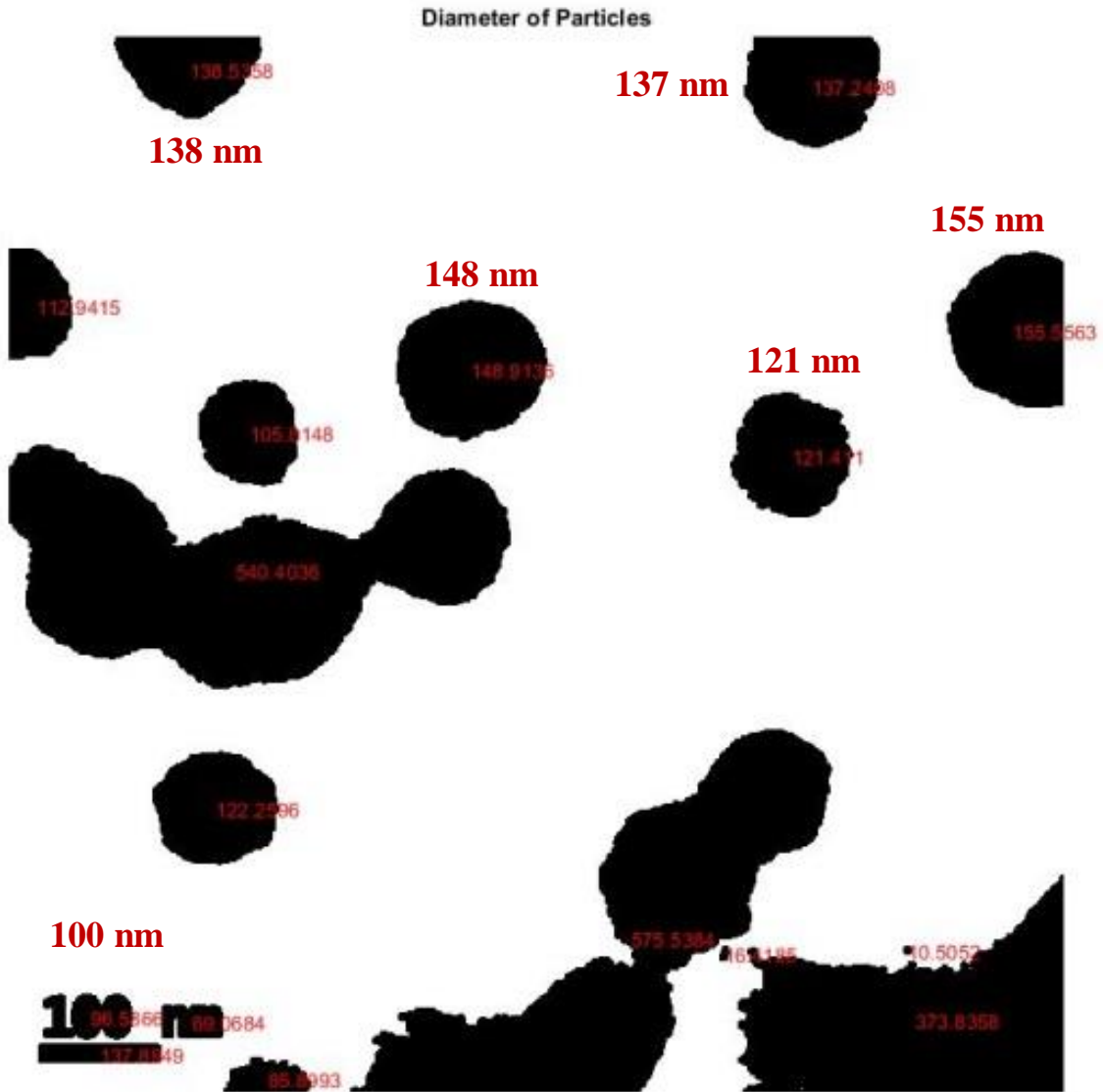
Figure 3.5 | MatLab Analysis of TEM Images
A program was written in MatLab that created a mask around the nanoparticles to separate them from the background. The process then counted the number of pixels that made up the longest diameter of each mask. The number of pixels is then compared to the number of pixels needed to make up the 100 nm scale bar, giving an accurate size of the nanoparticles. Individual nanoparticles can be seen to range from 105 nm up to 155 nm. The aggregation of particles prevents an accurate reading of all.

Chitosan siRNA entrapment:

Similarly, to the MSN studies, ChNPs were assessed for their ability to bind and retain siRNA.

Gel electrophoresis was used with the same method as the MSNs. The chitosan nanoparticles were too large to be pulled through the agarose gel, therefore any release of siRNA from serum will be pulled through the gel and form a band at the appropriate point. Chitosan nanoparticles solve many of the issues that were had with the MSNs, however, the siRNA is only held in the chitosan complex due to its cross linking and the cross linking of the TPP and Chitosan. Should a molecule in the serum have greater crosslinking abilities than siRNA or TPP, the nanoparticle will depolymerize and release the siRNA.

Chitosan nanoparticles loaded with fluorescently tagged siRNA (Alexafluor 448) were incubated in FCS for 30 minutes and 1 hour. After incubation the siRNA-ChNPs were loaded onto a 4% agarose gel along with unconjugated siRNA (not attached to a nanoparticle) and a positive release control (Heparin). Heparin causes release of siRNA by competing for binding with the positively charged chitosan. Competition between the siRNA and anionic proteins present in the cell cause the dissociation of the nanoparticle

and release of siRNA. The gel was run at 110 V for 30 minutes then imaged in the Li-COR

Odyssey Imaging System (Figure 3.6).

Figure 3.6
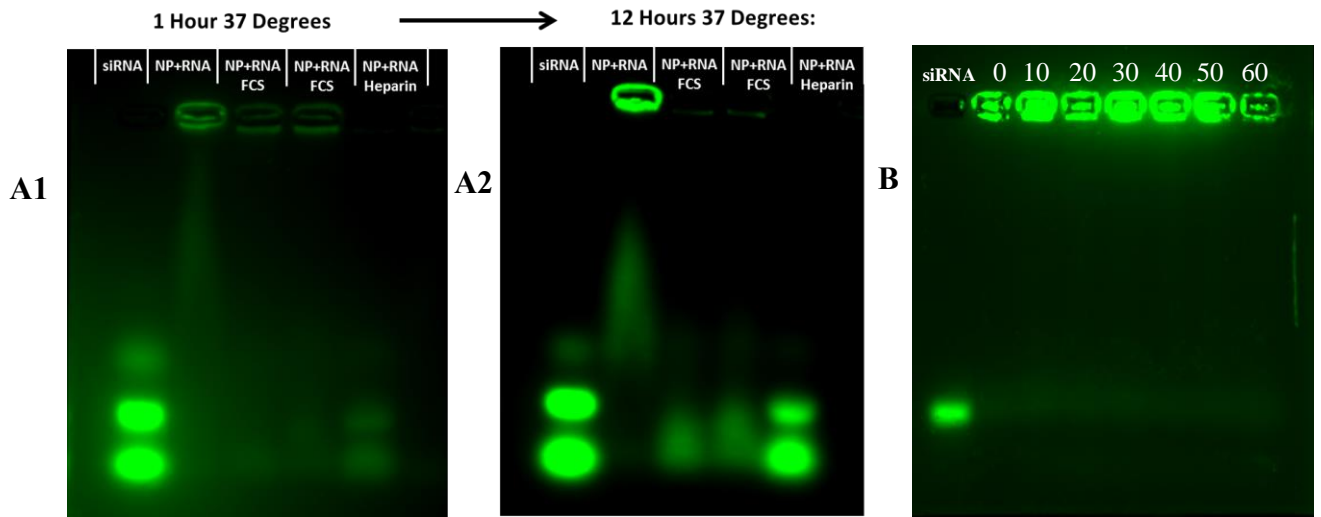
Figure 3.6 | Chitosan Nanoparticle siRNA entrapment and Release.
Agarose gel electrophoresis of chitosan nanoparticles and, fluorescently tagged, siRNA exposed to various conditions. (A1) shows a gel run with: Lane 1: fluorescent siRNA by itself **(siRNA).** Lane 2: ChNP-siRNA in PBS **(NP+RNA).** Lane 3: Nanoparticles exposed to 50% FCS for 30 mins **(NP+RNA FCS).** Lane 4: ChNP-siRNA in 50% FCS for 1 hour **(NP+RNA FCS).** Lane 5: ChNP-siRNA incubated with heparin for 1 hour **(NP+RNA Heparin)**.

(A2) shows exactly the same samples incubated overnight in the same conditions.

(B) shows chitosan nanoparticles exposed to 50% FCS at 37°C with samples taken every 10 minutes with each lane running a sample of ChNP-siRNA that has been exposed to 10 mins more than the previous lane.

The gels show that the in the 30 min and 1 hour incubations the fluorescence remains in the wells with no siRNA leaking from the ChNPs. The two samples in 50% FCS were then incubated at 37°C overnight. The nanoparticles in PBS were left at room temperature. A 12 hour incubation in 50% FCS sees almost no fluorescence left in the well and a greatly increased fluorescence further down the gel at the same level as the blank siRNA control.

To further assess any release of siRNA during the first hour of FCS incubation siRNA-ChNPs were incubated in 50% FCS at 37°C with samples removed and frozen every 10 minutes. Figure 3.6 (B) shows the western blot gel. The same amount of siRNA was added to each nanoparticle and each well. The naked siRNA lane appears brighter than the nanoparticle treated lanes due to siRNA being lost during nanoparticle synthesis, siRNA degradation by serum proteins and occlusion/quenching from the nanoparticles as well as loss during synthesis and collection.

Figure 3.6 (B) shows that the ChNPs retain the siRNA for over 1 hour in 50% FCS (simulating *in-vivo* conditions) which shows they are capable of delivering siRNA through the vasculature of an organism. It is ionic gelation that binds the siRNA to the chitosan nanoparticle and competition between the siRNA and anionic plasma proteins can cause depolymerisation of the chitosan mesh and premature release of siRNA.

99

This method for assessing siRNA binding to chitosan nanoparticles was developed for this thesis.

Confirmation of passive cellular uptake allows for progression to the next stage of nanoparticle development; attempting a knockdown.

ChNP-siRNA Cell uptake:

The electrophoresis studies showed that siRNA can be efficiently trapped in the ChNPs and can retain the siRNA for over an hour in FCS. The ChNPs have proven their ability to work as siRNA vectors but now their cellular uptake must be assessed.

Cellular uptake of nanoparticles can occur through several different methods. Untargeted nanoparticles are capable of being taken up by a cell through passive endocytosis, phagocytosis or by simply "punching" through the plasma membrane (A. Zubarevaa, 2016). Cellular uptake is not guaranteed for any particular nanoparticle. siRNA has been developed by the Bicknell group that successfully knocks down CLEC14A leaving only 2-5% expression (95-98% knockdown). Failure to induce a similar knockdown efficiency could be due to the nanoparticles failing to enter the cell to deliver the siRNA. To properly assess these questions studies were used to image the ChNPs inside cells and to ascertain the method of cellular uptake.

3.5×10^4 HEK293T cells were plated onto MatTek dishes the morning of the day before imaging. The cells were left overnight. The next morning 100 µL Alexafluor 488 tagged siRNA entrapped inside ChNPs were incubated with the cells for 2 hours. After 2 hours of incubation 10 µL Hoechst® 33342 stain was added to the cells and left for 5 minutes. After the 5 minutes the cells were washed three times with PBS to remove excess BacMam reagent, nanoparticles and Hoechst® 33342. The cells were then imaged in the Nikon A1R Inverted Confocal/TIRF microscope (Figures 3.7 and 3.8).

Figure 3.7
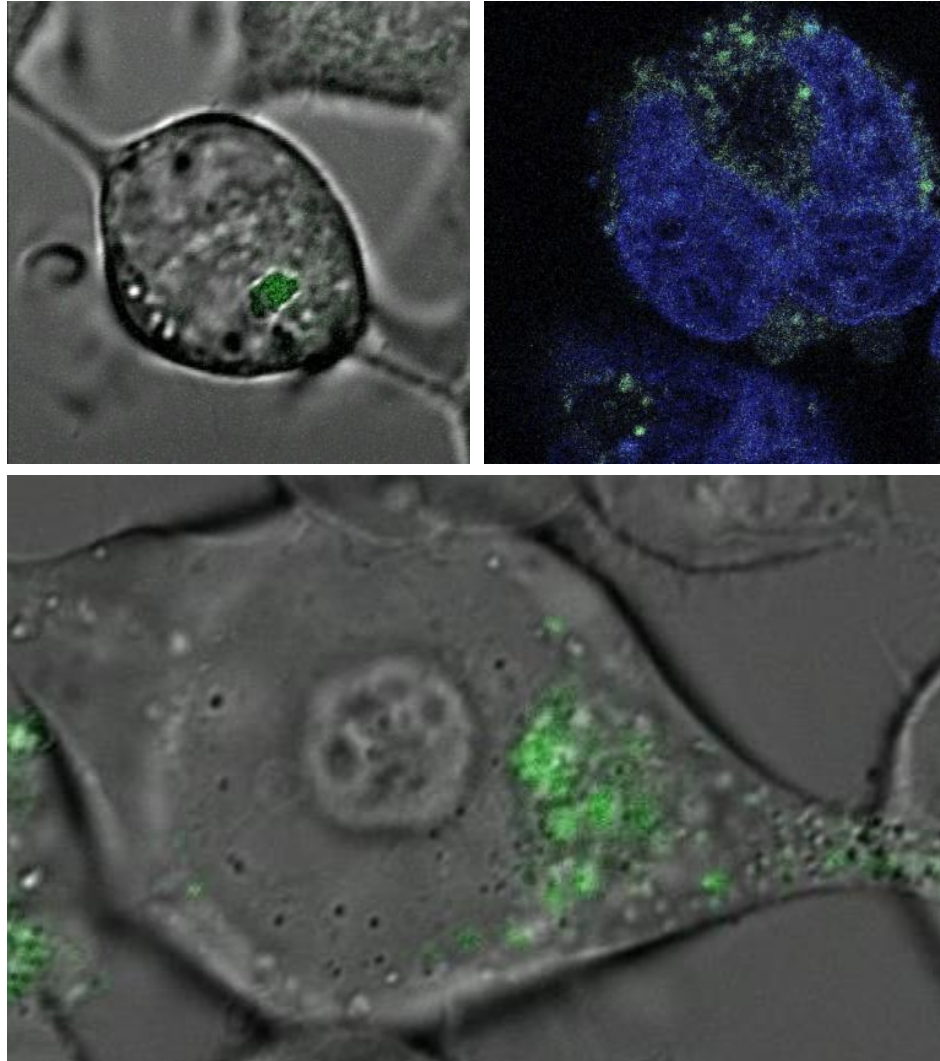
Figure 3.7 | Cellular Uptake of Chitosan Nanoparticles (ChNP-siRNA)
HEK293T cells were incubated with Alexafluor 488 tagged siRNA entrapped inside ChNP. (A)
and (C) show brightfield images with the green fluorescent nanoparticles overlaid. (B) shows the
blue Hoechst® 33342 nucleic acid stain and green fluorescent nanoparticles. The green
fluorescence of the nanoparticles can be seen to group together in sections of the cells leading to
the suggestion that they may be entering through endocytosis.

Nanoparticles labelled with the Alexafluor 488 siRNA can clearly be seen in green inside the HEK293T cells confirming the ChNPs were passively taken up by the cells (Figure 3.7). The nanoparticles can be seen to group together in sections inside the cells. This grouping suggests that the nanoparticles were inside endosomes and so further testing was done to assess the method of entry for the nanoparticles. The images in figure 3.7 show similarity to other nanoparticle uptake studies such as in a cellular uptake study with CADY self-assembling peptide-based nanoparticles (Rydstrom et al., 2011). However, in this paper the fluorescent siRNA containing particles were shown to enter the cell independent of endocytosis. The team use a lysotracker to show that the particles fluorescence does not overlap with nanoparticle fluorescence.

Other papers have confirmed the uptake of chitosan nanoparticles through endocytosis (Jiang et al., 2017, A. A. Zubarevaa, 2016). Jiang et al., incubated FITC-ChNPs for 2 hours before washing and imaging the macrophage cells. The nanoparticles used in the FITC-ChNP studies were ~250 nanometers in size however. The size of nanoparticles used varies in almost every study, so it is still necessary to confirm the method of cellular uptake for the particles used in this thesis.

Figure 3.8
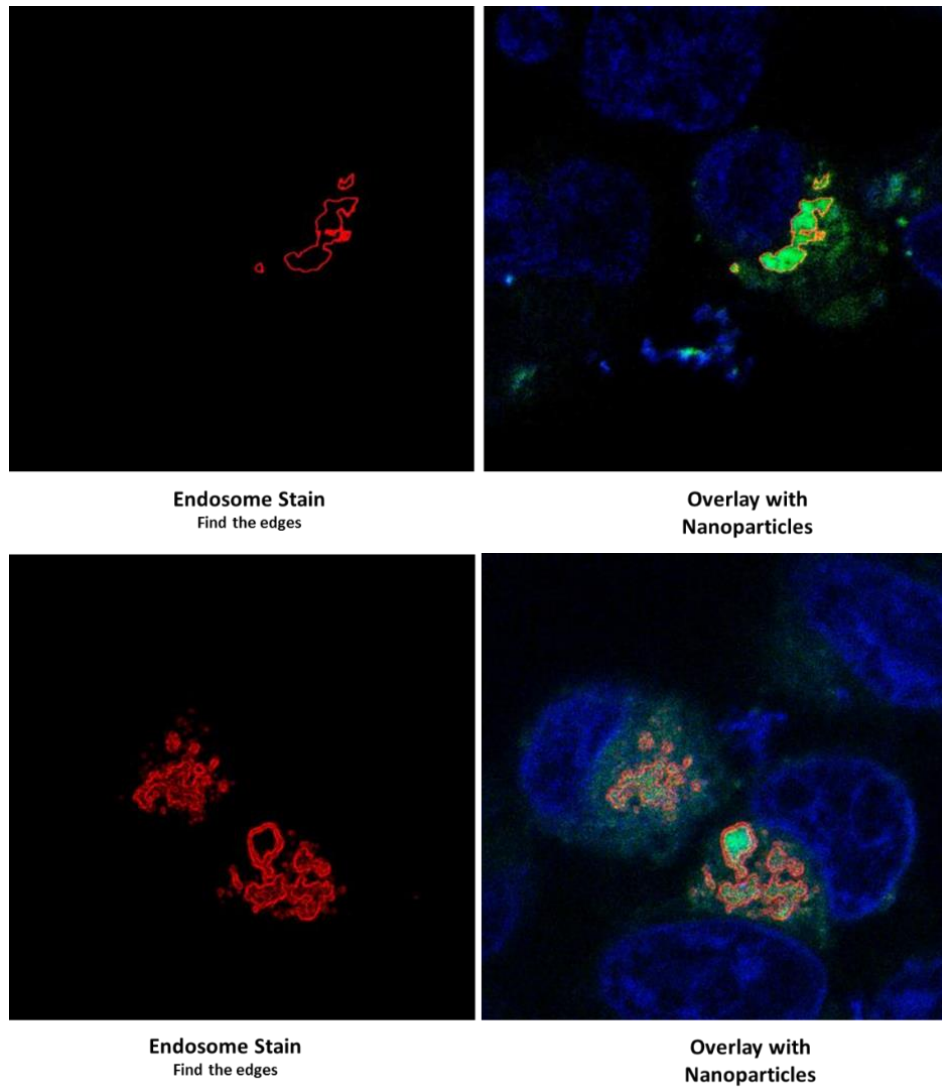
Figure 3.8 | Endosomal Uptake of Chitosan Nanoparticles (ChNP-siRNA)
Confocal images were taken to show cellular uptake of chitosan nanoparticles through endocytosis. The BacMam early endosome (RFP) stain was used to visualise endosomes. Nanoparticles were visualised through Alexafluor 488-siRNA entrapped inside the nanoparticles and Hoechst® 33342 nucleic acid stain visualised the nucleus. Cells were incubated with Alexafluor 488 tagged siRNA containing nanoparticles (2x concentration) The green nanoparticle fluorescence can clearly be seen inside the red endosome stain showing that the particles are present inside the endosomes.

To discern whether the nanoparticles in this thesis entered through endocytosis BacMam RFP early endosome stain was used. This particular stain was chosen due to its use in a previous study by another student in the Bicknell lab which aimed to visualise CLEC14A internalisation from the cell surface, using the BacMam RFP stain to visualise the early endosome (Puja Lodhia 2016). Should the red BacMam fluorescence and the green ChNP-siRNA fluorescence overlap, it can be concluded that the particles were inside endosomes.

The evening before imaging, 200 µL of BacMam 2.0 reagent was added to the cells and cell medium in the MatTek dish. The cells were left over night with the nanoparticles and Hoechst® 33342 added the next day. Images were taken with the Nikon A1R Inverted Confocal/TIRF microscope (Figure 3.8).

Figure 3.8 shows the green of the siRNA fluorescence can clearly overlapping with the red endosome stain confirming these 120 nm ChNPs were present in the early endosome.

ChNP-siRNA HUVEC Knockdown:

A 95-98% knockdown (2-5% remaining expression) of CLEC14A in HUVEC can be achieved with siRNA developed by the Bicknell lab. To achieve this Lipofectamine RNAi-Max (Invitrogen #12778-150) is used to deliver the siRNA into the cells. To test the ChNPs ability to deliver siRNA *in-vitro*, HUVEC were incubated with siRNA containing ChNPs at varying concentrations comparable to the concentrations used in a lipofectamine knockdown (1x, 2x, 3x and 4x concentration of siRNA delivered via lipofectamine, normally 50 nM). The concentration of siRNA inside any given nanoparticle remains the same, the increase in concentration of siRNA is achieved through the addition of more nanoparticles. Two duplexes were used in figure 3.9 (C) to knockdown CLEC14A in HUVEC using lipofectamine. This gel was used as a "gold standard" to compare to nanoparticle knockdowns later. It also served as a method to choose which duplex to use in the future nanoparticle experiments. As can be seen in figure 3.9 (C), D2 caused a greater level of CLEC14A knockdown and so was chosen as the duplex for all further experimentation.

The knockdown percentage achieved by the nanoparticles was compared to a lipofectamine siRNA knockdown (positive control) and a negative control lacking siRNA. Figure 3.9 shows the western blots from the ChNP-siRNA knockdown and figure 3.10 shows a graph of percentage expression remaining for the various concentrations of siRNA delivered by the nanoparticles. Knockdowns were assessed through polyacrylamide gel electrophoresis.

The gels were imaged and analysed using the Odyssey® Fc Imaging System (Li-COR). Pixel values of the ChNP knockdown bands were compared to the positive and negative controls to calculate the knockdown percentage of CLEC14A.

Figure 3.9
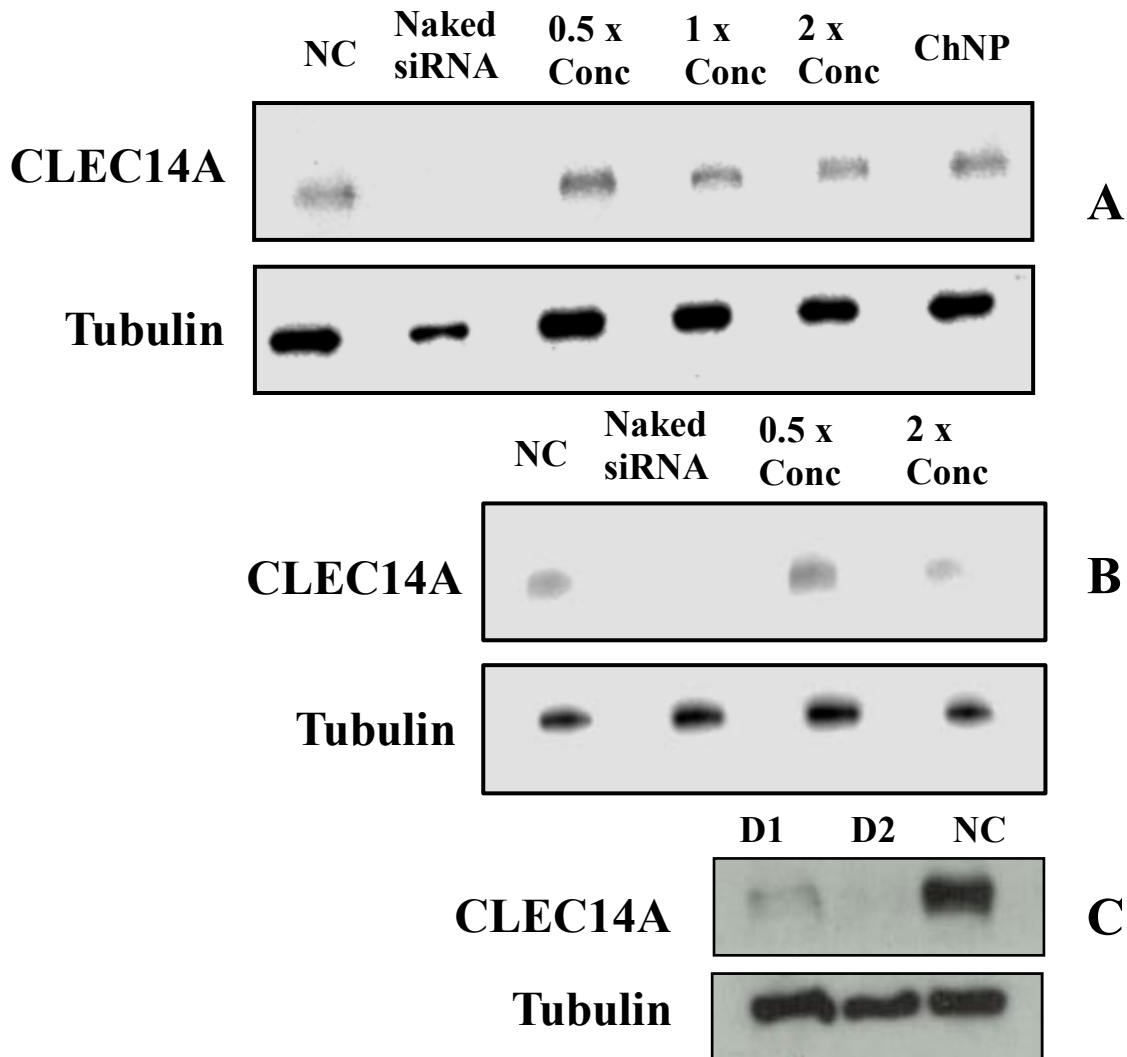
Figure 3.9 | CLEC14A Knockdown in HUVEC by NP-siRNA

(A) and (B) show examples of western blots imaged and analysed with the Odyssey® Fc Imaging System (Li-COR). Lane 1: Negative Control (No nanoparticles or siRNA). Lane 2 Naked siRNA (siRNA transfected with lipofectamine). Lane 3: ChNP-siRNA at a concentration equal to 25 nM siRNA added to the cells. Lane 4: ChNP-siRNA at a concentration equal to 50 nM siRNA added to the cells. Lane 5: ChNP-siRNA at a concentration equal to 100 nM siRNA added to the cells. Lane 6: ChNP without any siRNA.

(B) Shows another example of a western blot similar to (A).

(C) Shows a western blot of just lipofectamine transfected siRNA, the ideal result. Two different duplexes against CLEC14A (D1) and (D2) were used. Though some of the bands look similar, pixel density analysis was performed to account for protein loading differences to give the true knockdown percentage.

Figure 3.10
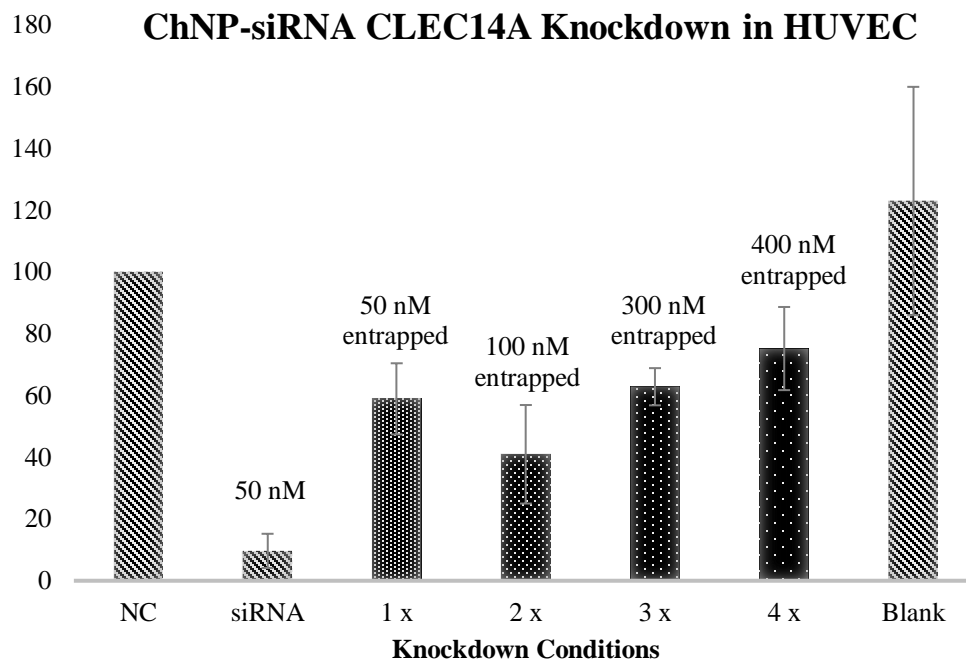
Figure 3.10 | CLEC14A Knockdown in HUVEC

This graph shows the relative remaining protein expression after incubation of HUVEC under various conditions. **NC:** Untreated HUVEC. **siRNA:** HUVEC treated with 50 nM siRNA via lipofectamine. **1x:** HUVEC incubated with ChNP-siRNA so that the total siRNA added to the cells equals 50nM. **2x:** HUVEC incubated with ChNP-siRNA so that the total siRNA added to the cells equals 100nM. **3x:** ChNP-siRNA concentration so that the total siRNA added to the cells equals 150nM. **4x:** ChNP-siRNA concentration so that the total siRNA added to the cells equals 200nM. The amount of siRNA per nanoparticle remains consistent between incubations. Concentration of siRNA is increased by increasing the number of nanoparticles added to the cells. **Blank:** ChNP without any siRNA entrapped inside. The 2x concentration represented the highest knockdown. "50 nM" represents the concentration of siRNA incubated with HUVEC. "entrapped" represents siRNA inside the chitosan nanoparticle.

Percentage knockdown decreases as concentrations go up due to nanoparticle aggregation.

n=3. Error bars = SD

As can be seen, the knockdown via lipofectamine achieved a 95% knockdown (5% remaining). As for the nanoparticles, knockdown effectiveness was best at 2x concentration (100 nm siRNA inside ChNPs). The 2x concentration achieved a 60% knockdown (40% remaining expression). From 2x onwards the knockdown percentage decreased. This decrease is likely due to the aggregation of nanoparticles preventing cellular uptake. Chitosan nanoparticles are known to aggregate because of charge neutralization (Quinones et al., 2018).

As the concentration of ChNPs increases the chance for aggregation increases as well as the size of the aggregates. As previously mentioned, <200 nm is ideal for passive uptake of nanoparticles (Geiser et al., 2005). The surface of chitosan nanoparticles, made with the TPP crosslinker, exhibit a highly positive net surface charge (~40 mV) over a large range of pH's. The isoelectric point for TPP-Chitosan nanoparticles was found to be pH 9.0 (Gan et al., 2005). The crosslinking ability of chitosan with any free –OH or –COOH as well as several other functional groups results in aggregation of the nanoparticles, especially at high concentrations. Aggregation dramatically increases the size of the particles, decreasing the cell uptake efficiency therefore decreasing the concentration of siRNA delivered.

Conclusion:

This chapter has outlined the successful development of a solid nanoparticle for the delivery of CLEC14A siRNA *in-vitro*. The MSN particles initially seemed ideal for the delivery of siRNA however, the issues with the weak electrostatic binding of siRNA made binding and retention studies inconclusive. It was decided that a new nanoparticle formulation should be used, and chitosan was chosen as the base chemical from which to compose these new particles.

ChNP's were shown to successfully bind siRNA and were shown to retain it inside the chitosan mesh under simulated *in-vivo* conditions. Cell uptake studies showed the particles, with siRNA present, inside the cells and further study with an endosome stain showed the location of the particles within the endosome.

Knockdown studies showed a 60% knockdown (40% expression remaining) achieved with 100M siRNA entrapped inside the ChNP. Knockdown percentage decreased as the concentration of nanoparticles increased.

It was hoped that after a successful knockdown with the ChNPs, experiments would move onto an *in-vivo* mouse model. With papers claiming 80-90% knockdown using various nanoparticles, 60% seems too low. The next chapter looks at attempts to increase the percentage knockdown before moving to an animal model.

Chapter IV

Nanoparticle Targeting

<u>Introduction:</u>

A 60% knockdown of CLEC14A was achieved with the siRNA-ChNPs. This is lower than other siRNA-Nanoparticle studies. Varying concentrations of siRNA containing ChNPs were incubated with HUVEC. The concentration of siRNA delivered to the cells was increased by keeping the amount of siRNA inside the ChNPs the same but increasing the number of nanoparticles per cell. The lower concentrations of nanoparticles had a better knockdown (60% at 2x conc) than the higher concentration (15% at 4x conc). The concentrations are comparable to the amount of siRNA delivered compared to a normal lipofectamine transfection (50 nM). 2x concentration is therefore 100 nM siRNA entrapped inside the ChNP. At the higher concentrations it is likely that the increased numbers of nanoparticles caused aggregation which prevented cell entry due to particle size increasing drastically. The lower concentration incubations achieved significant knockdown but still not near the 95% of a lipofectamine knockdown.

With a knockdown being achieved it can be assumed that the particles were entering the cells and releasing the siRNA in a way that it can bind to the RISC complex. Likely, inefficient release of siRNA is resulting in a lower knockdown than desired. This could be

combated by increasing the concentration of siRNA delivered however, as the previous chapter showed, increasing the concentration resulted in nanoparticle aggregation and a decrease in knockdown percentage.

One way to increase the amount of siRNA that reaches the cell is to target the nanoparticles directly at a membrane protein. Crosslinking between antibodies and membrane proteins induces membrane internalization (Moody et al., 2015). Conjugation of an antibody to the surface of a nanoparticle results in the nanoparticle being internalized with the membrane protein, increasing the rate of internalization of the siRNA containing ChNPs (Gao et al., 2013).

This chapter will focus on targeting the nanoparticles directly to the cells to increase cell uptake and therefore increase the amount of siRNA delivered increasing knockdown percentage.

Anti CLEC14A antibodies have previously been created for the study of CLEC14A *in-vivo* (Ki et al., 2013, Mura et al., 2012). Several antibodies targeting the extracellular domain of CLEC14A have been developed by the Bicknell lab. A study by a previous PhD student in the Bicknell lab looked at targeting CLEC14A with antibody drug conjugates (Khan, 2016). To visualise expression of CLEC14A in vivo, humanised antibodies (conjugated with Alexafluor 555) were administered to LLC tumour baring mice. CD32 was stained as a marker for the blood vessels. The localisation of CLEC14A was found to be mainly within the tumour, removing the concern for off target effects of ADC's.

Analysis of the ADC treatments showed that the hCRT4-ADC had anti-tumour effects in the LLC mouse model whereas the hCRT3-ADC did not. It was noted, however, that all ADC treatments reduced slowed tumour growth considerably faster than the control mouse. The discrepancy between hCRT3 and hCRT4 was surprising considering hCRT3 was shown to be more cytotoxic than hCRT4 in assays (Puja Lodhia unpublished data). Binding affinities could be different between the two species of antibody and could have different effects in human patients' vs mouse. The data from these studies lead to the choice to use hCRT4 for nanoparticle targeting.

Conjugation of the hCRT4 to the outside of the ChNPs should allow the particles to bind directly to the surface of HUVEC which have a high concentration of CLEC14A (Greene et al., 2018). As previously mentioned, CELC14A has a high internalization rate (Puja Lodhia unpublished data). A nanoparticle conjugated to an anti-CLEC14A antibody could take advantage of this high internalization rate and increase the cellular uptake rate.

Antibody-modified chitosan nanoparticles have been developed for delivering siRNA across the blood-brain barrier (Gu et al., 2017). They show up to a 68.9 ± 38.7 percent increase in cellular uptake through antibody conjugation. The study did not include evidence for antigen binding studies, prior to cell uptake. Scrambled (Non-targeted antibody Ab0) antibodies were used but only in combination with either of their targeted antibodies (Ab1 and Ab2) never by themselves.

Lee et al., conjugates CD7-specific single-chain antibodies to chitosan nanoparticles (Lee et al., 2012). The study also shows an increase in cellular uptake upon increased antibody conjugation, however, also fails to show specific receptor binding through antigen capture or ELISA.

Zhu et al., conjugates anti-CD147 antibodies to α-Hed-CS nanoparticles (Zhu et al., 2015). The study does perform a cell-based ELISA to show nanoparticle-antibody cell surface binding but no data for the ELISA experiments or proof of antigen binding was provided. FTIR characterization of α-Hed-CS-CD147-NPs was performed to determine the presence of any chemical substitution, elimination, or entrapped concealing of certain chemical groups. A $57.07\% \pm 0.60\%$ decrease in antibody activity was noted, however this does not prove that antigen binding was the reason for cellular uptake.

Results and Discussion:

Two methods were chosen for attaching antibodies to chitosan nanoparticles: (Lee et al., 2012) and (Zhu et al., 2015) referred to as NP-Antibody-1 and NP-Antibody-2 respectively. These methods were selected as it required the minimum amount of change to the nanoparticle used in the previous chapter.

Antibodies cannot be conjugated to the deacetylated chitosan used to synthesize the original ChNPs. Lee et al., and Zhu et al., both use chitosan-glutamate as the base for the

construction of the nanoparticles. The glutamate provides carboxyl groups that can be activated to form a peptide bond with other proteins. Carbodiimide crosslinking chemistry (EDC) is used to bind antibodies to the chitosan glutamate (Nakajima and Ikada, 1995).

Now that a new material is again being used to construct the nanoparticle, the initial sizing and siRNA retention and release studies must be repeated for this new formulation.

Chitosan glutamate nanoparticles (ChGlutNP) were synthesised using the same method as the ChNP particles in chapter 3 with the same concentrations of chitosan(glutamate), TPP and siRNA. The only difference is that chitosan glutamate is added dropwise instead of pure chitosan.

Sizing for the pre-antibody conjugated particle (ChGlutNP and ChGlutNP-siRNA) was achieved in the same manner as with the chitosan nanoparticles in the previous chapter. DLS was used to measure the particles with and without siRNA. Sizing and rough shape were also confirmed with TEM (Figure 4.1). The particles were bigger after the addition of siRNA measuring at roughly 250 nm. TEM was again used to ascertain the size and structure of the nanoparticles, confirming a size of around 220 nm. This change is due to steric hindrance from the glutamate sidechains and the fact that the increased deacetylation (75-90%) removes the amine groups that TPP and the negatively charged siRNA crosslink with. Decreasing the amine groups and replacing them with glutamate effectively decreases the concentration of the crosslinker and so is potentially the reason for the increase in the particle size.

siRNA release studies were performed using the same method as with the standard NP-siRNA particles; by synthesising fluorescently tagged-siRNA entrapped chitosan-glutamate nanoparticles and incubating them in 50% FCS for a range of times at 37˚C. The incubated samples were loaded onto 4% agarose gel for separation by electrophoresis. The samples were loaded along with siRNA not entrapped inside a nanoparticle, nanoparticles not exposed to FCS and nanoparticles incubated in heparin as a positive control (Figure 4.2). 38% of the siRNA was released after an hour in 50% FCS at 37 ˚C.

Figure 4.1

ChNP vs ChGlutNP Size
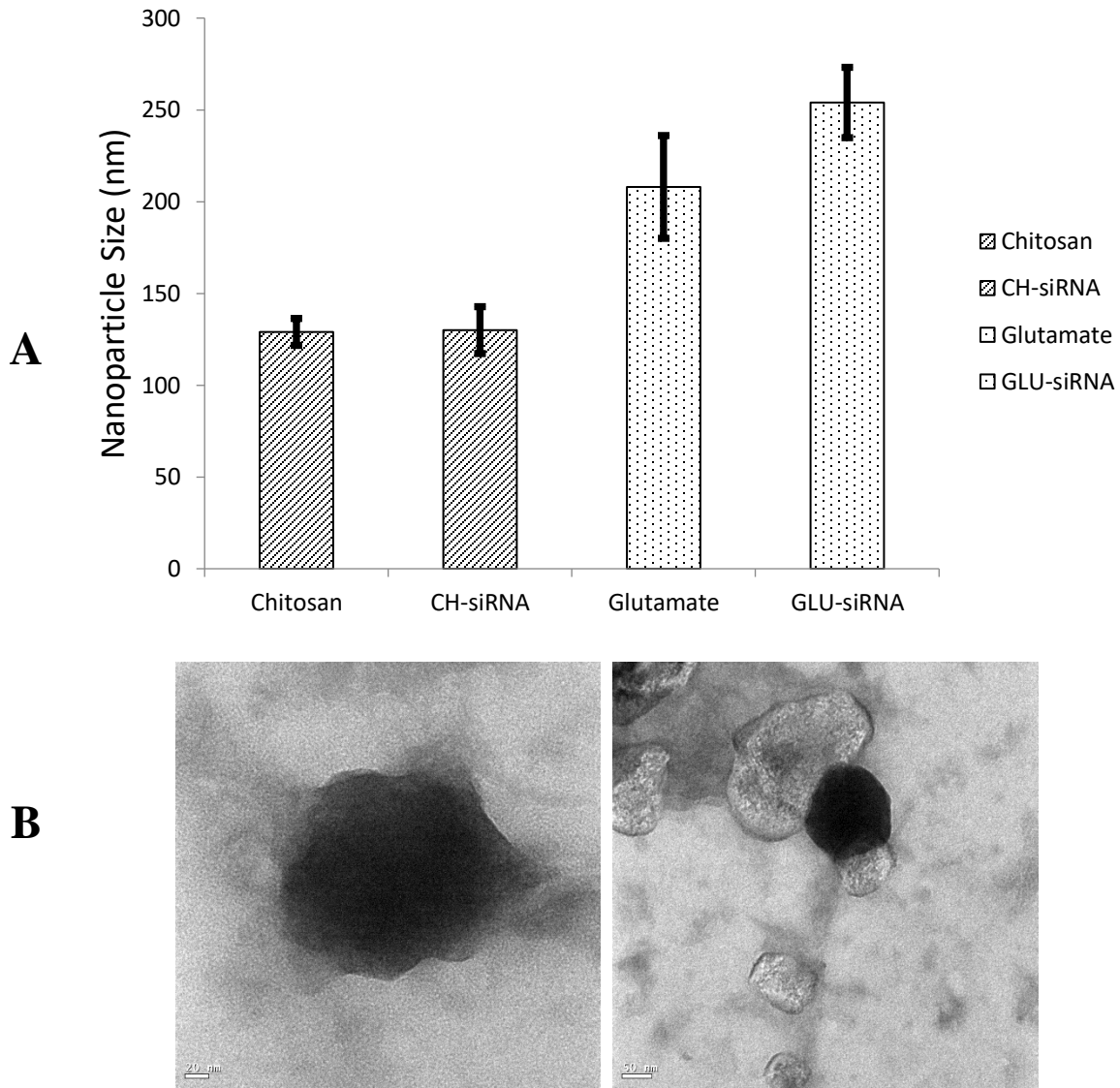
Figure 4.1 | Chitosan Glutamate Nanoparticle Sizing

Chitosan glutamate nanoparticles represent a slight change in composition and so were re-measured via DLS (A) and TEM (B). The particles were measured with and without siRNA to assess if siRNA affected nanoparticle size. For TEM, a negative stain (Phosphotungstic acid 3% w/v) was used. The Chitosan Glutamate particles were larger than the standard ChNPs. This is likely due to steric hinderance caused by the glutamate side chain. DLS sizing n=4

Figure 4.2

siRNA Entrapment and Release ChGlutNP
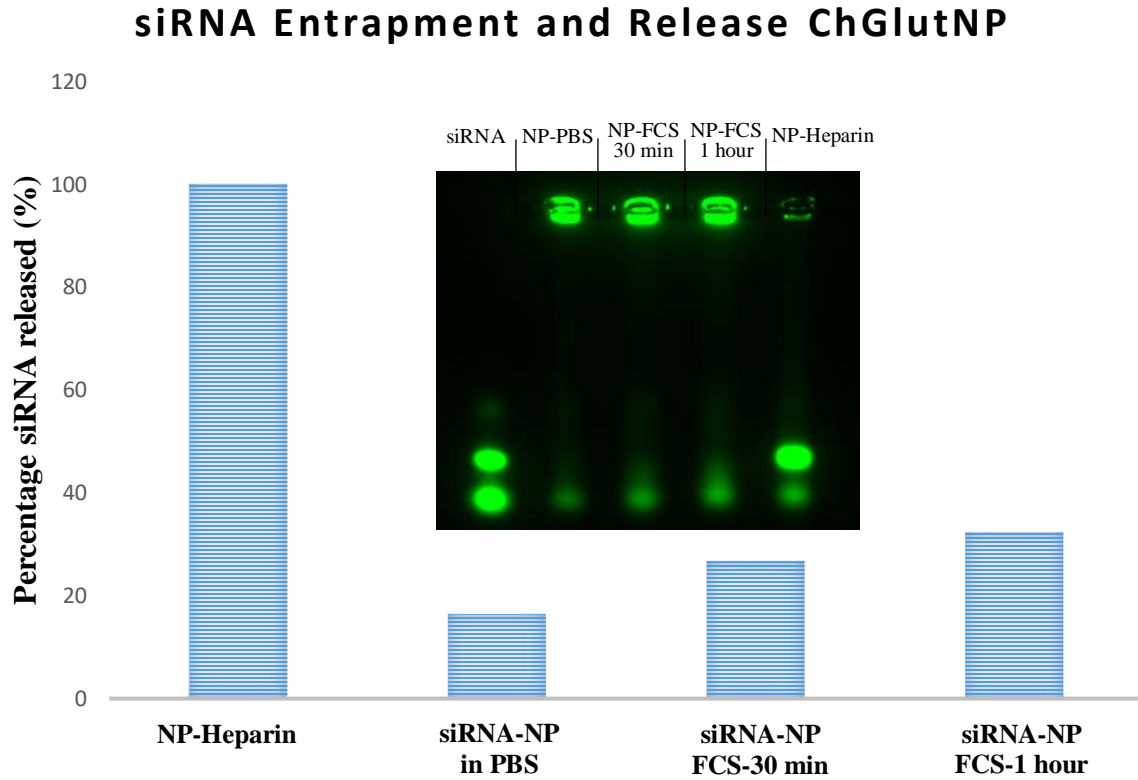
Figure 4.2 | Chitosan Glutamate siRNA Entrapment and Release

Alexafluor 488-siRNA entrapped Chitosan glutamate nanoparticles were incubated in 50% FCS for either 1 hour or half an hour at 37˚C. The release of siRNA was compared to nanoparticles in PBS at room temperature and Heparin for an hour at 37˚C shown in the graph above. Nanoparticles in PBS represent the entrapment efficiency. Particles suspended in PBS should lose no siRNA, so any siRNA found at the bottom of the gel failed to attach to the nanoparticle. Nanoparticles in heparin represent a positive control where the maximum amount of siRNA is released. Heparin competes with the siRNA for binding to the chitosan causing release of siRNA from the nanoparticle. As can be seen in picture of the gel above. The amount of fluorescence in each well increases with prolonged exposure to serum. The final lane shows a similar amount of fluorescence to the first lane showing that heparin induced a significant amunt of the siRNA to be released though some can still be seen in the well.

The ChGlutNP particles are larger than the ChNP particles, 223 nm to 137 nm respectively. Though the particles were larger than desired, antibodies were still to be added to the surface and so efforts to decrease the size were made later. siRNA binding and retention was confirmed so experiments moved onto the conjugation of antibodies to the surface of the particles. As mentioned, two methods were adopted for the conjugation of antibodies, designated NP-Antibody-1 and NP-Antibody-2. The methods used to attach the antibodies are detailed bellow.

NP-Antibody-1:

There are 2 steps in the formation of NP-Antibody-1 particles (Figure 4.3):

1: EDC reaction is used to conjugate antibodies to lose strands of chitosan in solution.

2: The chitosan strands that now have antibodies conjugated to them are used to synthesise the nanoparticle using the same method laid out in chapter 3. Chitosan-antibody conjugates are stirred at 15,000 rpm using a magnet bar and the crosslinker and siRNA are added dropwise over the course of 1 minute.

The first method for antibody conjugation to chitosan nanoparticles used the EDC sulfo-NHS reaction. 15 mg sulfo-NHS and 30 mg EDAC were added to 5 mL 0.1% chitosan glutamate in PBS (w/v). To this mixture 30 μL CRT4 was added (0.67 mg/mL). The

solution was agitated at room temperature for one hour to create a PBS-chitosan-antibody conjugate mixture.

The method was adapted from (Lee et al., 2012) by taking their method of antibody conjugation to chitosan but using the chitosan nanoparticle synthesis method detailed in chapter 3 which was also adapted for this thesis. Nanoparticles were synthesised using the method from the previous chapter however, the 3 mL Chitosan used previously was replaced with the PBS-chitosan-antibody conjugate mixture created through the EDAC reaction.

The particles were collected through centrifugation at 15,000 rpm for 30 minutes and washed with PBS twice to remove any unbound antibody. These particles will be referred to as NP-Antibody-1.

NP-Antibody-2:

There are 3 steps in the formation of NP-Antibody-2 particles (Figure 4.4):

1: EDC reaction is used to activate antibodies in sterile PBS solution.

2: A ChGlutNP particles are synthesised

3: The EDC reaction containing the activated antibodies and EDC reagents are added dropwise to the pre-synthesised ChGlutNP particles under 15,000 rpm magnetic stirring.

The second method of antibody conjugation involved conjugation of antibodies to the outside of an already synthesized chitosan glutamate nanoparticle. Synthesizing siRNA-ChGlutNP without conjugating antibodies to the chitosan first, ensured that antibodies were only present on the outside of the particle.

Before synthesis of the nanoparticles, 30 µL antibody was mixed with 30 mg EDAC and 15 mg sulfo-NHS in 5 mL PBS. The EDC reaction activates the carboxyl groups on the antibodies and prepares them for coupling to the glutamate on the nanoparticle surface. The siRNA-ChGlutNP were re-suspended in 800 µL PBS. With magnetic stirring at 3000 rpm, 375 µL activated antibody, EDAC, sulfo-NHS solution was added dropwise and left-over night at room temperature. The next day the antibody conjugate nanoparticles were collected by centrifugation at 15,000 rpm for 30 minutes. These particles will be referred to as NP-Antibody-2. This method was adapted from (Zhu et al., 2015) by changing the synthesis of the initial (non-conjugated) particle to fit the synthesis already outlined in chapter 3, with concentrations, timings and temperatures altered later on (detailed below).

Figure 4.3
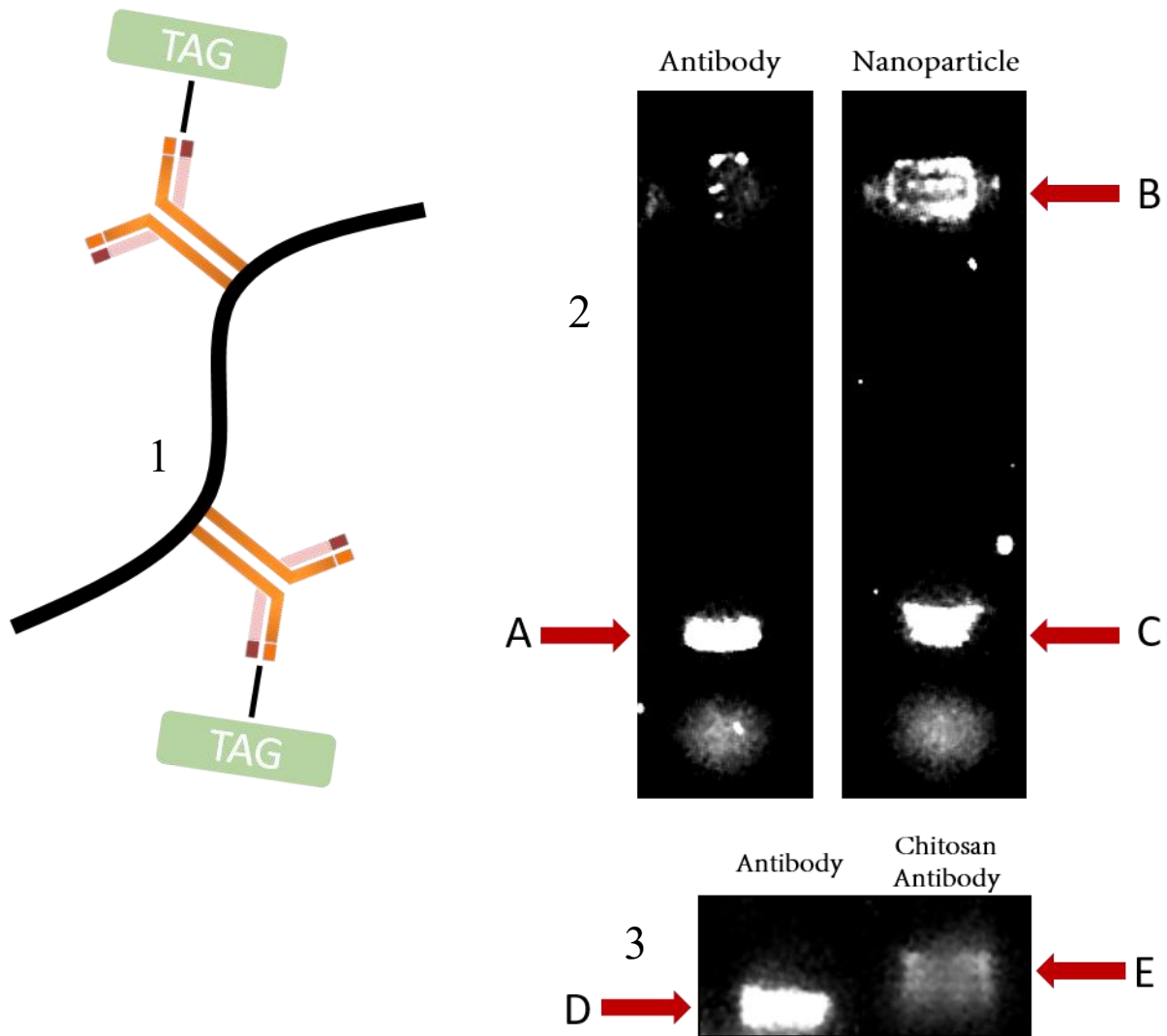
Figure 4.3 | NP-Antibody-1 Antibody Conjugation Confirmation

(1) is a representation of the NP-Antibody-1 antibody conjugation with antibodies (Orange), fluorescent tag (Green), conjugated to the chitosan glutamate polymer strand (Black line). These strands are taken and used in the synthesis of the particle.

(2) is an SDS-PAGE. Lane 1: Unconjugated Alexafluor-antibody. Lane 2: Alexafluor-antibody conjugated to the chitosan polymer and synthesised into a nanoparticle. Alexafluor-antibody can freely move through the gel (A) and (C). Antibodies conjugated to chitosan and then synthesized into a nanoparticle are trapped in the well (B).

(3) a gel electrophoresis (5%) of fluorescently tagged antibody in Lane 1 and antibody conjugated chitosan before nanoparticle synthesis. Again, Alexafluor-antibody is free to move through the gel (D). Chitosan conjugated antibodies appear higher and laddered due do varying numbers of chitosan strands attached (E).

Figure 4.4
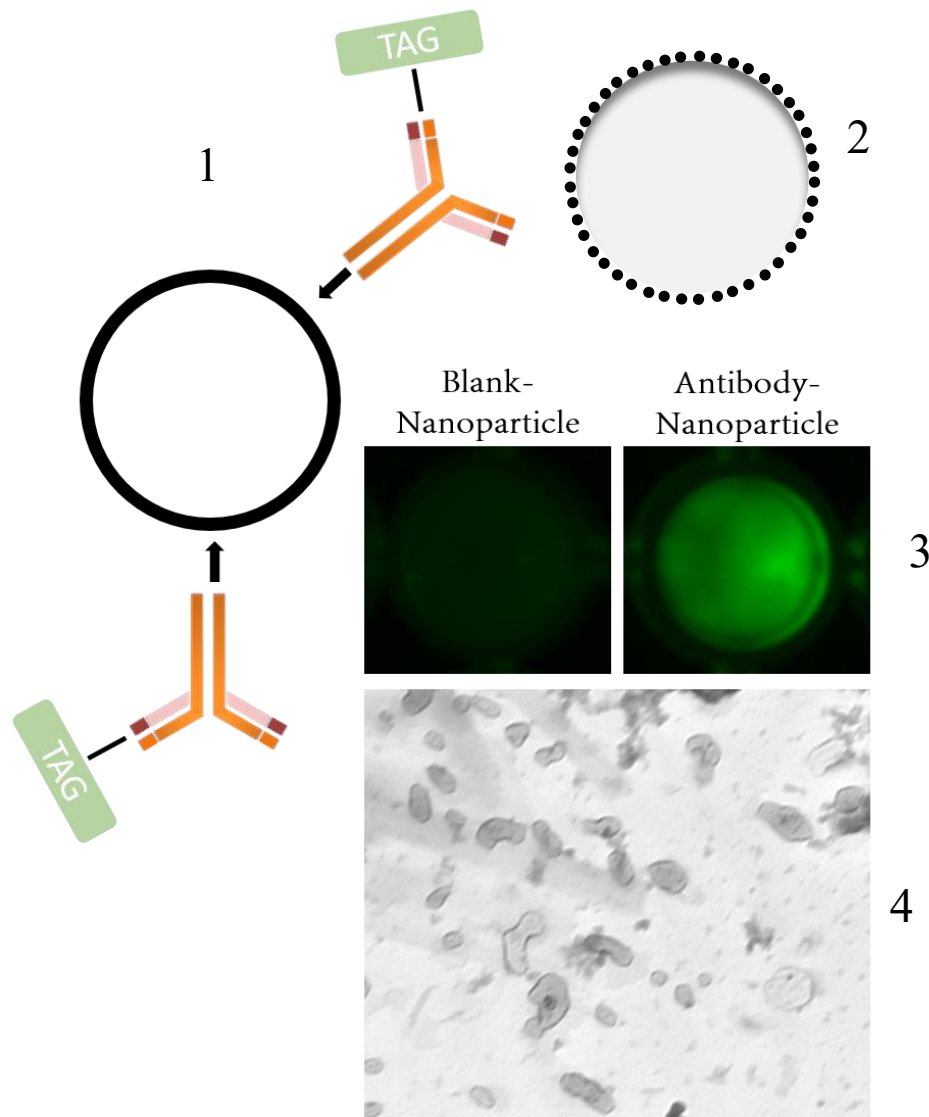
Figure 4.4 | NP-Antibody-2 Antibody Conjugation Confirmation

(1) is a representation of the NP-Antibody-2 antibody conjugation with antibodies (Orange), fluorescent tag (Green), conjugated to the chitosan glutamate nanoparticle (Black circle). ChGlutNP were synthesised first and EDC activated antibodies added to the particles dropwise.

(2) A representation of what gold labelled antibody-conjugated nanoparticles were expected to look like under TEM imaging.

(3) An image of the conjugation of the fluorescent antibody to the nanoparticle after 3 washing steps and compared to unconjugated particle.

(4) TEM image of gold labelled antibodies conjugated nanoparticles. No stain was used.

Figure 4.5
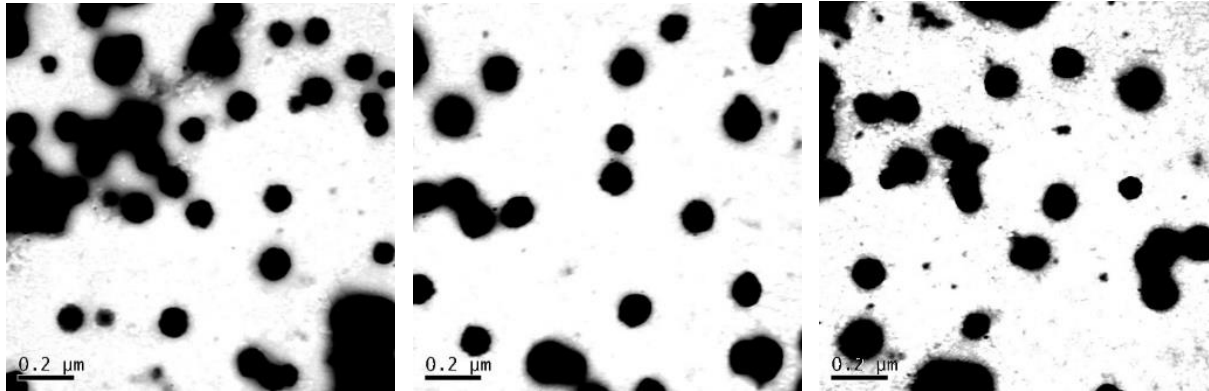
Figure 4.5 | NP-Antibody-2 Transmission Electron Microscope Images.
ChGlutNP-Antibodies were synthesised, washed and 2 µl added to a TEM copper grid. The nanoparticles were left to dry and were then stained with phosphotungstic acid. The images were taken with the JEOL 1200EX Transmission Electron Microscope. Phosphotungstic acid is a negative stain and is taken up into the chitosan polymer mesh and other carbon-based molecules. The nanoparticles appear black with a fainter coroner around them likely from the antibodies on the surface. Particles appear spherical and around 200 nm in size.

TEM:

A second method for imaging the antibodies conjugated to the surface was the utilization of TEM and the phosphotungstic acid negative stain. Phosphotungstic acid selectively binds to basic amino acid residues lysine and arginine thereby providing visualization of proteins via TEM (Sheridan and Barrnett, 1969).

As mentioned previously, phosphotungstic acid is used as a negative stain for the chitosan nanoparticles. If antibodies were present on the surface of the particle then a TEM image should look similar to the images captured in the previous chapter but with a lighter halo around the particle signifying the antibodies. Figure 4.5 clearly shows the expected halo not before seen in particles without the antibody conjugation.

Another TEM method was used to assess antibody conjugation using 12 nm gold nanoparticle conjugated antibodies. For this, TEM imaging a negative stain was not used so the chitosan nanoparticle cannot be seen at all. Figure 4.4 shows what successfully conjugated particles should look like. As the chitosan particles contain no negative stain, they will be invisible, however, the 12 nm gold particles show up without a stain. Therefore, the expected image will be a clear circle with a black ring of gold nanoparticles around it. Figure 4.5 show the TEM images of the gold-antibody conjugated ChGlutNP. Though the chitosan nanoparticles themselves were not stained, clear black rings can be

seen. The black rings show the gold labelled antibodies surrounding the chitosan nanoparticles and so confirm antibody conjugation. If the antibodies were not conjugated to the outside of the particles they would have been removed through washing and simply aggregated into black shapes on the TEM grid. No study so far has confirmed antibody conjugation to chitosan nanoparticles through TEM imaging and this method was developed expressly for this thesis.

Nanoparticle-antibody sizing:

The addition of antibodies to the nanoparticles was likely to affect the size of the particles and it was important to keep the particles as small as possible to avoid hindering cellular uptake. DLS was used to measure nanoparticle-antibody sizing as it was higher throughput for the large number experiments needed. Figure 4.6 shows all nanoparticle sizes resultant from the varying conditions of synthesis.

NP-Antibody-1 immediately presented an increased size. The NP-Antibody-1 synthesis involved conjugating the antibody to the chitosan strands before nanoparticle synthesis and was adapted from (Lee et al., 2011). NP-Antibody-1 particles showed initial promise with confirmation of antibody binding to the chitosan strands through gel electrophoresis. Unfortunately, due to the uncontrolled orientation of the antibodies the nanoparticle size and range increased greatly (>400 nm). The NP-Antibody-1 synthesis method could also result in all antibodies facing inwards or simply orientated in a way that prevented ligand binding. Lee et al., does in fact show their particles to be up to 345 nm in size (Lee at al.,

2011). 400 nm is too large for the purposes of this thesis due to the need for rapid cellular

uptake.

Figure 4.6
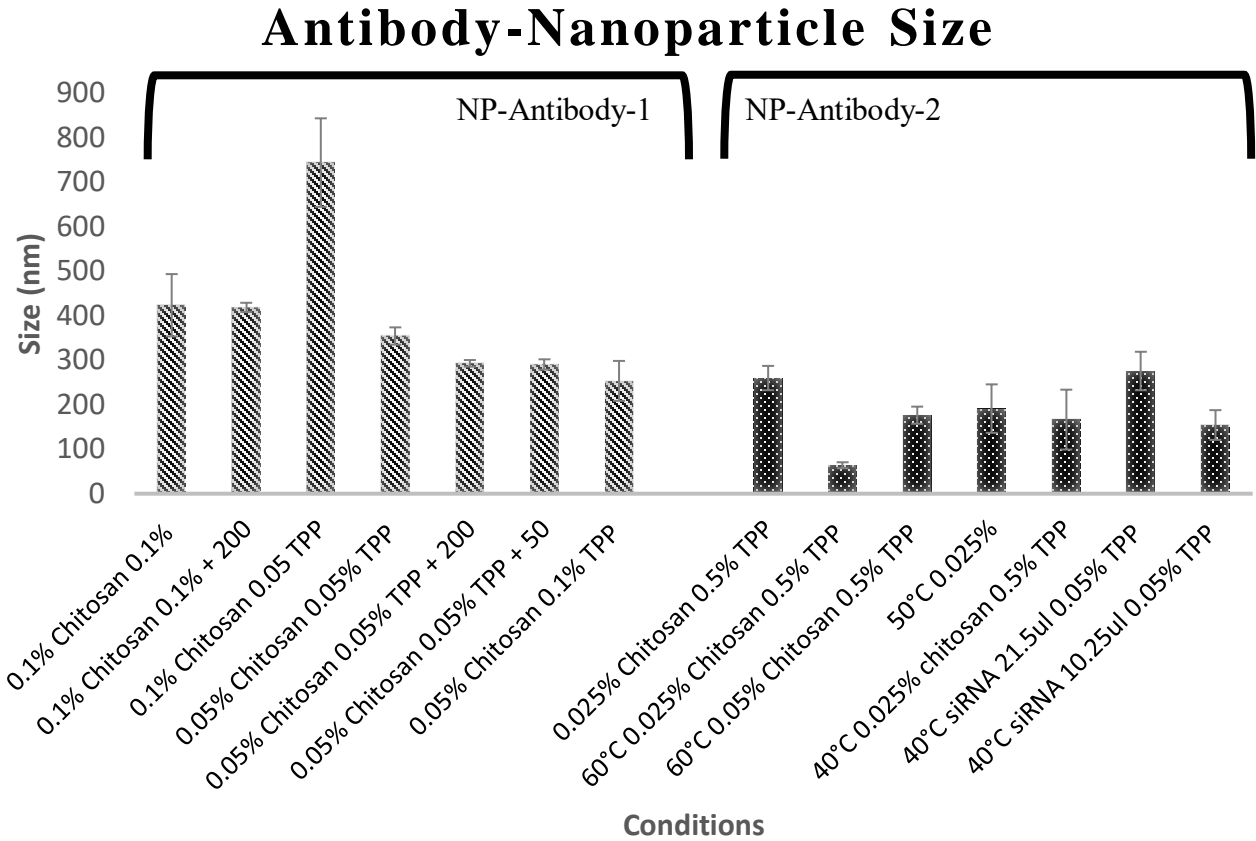
Figure 4.6 | Nanoparticle-Antibody Conjugation Sizing
The graph shows nanoparticle size with varying concentrations and conditions used to achieve the desired nanoparticle size. The graph represents a development from left to right as synthesis conditions were optimised. Varying concentrations of chitosan, TPP and siRNA were used as well as variations in temperature and order of addition of reagents. The first 7 bars represent NP-Antibody-1 synthesis with the last 7 NP-Antibody-2. It was realised that a higher synthesis temperature would produce smaller particles but must not exceed 60 degrees as this would result in antibody denaturation. n=3 for every condition)

NP-Antibody-2 particle synthesis should give more control over the size of the particle and the orientation/location of the antibodies. NP-Antibody-2 were adapted from Zhu et al., and involved synthesizing ChGlutNP without antibodies, then adding EDC activated antibody along with the activation reagents (EDS and sulfo-NHS), dropwise to the NP-ChGlutNP whilst being stirred magnetically at 3000 rpm (Figure 4.4) (Zhu et al., 2015). NP-Antibody-2 still resulted in particles >400 nm, however, the synthesis of the pre-conjugation particles could easily be altered and so change the final particle size.

Gan et al., demonstrated that increasing the temperature of the synthesis mixture results in a decrease in particle size (Gan et al., 2005). The change in particle size through increased temperature is due to lower viscosity of the chitosan glutamate solution. It was also necessary to decrease the concentration of chitosan glutamate and TPP. As stated previously, chitosan nanoparticles form by the aggregation of smaller particles as the crosslinker is added dropwise. The first drop of the crosslinker forms very small particles with the next drop binding those small particles together. The drop after that then binds the second particles together, again increasing the size of the nanoparticles present through aggregation.

Bellow the process of reaching an antibody conjugated nanoparticle is described. First the different conditions for NP-Antibody-1 then the conditions used for NP-Antibody-2. A graph showing the sizes resultant from each condition can be seen in Figure 4.6.

NP-Antibody-1 Conditions:

C = Chitosan Glutamate (no antibody conjugated)

CA = Chitosan Glutamate-Antibody Conjugate

T = Tripolyphosphate

CA mix 0.1% C 0.1%T:

The first condition used was simply to conjugate the antibody to the chitosan strands and form a nanoparticle from the resultant conjugate in precisely the same method as in the previous chapter. 0.1% chitosan-antibody conjugate was used with 0.1% TPP added dropwise under 3000 rpm magnetic stirring. A size of 423 nm was created from these conditions.

0.1% C 0.1%T 200 μl CA mix added at the end:

The drastic increase in size was likely due to the steric hindrance of the antibodies conjugated to the chitosan strands. To decrease this effect ChGlutNP particles were synthesized using unconjugated chitosan glutamate. TPP was added dropwise, however, 200 μL TPP and 200 μL antibody conjugated chitosan glutamate were added dropwise

simultaneously after finishing the initial dropwise addition of TPP to the unconjugated chitosan glutamate. As previously mentioned, chitosan nanoparticles form through aggregation. Upon the first drop of TPP very small nanoparticles form. Each subsequent drop of TPP aggregates these smaller nanoparticles together. The rapid 3000 rpm stirring is to prevent too much aggregation. It was thought that the addition of the chitosan glutamate-antibody conjugate and TPP after synthesis of the ChGlutNP base could result in a coating of the existing nanoparticles in a surface layer of chitosan glutamate-antibody conjugate. These conditions resulted in particles 418 nm in size.

0.1% C 0.05%T:

The adding of the conjugated chitosan at the end rather than at the start of synthesis appeared to have little effect on the size of the particle. The next condition went back to using the chitosan glutamate-antibody conjugate from the start, however the concentration of TPP was halved. As expected, the size of the particle almost doubled resulting in a nanoparticle that was 744 nm. This doubling in size is due to there being less TPP to crosslink with the chitosan strands resulting in them being held less tightly together and producing a particle much larger in size.

0.05% C 0.05%T:

To further test the effect of the ratio between chitosan and TPP, the concentration of chitosan-glutamate-antibody conjugate was also halved. The halving of both chitosan glutamate-antibody conjugate and TPP resulted in a particle of 354 nm. This is smaller than

the original particle (likely due to there being less chitosan to form particles from), however still nowhere near the 200 nm needed.

0.05% C 0.05%T - 200 µl CA mix added at the end:

To ensure the conditions were tested fairly, the conditions used in the second attempt were tried again with the same concentrations as the previous method. These conditions involved the synthesis of a chitosan-glutamate particle (no antibody conjugated) using 0.05% chitosan and 0.05% TPP with 200 µL of the chitosan glutamate-antibody conjugate added along with 200 µL, dropwise at the end. These conditions produce a particle that was, again, smaller at 293 nm but still about 100 nm too large.

0.05% C 0.05%T 50 µl - CA mix added at the end:

In an attempt to reduce the effect, the antibodies had on size, the amount of chitosan glutamate-antibody conjugate that was added at the end was reduced from 200µL to 50 µL. This reduced the particle size to 290 nm, effectively no different from the previous results.

0.05% C 0.1%T:

The final method tried was to increase the ratio of TPP to chitosan glutamate-antibody conjugate. By increasing the amount of TPP, the chitosan strands should be held more tightly together and so decrease the particles size. These conditions resulted in a particle 253 nm in size which is far closer to the desired 200 nm. Increasing the concentration of

TPP further could have resulted in an even smaller particle but it was thought that this would negatively affect the siRNA release and so a different method was required.

NP-Antibody-2 Conditions:

0.025% C 0.5%T:

Learning from the previous conditions the concentrations of chitosan glutamate and TPP were kept low: 0.025% and 0.5% respectively. Method 2 differs from the first in that antibodies were never conjugated to the chitosan strands. Instead, antibodies were conjugated to the outside of a pre-synthesised ChGlutNP. Antibodies were activated separately from the nanoparticles and added dropwise along with the EDC activating agents once the ChGlutNP were synthesised. The concentration of chitosan was reduced to 0.025% with a TPP concentration double as to ensure smaller particles before antibody conjugation. The particles produced through this method were 259 nm.

0.025% C 0.5%T (60°C):

The size of nanoparticles is directly affected by chitosan:TPP weight ratio and must be kept between 3:1 and 6:1, however, increasing temperature has also been shown to decrease particle size (HueiChen, 2008b). To this end, the temperature of the initial synthesis (ChGlutNP without antibodies) was increased to 60 degrees. This could not be performed using method 1 particles as 60 degrees would denature the antibodies. The particles were

left to cool then stirred at 3000 rpm whilst activated antibodies and EDC reagents were added dropwise. These conditions created particles that were 64 nm.

0.05% C 0.5%T (60°C):

64 nm had overstepped the target size, so the concentration of chitosan glutamate was increased, lowering the ratio of TPP to chitosan. The temperature was kept at 60 degrees. The synthesis under these conditions resulted in a particle 175 nm in size.

0.025% C 0.5%T (50°C):

176 nm is almost perfect, however, siRNA must be present during the nanoparticle synthesis, to allow it to crosslink with the chitosan-glutamate. 60 degrees will cause separation of the siRNA double strands which will likely crosslink with the chitosan separately resulting in ineffective siRNA. To overcome this the temperature was lowered to 50 degrees. PCR annealing is performed at 50 degrees. These conditions resulted in particles 191 nm in size.

0.025% C 0.5%T (40°C):

40 degrees was attempted as this was a safer temperature to ensure siRNA was annealed, producing particles 166 nm in size.

0.025% C 0.5%T siRNA (21.5µl, 100 M) (40°C):

siRNA had not yet been added to the synthesis mixture. 21.5 µL of 100 M siRNA is the normal amount added during synthesis. With the addition of 21.5 µL and a synthesis temperature of 40 degrees the nanoparticles were 275 nm.

0.025% C 0.5%T siRNA (10.25µl 100 M) (40°C):

The size of the particles were now above 200 nm again. As the cause of this increase in size was the addition of siRNA, the volume of siRNA added during synthesis was halved. 10.25 µL 100 M siRNA was added at a synthesis temperature of 40 degrees produced 154 nm particles.

Conformation of Conjugation:

Conjugation of the antibody to the ChGlutNPs was confirmed through several methods detailed below.

Gel Electrophoresis: NP-Antibody-1:

NP-Antibody-1 is the conjugation of antibodies to the chitosan polymer before the synthesis of the particle. A method was independently devised to use SDS-Page to confirm the conjugation of the antibody to the chitosan polymer (Figure 4.3). Similar to the siRNA binding and retention studies, a fluorescent antibody was used. Conjugation to the nanoparticle was confirmed through the retention of the nanoparticle in the well of the gels.

Any fluorescent antibody conjugated to the particle will remain stuck in the well. Any unconjugated antibody will be pulled through the gel.

Figure 4.3 shows two lanes, "Antibody" and "Nanoparticle." The "Antibody" lane has just fluorescently tagged antibody before conjugation to a nanoparticle. The "Nanoparticle Lane" has that same fluorescent antibody conjugated to a nanoparticle. At the bottom of both lanes (A and C) the band for the unconjugated antibody can be seen. The "Antibody" lane has very little fluorescence left in the well. Any fluorescence there is likely due to aggregated antibodies.

The "Nanoparticle" lane has a large amount of fluorescence remaining in the well with some antibody remaining unconjugated and forming a band at the same place as in the "Antibody" lane. The large amount of fluorescence in the well of the "Nanoparticle" lane, confirms the conjugation of the antibody to the nanoparticle surface. It can also be concluded that this conjugation is indeed through a strong bond like a peptide bond as previous experiments with the chitosan nanoparticles showed that electrostatic interactions were not enough to keep a chemical bound to the particle during electrophoresis.

The third gel image (Figure 4.3 (3)) was of the antibody-chitosan conjugate prior to nanoparticle formation. Next to the unconjugated antibody band it can be seen that the chitosan-antibody conjugates have migrated less than the unconjugated antibodies due to their increased molecular weight. The chitosan-antibody conjugate also appears to have

separated out into several lines suggesting antibodies with differing numbers of chitosan polymers attached.

Fluorescence and TEM: NP-Antibody-2:

The confirmation of antibody conjugation for NP-Antibody-1 suggested that NP-Antibody-2 should also be a success as the methods were similar. NP-Antibody-2 involves conjugation of the antibodies to the surface of a pre-synthesized ChGlutNP rather than to the chitosan before particle synthesis. This method aims to guarantee antibodies are on the outside of the particle and increase the chance of them remaining in the correct orientation.

Fluorescence:

Again, fluorescently tagged antibodies were used to confirm antibody conjugation. ChGlutNP particles were synthesized and then fluorescent antibody conjugated to their surface. The particles were centrifuged and washed 3 times then imaged in the Odyssey® Fc Imaging System (Li-COR).

Figure 4.4 (3) shows two wells containing unconjugated vs washed conjugated particles. A large amount of fluorescence can be seen in the conjugated well showing that the antibodies were indeed conjugated to the surface.

Antibody-Ligand Binding:

Antibody conjugation had been confirmed. The particle size had successfully been reduced below 200 nm. Next, antibody ligand binding was tested.

Confirmation of antibody conjugation proves that the antibodies were bound strongly to the surface of the nanoparticles, however, it did not confirm the orientation or binding capabilities of the antibody. There is little control over the orientation of the antibody upon conjugation and so it is unknown if the FC binding sites were still accessible. Additionally, EDAC activation and conjugation to the particles may have affected the antibodies in other, unknown ways.

To confirm antibody ligand binding several methods were used:

Ligand Capture:

Ligand capture was assessed through a newly invented method involving biotin streptavidin interactions. Biotinylation of CLEC14A allows for the binding of fluorescent streptavidin to biotinylated CLEC14A. A method was devised that would synthesise antibody conjugated chitosan glutamate particles with antibodies that would bind CLEC14A. Figure 4.7 (B) shows confirmation of CLEC14A biotinylation through western blot. The presence of an extra band with an increased molecular weight the size of CLEC14A + biotin confirms the successful biotinylation of CLEC14A. Biotinylated CLEC14A was washed over the particles resulting in the binding of CLEC14A to the conjugated antibodies on the surface of the particle. The particles were then washed in PBS

3 times and collected through centrifugation. After removal of unbound CLEC14A with PBS the particles were washed with Alexafluor 488 tagged streptavidin. The particles were again washed 3 times with PBS, collected through centrifugation and imaged using the Odyssey® Fc Imaging System (Li-COR).

A negative control of antibody conjugated particles that were not washed with biotinylated CLEC14A was used. There was no significant difference between the fluorescence of the negative control and CLEC14A-biotin bound particles. This lack of disparity is again likely due to the protein corona effect common among nanoparticles (Oh et al., 2018) (Barbero et al., 2017). To negate this problem the nanoparticles were blocked with 10% FCS before and during binding the CLEC14A-biotin as well as before and during streptavidin binding. Unfortunately, figure 4.7 shows that there was still no significant difference between CLEC14A bound and the negative control particles. The binding of proteins to the surface of the nanoparticles is a complex but powerful interaction that is hard to overcome (Kokkinopoulou et al., 2017).

Adapted ELISA:

A new method was required to assess antibody binding. A literature search showed that ELISA's were a common method used for nanoparticle-antibody antigen binding tests. A method was adapted from the standard ELISA method to test the antibody bound nanoparticles. Maxisorb 96 well plates (Nunc™ 44-2404-21) were used to bind antigens wells to test antigen specific binding of the antibody conjugated nanoparticles.

Nanoparticles were synthesised with Alexafluor-488 tagged anti-mouse IgG antibodies on the surface. The wells were divided into either CLEC14A adsorbed or BSA absorbed. The BSA worked as a negative control that the anti-mouse IgG antibody should not bind to it.

Mouse-CLEC14A and Human-CLEC14A were absorbed to the Maxisorb wells. Each well was washed PBS 5 times then with Anti-CLEC14A (Mouse IgG). The wells were washed 5 times again then with Anti-Mouse IgG bound nanoparticles or unconjugated anti-mouse IgG. All wells were washed 5 times with PBS and imaged with the Odyssey® Fc Imaging System (Li-COR), Figure 4.8.

Figure 4.7

Measuring Antigen Capture: ChGlutNP-Antibody

A

y-axis: Arbitary Units (Fluorescence) — 0, 50, 100, 150, 200, 250, 300, 350, 400, 450

x-axis: No Antigen, CLEC-Biotin

State of Antigen Capture

B

Biotinylated CLEC14A

Un-Biotinylated CLEC14A
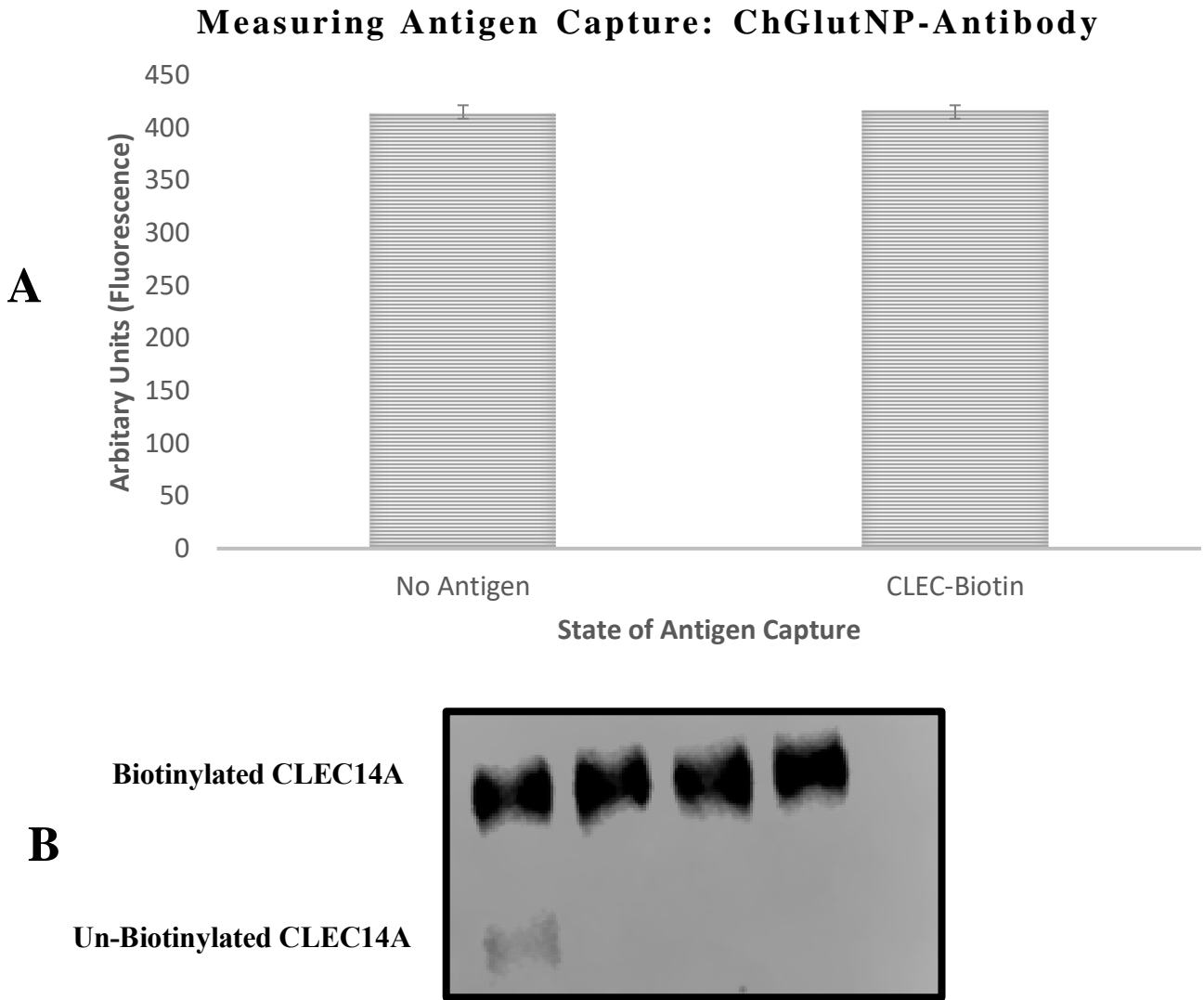
Figure 4.7 | Nanoparticle-Antibody Antigen Capture
(A) shows the ability for antibody conjugated nanoparticles to bind streptavidin. Two conditions were used: Half of the antibody conjugates were washed with CLEC-Biotin and the other half were blocked in FCS. Both were washed and incubated with fluorescently tagged streptavidin. Biotin-streptavidin affinity should result in higher level of fluorescence in the case of successful capture of the CLEC-Biotin however, there was equal fluorescence whether the CLEC-Biotin was present or not. This shows that this test was not useful to show antibody-ligand binding. n=10.
(B) The western blot gel below the graph shows the purified fractions of the biotinylated CLEC14A.

Figure 4.8

Antibody-Nanoparticle ELISA
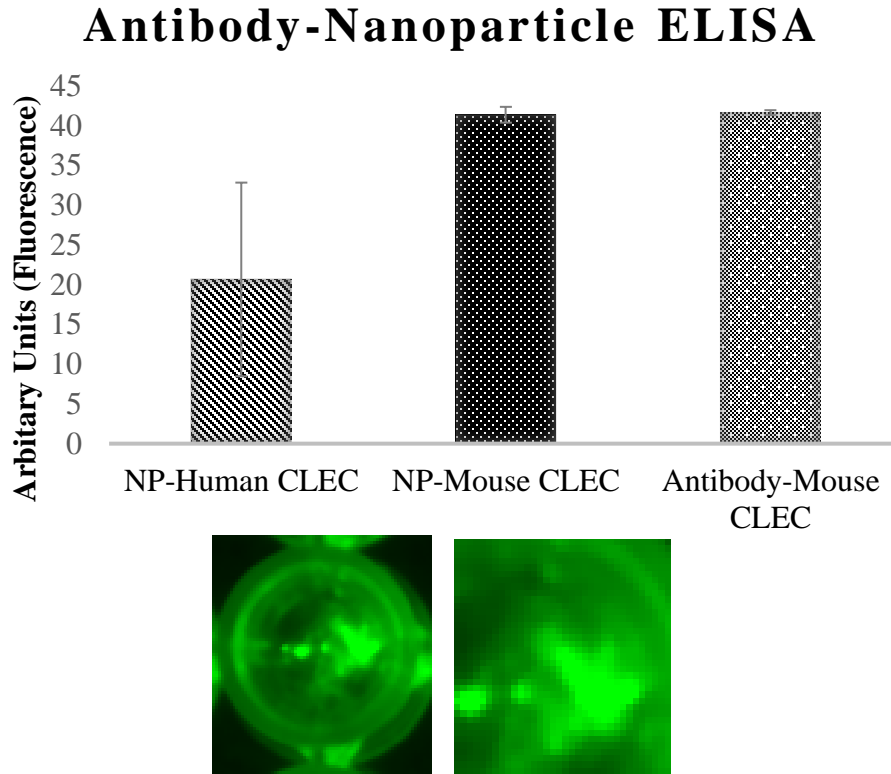
Figure 4.8 | Nanoparticle-Antibody Antigen ELISA

(A) shows the results of the ELISA for Alexafluor448-antibody conjugated nanoparticles to the antigen on an ELISA plate. Wells contained either human or mouse CLEC14A as the CRT4 antibody is known to bind more preferentially to mouse than human CLEC14A. These two conditions were compared to binding of the unconjugated antibody to mouse CLEC14A as the positive control (Far Right). The antibody conjugated nanoparticles bound to the (B) shows aggregation of the antibody-nanoparticle conjugates at high concentrations. n=3

As can be seen, there is a clear difference in binding between Human and Mouse CLEC14A as CRT4 has preference for mouse-CLEC14A. Nanoparticle binding to Mouse-CLEC14A is comparable to unconjugated antibody and has lower binding to Human-CLEC14A. These ELISA tests show that the antibody on the surface of the nanoparticles is binding its antigen and indeed binding preferentially.

Knockdown using Ch-Glut-Antibody-2:

Confirmation of antigen binding allows for progression to knockdown. The knockdown procedure was performed in exactly the same manner as the previous chapter.

HUVEC were incubated with siRNA containing ChGlutNP-(CLEC14A Antibody) at varying concentrations comparable to the concentrations used in a lipofectamine knockdown 1x, 2x, 3x and 4x concentration. (1x concentration is equal to 50 nM of siRNA delivered via lipofectamine, in "gold standard" *in-vitro* test). The concentration of siRNA inside any given nanoparticle remains the same, the increase in concentration of siRNA is achieved through the addition of more nanoparticles. The knockdown percentage achieved by the nanoparticles was compared to a lipofectamine siRNA knockdown (positive control) and a negative control lacking siRNA. Figure 4.9 shows the western blots from the knockdown of CLEC14A and figure 4.10 shows a graph of the percentage expression remaining for the various concentrations of nanoparticles used. Knockdowns were assessed

through polyacrylamide gel electrophoresis. The gels were imaged and analysed using the Odyssey® Fc Imaging System (Li-COR). Pixel values of the ChGlutNP-Antibody knockdown bands were compared to the positive and negative controls to calculate the knockdown percentage of CLEC14A.

Figure 4.9 shows images of a selection of Western Blot gels from the knockdowns. Figure 4.10 shows the percentage expression remaining after knockdown using ChGlutNP-Antibody's calculated from the western blots (Figure 4.9 shows only 2 of the gels) using pixel density analysis in ImageJ.

As can be seen, similarly to with the unconjugated ChNP's the effectiveness of the knockdown decreases as concentration goes up. Interestingly, the knockdown percentage for each concentration is actually less than with the ChNP's (Figure 4.11). The variation in knockdown percentage is also increased.

Monoclonal antibodies are known to aggregate under a variety of conditions similarly to many proteins in biological systems (Maas et al., 2007, Wang et al., 2010b). It is likely that the addition of antibodies to the surface of the nanoparticles increased the aggregation problems seen in the previous ChNP chapter. Due to this increased aggregation, cellular uptake was reduced and so knockdown was reduced. Aggregation would also prevent antigen binding, further decreasing cell uptake.

Figure 4.9
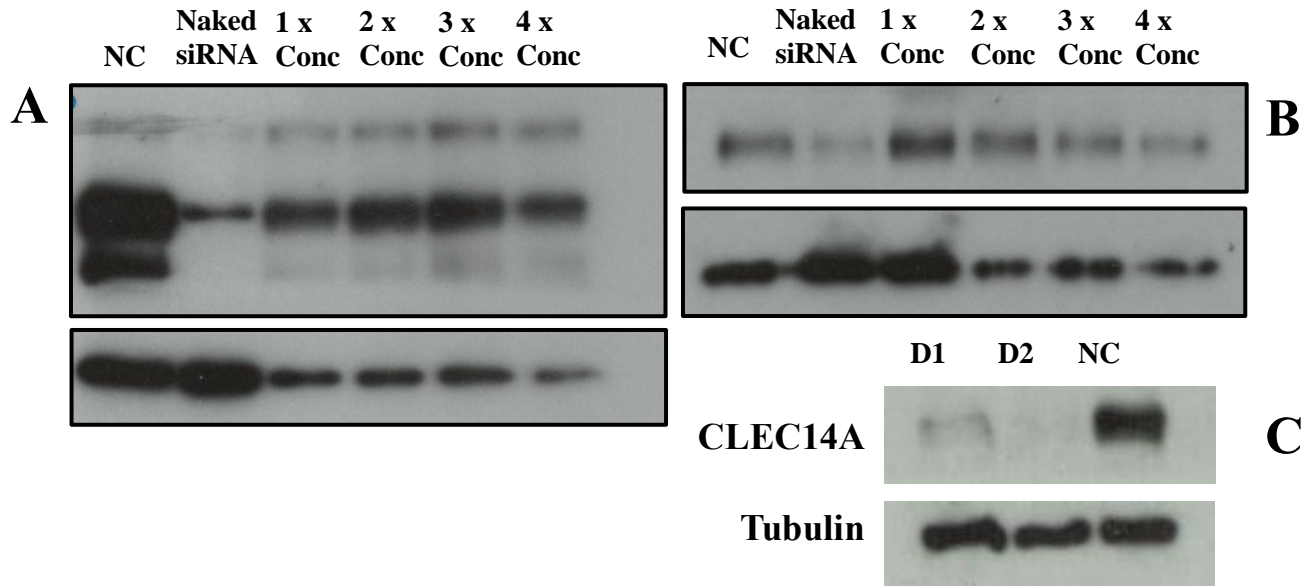
Figure 4.9 | CLEC14A Knockdown in HUVEC Antibody-Nanoparticles

((A) and (B) show examples of western blots imaged and analysed with the Odyssey® Fc Imaging System (Li-COR). Lane 1: Negative Control (No nanoparticles or siRNA). Lane 2 Naked siRNA (siRNA transfected with lipofectamine). Lane 3: ChNP-siRNA at a concentration equal to 25 nM siRNA added to the cells. Lane 4: ChNP-siRNA at a concentration equal to 50 nM siRNA added to the cells. Lane 5: ChNP-siRNA at a concentration equal to 100 nM siRNA added to the cells. Lane 6: ChNP-siRNA at a concentration equal to 150 nM siRNA added to the cells.

(B) Shows another example of a western blot similar to (A).

(C) Shows a western blot of just lipofectamine transfected siRNA, the ideal result. Two different duplexes against CLEC14A (D1) and (D2) were used. Though some of the bands look similar, pixel density analysis was performed to account for protein loading differences to give the true knockdown percentage.

Figure 4.10

Antibody-Nanoparticle Knockdown
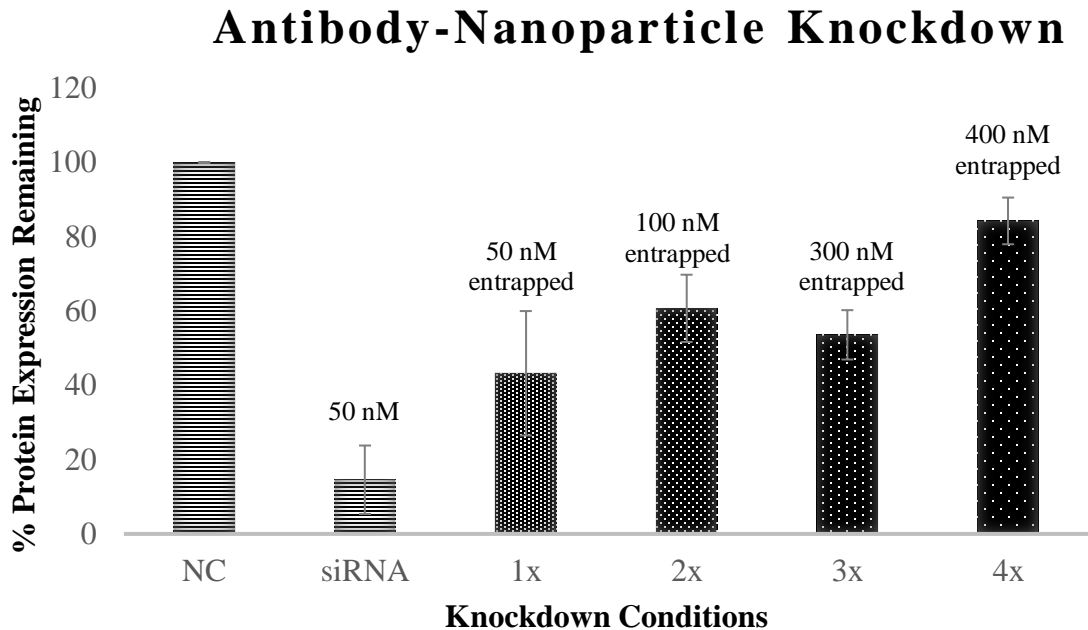
Figure 4.10 | CLEC14A Knockdown in HUVEC Antibody-Nanoparticles

Relative remaining protein expression after incubation with siRNA and ChGlutNP-Antibody-siRNA.

NC: HUVEC not exposed to siRNA, **siRNA:** HUVEC transfect with 50 nM siRNA using lipofectamine. **1x:** HUVEC incubated with ChNP-siRNA so that the total siRNA added to the cells equals 50nM. **2x:** HUVEC incubated with ChNP-siRNA so that the total siRNA added to the cells equals 100nM. **3x:** ChNP-siRNA concentration so that the total siRNA added to the cells equals 150nM. **4x:** ChNP-siRNA concentration so that the total siRNA added to the cells equals 200nM. The amount of siRNA per nanoparticle remains consistent between incubations. Concentration of siRNA is increased by increasing the number of nanoparticles added to the cells (concentration of siRNA labelled above respective bar).

The 1x concentration represented the highest knockdown. "50 nM" represents the concentration of siRNA incubated with HUVEC. "entrapped" represents siRNA inside the chitosan nanoparticle. Percentage knockdown decreases as concentrations go up due to nanoparticle aggregation.

n=3, error bars = SD

Figure 4.11

ChNP-siRNA vs NP-Antibody- 2
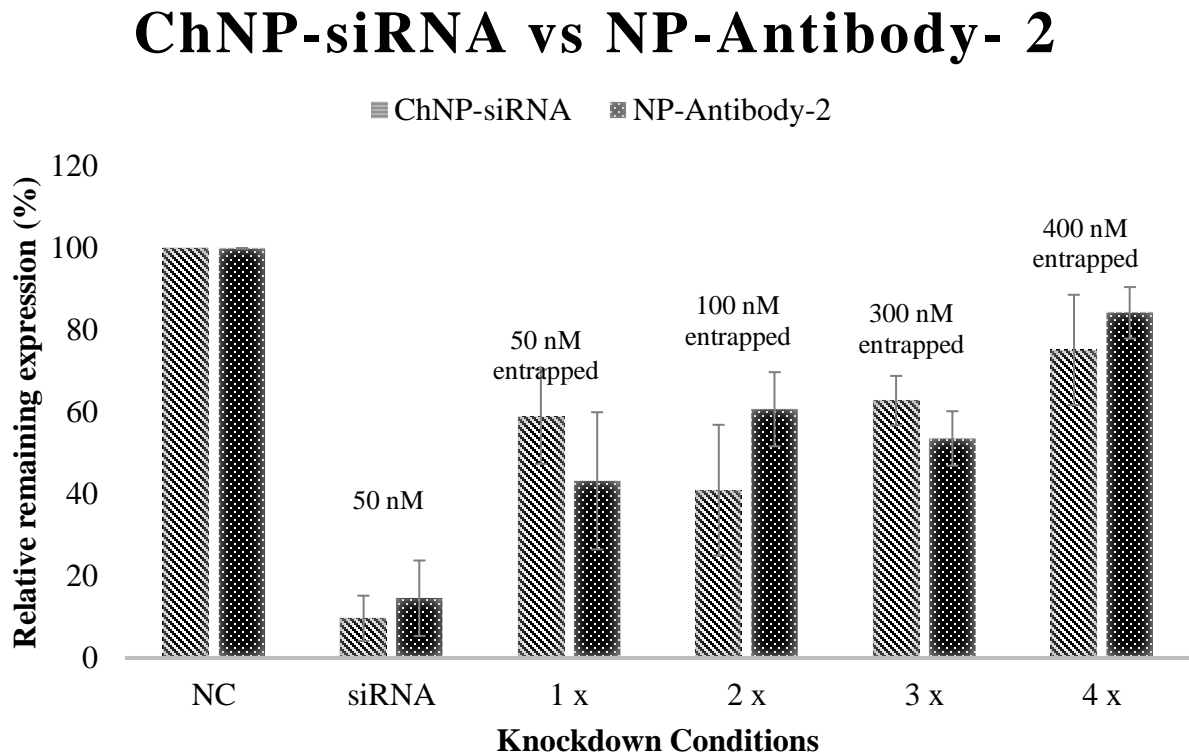
Figure 4.11 | NP-siRNA VS Antibody Targeted Nanoparticles:
This graph is for the visual comparison of the knockdown of CLEC14A using ChNP-siRNA nanoparticles (Light Grey) vs ChGlutNP-Antibody-siRNA (Dark Grey). **NC:** HUVEC not exposed to siRNA, **siRNA:** HUVEC transfect with 50 nM siRNA using lipofectamine. **1x:** HUVEC incubated with ChNP-siRNA so that the total siRNA added to the cells equals 50nM. **2x:** HUVEC incubated with ChNP-siRNA so that the total siRNA added to the cells equals 100nM. **3x:** ChNP-siRNA concentration so that the total siRNA added to the cells equals 150nM. **4x:** ChNP-siRNA concentration so that the total siRNA added to the cells equals 200nM. The amount of siRNA per nanoparticle remains consistent between incubations. Concentration of siRNA is increased by increasing the number of nanoparticles added to the cells. n=3.
.

Conclusion:

In conclusion, ChGlutNP were shown to be effective in binding and retaining CLEC14A siRNA (comparable to the ChNP). The addition of antibodies to the surface of the particles drastically increased the size of the particles and a series of trial and improvement experiments were conducted to attempt to bring the size of the particles back down to below 200 nm.

The size was corrected, however, the addition of antibodies to the chitosan nanoparticles did not increase knockdown efficiency and, in fact, decreased it. This decrease is likely due to protein-protein induced aggregation decreasing cell uptake. The ChNP achieved a 60% knockdown which was comparable to other nanoparticle knockdown studies. There are other methods for potentially increasing knockdown, but it was decided that from here on, further studies will revert to using the ChNP's without antibody conjugation.

Chapter V

CLEC14A Vaccine:

Introduction:

The work done in this chapter was done in collaboration with an undergraduate student. (Elliot Brown: elliotjbrown@doctors.org.uk) *and is included with his permission.*

Previous chapters attempted to develop a vector for the delivery of siRNA. It was shown that a chitosan nanoparticle formed through crosslinking with TPP was a sufficient vector for the binding and release of siRNA. siRNA can be bound inside the chitosan particle through a process called ionic gelation. Due to the negative charge of siRNA it can act as a crosslinker, similarly to TPP. Ionic gelation is based on the method of electrostatic interaction between carboxyl groups on the chitosan polymer with negatively charged groups of polyanions. Any negatively charged polyanion can act as a crosslinker. As long as a protein can be maintained in a pH above is pI during synthesis of the chitosan nanoparticle then it will be entrapped inside the particle in a similar way to the siRNA.

Over the past decade nano-sized vectors such as viruses, liposomes and nanoparticles have garnered greater attention as delivery vehicles for vaccines (Gregory A.E., 2013). Nanoparticles have the ability to stabilize proteins or even act as adjuvants to break

tolerance. These vectors are able to enter antigen-presenting cells and modulate the immune response (Uto et al., 2009).

Vaccines against endothelial markers have been studied. Facciponte et al., (2014) studied a murine TEM1 DNA vaccine that produced a CD8+/CD4+ T-cell response resulting in slowed progression of tumours *in-vivo* (Facciponte et al., 2014). The vaccine consisted of a plasmid containing the cDNA for mouse TEM1 joined with the cDNA sequence for fragment C of tetanus toxoid (FrC). DNA-fusion vaccines have the advantage of not needing extensive protein production, however they have been shown to have weaker immune responses in humans. The anti-cancer effect of the vaccine was seen through induction of CD3-T cells, however, no anti-TEM1 antibodies were found in the serum

.

Zuagn et al., showed the efficacy of the Fc domain from human immunoglobulin in a fusion protein vaccine against ROBO4. The vaccine successfully reduced tumour growth by inhibiting angiogenesis in mice without affecting wound healing (Zhuang et al., 2015). The success of the tetanus toxoid fragment c (FrC) fusion in breaking tolerance and inducing a T cell response lead to the development of a CLEC14A-FrC fusion protein.

Delivering this fusion protein directly to antigen presenting cells in the vicinity of the tumour, via a nanoparticle vector, could have a dramatic effect on vaccine viability (Uto et al., 2009).

(Saupe et al., 2017) developed a fusion protein based around the variable lymphocyte receptor B (VLRB) from jawless fish Sea Lamprey. (Saupe et al., 2017) compare the efficacy of VLRB as a carrier for a fusion protein compared to bacterial thioredoxin (TRX), a proven and efficient carrier protein. Antibody titre, binding properties and duration of response were compared. VLRB carrier vaccines demonstrated a 2 – 10 fold increase in antibodies against self-titres and even more impressively, a decrease in foreign protein antibodies when compared to TRX fusion vaccines (Saupe et al., 2017).

This chapter will look at the viability of entrapping a protein-based vaccine inside a chitosan nanoparticle for more effective delivery to antigen presenting cells. Entrapping proteins inside chitosan nanoparticles has been done before but the method used in this thesis is novel (Sawaengsak et al., 2014). Several CLEC14A fusion proteins (including Tetanus Toxoid FrC and the Sea Lamprey VLRB) will have sequences generated and cloned into plasmids for lentiviral and bacterial transformation. The proteins will be produced in either HEK293T cells or a relatively new bacterial strain, SHuffle® T7 Express lysY Competent *E. coli.*

Upon successful infection of mammalian cells or transformation of bacterial cells, the proteins were harvested from the cell medium or cell lysate, purified and identified by western blot analysis.

Results and Discussion:

Nanoparticle Entrapment of Recombinant Protein:

Before producing any of the fusion protein vaccines, the possibility of entrapping the resultant recombinant protein inside a chitosan nanoparticle must be tested first. A method was developed to test the entrapment of a protein inside chitosan nanoparticles.

Streptavidin has a pI of ~ 5. To give streptavidin an overall negative charge, producing a polyanion, the nanoparticle synthesis must be conducted in a pH above this. The current nanoparticle synthesis is done at pH 5.5. Increasing the pH from 5.5 to 6 maintains the slight acidic conditions required for chitosan nanoparticle synthesis and keeps the pH above the pI of streptavidin. Dropwise addition of Alexafluor-488 tagged streptavidin, along with TPP, during chitosan nanoparticle synthesis at pH 6 will produce a nanoparticle with streptavidin entrapped inside.

The streptavidin nanoparticles were synthesised and loaded onto a 5% agarose gel at 110 V, 400 A for 30 minutes. Lanes were run with: 1) non-entrapped fluorescently tagged streptavidin and 2) with fluorescently tagged streptavidin entrapped nanoparticles. The same two lanes were run with and without SDS loading buffer as the buffer resulted in a

large amount of background noise on the gel during imaging. It was also not known whether the loading buffer would affect the integrity of the nanoparticle and cause it to release the streptavidin (Figure 5.1). This method for checking the entrapment of a protein inside chitosan nanoparticles is novel and was developed for this thesis.

Figure 5.1
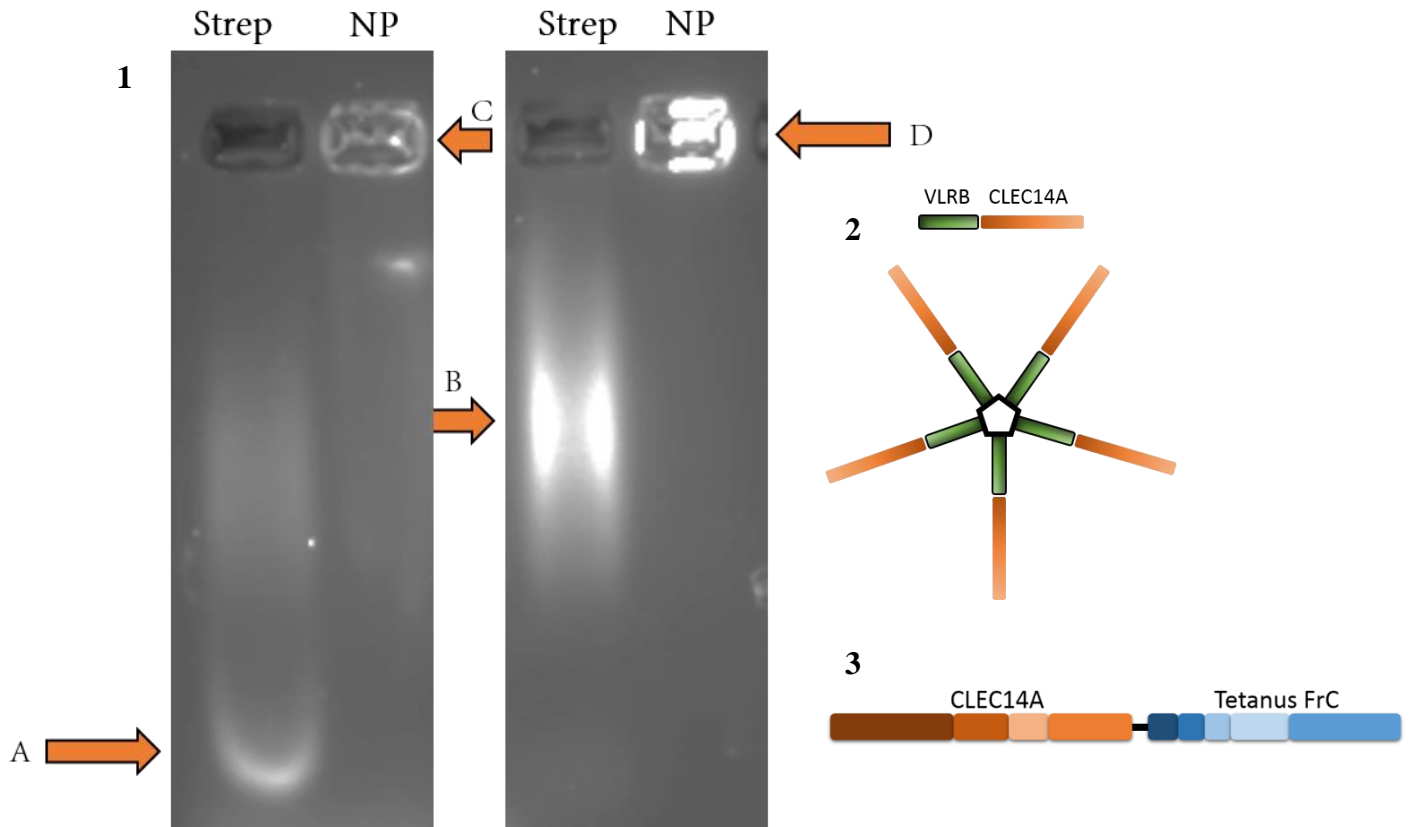
Figure 5.1 | Chitosan Nanoparticle Protein Entrapment :

(1) A gel electrophoresis showing entrapment of fluorescently tagged (Alexafluor 488) streptavidin inside chitosan nanoparticles. Nanoparticles were synthesised in pH 6 rather than pH 5.5 to ensure pH was greater than the Pi of streptavidin (~5). Streptavidin alone (strep) was run next to streptavidin entrapped inside chitosan nanoparticles (NP). The gel was run with (Left) and without (Right) SDS-loading buffer. The loading buffer created a large amount of background noise upon imaging and may induce protein release from the nanoparticles. Streptavidin can be seen to move through the gel in both images (A and B). Nanoparticles with streptavidin entrapped inside can still be visualised in the wells (C and D) showing that a protein can remain entrapped inside the chitosan nanoparticles.

(2) The CLEC14A-VLRB Fusion Protein. VLRB (Green), CLEC14A (Orange). VLRB fusion proteins can form multimers of up to 12 units. Only a single domain of CLEC14A was used in the VLRB fusion protein.

(3) CLEC14A-FrC Fusion protein. CLEC14A (Orange), FrC (Blue). The FrC Fusion does not form multimers. The entire extracellular domain of CLEC14A was used in the FrC fusion protein.

As can be seen, in both lanes (with and without SDS loading buffer), the non-entrapped streptavidin travels through the gel, showing up as a fluorescent band. The lane containing the streptavidin entrapped inside the ChNP's maintains the bulk of the fluorescence in the well. This show that streptavidin has the ability to migrate through the gel, however, due to it being entrapped inside the ChNP's it is retarded in the wells due to the ChNP's being too large to move through the 5% gel. This confirms the stable entrapment of a protein inside the chitosan nanoparticles.

Production of CLEC14A-FrC:

As previously mentioned, the FrC portion of tetanus toxoid used for vaccinating against tetanus represents as a potential biological adjuvant for breaking tolerance against self-antigens. A plasmid containing the CLEC14A-FrC fusion gene was previously produced by Kai Tolner's group (University of Birmingham, IBR). The plasmid had been made and sequenced, however the protein had never been produced. For Plasmid structure and sequence see Appendix 3 and 5.

The plasmid was amplified from the original stock through transformation of competent gold efficiency DH5α *E. coli*. The plasmid was purified from the *E.coli* using a miniprep

kit and a concentration of 267.9 ng/µl was quantified through spectrophotometry (Figure

5.2).

Figure 5.2
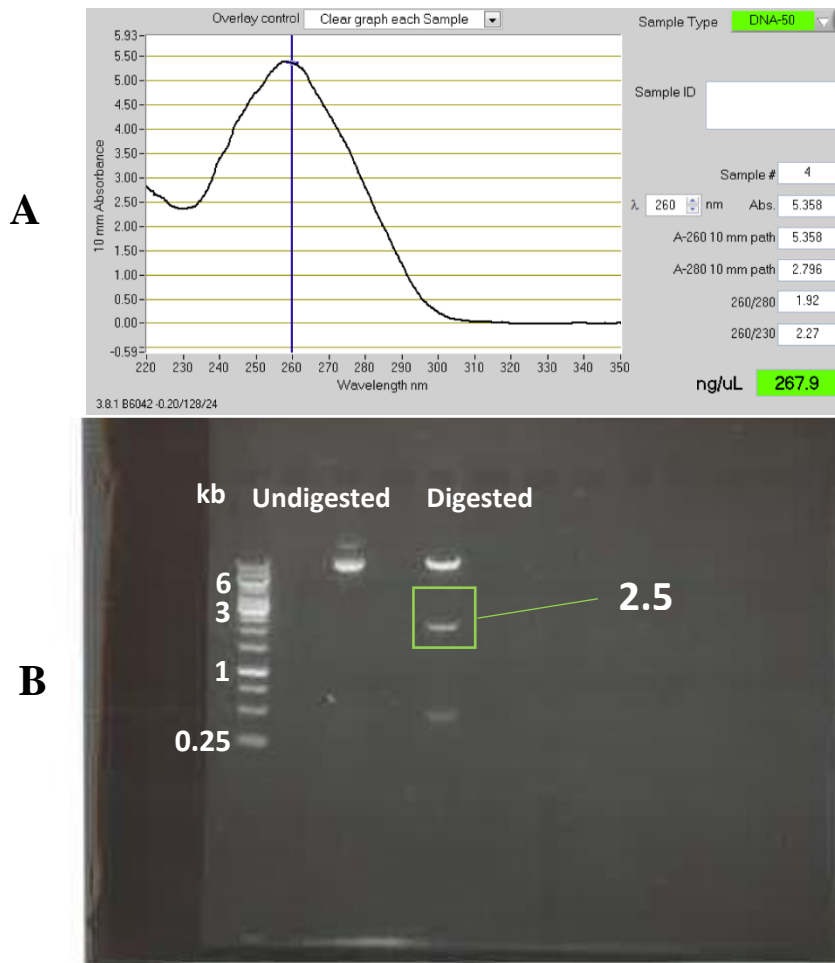
Figure 5.2 | CLEC14A-FrC Plasmid Amplification and Restriction Enzyme Digest:

(A) Eluted DNA from CLEC14A-FrC plasmid amplified bacteria measured through spectrophotometry using the Nanodrop 1000 spectrophotometer at 260 nm. A concentration of 267.9 ng/µL DNA material can be seen.

(B) A restriction enzyme digest of the eluted plasmid showing a fragment, 2.5 kb in size in the digested lane corresponding to the expected size of the CLEC14A-FrC inset into the pWPI plasmid.

A restriction enzyme digest was performed on the purified plasmid to extract the CLEC14A-FrC insert. The digested plasmid and full plasmid were run on a 1% agarose electrophoresis gel (Figure 5.2). A fragment, 2.5 kb in size in the digested lane corresponding to the expected size of the CLEC14A-FrC inset into the pWPI plasmid.

A Lentivirus transduction of the plasmid was undertaken in HEK293T cells. The pWPI plasmid contains an IRES site connected to the GFP gene resulting in the co-translation of GFP along with the protein of interest. The transformation of HEK293T cells were assessed through fluorescence microscopy. The presence of green fluorescence in the transformed cells shows a successful lentivirus infection with the pWPI plasmid containing the CLEC14A-FrC fusion protein (Figure 5.3).

Figure 5.3

Figure 5.3 |CLEC14A-FrC Transduced HEK293T Images:

(A) A fluorescence image showing the green fluorescence given off by cells transduced with the CLEC14A-FrC pWPI plasmid containing the GFP gene. Cells in (A) were compared with un-transduced cells (B) to show successful transduction. Due to the IRES site in pWPI, green fluorescence shows successful transduction and transcription of the gene of interest.

Production of CLEC14A-FrC Fusion Protein:

Confirmation of successful lentiviral infection allowed for progression to growth of cells and collection of the synthesised protein from the cell medium. The inserted gene contained a signal peptide and so should be excreted upon production.

Western blots were used to assess the presence of the fusion protein in transduced HEK293T cells. The cell medium was collected after two days of cell growth in DMEM. A cell lysis was also collected to assess if the protein was failing to be excreted. Cells were grown on a 10 cm cell culture plate and were collected at 80% confluence. Cells were lysed either by RIPA buffer or sonication in PBS with protease inhibitors. Un-transduced cell medium and lysate was used as a negative control for the western blots. Purified CLEC14A-FC was used as a positive control for the antibodies, though the protein is a different molecular weight. The primary antibody bound to extracellular CLEC14A. Initial western blots can be seen in figure 5.4.

Figure 5.4
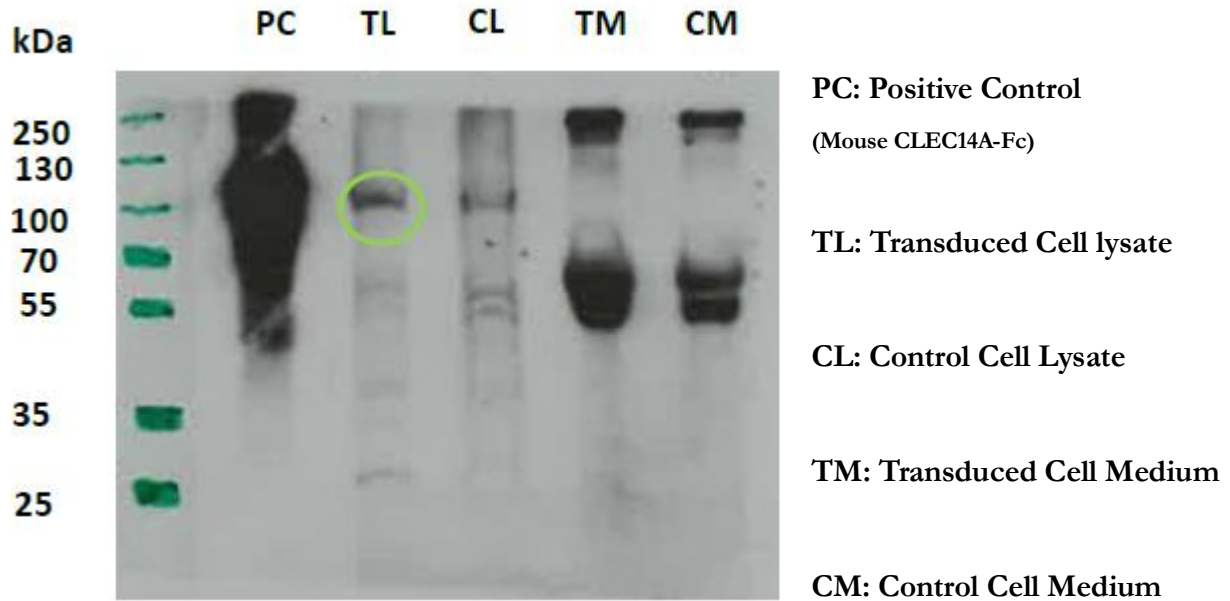
Figure 5.4 | Western Blot CLEC14A-FrC HEK293T:

A western blot showing a western blot from a 10% SDS-PAGE looking for the presence of the CLEC14A-FrC fusion protein. The cell lysis of transduced cells (TL) was compared to the cell lysis from un-transduced cells (CL) and mouse CLEC14A-FC (PC) as a positive control. Primary antibody: R&D anti-CLEC14A. Secondary Antibody: polyclonal anti-sheep HRP. A band can be seen (green circle) in the transduced lysis lane that is of the correct size for the fusion protein, however a band of the same size can be seen in the control (un-transduced) cell lysis. Co-migration may be the reason for bands that appear the to be the same molecular weight but are in-fact different proteins. This was studied further (Figure 5.6).

No protein was found at the right molecular weight in the cell medium, however a band of the correct molecular weight could be seen in the cell lysis. A similar band can also be seen in the control (un-transduced) cell lysis. The expected outcome from the gel would have been a band at around 110 kDa in the cell medium from the transduced cells. No protein was found in the medium, so the next location expected was the cell lysate. A band of the correct molecular weight does show up in the transduced cell lysate, however, an identical band also shows in the untraduced cell lysate. Non-specific binding can also be seen in the cell medium and further tests were performed to show that the bands found in the cell medium were non-specific binding of the secondary antibody, not the primary targeting CLEC14A.

There was the possibility that two proteins, both binding the primary or secondary antibody, had similar molecular weights and so co-localized on a western blot in the transduced cell lysis (Bass et al., 2017). To remove this possibility, a gradient gel was made. The gradient gel ran from 10-18% was created with the two cell lysates run with a positive control (Figure 5.5). HEK293T cells were grown to 80% confluency on 20 cm plates to increase the amount of protein present in the cell lysate.

Figure 5.5
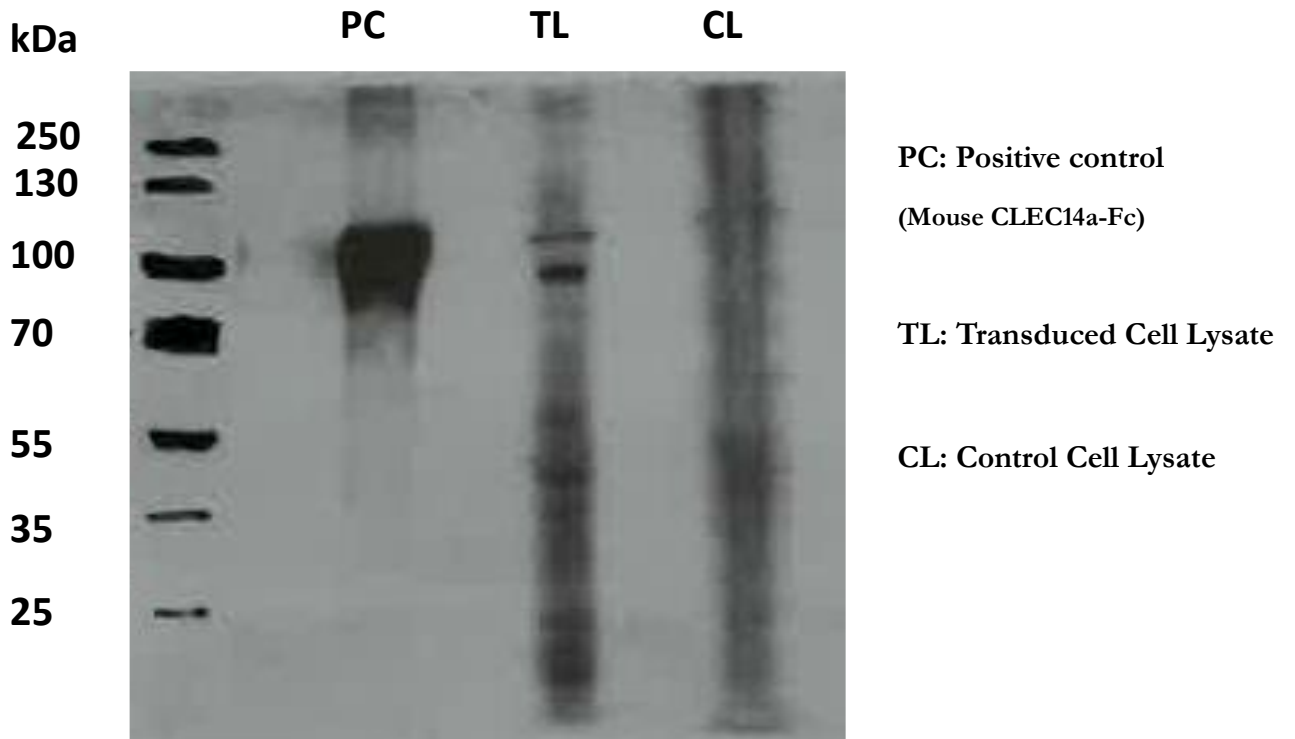
Figure 5.5 |Western Blot CLEC14A-FrC HEK293T Gradient Gel:

A western blot showing the gradient gel (10-18%) for the production of the CLEC14A-FrC fusion protein. The cell lysis of transduced cells (TL) was compared to the cell lysis from un-transduced cells (CL) and mouse CLEC14A-FC (PC) as a positive control. Primary antibody: R&D anti-CLEC14A. Secondary Antibody: polyclonal anti-sheep HRP. Two bands can be seen in TL proving the co-migration of 1 protein separated by the gradient gel.

As can be seen, two bands were separated in the TL (Transduced cell lysate) lane. These two bands previously co-localised but can now be seen to, in fact, be two separate proteins.

The yield for the fusion protein was calculated at 45 µg of protein per 20 cm plate of HEK293T cells. As can be seen, in comparison to the positive control (Figure 5.5), the protein concentration gathered from the transduced cells was low. The failure to excrete the protein may have been a result of the unfolded protein response as the addition of a bacterial protein will likely effect the folding of CLEC14A (Hetz, 2012). Eukaryotic translation initiator factor 2α (elF2α) halts translation of proteins after phosphorylation and can affect endoplasmic reticulum function on a broad scale. The unfolded protein response is a likely reason for failure of protein secretion as the FrC protein is a bacterial protein and so contains no glycosylation which would likely impact the correct folding of CLEC14A. To check that the protein had indeed been properly transduced, and the band seen on the gradient gel was still unspecific binding, RNA expression was assessed to check that the gene was correctly transduced.

RNA was collected using the miniprep kit (Qiagen #27104). 520.2 ng/µl of RNA was collected from a 10 cm plate. A 1% agarose gel was run using cDNA of mRNA collected from transduced HEK293T cells. A band at roughly 1 kb shows the presence of a protein

the expected size (1.197 kb) for the mRNA from the CLEC14A-FrC fusion gene (Figure 5.6).

Figure 5.6
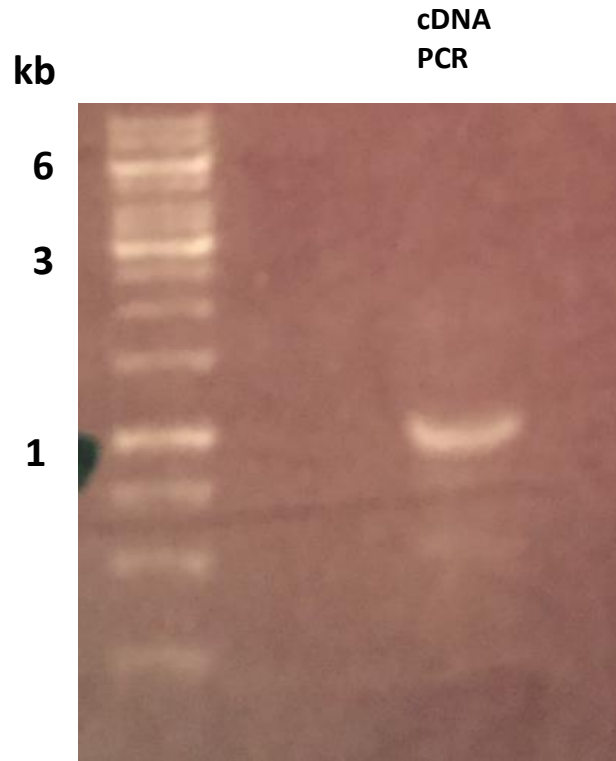
Figure 5.6 |Gel electrophoresis of HEK293T mRNA:

1% agarose gel of cDNA of mRNA collected from transduced HEK293T cells. A band at roughly 1 kb shows the presence of the expected size (1.197 kb) for the mRNA from the CLEC14A-FrC fusion gene.

Two primers were designed to sequence the entire construct and check for mutations. No mutations were found, see appendix 3 for sequence details.

Several tests were performed to check that the plasmid was transduced correctly, and that the gene was being transcribed into mRNA. The folding issues and lack of excretion would result in a very small yield of protein. It was decided that a different method of protein production should be used which would require designing a new fusion protein.

VLRB-CLEC14A Fusion

The production of the CLEC14A-FrC fusion resulted in an extremely low yield due to the protein failing to be excreted, likely due to protein miss-folding. Bacteria proteins do not undergo glycosylation compared to eukaryotic proteins and so would likely cause large folding issues in eukaryotic cells (Nothaft and Szymanski, 2013). A new fusion protein was needed to allow for better excretion and more rapid synthesis.

Saupe et al., developed the VLRB fusion protein base, stemming from a Sea Lamprey fish protein (Saupe et al., 2017). They compared the efficacy of VLRB as a carrier for a fusion protein compared to bacterial thioredoxin (TRX), a proven and efficient carrier protein. Antibody titre, binding properties and duration of response were compared. VLRB carrier

vaccines demonstrated a 2 – 10 fold increase in antibodies against self-titres and even more impressively, a decrease in foreign protein antibodies when compared to TRX fusion vaccines. Interestingly, the VLRB multimer structure could generate and sustain immune responses against several targets simultaneously.

Due to the exciting possibilities provided by VLRB fusion proteins, two CLEC14A fusion proteins was developed. Multimers form by disulphide bonds between VLRB domains and can form multimers of anything from 2 to ≥10 monomers. The range of these multimers (from monomers to 4-unit multimers) can be seen on a reducing SDS-PAGE. Only a 12 unit multimer could be seen in non-reducing conditions showing the propensity to form high number multimers (Tesniere et al., 2008, van der Most et al., 2008, Ullrich et al., 2008).

The two VLRB fusion protein plasmids was designed based of work done by Anna Karren (Saupe et al., 2017). The sequence was sent to Genscript to be synthesized. 5 µg of plasmid were provided and amplified in gold efficiency DH5α E. coli. See the gene sequence, amino acid sequence and protein domains of the fusion proteins in appendix 4. The amplified plasmids were assessed for the presence of the VLRB fusion protein gene fragments through restriction enzyme digests. The samples were digested and run on a 1% agarose gel with a 10 kb ladder. Undigested plasmid was also added as a negative control (Figure 5.7)

Figure 5.7
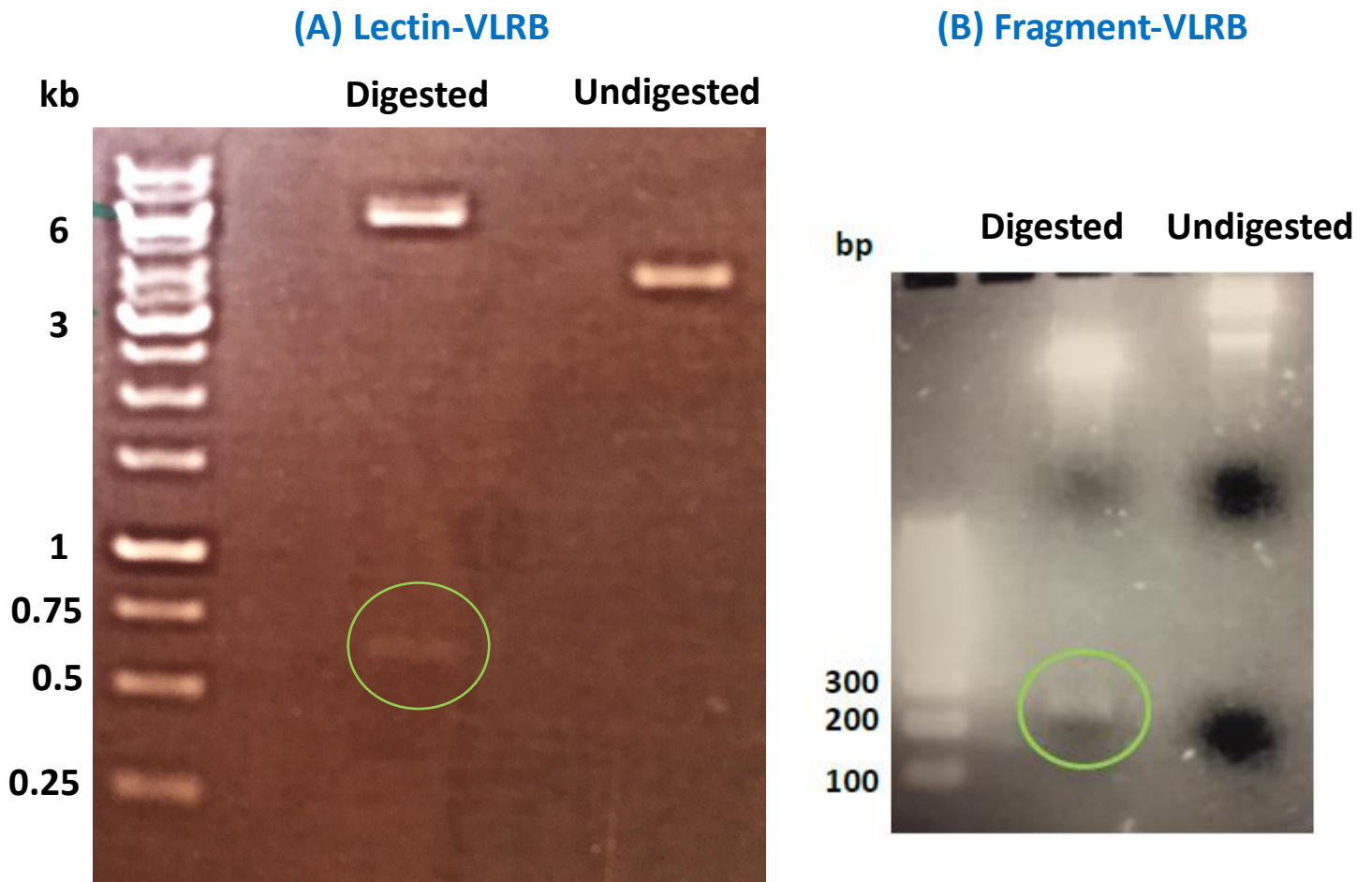
Figure 5.7 |CLEC14A-VLRB Restriction Enzyme Digest :

(A) A restriction enzyme digest of the L-VLRB plasmid after amplification in competent gold efficiency DH5α *E. coli*. A band can be seen at 0.6 kb (green circle) which is of the expected size for the L-VLRB fusion protein DNA fragment. (B) Shows a restriction enzyme digest of the F-VLRB collected from SHuffle® T7 Express lysY Competent *E. coli.* A band at 0.6 kb can be seen in the digested lane (green circle) signifying the presence of the F-VLRB fusion protein.

Protein 1 which made from the lectin domain of CLEC14A and VLRB (L-VLRB) and Protein 2 made from an immunogenic fragment from residues 97-108 of CLEC14A (F-VLRB) shown to bind multimerin (Khan 2016). This immunogenic fragment for the F-VLRB was chosen as it was thought the large domain from CLEC14A would result in difficulties for protein folding in bacteria similarly to the CLEC14A-FrC fusion.

The plasmids were ordered and amplified in competent gold efficiency DH5α *E. coli*. The presence of the fragments was again tested using a restriction enzyme digest using the NdeI and XhoI restriction digest sites (Figure 5.7). Figure 5.7 (A) shows a band at 0.6 kb (green circle) which is of the expected size for the L-VLRB fusion protein DNA fragment. Figure 5.7 (B) Shows a restriction enzyme digest of the F-VLRB collected from SHuffle® T7 Express lysY Competent *E. coli* (NEB #C3030J). A band at 200 base pairs can be seen in the digested lane (green circle) signifying the presence of the F-VLRB fusion protein.

Confirmation of the presence of both gene fragments, the plasmids were introduced into SHuffle® T7 Express lysY Competent *E. coli* (NEB #C3030J) through the heat shock method (Froger and Hall, 2007).

Issues in Transformation of the F-VLRB into SHuffle® T7 Express lysY Competent *E. coli* (NEB #C3030J) that were later resolved lead to progression with protein production in L-VLRB alone.

To assess protein expression of L-VLRB, a Bradford assay with BSA standards was used. Un-induced bacteria were used as a negative control and the pellet from the lysate was loaded as to check in the protein was left stuck to cell fragments. It was expected that a band around the 21 kDA size would be seen in the cell lysis, slowly increasing in concentration as the cells from which the lysis was taken produced more protein (Figure 5.8).

Figure 5.8
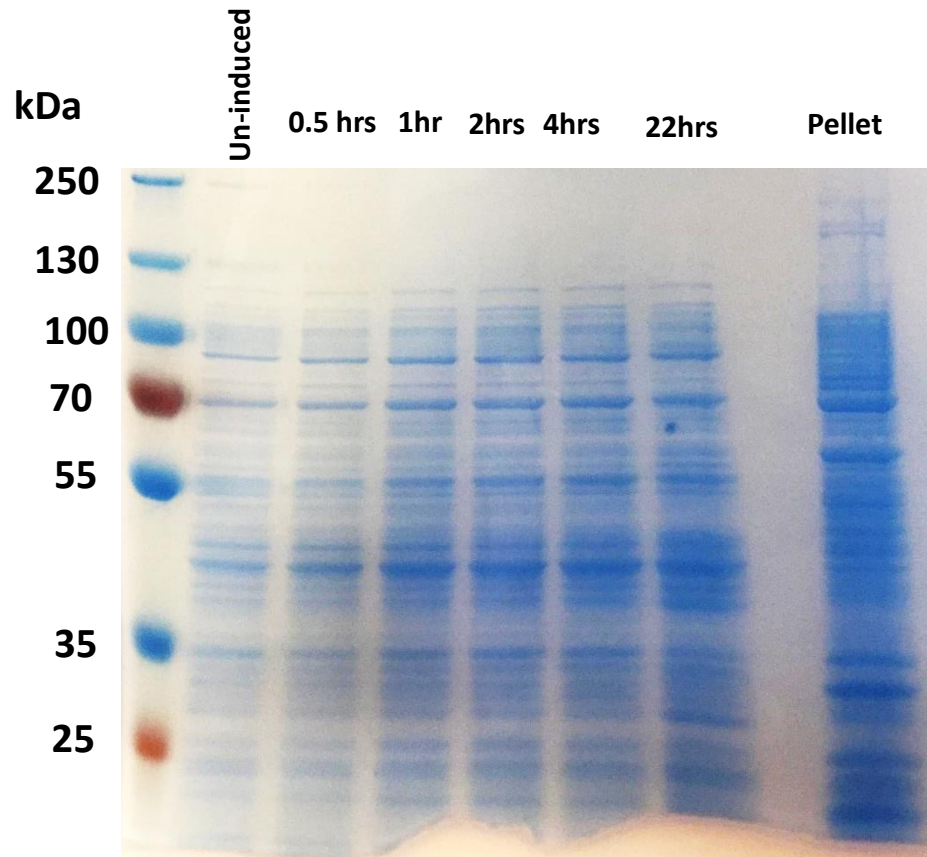
Figure 5.8 |L-VLRB Protein Production:

An SDS-PAGE stained with Coomassie Brilliant Blue Dye showing the production of L-VLRB in SHuffle® T7 Express lysY Competent E. coli. The bacteria were induced with isopropyl β-D-thiogalactopyranoside and collected at various time points. No increase in protein production can be seen at the target size (21 kDa) however, a band can be seen at the correct size in the pellet.

There appeared to be an increasing production of protein as time progresses, however, a band of the correct size can also be seen in the pellet lane. The target protein was likely sticking to cell fragments and so some remained in the pellet. In an attempt to ensure the target protein can be found in the cell lysis the bacteria were sonicated in PBS with 5 M urea to prevent the protein binding to cell fragments. This protocol was adapted from Saupe et al., (2017). The bacterial cell lysis, either through sonication or RIPA buffer (Lysis negative control), was purified through the use of Ni-NTA agarose beads with affinity for the His-tag. Beads were directly loaded onto an SDS-PAGE gel after boiling at 100 degrees to release the proteins. Supernatant from the purification steps was also loaded in case the protein failed to bind to the Ni-NTA beads. Again, lysate from the un-induced bacteria was purified and used as a negative control. Due to the His-tag on the target protein, an anti-polyhistidine tag monoclonal primary antibody was used to bind to the protein on the western blot after transfer to a membrane. Two bands can be seen in the His-beads (sonication) lane (Figure 5.9). The band at the top of the gel is the protein left on the beads that was not removed by boiling. Cells were lysed through sonication. RIPA buffer was used as a negative control as well as to remain consistent with the CLEC14A-FrC cell lysis protocol.

Figure 5.9
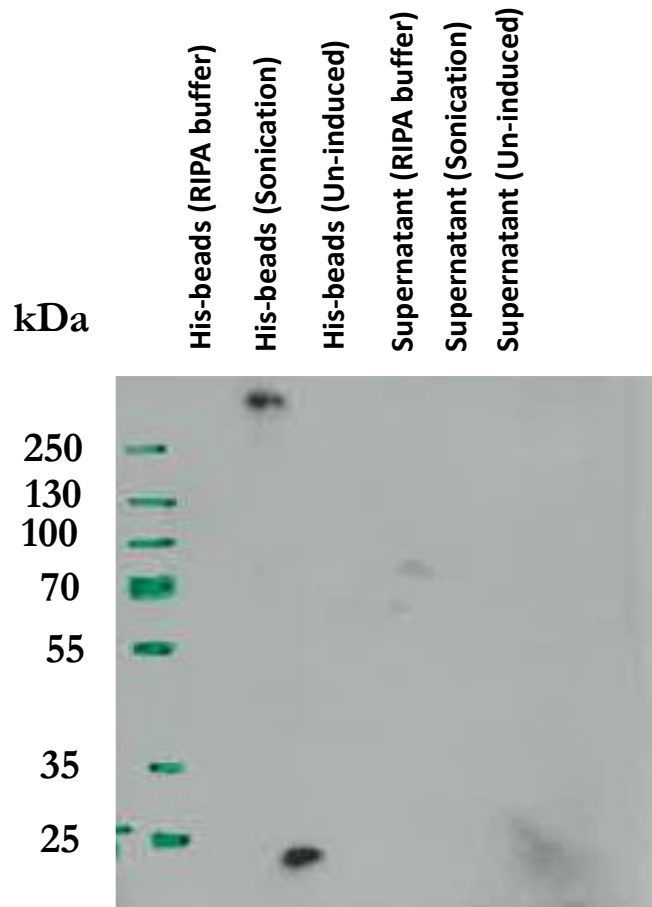
Figure 5.9 |L-VLRB Protein Purification :

An SDS-PAGE loaded with Ni-NTA beads from various protein production conditions. Ni-NTA beads were washed with the induced proteins from two methods of cell lysis (RIPA Buffer) and (Sonication). These were compared to un-induced cell lysis and the supernatant gathered after bead the bead washing steps. No bands were present except in the sonicated-induced cell lysis.

Spectrophotometry was used to initially assess the yield of protein eluted from His-tagged beads. From 250 ml of culture lysed in the presence of 5 M urea, 100 μL of protein with a concentration of 1.95 mg/ml was eluted from His-tagged beads.

Protein yield was assessed through western blot analysis. Purified protein from specified volumes of bacteria was loaded onto SDS-PAGE and run with known concentrations of BSA (Figure 5.10). (Initial absorption studies estimated the protein gathered from the His-tag beads to be roughly 1.95 mg/mL). To replicate Saupe et al., the bacteria were sonicated in the presence of 5 M urea which was reported to result in the highest protein yield. The protein was run with and without urea to see the effect of urea on protein concentration. Urea is a powerful denaturing agent and has been shown to unfold proteins (Saupe et al., 2017). A strong denaturing agent is useful as it prevents the aggregation of proteins into inclusion bodies, lowing the effectiveness of purification beads.

Figure 5.10
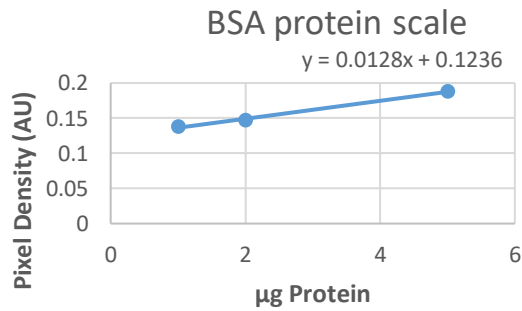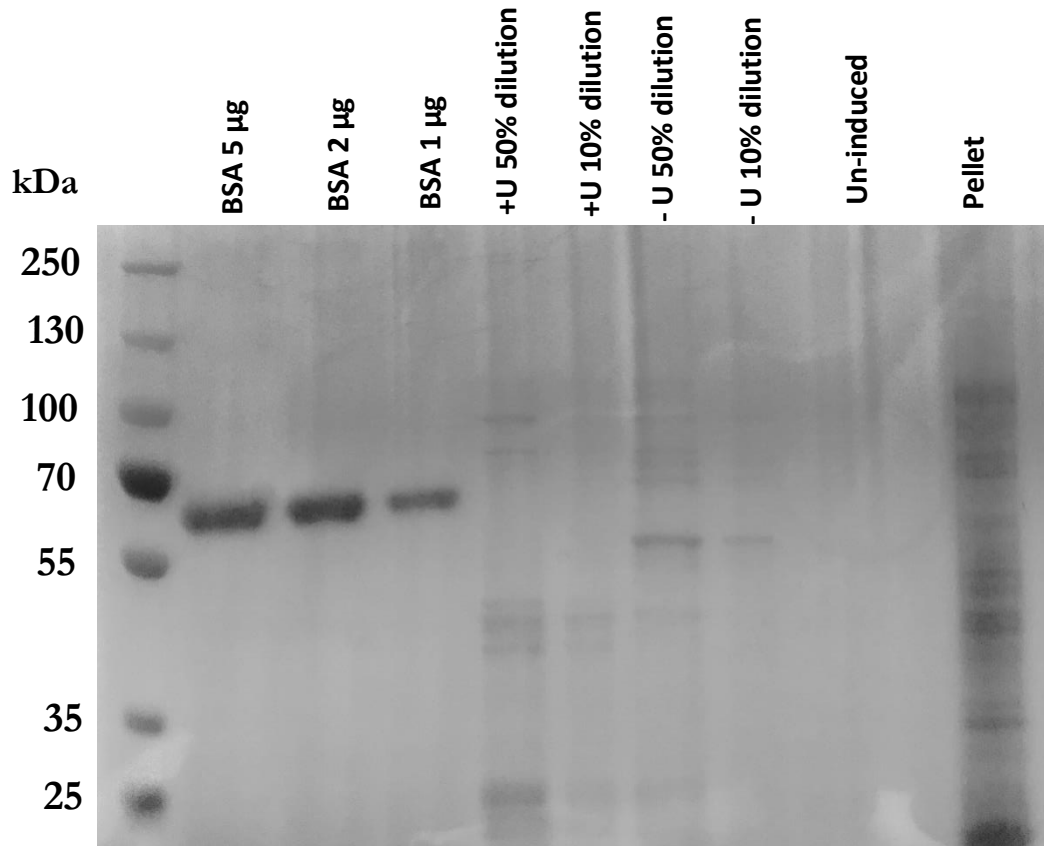
Figure 5.10 |L-VLRB Protein Yield:

A reducing SDS-PAGE stained with Coomassie Brilliant Blue Dye. The gel was loaded with BSA standards so as to assess protein yield, L-VLRB with and without urea at two different dilutions. The protein containing lanes were compared to un-induced cell lysis and the pellet.

Figure 5.10 shows the reducing gel with 5 μg, 2 μg and 1 μg BSA samples and protein eluted from the His-tagged beads in the presence (+U) or absence (-U) of urea and at two dilutions (50% and 10%). Purified protein was visualised through an anti-CLEC14A-antibody with an HRP tagged secondary antibody. A band at 21 kDa can be seen in all 4 conditions though it is far clearer in lanes with urea present (+U) though the same band is present in all purified protein lanes. No protein can be seen in the pellet, confirming the beads removed all of the target protein after sonication.

Interestingly a band at 55 kDa can be seen in the (-U) lanes. VLRB proteins are well known for multimerising and the lack of urea to properly dissolve the protein allowed for multimerization (Saupe et al., 2017). 55 kDa is not a multiple of the CLEC14A-VLRB monomer protein size and so is likely an aggregation with other cytoplasmic proteins. Conservative calculations from the BSA standards put the purified protein yield at 0.178 mg of L-VLRB per litre of bacterial culture.

The purified L-VLRB protein was also run on a non-reduced gel (Figure 5.11) to check for effects on protein multimerization. The band for the monomer at 55 kDa in the (+U) and (-U) can still be seen however extra bands at 250 kDa can also be seen in both lanes. 250 kDa is 12 times the size of the monomer and is not seen under reducing conditions

suggesting that non-reducing conditions allow for the protein to multimerise to its maximum of 12.

Figure 5.11
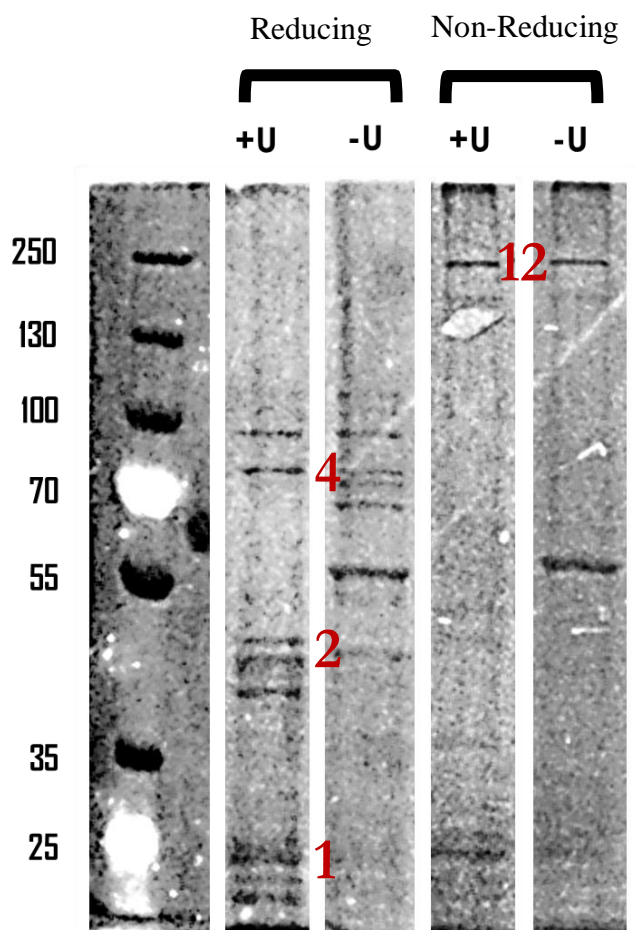
Figure 5.11 |L-VLRB Protein Multimers:

Reducing and non-reducing SDS-PAGE stained with Coomassie Brilliant Blue Dye. The gel was loaded with bacterial cell lysis containing L-VLRB fusion protein with and without 5 M urea. The reducing gel (left two) shows a monomer and multimers of 2 and 4 units. The non-reducing gel (right two lanes) shows a band for monomers and multimers of 12 units. This range of multimers is expected from studies performed by Saupe el al., 2017). The presence of urea prevents multimerization. Reducing and non-reducing gels were used to further assess multimerization of the fusion protein.

In agreement with Saupe et al., Multimers of the CLEC14A-VLRB protein can be seen in a close up of the reduced and non-reduced gels (Figure 5.11). A monomer, 2 unit and 4-unit multimer can be seen in the reducing gel whereas only monomer and 12-unit multimers can be seen in the non-reducing gel. Saupe et al., suggests that it is the formation of these large multimers that allows for a consistent antibody titre after vaccination and so their presence is a clear indication of the successful production of this protein.

VLRB has been shown to readily form multimers and so without the addition of urea (Figure 5.11) shows a band at 55 kDa that is recognised by the CLEC14A antibody. In agreement with Saupe et al., Multimers of the CLEC14A-VLRB protein can be seen in figure 5.13. A monomer, 2 unit and 4-unit multimer can be seen in the reducing gel whereas only monomer and 12-unit multimers can be seen in the non-reducing gel. Saupe et al., suggests that it is the formation of these large multimers that allows for a consistent antibody titre after vaccination.

For the yield experiments a protein yield of 178 µg per litre of bacterial culture was calculated. 178 µg was lower than expected and it was hypothesised that the formation and presence of proteins with di-sulphide bonds inside the bacteria puts them under stress. Further experiments would be needed to optimise bacterial growth through pH, growth medium and temperature to maintain high protein yields.

Conclusion:

These experiments show the potential for entrapment of a protein within the chitosan mesh of a chitosan-TPP nanoparticle as well as the production of a CLEC14A fusion protein with the potential for high immunogenicity. They also showed the difficulties of producing a fusion protein containing a prokaryotic protein which resulted in misfolding and failure to secrete the protein.

The synthesis of two fusion proteins of CLEC14A and VLRB were attempted. One fusion was with the entire lectin domain and the other a small immunogenic fragment from CLEC14A. The large lectin domain protein proved problematic to produce in shuffle bacteria and the transformation never took hold, however, the immunogenic fragment fusion was produced and purified using Ni-NTA beads.

Future work would look at the immunogenicity of the F-VLRB protein in a mouse model through the measure of antibody titres. Nanoparticle delivery, potentially targeted at dendritic cells, vs injection without nanoparticles would be compared to see if nanoparticle delivery improved antibody titre.

Chapter VI

Gene Array Data:

Introduction:

The overall aim of this project was the development of a vector for delivering siRNA to the endothelial cells in tumour blood vessels. The original ChNPs generated a 60% knockdown of CLEC14A. The particles were not as effective as other examples in the literature and that aiding cellular uptake with antibodies may improve the knockdown efficiency. Antibody conjugation was attempted to try and increase cellular uptake and thereby the concentration of siRNA delivered to each cell. The conjugation of antibodies to the surface, in fact, decreased the knockdown effectiveness rather than increasing it. This was thought to be due to increased aggregation caused by the antibodies. Due to this decrease in knockdown efficiency, it was decided that experiments would progress with the ChNPs without antibody conjugation.

ChNP's had been shown to successfully bind siRNA and retain it in serum conditions. They had been shown to enter cells and to induce protein knockdown of CLEC14A which was studied through western blot (Chapter 3).

In-vitro, siRNA delivery through chitosan nanoparticle delivery has been shown to knock down CLEC14A on a protein level. It was thought that microarray analysis of HUVEC

treated with siRNA containing ChNP's could further elucidate the action of chitosan nanoparticles (aimed at knocking down CLEC14A) on endothelial cells.

Microarrays are miniature, extremely sensitive and specific devises that are used to detect changes in gene expression on a genome wide scale. Analysis can study mutations or gene expression profiles of affected genes. It is difficult to compare this study to others from the literature regarding nanoparticle-based siRNA therapies as there are very few nanoparticle-siRNA studies analysed using microarrays.

Previous work done by the Bicknell group looked at the expression of genes related to blood flow in developing zebrafish embryos (Mura et al., 2012). This study highlighted many genes, including CLEC14A, as being affected by blood flow. Using the Ingenuity® Pathway Analysis (IPA) software package, gene expression in the blood flow experiments can be compared with the gene expression in the NP-siRNA knockdown studies.

This chapter aims to look at the effects of siRNA-ChNP's on the gene expression of CLEC14A and other endothelial specific genes compared to other microarray data on endothelial related genes.

Results and Discussion:

HUVEC were incubated with siRNA containing ChNP-siRNA at the 2x concentration (100 nM siRNA delivered) as this was found to be the most effective concentration in chapter 2. A control group was also incubated for the same time but treated with cell medium containing no ChNP or siRNA.

The cells were harvested, and RNA extracted using the RNeasy mini kit (QIAGEN 74104)

Analysis of Data:

Microarray layout data was collated using the feature extraction programme. The 6x60K Whole Human Genome microarrays were processed to analyse the effect of the ChNP-siRNA on endothelial cell genes in HUVEC. A link to the full data set can be found in Appendix 5.

Statistical analysis of gene expression was performed for all endothelial cell related genes using the "Statistical Analysis of Microarray" software (SAM). An unpaired, two sample T-Test was performed for each gene in the group of interest compared to the control cells. Genes that present with an estimated false discovery rate (FDR) above 5% and 10% were put into separate groups. SAM was performed with 1000 permutations with duplicates removed from the output.

Functional analysis of genes of interest that were differentially regulated were carried out in IPA Ingenuity. Cluster and Tree View programs were used to create visualisations for analysis from the microarray results (Eisen et al., 1998).

The flow studies were performed by the Bicknell group and analysed using microarrays. The array data showed that CLEC14A, among other endothelial specific genes, was down-regulated by an increase in blood flow and up-regulated by low blood flow. The study exposed HUVEC to differing levels of laminar flow shear stress (1.5 Pa vs 0 Pa for 24 hours).

CLEC14A was identified to be of particular interest as its expression was 10-fold higher in the static cells compared to the shear stress, laminar flow, HUVEC. Real time PCR confirmed the down-regulation of CLEC14A in response to shear stress (Mura et al., 2012). The data from this study was compared to the gene expression profile produced by the ChNP-siRNA knockdown of CLEC14A. Nearly half (297 out of 641) endothelial related genes had similar altered expressions in both the blood flow and NP-siRNA gene array studies. (Figure 6.1).

Figure 6.1

A
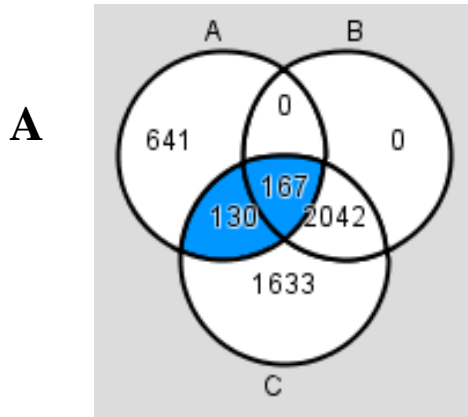
(A) NP-siRNA Dataset
(B) Blood Flow (More than 10-fold) Dataset
(C) Blood Flow (More than 5 FDR) Dataset

B

Gene	NC	NC	NC	NP-siRNA	NP-siRNA	NP-siRNA
CLEC14A	14.28	14.85	14.71	14.70	14.43	14.89

CLEC14A Average: 0.996-Fold Change

Figure 6.1 | Blood Flow vs NP-siRNA gene array datasets:

(A) A representation of genes that were similarly regulated in the Zebra Fish blood flow experiments vs the NP-siRNA knockdown experiments. (A) NP-siRNA dataset, (B) Blood Flow (More than 10-fold) dataset, (C) Blood Flow (More than 5-fold) dataset. Nearly half (297 out of 641) genes from the NP-siRNA data set had similar alterations to expression in the blood flow data set. This correlation suggests a high similarity between the effects of an increase in blood flow and a decrease in expression of CLEC14A.

(B) a table showing the fluorescence level of the CLEC14A wells from the microarray data showing a 0.0996-fold change in fluorescence between the control cells and ChNP-siRNA treated cells.

Interestingly, analysis of the ChNP-siRNA knockdown shows that CLEC14A mRNA expression does not change. CLEC14A knockdown was confirmed through western blot analysis but a lack of mRNA knockdown suggests that loss of protein expression must be happening through a different rout.

Though the NP-siRNA gene arrays show no knockdown of CLEC14A mRNA there were marked changes in expression of other genes related to blood flow. The comparison of the two experiments (Mura Lamina Flow and NP-siRNA gene arrays) lead to an interesting conclusion. CLEC14A mRNA is not knocked down (Figure 6.1 B), however, the changes in the expression of other endothelial genes were consistent with changes due to an increase in laminar flow. Using the data from both the NP-siRNA gene array and blood flow gene array gives an interesting view of CLEC14A.

Changes in gene expression after exposure to ChNP-siRNA were similar to the expression changes induced by an increase in laminar flow. CLEC14A expression is known to decrease due to an increase in laminar flow. These changes suggest that CLEC14A signalling was indeed inhibited though the gene was not knocked down at the mRNA level. Additionally, this suggests CLEC14A is a is a flow gene regulator rather than being regulated itself by another gene. Alterations in CLEC14A protein have the same effect as alterations to blood flow. This also suggest that the up and down regulation of CLEC14A protein expression could be directly controlled by the physical stimulus of laminar flow.

This correlation suggests that therapies that can alter CLEC14A protein expression can have drastic effects on physiology. At the start of this thesis it was stated that angiogenesis was a vital area of research as it is a major factor in the homeostasis of the tumour microenvironment. Comparing these two sets of data suggests that CLEC14A could potentially be a *regulating* gene rather than a *regulated* gene meaning that large, micro-environmental, changes can be made by altering the expression of CLEC14A.

The nanoparticle knockdown experiments did not knockdown CLEC14A mRNA but multiple CLEC14A regulated genes were changed. Studies have shown that CLEC14A expression decreases in zebra fish embryos as the heart develops (Mura et al., 2012). As the vascular system of a zebra fish develops the blood flow increases and down-regulates CLEC14A (Pociute et al., 2019). Combining the data from the zebra fish studies, the laminar flow studies and the data from the gene arrays I suggest that CLEC14A down-regulation stimulates endothelial cell maturation.

As previously stated, CLEC14A was not knocked down at the mRNA level but I have suggested that it *was* knocked down at the protein level. As a result, genes that are regulated by CLEC14A are also altered in their expression. IPA analysis of the array data compared to the laminar flow data suggested that the ChNP-siRNA affected several signalling pathways.

Figure 6.2 shows several pathways that were affected in HUVEC through the incubation of ChNP-siRNA particles. As can be seen the VEGF pathway is directly affected resulting in a decrease in angiogenesis and lyphanogenesis.

Figure 6.3 shows that the NP-siRNA particles cause an inhibitory effect on the mTOR pathway. The mTORC1 pathway is known to regulate many oncogenes and tumour suppressors such as the Ras/Raf/MEK/ERK pathway, the phosphoinositide 3-kinase (PI3K)/AKT (PKB) pathway and the protein synthesis machinery, eukaryotic initiation factor eIF4E. mTORC1 function is estimated to be hyperactivated in up to 70% of all human tumours. Reduced VEGF production and decreased angiogenesis have been suggested to contribute to the anti-tumour effects of mTOR inhibitors (Falcon et al., 2011). Rapamycin is a well-known mTOR inhibitor and which has key roles in cell growth, proliferation. mTORC1 and mTORC2 are kinases that form a complex to induce signalling.

Figure 6.2
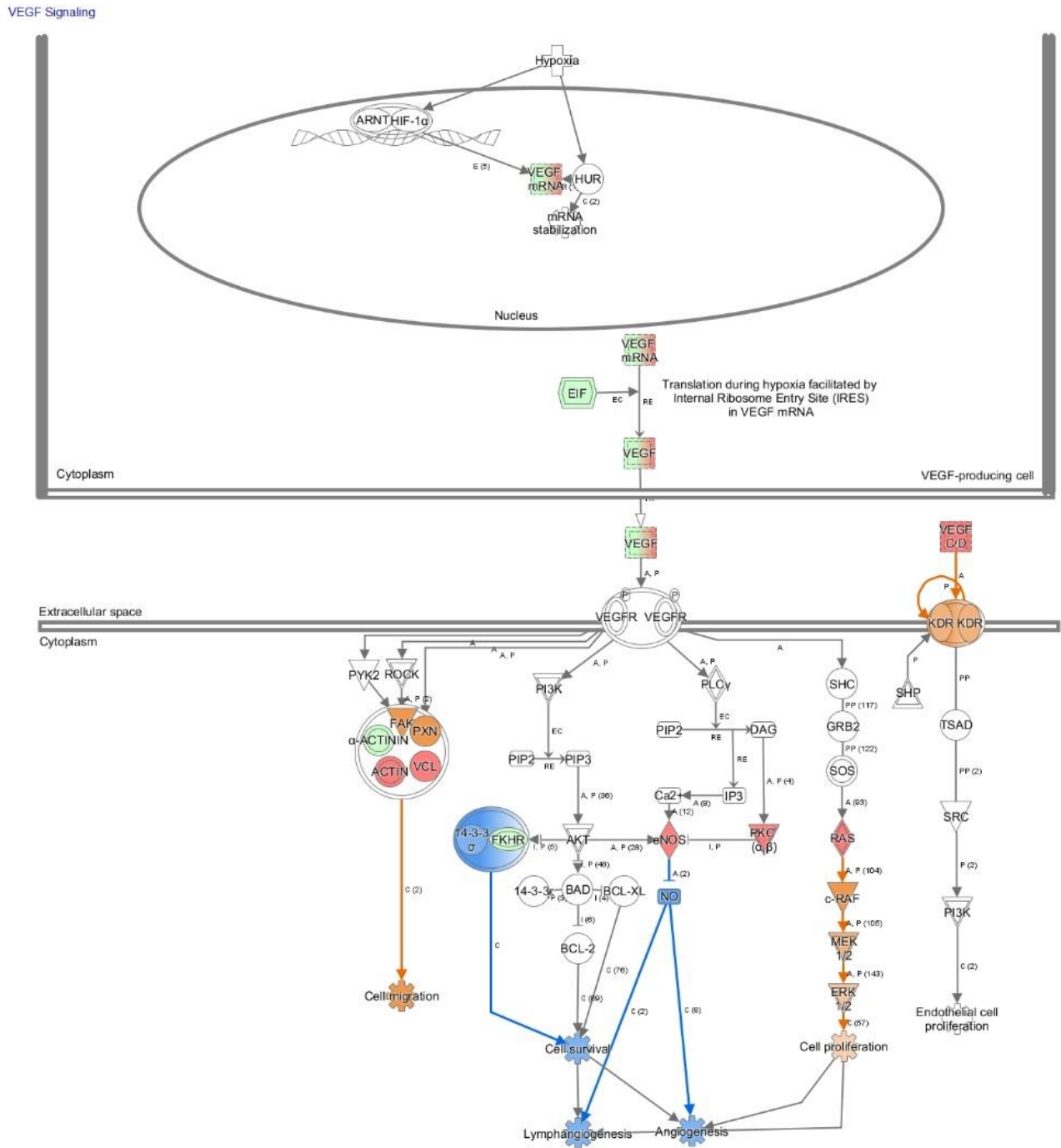
Figure 6.2 | NP-siRNA effect on endothelial related genes 1:

Here can be seen a representation of the effects of NP-siRNA on the VEGF cell signalling pathway. This diagram was generated using the IPA software package. (Orange = up-regulation) (Blue = down-regulation). As can be seen, NP-siRNA induce the upregulation of cell migration and cell proliferation whilst down-regulating angiogenesis, Lymphanogenesis and cell survival. This image was generated from IPO analysis of endothelial gene regulation by the ChNPs (microarray data).

191
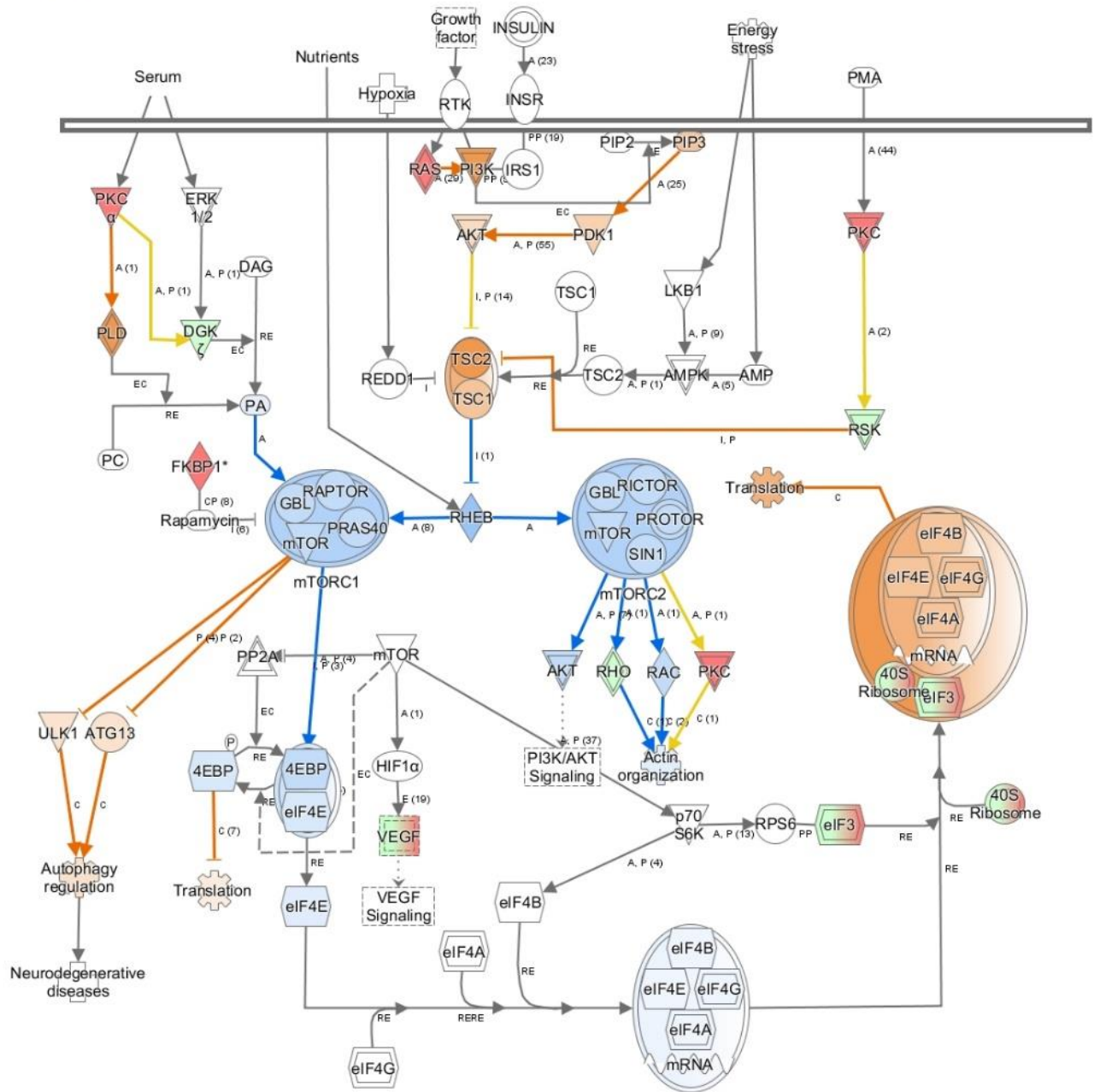
Figure 6.3

Figure 6.3 | NP-siRNA effect on endothelial related genes 2:

Here can be seen a representation of the effects of NP-siRNA on the VEGF cell signalling pathway. This diagram was generated using the IPA software package. (Orange = up-regulation) (Blue = down-regulation). It can be seen that NP-siRNA cause a down-regulation of mTORC1 and mTORC2 resulting in an upregulation of autophagy and translation. This image was generated from IPO analysis of endothelial gene regulation by the ChNPs (microarray data).

mTORC1 promotes several anabolic pathways such as protein synthesis, ribosome production, nucleotide synthesis and lipogenesis which all contribute to cell growth proliferation and tissue growth (Kennedy and Lamming, 2016). Suppression of key catabolic process and induction of autophagy by inhibiting its activation or suppressing production of lysosomes by mTORC1 makes its inhibitors attractive for anti-cancer or anti-aging therapies (Kim and Guan, 2015).

Eukaryotic initiation factor (eIF4E) is a key component in the positive regulation of protein synthesis machinery. eIF4E mediates recruitment of ribosomes to mRNA for translation (Brunn et al., 1997). eIF4E-binding proteins (4E-BPs) are small phosphoproteins that inhibit eIF4E. mTORC1 induces release of the 4E-BPs, thereby removing their inhibition of eIF4E. Other links of mTORC1 to the activation of protein synesis can be found here (Huo et al., 2011, Iadevaia et al., 2012).

Given the multitude of oncogenic pathways, oncogenes and tumour suppressors linked to mTOR signalling it is unsurprising that it is hyperactivated in most human tumours. This hyperactivation and prolific involvement in cell growth, proliferation and autophagy means that any perturbation of its signalling is of great interest.

Even though CLEC14A did not appear to be knocked down at an mRNA level it appears that the nanoparticles have the desired effect by down-regulating angiogenesis. The Zebra

Fish experiments show that, as the embryo develops and blood flow increases, CLEC14A expression is decreased. This down-regulation of CLEC14A coincides with the maturation of endothelial cells and decrease in angiogenesis. The NP-siRNA gene array data suggests that down-regulation of CLEC14A on a protein level has the same physiological effects as an increase in blood flow. Therefore, decreasing the expression of CLEC14A in tumour blood vessels would result in maturation of endothelial cells and a decrease in angiogenesis.

One focus of future work would be to study the reason for CLEC14A being knocked down at a protein level and not at the mRNA level. Sometimes cleavage of the target mRNA molecule does not occur. In some instances, endonucleolytic cleavage of the siRNA phosphodiester backbone may be suppressed by mismatches of siRNA and the target mRNA near the RISC cleaving site. Other times, the, patient specific, Argonaute proteins of the RISC lack endonuclease activity even when the target mRNA and siRNA are perfectly paired (Tomari and Zamore, 2005). If this occurs then gene expression will be silenced by miRNA induced mechanism rather than through RISC cleavage (Carthew and Sontheimer, 2009). The gene array data here was gathered from one umbilical cord and so future work would look at repeating the analysis with multiple cords. It is also possible that the nanoparticles themselves caused the alteration in the method of knockdown. Chitosan nanoparticles are well known to generate a protein corona from endogenous proteins inside cells or from the serum (Lundqvist et al., 2011). Should the RISC complex get entrapped inside the protein corona, this could affect its siRNA cleavage efficiency, again, resulting in a miRNA induced knockdown.

Other future work would include QPCR analysis of western blot knockdowns. Western blots were used to confirm a ~60% knockdown of CLEC14A at a protein level by NP-siRNA. Future work would investigate combining western blot analysis with QPCR to ascertain the true nature of the CLEC14A knockdown.

Conclusion:

The discovery that the ChNP's did not induce knockdown at an mRNA level was at first confusing. However, after studying the gene data and comparing it to already published data an image immerged that gave a deeper understanding of the role of CLEC14A in angiogenesis.

Genes and proteins can be either regulated or regulators, i.e. either their expression is controlled by another gene/protein or an outside stimulus affect them resulting in their regulation of the expression of other genes/proteins. Thee gene array data shows the knockdown of CLEC14A on a protein level resulted in changes in the expression of endothelial genes similar to if the cells experienced an increase in laminar blood flow.

It was already known that CLEC14A expression was affected by low sheer stress, but it has not been shown the drastic effects its loss of expression has on the expression of other endothelial related genes. This regulatory nature of CLEC14A shows its value as a prominent tumour endothelial marker.

As well as its regulatory role, the ChNP-siRNA's effects on the mTORC1 pathway suggest potentially useful anti-cancer properties through the targeting of CLEC14A on endothelial cells.

Chapter VII

In-Vivo:

<u>Introduction:</u>

The aim of this project was the development of a vector for delivering siRNA to the endothelial cells in tumour blood vessels. The original ChNPs generated a 60% knockdown of CLEC14A. It was thought that the particles were not as effective as they could be, and antibody conjugation was attempted to try and increase cellular uptake and thereby the concentration of siRNA delivered to each cell. The conjugated of antibodies to the surface, in fact, decreased the knockdown effectiveness rather than increasing it. This was thought to be due to increased aggregation caused by the antibodies. Due to this decrease in efficacy, it was decided that experiments would progress with the ChNPs without antibody conjugation.

The attempts at conjugating targeting moieties to the chitosan nanoparticles decreased their effectiveness in knocking down CLEC14A. It was decided to progress with the un-targeted ChNP's as many papers have shown their passive uptake by tumours (Lu et al., 2010 Geiser

et al., 2005). Rather than targeting tumour cells, the ChNP's developed in this thesis aim to be taken up by endothelial cells.

Relying on passive uptake of nanoparticles risks distribution of the siRNA to organs other than the tumour blood vessel endothelium. Lu et al., studies the biodistribution of siRNA containing chitosan nanoparticles aimed at knocking down Enhancer of zeste homolog 2 is a histone-lysine N-methyltransferase enzyme (EZH2), another endothelial marker (Lu et al., 2010). The study shows the distribution of fluorescently labelled nanoparticles between organs showing qualitatively that the particles were not taken up predominantly by macrophages as was feared but that distribution was spread between the lungs, kidney, spleen, liver and tumour. It appeared that the greatest deposit of siRNA was in the kidneys. The liver and tumour next with a similar concentration of siRNA fluorescence. The study shows the distribution of the nanoparticles/siRNA, however, they fail to show that the siRNA has, in fact, reached the endothelial cells. Admittedly the western blot of the tumour tissue shows that there appears to be an effect, but it would have been more complete with evidence of siRNA present in the target cells. Howard et al., targets siRNA containing chitosan nanoparticles to the bronchioles of mice and shows pictures of the fluorescently tagged particles inside the target cells (Howard et al., 2006).

A 60% knockdown was achieved by the nanoparticles produced in this thesis but to provide a complete study of these particles a biodistribution study was conducted. The aim was to see siRNA fluorescence in the endothelium of tumour blood vessels.

An *in-vivo* knockdown of CLEC14A and perturbation of its signalling could have a drastic effect on angiogenesis in tumours. A study by a previous PhD student in the Bicknell lab looked at targeting CLEC14A with antibody drug conjugates and protein fragments (Khan, 2016). To visualise expression of CLEC14iA in vivo, humanised antibodies (conjugated with Alexafluor 555) were administered to LLC tumour baring mice. CD32 was stained as a marker for the blood vessels. The localisation of CLEC14A was found to be mainly within the tumour, removing the concern for off target effects of ADC's.

Additionally, the study looked at using a binding fragment from MMRN2 to prevent the pro-angiogenic signalling of CLEC14A and CD93. LLC cells were transduced with the gene for the production of the MMRN2 fragment rather than use recombinant proteins. The transduced cells were injected subcutaneously into the flank of 7, C57BL6 mice. Tumour growth was monitored daily with callipers. Tumours made from the MMRN2 expressing LLC cells showed a clear decrease in growth rate compared to the wild type. Growth difference became significantly different on days 11 and 14. From days 12 onwards the difference in tumour growth appeared to reduce and tumour growth caught up with the wild type. After 14 days the mice were culled, and tumour weighed. No significant difference was found when comparing fragment expressing cells vs wild type.

This data reinforced the potential anti-angiogenic effect of disrupting CLEC14A signalling. This PhD, rather than blocking signalling, aims to reduce expression of the protein entirely which may have a longer lasting effect.

This chapter will look at the biodistribution of ChNP with entrapped fluorescent siRNA inside a mouse model. Two experiment were performed, each with 3 mice. The experiments looked at the distribution of ChNPs. The two experiments were identical apart from the use of different fluorophores to tag the ChNP-siRNA.

Results and Discussion:

Alexafluor 488 stained nanoparticles:

1 million Lewis Lung Carcinoma cells (LLC) were implanted in the left flank of 6 week BALBC mice and left to grow for 15 days or until 1 cm in size. At 15 days the mice were injected with Alexafluor 488 tagged siRNA containing chitosan nanoparticles through the tail vain. 3 mice were used for the Alexafluor tagged nanoparticles: Control (Injected with solution containing no nanoparticles), Nanoparticles (culled 2 hours after injection), Nanoparticles (culled 24 hours after injection). The organs and tumour were extracted and fixed in paraformaldehyde. The organs and tumour were imbedded in paraffin wax and cut into sections 10 micrometres in thickness. The sections were fixed to microscope slides, stained with H&E and imaged on the Leica DM6000 Fluorescence microscope.

.

10 micrometre sections from the tumour and each organ were imaged and can be seen in Figure 7.1. The sections are of organs including, heart, kidney, liver and lungs, as well as

from the tumour itself. One mouse was culled 2 hours after injection with nanoparticles and the other 24 hours after injection.

Figure 7.1 (Culled 2 hours after nanoparticle injection) clearly shows the difference in the presence of green fluorescence in different organs. Strong green fluorescence can be seen in surrounding the blood vessel in the tumour and some can also be seen in the kidneys. Localisation of chitosan nanoparticles to the kidneys is consistent with other published data (PengZhou, et al., 2014). Figure 6.2 (Culled 24 hours after nanoparticle injection) shows a similar disparity of green fluorescence in the tumour vs other organs. Interestingly, fluorescence could not be found in the kidneys, but a small amount was found in the lungs. This may have been due to a large aggregation of particles becoming wedged in a vessel or lymph.

Figure 7.1
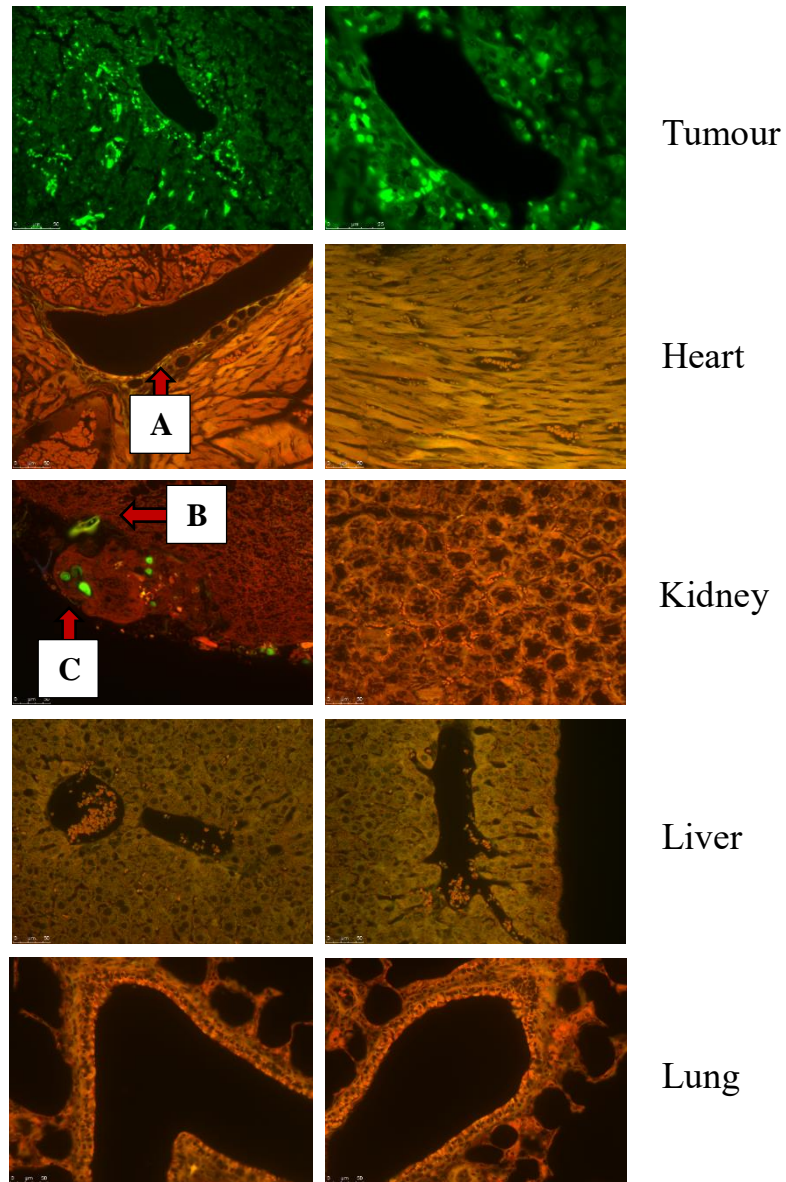
Figure 7.1 |Alexafluor 488 Mouse Sections 2 hours:

Fluorescent images of sections made from the organs and LLC tumours in mouse culled 2 hours after injection with Alexafluor 488 tagged siRNA-nanoparticles without antibody targeting. ChNP-siRNA particles were tagged with Alexafluor 488. High levels of green fluorescence can be seen in the tumour sections suggesting a high concentration of nanoparticles. Fluorescence appears to aggregate around blood vessels. Some green fluorescence can be seen in the lining of the heart (Arrow A). Clear green fluorescence can be seen surrounding blood vessels in the kidney (Arrows B and C) Greater magnification images can be seen in figure 6.3 and 6.4.

Figure 7.2
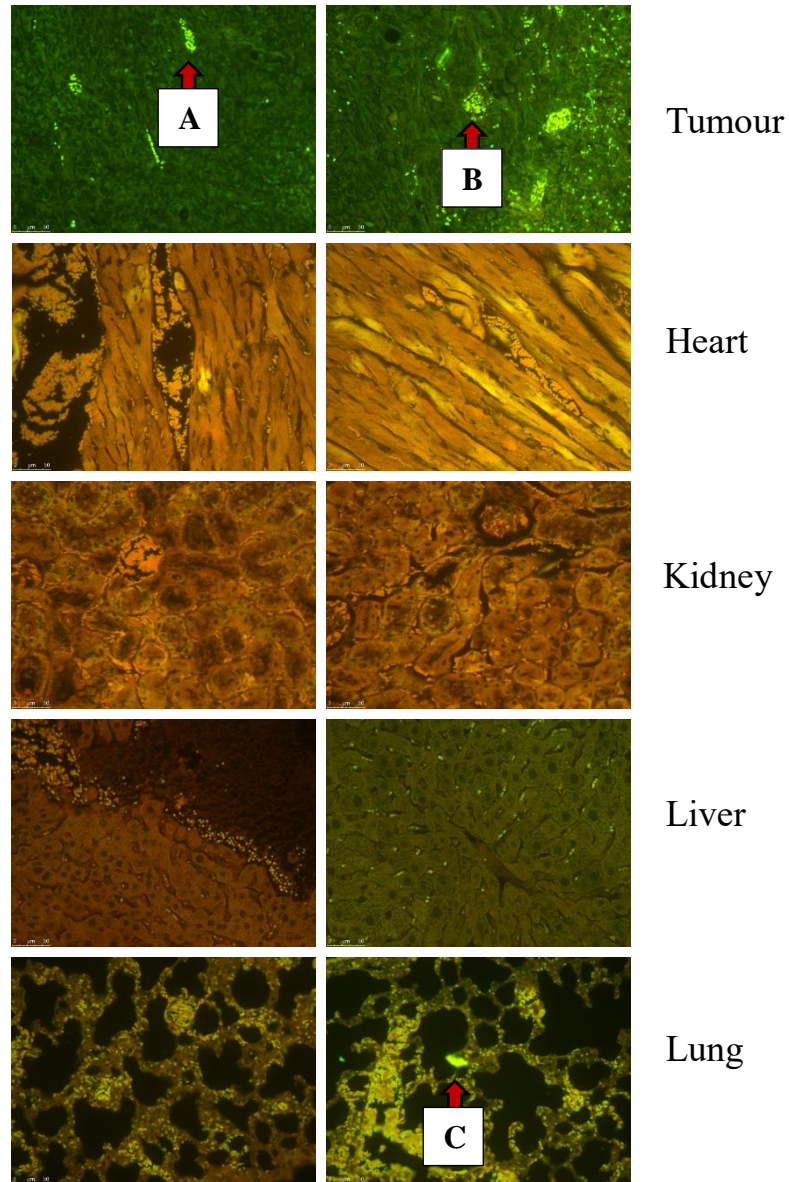
Figure 7.2 | Alexafluor 488 Mouse Sections 24 hours:

Fluorescent images of LLC tumour sections from mouse culled 24 hours after injection with Alexafluor 488 tagged siRNA-nanoparticles without antibody targeting. High levels of green fluorescence can still be seen in the tumour sections (Arrows A and B). Some green fluorescence can be seen in in the lung though this was one of only 3 examples found (Arrow C). Higher magnification images can be seen in figure 6.3 and 6.4.

Figure 7.3
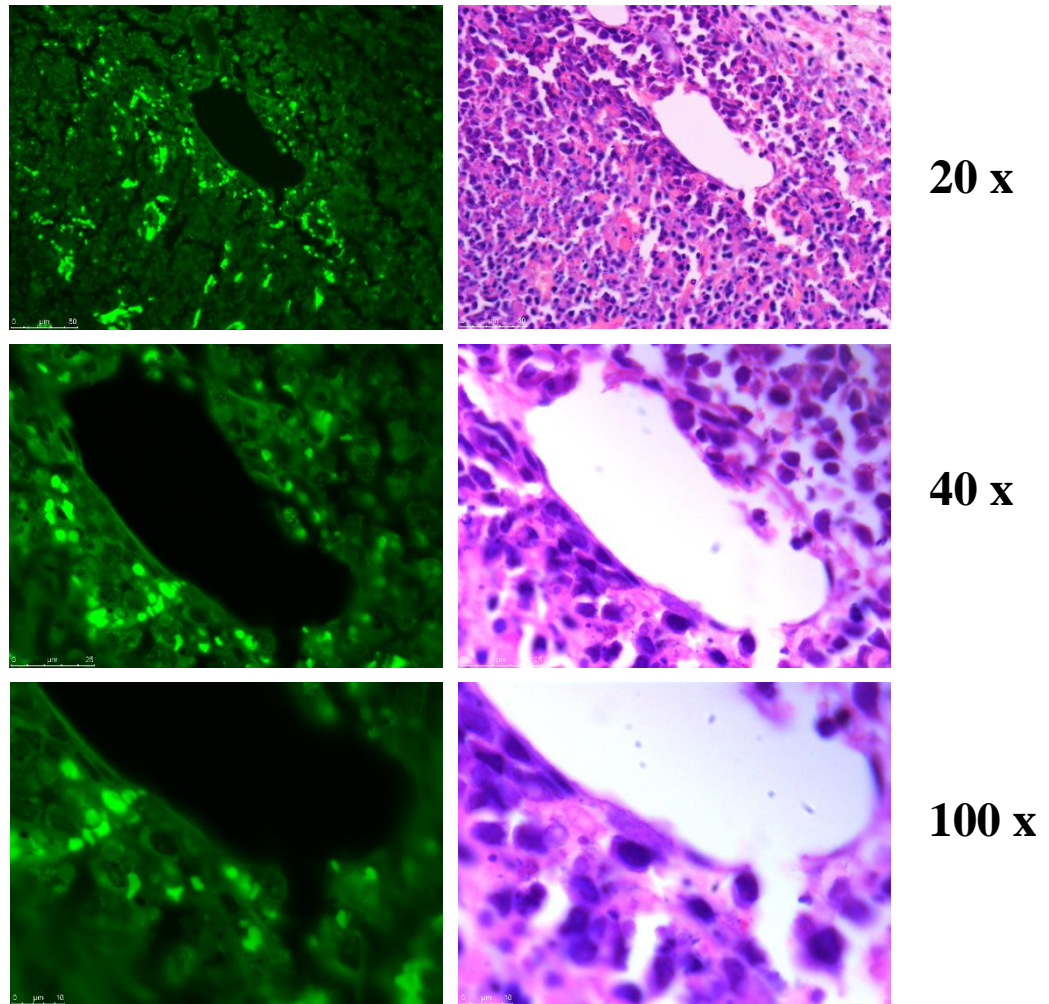
Figure 7.3 | Alexafluor 488 Tumour Sections (Increased Magnification):

Fluorescent images of LLC tumour sections from mouse culled 24 hours after injection with Alexafluor 488 tagged siRNA-nanoparticles without antibody targeting. High levels of green fluorescence can still be seen surrounding the blood vessel. Bright field images of the H&E stain show no presence of red blood cells which are known to exhibit green auto-fluorescence. The ChNP are tagged with a green Alexafluor (488). The presence of large amounts of green fluorescence in the cells surrounding a blood vessel indicate that the nanoparticles are present in high concentrations within the tumour vessel endothelium.

Figure 7.4
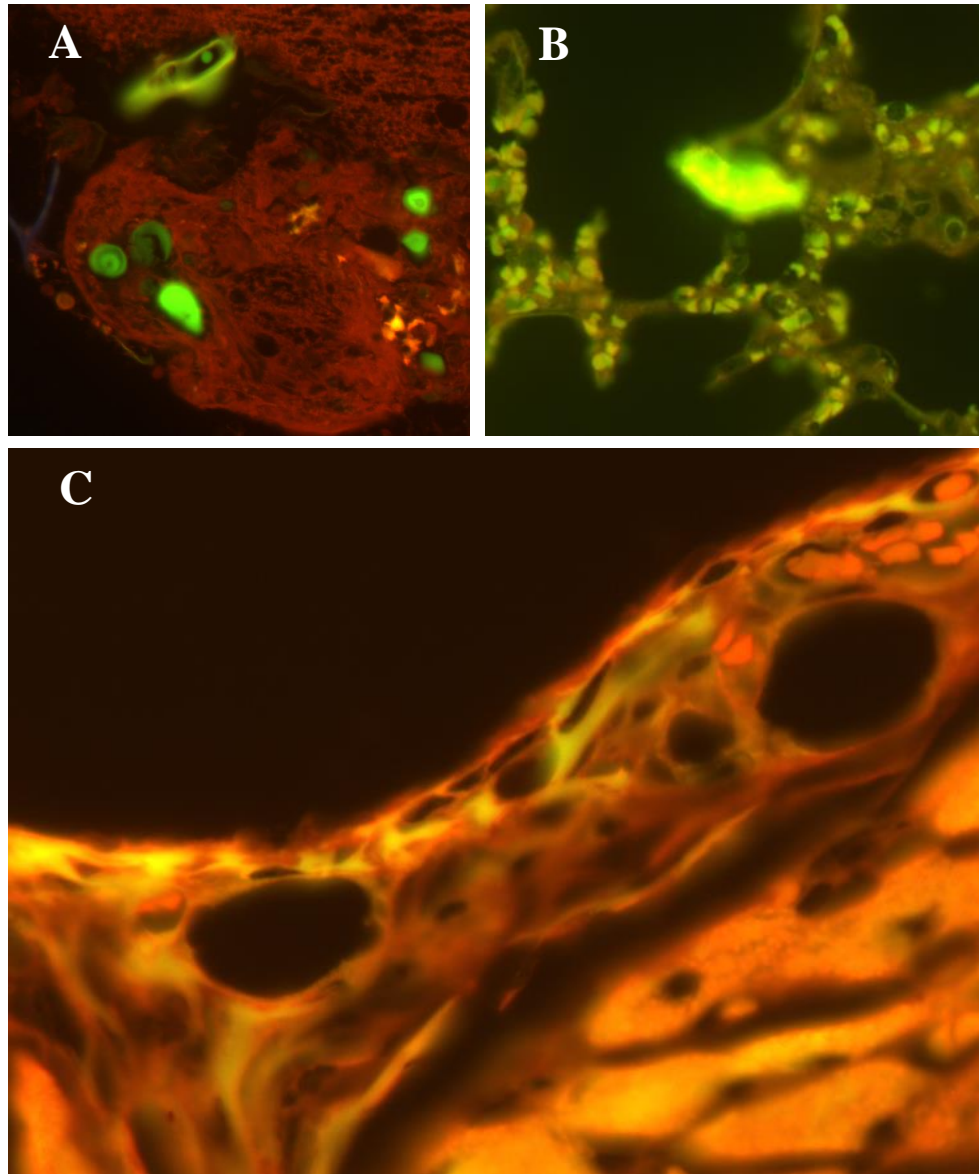
Figure 7.4 | Alexafluor 488 Organ Sections (Magnified):

Fluorescent images of organs sections from mouse after treatment with Alexafluor 488 tagged siRNA-nanoparticles. (A) shows spots of green fluorescence in the liver. (B) shows a spot of strong green fluorescence in the lung. (C) shows a more yellow stain around the lining of the heart ventricle showing an increased green fluorescence.

Figure 7.3 shows images of the tumour sections at greater magnification next to bright field images of the H&E stain. The H&E stain is useful to observe as it was noticed that red blood cells gave off a large amount of green auto-fluorescence. No red blood cells can be seen in the tissue. It must also be noted that the green fluorescence seems to predominate in cells adjacent to the blood vessel walls suggesting that the siRNA does, in fact, end up in its target cells i.e. tumour blood vessel endothelium. Sections taken from the mouse culled after two hours (Figure 7.1) show significantly more strong green fluorescence in other organs compared to the 24 hour incubation (Figure 7.2). At greater magnification the images of the relevant organs can be seen in figure 7.3. The kidney is unsurprisingly a location of strong green fluorescence due to the established preference of chitosan nanoparticles for the kidney tissue (PengZhou, et al., 2014). Lu et al., found the greatest concentration of fluorescent siRNA deposited in the kidneys with the liver showing the next greatest (Lu et al., 2010). This study therefore agrees with the distribution of chitosan nanoparticles; however, far greater fluorescence was found in the tumour than the kidney.

ATTO 395 stained nanoparticles:

The large amount of green auto-fluorescence in mammalian cells, especially red blood cells, made distinguishing true nanoparticle signals in the endothelium challenging. To ensure that any fluorescence see was coming from the siRNA entrapped inside the

nanoparticles, a second experiment was conducted with ATTO 395 fluorophore (Blue) - tagged to siRNA instead of Alexafluor488. There was negligible blue auto-fluorescence in the previous images so any strong blue fluorescent signal would only be from siRNA entrapped nanoparticles.

1 million LLC were implanted in the left flank of 6 week BALBC mice and left to grow for 15 days or until 1 cm in size. At 15 days the mice were injected with ATTO 395 tagged siRNA containing chitosan nanoparticles. Mice were left for 24 hours before being culled. The organs and tumour were extracted and fixed in paraformaldehyde. The organs and tumour were imbedded in paraffin wax and cut into sections 10 micrometres in thickness. The sections were fixed to microscope slides, stained with H&E and imaged on the Leica DM6000 Fluorescence microscope.

Figure 7.5 shows the prevalence of blue fluorescence surrounding blood vessels in the tumour. There was a complete lack of blue stained blood vessels in tumour sections from the control mouse (not injected with nanoparticles).

Figure 7.5
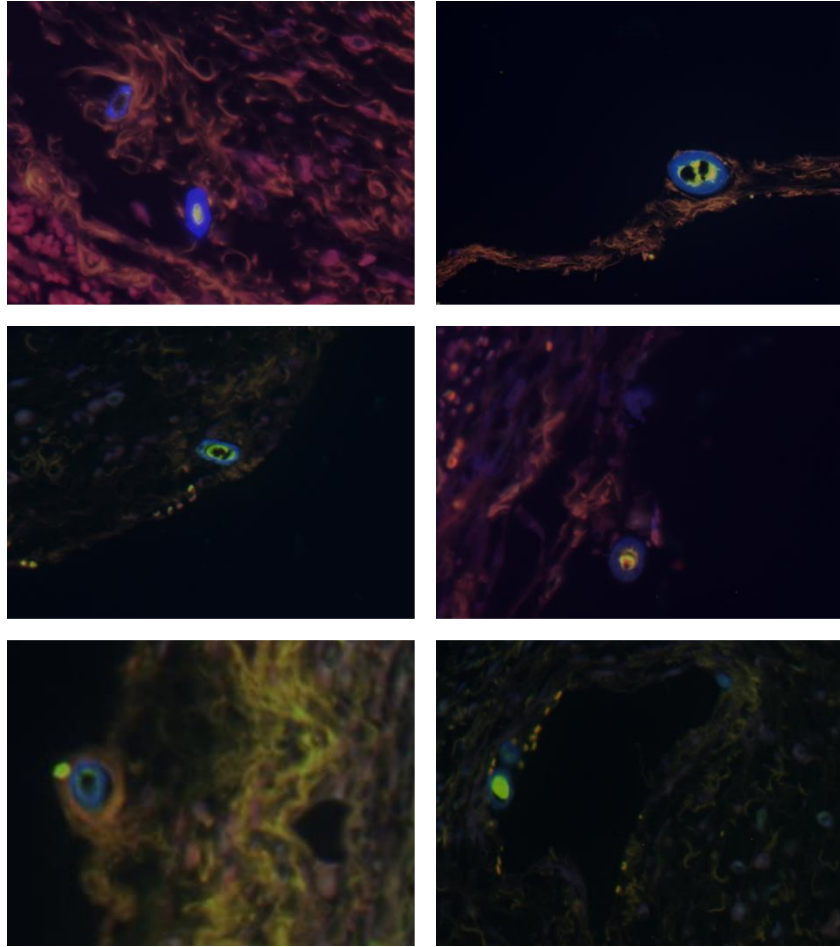
Figure 7.5 | ATTO 395 tagged nanoparticles, 24-hour Tumour Sections:

Fluorescent images of sections made from the LLC tumours in mouse culled 24 hours after injection with ATTO 395 tagged siRNA-nanoparticles without antibody targeting. High levels of blue fluorescence can be seen in the tumour sections. Fluorescence appears to aggregate around blood vessels suggesting that the blue fluorophore tagged nanoparticles are present in the tumour vessel endothelium cells.
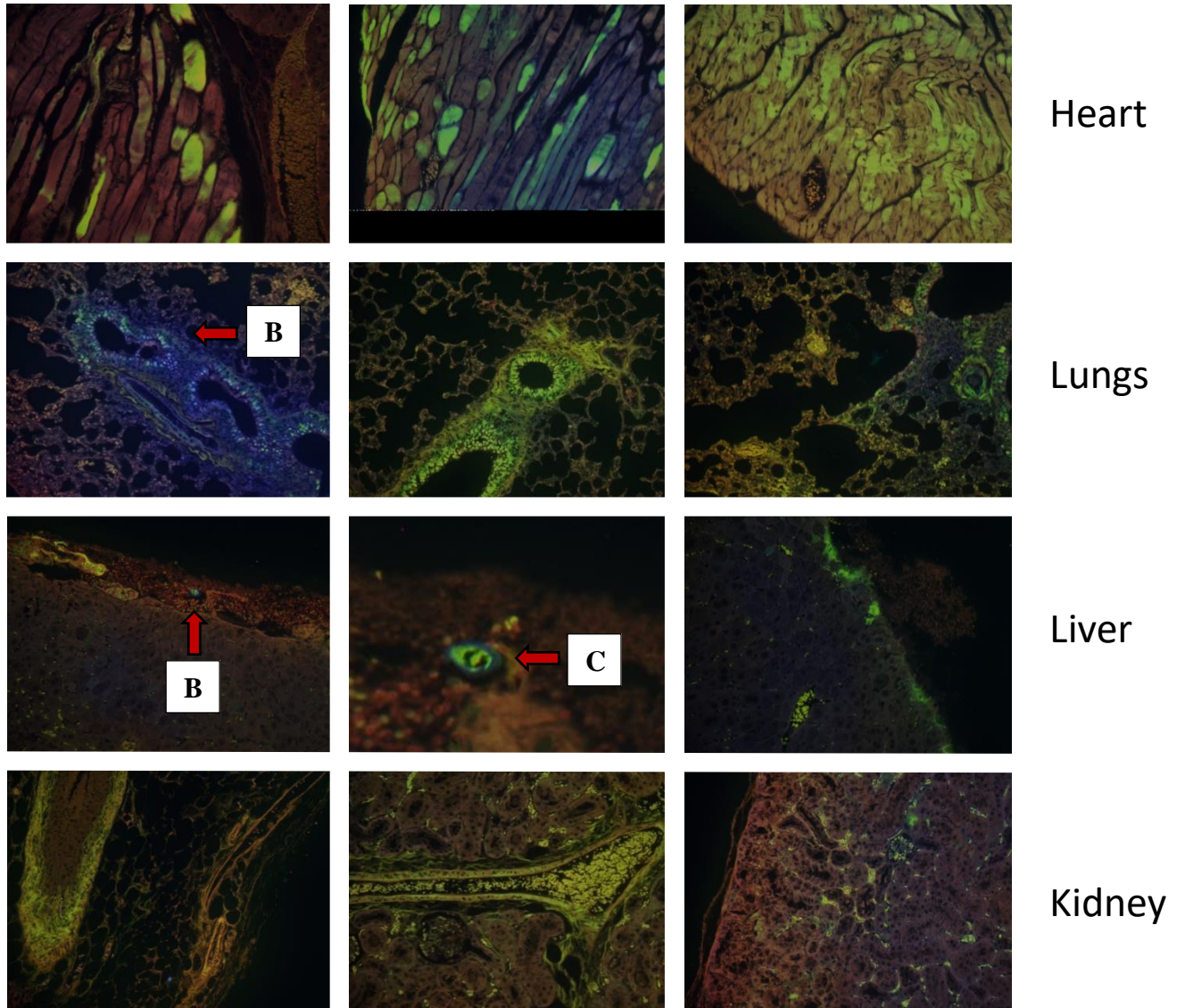
Figure 7.6 | ATTO 395 24-hour Organ Sections:

Fluorescent images of organs sections from mouse after treatment with ATTO 395 tagged siRNA-nanoparticles. There is a large amount of blue fluorescence in lung, however, due to the dispersed nature of this fluorescence it was concluded that this was autofluorescence from the lung cells (Arrows B and C).

Blue fluorescence can be seen surrounding some blood vessels in liver (Arrow A).

Figure 7.6 shows sections from organs from mice treated with ATTO 395 staining nanoparticles. There is a distinct lack of blue fluorescence found in most organs with a few vessels in the liver and some staining in the lungs. These images are from sections of a mouse culled 24 hours after injection and the distribution of fluorescence is constant with the 24 hour Alexafluor 488 tagged nanoparticle mouse.

The presence of clear green fluorescence in endothelial cells from the Alexafluor 488 tagged particles and blue surrounding the blood vessels from the ATTO 395 stained nanoparticles shows that the nanoparticles are distributing mainly to the tumour vasculature. The presence of fluorescence in the kidney and liver agree with other literature on chitosan nanoparticle distribution (Lu et al., 2010, Howard et al., 2006).

Conclusion:

Both fluorescently tagged nanoparticles confirm the presence of (and preference of) chitosan nanoparticles in the tumour. Magnified images show the presence of nanoparticles in the endothelial cells surrounding blood vessels. This *in-vivo* study shows that the nanoparticles end up predominantly in the tumour blood vessels as well as the fluorescent tagged siRNA being present in the endothelial cells. This study contradicted some of the

literature which states that nanoparticles predominantly end up in the kidneys but still agrees that the main area of distribution is the tumour (Lu et al., 2010, Howard et al., 2006). More *in-vivo* work would look at isolating tumour blood vessel endothelium to perform western blot analysis on to assess the *in-vivo* knockdown ability of the ChNP.

Chapter VIII

General Discussion:

<u>Introduction:</u>

CLEC14A is a tumour endothelial marker that has been studied for its involvement in angiogenesis and its potential in anti-cancer therapeutics. Multiple studies within the Bicknell group, coming before and running parallel with this PhD project, have studied the mechanics, interactions, function and methods for perturbation of its expression. Such projects include the targeting of chimeric antigen receptors (CAR) T-Cell targeting (Dr Steve Lee University Birmingham unpublished data), vaccine approaches, antibody drug conjugates and elucidating the interactions between CLEC14A and multimerin 2 (MMRN2) (Khan, 2016). The use of data previously and currently being gathered has led to the development of a therapy aimed at targeting CLEC14A to reduce its expression inside tumour blood vessels thereby preventing growth of new blood vessels.

A key study that reinforced the role of CLEC14A in angiogenesis looked at a homozygous knockout in mice (Noy et al., 2015). The mice were viable and showed no defects during development. Lewis lung carcinomas (LLC) were introduced and it was shown that tumour growth and angiogenesis were reduced compared to wild type mice. Subcutaneous sponge implants also showed FGF2-induced angiogenesis to be reduced.

Previous studies looked at targeting CLEC14A with antibody drug conjugates and protein fragments (Khan, 2016). MMRN2 protein fragments were shown to reduce the rate of tumour growth in LLC implanted tumours in a BALBC mouse models by binding to and inhibiting CLEC14A signalling. hCRT4-bevacizumab ADC's were also shown to successfully target and destroy tumour blood vessels.

This thesis has looked at the disruption of pro-angiogenic CLEC14A signalling through two methods. Firstly, the delivery of small interfering RNA molecules with the aim of knocking down CLEC14A in tumour blood vessels. Secondly, the production and delivery of a CLEC14A based fusion protein that could be used as an anti-cancer vaccine.

It was realised that, to achieve the delivery of siRNA *in-vivo*, a protective vector was needed. Nanoparticles are becoming more important as modern drugs require precise dosage or protection due to the presence of proteins or nucleic acids (Vo et al., 2012, Tatiparti et al., 2017, Infante, 2018).

Additionally, over the past decade nano-sized vectors such as viruses, liposomes and nanoparticles have garnered greater attention as delivery vehicles for vaccines (Gregory A.E., 2013). Nanoparticles have the ability to stabilize proteins or even act as adjuvants to break tolerance (Kishimoto and Maldonado, 2018). These vectors are able to enter antigen-

presenting cells and modulate the immune response (Uto et al., 2009, Chesson and Zloza, 2017).

The efficiency of most existing drug delivery methods is directly related to their size. Smaller nanoparticle carriers present with higher bioavailability, can cross the blood brain barrier, enter the pulmonary system, be absorbed directly by cells or move through tight junctions of endothelial cells (Kohane, 2007, Xie et al., 2017).

The first aim of this project was to develop a nanoparticle that was below 200 nm in size. It has been demonstrated that nanoparticles synthesized at greater than 200 nm are more likely to activate the lymphatic system and be removed from the vascular system sooner (Prokop and Davidson, 2008) A study also found that particles smaller than 200 nm were capable of passive cellular uptake (Geiser et al., 2005, Howard et al., 2006).

Mesoporous silica nanoparticles were chosen as a suitable vector for the protection of siRNA *in-vivo*. It was found that the silica particles failed to "hold onto" the siRNA effectively whilst exposed to vasculature. Gel electrophoresis caused 10% dissociation of the siRNA from the particles. To this end chitosan nanoparticles were selected as a replacement. The chitosan particles succeeded in binding and retaining siRNA when exposed to 50% serum at 37°C for over an hour. It is widely understood that endonuclease enzymes in the serum digest siRNA and using a nanoparticle vector can mitigate these effects (Choung et al., 2006). Generally, studies will expose the nanoparticle-siRNA to serum then actively dissociate the siRNA with something like heparin and test the siRNA

for its integrity in a comet assay for example. Exposure to serum is an important test for the ChNPs as it has been shown that animal serum contains factors that induce depolymerisation of chitosan-TPP nanoparticles. Any study of siRNA release must therefore be considered under near physiological conditions (Raja et al., 2015). The particles were synthesised at roughly 130 nm, TEM imaging allowed for visual analysis of size and also the development of a MatLab program that could automatically calculate the size of any particles imaged through TEM (see appendix 1). This analysis of TEM images via MatLab was developed from the ground up for this thesis and represents a useful tool for future nanoparticle size analysis.

Studies with fluorescent tagged siRNA and confocal microscopy showed that the ChNPs were capable of passive cell uptake. Further study with an early endosome marker, (a marker previously used to study CLEC14A internalisation rates), showed that the green fluorescence of the ChNP-siRNA overlapped with the red of the BacMam RFP early endosome stain.

ChNP's achieved a 60% knockdown of CLEC14A. Varying forms of nanoparticles have been developed for the delivery of siRNA and the results gained for this thesis are consistent with some of the literature, if not better than. A study silencing the pGL3 luciferase gene transfected into CHO K1 cells showed an 82% silencing with chitosan nanoparticles (Li et al., 2003). A similar study showed a 61% reduction in expression of EGFP in PANC-1 cells through the use of siRNA-PEI-MSNs (Hom et al., 2010). Han et al., showed a 51% reduction in POSTN expression, however this was (Han et al., 2010).

Deshpande and Singh used a variety of nanoparticles, eventually achieving a 50% knockdown of the PLK1 gene (Singh, 2018). The knockdown effectiveness of nanoparticles appears to vary greatly from particle to particle. 60% knockdown seems to be average within the current literature, however some are far higher. To attempt to increase the knockdown percentage, efforts were made to improve the knockdown effectiveness of the ChNPs by targeting them directly at CLEC14A on the surface of endothelial cells.

The addition of antibodies to the surface of the nanoparticles aimed to increase the knockdown effectiveness to above 60%. Lee at al., saw a ~30% increase in knockdown effectiveness after the addition of anti-CD7 antibodies to the surface of chitosan nanoparticles (Lee et al., 2012). Similarly, Zhu et al., used CD147-mediated internalization through the Caveolae-dependent pathway and lysosomal escape to improve cellular uptake of their chitosan based nanoparticles in liver cancer cells (Zhu et al., 2015).

The addition of antibodies to the surface of the particles required a modification from chitosan to chitosan glutamate. The glutamate side chains provided a carboxyl group for the EDC reaction to act on and form a peptide bond with activated antibodies. Due to the success of the two studies mentioned above, both their methods for attaching antibodies to chitosan nanoparticles were used in this project to attempt to increase the effectiveness of the nanoparticle knockdown.

The siRNA entrapment/release studies showed that ChGlutNP were able to entrap 84% of the siRNA added during synthesis. The particle size was unaltered by addition of siRNA.

NP-siRNA also retained the siRNA under near physiological conditions, releasing only 32% of the siRNA after an hour in 50% FCS at 37°C. It is difficult to compare this to other chitosan nanoparticle studies as most do not study the effect of serum on release of siRNA, only the effect of endonuclease enzymes. Considering 32% of the siRNA was lost within an hour it is potentially an important area for future studies to look at.

Nanoparticles are expected to be taken up by cells within an hour (Geiser et al., 2005) but the 32% release explains why the 2x concentration of nanoparticles results in a greater knockdown than the 1x for unconjugated particles. The best knockdown with non-antibody conjugated nanoparticles was around a 60% knockdown or 40% remaining expression figure 3.10.

It was thought that improving cell uptake may increase the knockdown percentages achieved by the nanoparticles. Antibodies, targeted at CLEC14A, were conjugated to the surface of the particles to increase cell uptake of the siRNA containing particles.

Two methods were used to attempt to conjugate antibodies. Method 1 resulted in particles that were too large >400 nm. This increase in size is consistent with that observed in the paper from which the method was adapted (Lee et al., 2012). The addition of anti-CD7 antibodies in the Lee et al., study produced particles ranging from 305-345 nm. The study did show that nanoparticle size decreased with a lower percentage of antibody added to the particle. Attempts were made to reduce the size of the particle by modulating the percentage of antibody and other chemicals during synthesis as well as changing the timing

of the addition of reagents. All these methods were developed and adapted for this thesis and can be seen in chapter 4.

A second method was developed and altered to eventually synthesise particles that were less than 200 nm (Zhu et al., 2015). This second method mirrored methods for attaching antibodies to other nanoparticles by attaching them to pre-synthesised particles (Bailes et al., 2012, Khashayar et al., 2017, Dreau et al., 2016). Again, a range of conditions were experimented with such as concentration of Chitosan, concentration of cross linker, concentration of siRNA, temperature and stage at which each of the constituent elements were added to the synthesis. Eventually the particles were brought down to below 200 nm.

The conjugation of antibodies to the surface of the nanoparticles did not drastically increase the knockdown efficiency and in-fact, decreased the knockdown at higher concentrations (Figure 4.10).

Antibody-modified chitosan nanoparticles have been developed for delivering siRNA across the blood-brain barrier (Gu et al., 2017). In this study, antibody conjugation resulted in a 68.9 ± 38.7 percent increase in cellular uptake and 1.57-fold increase in knockdown effectiveness through antibody conjugation. The study did not include evidence for antigen binding studies, prior to cell uptake which were demonstrated in this thesis (Figure 4.7 and 4.8). Scrambled (Non-targeted antibody Ab0) antibodies were used but only in combination with either of their targeted antibodies (Ab1 and Ab2) never by themselves, however they suggest a significant increase in cellular uptake after conjugation of

antibodies to the particles. No extra steps were taken to reduce aggregation. It would be interesting to study potential ways to mitigate this aggregation in future work with the particles in this thesis.

The decrease in knockdown effectiveness seen after antibody conjugation in this project was thought to be due to increased aggregation caused by antibody-antibody attraction. Monoclonal antibodies are known to aggregate under a variety of conditions similarly to many proteins in biological systems (Maas et al., 2007, Wang et al., 2010b). Figure 4.7 shows the aggregation of antibody conjugated particles at higher concentrations.

ELISA studies provided a comprehensive view of antibody-antigen interaction. The discrepancy in binding human vs mouse CLEC14A for the CRT4 antibody was repeated in the nanoparticle-antibody ELISA studies. Wells treated with fluorescently tagged antibody conjugated nanoparticles bound to the mouse variant of CLEC14A with greater specificity than to the human variant. This preference shows the CRT4 preference for human CLEC14A thus showing successful antigen binding by the antibody after being conjugated to the surface of the nanoparticle (figure 4.7). Unfortunately, the positive results from the ELISA experiments did not translate to the HUVEC knockdown experiments which did not improve the knockdown efficiency from the ChNP study. The knockdown percentages were, in fact, worse than without the antibodies. This is likely due to antibody induced aggregation (Li et al., 2016a)

It has been suggested the efficacy of vaccines could be improved through the use of nanoparticles in their delivery (Salem, 2015). Nanoparticles have been identified as potentially helpful in increasing the efficacy of vaccines (Pati et al., 2018). Several nanoparticle formulations have been tested in the literature including Chitosan nanoparticles, liposomes, gold nanoparticles, Poly(D,L-lactic-co-glycolic acid) nanospheres, Polypeptide Nanoparticles, Iron oxide Nanoparticles and virus like particles (O'Neal et al., 1997, Pusic et al., 2013, Raghuvanshi et al., 2002, Chen et al., 2010, Abraham, 1992, Feng et al., 2013).

Nanoparticle vectors for vaccines can improve antigen stability, targeted delivery and enhance the immunogenicity of the vaccine itself (Brouwer et al., 2019). A large number of soluble antigens are not endocytosed effectively by antigen presenting cells and being incorporated into an insoluble vector can resolve this (Vetro et al., 2017).

Polymeric nanoparticles such as chitosan nanoparticles have attracted much attention for their ability to deliver drugs and biological molecules as well as being biodegradable and generally non-toxic (Peng et al., 2008). Additionally, the release of molecules loaded into the particles can be controlled by compositional changes to the copolymer.

Chitosan nanoparticles were selected for this project due to their biodegradability into non-toxic products *in vivo* and the particles innate ability to open up tight junctions between

epithelial cells (Sonaje et al., 2012). Tokumitsu et al., 1999 used chitosan nanoparticles to enhance the uptake of insulin through a nasal spray.

Vaccines are generally protein based and so the first experiments for this section of the thesis were to test the ability for chitosan nanoparticles to entrap proteins inside their polymer mesh. Figure 5.1 shows a gel electrophoresis of fluorescently tagged streptavidin entrapped inside the nanoparticle. As can be seen, the fluorescent streptavidin remains in the well suggesting it remains trapped inside the large nanoparticles. The *in-vivo* studies seen in chapter six show the, untargeted, nanoparticles predominantly distributing to the tumour. The review "Vaccine delivery using nanoparticles" by Gregory et al., (2013) suggests that, for an effective vaccine, particles should be targeted at dendritic cells. This presents potential further experimentation though the targeting experiments with CLEC14A failed to increase knockdown efficiency, maybe a different cellular target would result in a better outcome.

A novel fusion protein was also developed to vaccinate against tumour derived angiogenesis. The development of this protein took on two stages. The initial construct consisted of a fragment of the tetanus protein form the FRC domain – fused to full length CLEC14A. The protein was successfully transfected into HEK293 cells using lentiviral infection. The protein was synthesised and seen clearly on a western blot. A gradient gel was used to visualise the fusion protein as it co-ran with a protein which also exhibited non-specific antibody binding. Yield quantity analysis showed that the protein was being synthesised at very low concentrations. It was thought that this low production was likely

221

due to folding issues and therefore the protein remaining stuck in the endoplasmic reticulum. CLEC14A has an excretion signal meaning the protein should have been excreted and allowed to gather in the cell medium. No protein was found in the cell medium and the only method to harvest the fusion protein was through cell lysis. Due to the infeasibility of high yield production of the tetanus fusion protein, new candidate proteins were selected.

The second fusion protein tested fused fragments of CLEC14A to a protein from the Sea Lamprey fish. The VLRB fragment from Sea Lamprey was shown by Saupe et al., to form massive multimers that were also highly immunogenic (Figure 5.1). Two fragments from CLEC14A were synthesised, the Lectin domain (L-VLRB) and an immunogenic fragment (F-VLRB). The template for the cloned fusion proteins was taken from Saupe et al., The two fragments were transduced into SHuffle® T7 Express lysY Competent *E. coli.* and grown on ampicillin containing agar plates to check for successful transduction. Multiple attempts failed to transduce the lectin-domain fusion protein. It was thought that this was most likely due to a failure of folding due to the lack of glycosylation in bacteria.

The immunogenic fragment was successfully transduced, and SHuffle bacteria were cultured and grown to produce the protein at higher yields. The F-VLRB was collected and purified using Ni-NTA Agarose beads which bound to the his tag on the fusion protein. Western blot analysis (figure 5.9) identified the fragment with an anti-CLEC14A antibody. A band can be seen at the top of the gel which identifies the protein still stuck to the beads after most was removed.

In agreement with Saupe et al., Multimers of the CLEC14A-VLRB protein can be seen in (Figure 5.12). A monomer, 2 unit and 4 unit multimer can be seen in the reducing gel whereas only monomer and 12 unit multimers can be seen in the non-reducing gel. Saupe et al., suggests that it is the formation of these large multimers that allows for a consistent antibody titre after vaccination and so their presence is a clear indication of the successful production of this protein.

Future work will look at incorporation of the successfully purified fragment into chitosan nanoparticles as well as checking immunogenicity of the fragment by itself in mice.
It is difficult to compare this study to others from the literature regarding nanoparticle-based siRNA therapies as there are very few nanoparticle-siRNA studies analysed using microarrays.

The gene array analysis provided more compelling reasons for further study of CLEC14A knockdown via ChNP-siRNA. As previously discussed, it was shown that the ChNP-siRNA did not cause an mRNA knockdown of CLEC14A, however, gene regulatory effects consistent with a decrease in blood flow were seen. The western blots from chapter 3 showed that CLEC14A protein expression was diminished by the NP-siRNA. There is precedent for siRNA molecules to cause protein knockdown without affecting mRNA expression.

There are several potential ways that siRNA could cause a protein knockdown without affecting the mRNA levels. Sometimes cleavage of the target mRNA molecule does not occur. In some instances, endonucleolytic cleavage of the siRNA phosphodiester backbone may be suppressed by mismatches of siRNA and the target mRNA near the RISC cleaving site. Other times, the, patient specific, Argonaute proteins of the RISC lack endonuclease activity even when the target mRNA and siRNA are perfectly paired (Tomari and Zamore, 2005). If this occurs then gene expression will be silenced by miRNA induced mechanism rather than through RISC cleavage (Carthew and Sontheimer, 2009). The gene array data here was gathered from one umbilical cord and so future work would look at repeating the analysis with multiple cords. It is also possible that the nanoparticles themselves caused the alteration in the method of knockdown. Chitosan nanoparticles are well known to generate a protein corona from endogenous proteins inside cells or from the serum (Lundqvist et al., 2011). Should the RISC complex get entrapped inside the protein corona, this could affect its siRNA cleavage efficiency, again, resulting in a miRNA induced knockdown. Additionally, CLEC14A mRNA may get trapped inside the protein corona without being cleaved which would produce the same effect as an siRNA induced knockdown, however, when it came to collection of the mRNA the various reagents used to purify the mRNA would elute it from the particle surface.

Microarray analysis of the delivery of siRNA to tumours using lipid nanoparticles containing PEG-lipid targeting moiety revealed 7 genes and 21 genes were upregulated in the liver and spleen respectively, after i.v injection of the siRNA-lipid nanoparticles (Hatakeyama et al., 2011). Toll-like receptors 3 and 7 are known to mediate the immune

response to siRNA due to the production of inflammatory cytokines and type I IFN (Judge et al., 2005, Hornung et al., 2005, Kawai and Akira, 2010). The up-regulation of interferon associated genes in patients treated with the siRNA-nanoparticles is consistent with an siRNA mediated innate immune response suggesting that siRNA was indeed taken up into these organs and not digested in the serum beforehand. This does not answer the question of the siRNA knockdown but does show that an immune response can be elicited by siRNA bound to a nanoparticle.

Analysis of the microarray data from the ChNP-siRNA using IPA software suggests that ChNP-siRNA particles affect the VEGF and mTOR pathways (Figure 6.2 and 6.3). The mTORC1 pathway is of interest to any anti-cancer therapy as it is known to regulate many oncogenes and tumour suppressors, including, Ras/Raf/MEK/ERK, phosphoinositide 3-kinase (PI3K)/AKT (PKB), the protein synthesis machinery and eukaryotic initiation factor eIF4E. The large prevalence of mTORC1 hyperactivation in human tumours makes it an interesting target for an anti-cancer therapy.

NP-siRNA particles also appear to affect the VEGF pathway. This analysis in combination with the bio-distribution studies strengthens the case that the NP-siRNA particles have the desired anti-angiogenic effects. The VEGF pathway as well as mTOR signalling is being perturbed and the distribution studies show that the particles locate predominantly to the tumour blood vessels.

Of great interest was the realisation that CLEC14A is a regulatory gene rather than a regulated gene. By comparing the microarray data from this thesis and the data gathered in Mura et al., 2012, it can be seen that a reduction of CLEC14A on a protein level, not an mRNA level, causes alterations to endothelial gene expression in the same way that increasing laminar blood flow would. This finding suggests that pertubation of CLEC14A can have wide reaching effects similar to physilogical stimulus and changes in blood flow.

Biodistribution studies were performed with ChNP as it was shown that the addition of antibodies did not increase the knockdown effectiveness of the ChNPs. Experiments with CLEC14A knockout mice as well as monoclonal antibody-based therapies targeting CLEC14A in LLC tumour implanted in mice provided a good basis for study into the in-vivo potential of the ChNP-siRNA (Khan 2016).

1 million Lewis Lung Carcinoma cells (LLC) were implanted in the left flank of 6 week BALBC mice and left to grow for 15 days or until 1 cm in size. At 15 days the mice were injected with Alexafluor 488 tagged siRNA containing chitosan nanoparticles through the tail vain.

First the tumours and organs were harvested, fixed in paraffin wax, cut into 10 micron sections and stained with the H&E stain. Two fluorophores were used to image the ChNPs in the mouse sections: Alexafluor 488 and ATTO 395.

It was seen that the NP-siRNA particles were predominantly distributed to the tumour, though a small amount went to the liver and kidneys. The kidney is unsurprisingly a location of strong green fluorescence due to the established preference of chitosan nanoparticles for the kidney tissue (PengZhou, et al., 2014). Lu et al., found the greatest concentration of fluorescent siRNA deposited in the kidneys with the liver showing the next greatest (Lu et al., 2010). This study therefore agrees with the distribution of chitosan nanoparticles; however, far greater fluorescence was found in the tumour than the kidney.

The ATTO 395 fluorophore can be seen in the circumference of the blood vessel lumens within the tumour figure 6.5. The combination of this tumour blood vessel localisation and the confirmation of the 60% knockdown in cell culture, suggests a positive future for the particles. A vital future experiment would be the isolation of mouse tumour endothelial cells, from an *in-vivo* model, for western blot analysis. Han et al., showed a 51% reduction in POSTN expression, (Han et al., 2010). Analysis was performed through western blot and future studies into the *in-vivo* effects of the ChNP-siRNA would likely follow the protocol set out in this study.

Conclusion:

This thesis documents the development and characterisation of a vector for the delivery of CLEC14A siRNA or a potential CLEC14A based fusion protein for anti-cancer vaccination. To improve on some of the published examples that use a nanoparticle vectors, this thesis assessed every required ability of the vector. MSN particles were initially synthesised and studied but presented issues with siRNA binding and retention. Chitosan nanoparticles were chosen as a replacement for the MSNs. Studies were done to look at nanoparticle sizing, siRNA/protein entrapment, siRNA release, *in-vitro* knockdown, antibody conjugation, antibody targeted *in-vitro* knockdown and distribution studies. The *in-vitro* studies confirmed the ability for chitosan nanoparticles to enter HUVECs and knockdown CLEC14A to around 40% relative expression remaining. The studies confirmed the predominant distribution of nanoparticles to endothelial cells inside the tumour blood vessels. The protein studies showed that the nanoparticles could entrap protein inside them. The vaccine synthesis experiments successfully produced a CLEC14A fragment-VLRB fusion protein that is read for immunisation experiments.

Combining all the previous data with the gene array data paints an interesting picture for the NP-siRNA particles. The particles retain the siRNA entrapped inside and are able to

enter mammalian cells through endocytosis. The nanoparticles appear to distribute predominantly to the tumour blood vessels when tested with a mouse model. The *in-vitro* cell uptake studies, in combination with the distribution, suggest that the particles do reach their target. Western blot analysis suggests they have the desired effect of knocking down CLEC14A in endothelial cells. The gene array data suggests that CLEC14A is not knocked down at an mRNA level, however, alterations to other endothelial related genes are consistent with a decrease in expression of CLEC14A as seen previously in a blood flow gene array analysis. Not only this, but through IPA analysis it appears as if the NP-siRNA particles also effect the VEGF and mTOR pathways providing interest for future projects exploring potential additional anti-cancer characteristics of the ChNP-(CLEC14A siRNA).

Bibliography

A. A. ZUBAREVAA, A. E. V. S. 2016. Interactions of Chitosan and Its Derivatives with Cells (Review). *Applied Biochemistry and Microbiology,* 52**,** 465–470.

ABRAHAM, E. 1992. Intranasal immunization with bacterial polysaccharide containing liposomes enhances antigen-specific pulmonary secretory antibody response. *Vaccine,* 10**,** 461-8.

AIGNER, A. 2007. Nonviral in vivo delivery of therapeutic small interfering RNAs. *Curr Opin Mol Ther,* 9**,** 345-52.

AMANI, N., DORKOOSH, F. A. & MOBEDI, H. 2019. ADCs, as novel revolutionary weapons for providing a step forward in targeted therapy of malignancies. *Curr Drug Deliv*.

AMBROSE, S. R., GORDON, N. S., GOLDSMITH, J. C., WEI, W., ZEEGERS, M. P., JAMES, N. D., KNOWLES, M. A., BRYAN, R. T. & WARD, D. G. 2015. Use of Aleuria alantia Lectin Affinity Chromatography to Enrich Candidate Biomarkers from the Urine of Patients with Bladder Cancer. *Proteomes,* 3**,** 266-282.

ARAUJO, L., LOBENBERG, R. & KREUTER, J. 1999. Influence of the surfactant concentration on the body distribution of nanoparticles. *J Drug Target,* 6**,** 373-85.

AUSPRUNK, D. H. & FOLKMAN, J. 1977. Migration and proliferation of endothelial cells in preformed and newly formed blood vessels during tumor angiogenesis. *Microvasc Res,* 14**,** 53-65.

BAILES, J., MAYOSS, S., TEALE, P. & SOLOVIEV, M. 2012. Gold nanoparticle antibody conjugates for use in competitive lateral flow assays. *Methods Mol Biol,* 906**,** 45-55.

BAIS, C., SINGH, M., KAMINKER, J., & BRAUER, M.. 2011. Biological markers for monitoring patient response to vegf antagonists.

BANTZ, C., KOSHKINA, O., LANG, T., GALLA, H. J., KIRKPATRICK, C. J., STAUBER, R. H. & MASKOS, M. 2014. The surface properties of nanoparticles determine the agglomeration state and the size of the particles under physiological conditions. *Beilstein J Nanotechnol,* 5**,** 1774-1786.

BARBERO, F., RUSSO, L., VITALI, M., PIELLA, J., SALVO, I., BORRAJO, M. L., BUSQUETS-FITE, M., GRANDORI, R., BASTUS, N. G., CASALS, E. & PUNTES, V. 2017. Formation of the Protein Corona: The Interface between Nanoparticles and the Immune System. *Semin Immunol,* 34**,** 52-60.

BASS, J. J., WILKINSON, D. J., RANKIN, D., PHILLIPS, B. E., SZEWCZYK, N. J., SMITH, K. & ATHERTON, P. J. 2017. An overview of technical considerations for Western blotting applications to physiological research. *Scand J Med Sci Sports,* 27**,** 4-25.

BIRAGYN, A., SURENHU, M., YANG, D., RUFFINI, P. A., HAINES, B. A., KLYUSHNENKOVA, E., OPPENHEIM, J. J. & KWAK, L. W. 2001. Mediators of innate immunity that target immature, but not mature, dendritic cells induce antitumor immunity when genetically fused with nonimmunogenic tumor antigens. *J Immunol,* 167**,** 6644-53.

BJARNEGARD, M., ENGE, M., NORLIN, J., GUSTAFSDOTTIR, S., FREDRIKSSON, S., ABRAMSSON, A., TAKEMOTO, M., GUSTAFSSON, E., FASSLER, R. & BETSHOLTZ, C. 2004. Endothelium-specific ablation of PDGFB leads to pericyte loss and glomerular, cardiac and placental abnormalities. *Development,* 131**,** 1847-57.

BROUWER, P. J. M., ANTANASIJEVIC, A., BERNDSEN, Z., YASMEEN, A., FIALA, B., BIJL, T. P. L., BONTJER, I., BALE, J. B., SHEFFLER, W., ALLEN, J. D., SCHORCHT, A., BURGER, J. A., CAMACHO, M., ELLIS, D., COTTRELL, C. A., BEHRENS, A. J., CATALANO, M., DEL MORAL-SANCHEZ, I., KETAS, T. J., LABRANCHE, C., VAN GILS, M. J., SLIEPEN, K., STEWART, L. J., CRISPIN, M., MONTEFIORI, D. C., BAKER, D., MOORE, J. P., KLASSE, P. J., WARD, A. B., KING, N. P. & SANDERS, R. W. 2019. Enhancing and shaping the immunogenicity of native-like HIV-1 envelope trimers with a two-component protein nanoparticle. *Nat Commun,* 10**,** 4272.

BRUNN, G. J., HUDSON, C. C., SEKULIC, A., WILLIAMS, J. M., HOSOI, H., HOUGHTON, P. J., LAWRENCE, J. C., JR. & ABRAHAM, R. T. 1997. Phosphorylation of the translational repressor PHAS-I by the mammalian target of rapamycin. *Science,* 277**,** 99-101.

BURRI, P. H., HLUSHCHUK, R. & DJONOV, V. 2004. Intussusceptive angiogenesis: its emergence, its characteristics, and its significance. *Dev Dyn,* 231**,** 474-88.

BURROWS, F. J. & THORPE, P. E. 1993. Eradication of large solid tumors in mice with an immunotoxin directed against tumor vasculature. *Proc Natl Acad Sci U S A,* 90**,** 8996-9000.

BUZEA, C., PACHECO, II & ROBBIE, K. 2007. Nanomaterials and nanoparticles: sources and toxicity. *Biointerphases,* 2**,** MR17-71.

CARMELIET, P. 2003. Angiogenesis in health and disease. *Nature Medicine,* 9**,** 653-660.

CARMELIET, P. & JAIN, R. K. 2011. Molecular mechanisms and clinical applications of angiogenesis. *Nature,* 473**,** 298-307.

CARTHEW, R. W. & SONTHEIMER, E. J. 2009. Origins and Mechanisms of miRNAs and siRNAs. *Cell,* 136**,** 642-55.

CASANOVAS, O., HICKLIN, D. J., BERGERS, G. & HANAHAN, D. 2005. Drug resistance by evasion of antiangiogenic targeting of VEGF signaling in late-stage pancreatic islet tumors. *Cancer Cell,* 8**,** 299-309.

CERNIGLIA, G. J., PORE, N., TSAI, J. H., SCHULTZ, S., MICK, R., CHOE, R., XING, X., DURDURAN, T., YODH, A. G., EVANS, S. M., KOCH, C. J., HAHN, S. M., QUON, H., SEHGAL, C. M., LEE, W. M. & MAITY, A. 2009. Epidermal growth factor receptor inhibition modulates the microenvironment by vascular normalization to improve chemotherapy and radiotherapy efficacy. *PLoS One,* 4**,** e6539.

CHEN, Y. S., HUNG, Y. C., LIN, W. H. & HUANG, G. S. 2010. Assessment of gold nanoparticles as a size-dependent vaccine carrier for enhancing the antibody response against synthetic foot-and-mouth disease virus peptide. *Nanotechnology,* 21**,** 195101.

CHESSON, C. B. & ZLOZA, A. 2017. Nanoparticles: augmenting tumor antigen presentation for vaccine and immunotherapy treatments of cancer. *Nanomedicine (Lond),* 12**,** 2693-2706.

CHOUNG, S., KIM, Y. J., KIM, S., PARK, H. O. & CHOI, Y. C. 2006. Chemical modification of siRNAs to improve serum stability without loss of efficacy. *Biochem Biophys Res Commun,* 342**,** 919-27.

CHOWDHURY, A., CHOUDHURY, A., BANERJEE, V., BANERJEE, R. & DAS, K. P. 2014. Spectroscopic studies of the unfolding of a multimeric protein alpha-crystallin. *Biopolymers,* 101**,** 549-60.

DESAI, M. P., LABHASETWAR, V., WALTER, E., LEVY, R. J. & AMIDON, G. L. 1997. The mechanism of uptake of biodegradable microparticles in Caco-2 cells is size dependent. *Pharm Res,* 14**,** 1568-73.

DESGROSELLIER, J. S. & CHERESH, D. A. 2010. Integrins in cancer: biological implications and therapeutic opportunities. *Nat Rev Cancer,* 10**,** 9-22.

DIAZ, L. A., JR., WILLIAMS, R. T., WU, J., KINDE, I., HECHT, J. R., BERLIN, J., ALLEN, B., BOZIC, I., REITER, J. G., NOWAK, M. A., KINZLER, K. W., OLINER, K. S. & VOGELSTEIN, B. 2012. The molecular evolution of acquired resistance to targeted EGFR blockade in colorectal cancers. *Nature,* 486**,** 537-40.

DODANE V., V. V. D. *Pharm. Sci. Tech,* 1**,** 246—253.

DREAU, D., MOORE, L. J., ALVAREZ-BERRIOS, M. P., TARANNUM, M., MUKHERJEE, P. & VIVERO-ESCOTO, J. L. 2016. Mucin-1-Antibody-Conjugated Mesoporous Silica Nanoparticles for Selective Breast Cancer Detection in a Mucin-1 Transgenic Murine Mouse Model. *J Biomed Nanotechnol,* 12**,** 2172-2184.

EBOS, J. M., LEE, C. R., CRUZ-MUNOZ, W., BJARNASON, G. A., CHRISTENSEN, J. G. & KERBEL, R. S. 2009. Accelerated metastasis after short-term treatment with a potent inhibitor of tumor angiogenesis. *Cancer Cell,* 15**,** 232-9.

EISEN, M. B., SPELLMAN, P. T., BROWN, P. O. & BOTSTEIN, D. 1998. Cluster analysis and display of genome-wide expression patterns. *Proc Natl Acad Sci U S A,* 95**,** 14863-8.

ELBASHIR, S. M., MARTINEZ, J., PATKANIOWSKA, A., LENDECKEL, W. & TUSCHL, T. 2001. Functional anatomy of siRNAs for mediating efficient RNAi in Drosophila melanogaster embryo lysate. *EMBO J,* 20**,** 6877-88.

ENGVALL, E. & PERLMANN, P. 1972. Enzyme-linked immunosorbent assay, Elisa. 3. Quantitation of specific antibodies by enzyme-labeled anti-immunoglobulin in antigen-coated tubes. *J Immunol,* 109**,** 129-35.

FACCIPONTE, J. G., UGEL, S., DE SANCTIS, F., LI, C., WANG, L., NAIR, G., SEHGAL, S., RAJ, A., MATTHAIOU, E., COUKOS, G. & FACCIABENE, A. 2014. Tumor endothelial marker 1-specific DNA vaccination targets tumor vasculature. *J Clin Invest,* 124**,** 1497-511.

FALCON, B. L., BARR, S., GOKHALE, P. C., CHOU, J. L., FOGARTY, J., DEPEILLE, P., MIGLARESE, M., EPSTEIN, D. M. & MCDONALD, D. M. 2011. Reduced VEGF Production, Angiogenesis, and Vascular Regrowth Contribute to the Antitumor Properties of Dual mTORC1/mTORC2 Inhibitors. *Cancer Research,* 71**,** 1573-1583.

FEMEL, J., HUIJBERS, E. J., SAUPE, F., CEDERVALL, J., ZHANG, L., ROSWALL, P., LARSSON, E., OLOFSSON, H., PIETRAS, K., DIMBERG, A., HELLMAN, L. & OLSSON, A. K. 2014. Therapeutic vaccination against fibronectin ED-A attenuates progression of metastatic breast cancer. *Oncotarget,* 5**,** 12418-27.

FENG, G., JIANG, Q., XIA, M., LU, Y., QIU, W., ZHAO, D., LU, L., PENG, G. & WANG, Y. 2013. Enhanced immune response and protective effects of nano-chitosan-based DNA vaccine encoding T cell epitopes of Esat-6 and FL against Mycobacterium tuberculosis infection. *PLoS One,* 8**,** e61135.

FILLEUR, S., COURTIN, A., AIT-SI-ALI, S., GUGLIELMI, J., MERLE, C., HAREL-BELLAN, A., CLEZARDIN, P. & CABON, F. 2003. SiRNA-mediated inhibition of vascular endothelial growth factor severely limits tumor resistance to antiangiogenic thrombospondin-1 and slows tumor vascularization and growth. *Cancer Res,* 63**,** 3919-22.

FIRE, A., XU, S., MONTGOMERY, M. K., KOSTAS, S. A., DRIVER, S. E. & MELLO, C. C. 1998. Potent and specific genetic interference by double-stranded RNA in Caenorhabditis elegans. *Nature,* 391**,** 806-11.

FOLKMAN, J. 1971. Tumor angiogenesis: therapeutic implications. *N Engl J Med,* 285**,** 1182-6.

FOLKMAN, J. & HAUDENSCHILD, C. 1980. Angiogenesis in vitro. *Nature,* 288**,** 551-6.

FRIEDMAN, A. D., CLAYPOOL, S. E. & LIU, R. 2013. The smart targeting of nanoparticles. *Curr Pharm Des,* 19**,** 6315-29.

FROGER, A. & HALL, J. E. 2007. Transformation of plasmid DNA into E. coli using the heat shock method. *J Vis Exp***,** 253.

GAN, Q., WANG, T., COCHRANE, C. & MCCARRON, P. 2005. Modulation of surface charge, particle size and morphological properties of chitosan-TPP nanoparticles intended for gene delivery. *Colloids Surf B Biointerfaces,* 44**,** 65-73.

GAO, H., YANG, Z., ZHANG, S., CAO, S., SHEN, S., PANG, Z. & JIANG, X. 2013. Ligand modified nanoparticles increases cell uptake, alters endocytosis and elevates glioma distribution and internalization. *Sci Rep,* 3**,** 2534.

GEISER, M., ROTHEN-RUTISHAUSER, B., KAPP, N., SCHURCH, S., KREYLING, W., SCHULZ, H., SEMMLER, M., IM HOF, V., HEYDER, J. & GEHR, P. 2005. Ultrafine particles cross cellular membranes by nonphagocytic mechanisms in lungs and in cultured cells. *Environ Health Perspect,* 113**,** 1555-60.

GNASSO, A., IRACE, C., CARALLO, C., DE FRANCESCHI, M. S., MOTTI, C., MATTIOLI, P. L. & PUJIA, A. 1997. In vivo association between low wall shear stress and plaque in subjects with asymmetrical carotid atherosclerosis. *Stroke,* 28**,** 993-8.

GRANT, D. S., LELKES, P. I., FUKUDA, K. & KLEINMAN, H. K. 1991. Intracellular mechanisms involved in basement membrane induced blood vessel differentiation in vitro. *In Vitro Cell Dev Biol,* 27A**,** 327-36.

GREENE, M. K., RICHARDS, D. A., NOGUEIRA, J. C. F., CAMPBELL, K., SMYTH, P., FERNANDEZ, M., SCOTT, C. J. & CHUDASAMA, V. 2018. Forming next-generation antibody-nanoparticle conjugates through the oriented installation of non-engineered antibody fragments. *Chem Sci,* 9**,** 79-87.

GREGORY A.E., T. R., WILLIAMSON D. 2013. Vaccine delivery using nanoparticles.

. *Front Cell Infect Microbiol.*

GU, J., AL-BAYATI, K. & HO, E. A. 2017. Development of antibody-modified chitosan nanoparticles for the targeted delivery of siRNA across the blood-brain barrier as a strategy for inhibiting HIV replication in astrocytes. *Drug Deliv Transl Res,* 7**,** 497-506.

HAGG, S., SKOGSBERG, J., LUNDSTROM, J., NOORI, P., NILSSON, R., ZHONG, H., MALEKI, S., SHANG, M. M., BRINNE, B., BRADSHAW, M., BAJIC, V. B., SAMNEGARD, A., SILVEIRA, A., KAPLAN, L. M., GIGANTE, B., LEANDER, K., DE FAIRE, U., ROSFORS, S., LOCKOWANDT, U., LISKA, J., KONRAD, P., TAKOLANDER, R., FRANCO-CERECEDA, A., SCHADT, E. E., IVERT, T., HAMSTEN, A., TEGNER, J. & BJORKEGREN, J. 2009. Multi-organ expression profiling uncovers a gene module in coronary artery disease involving transendothelial migration of leukocytes and LIM domain binding 2: the Stockholm Atherosclerosis Gene Expression (STAGE) study. *PLoS Genet,* 5**,** e1000754.

HAMZAH, J., JUGOLD, M., KIESSLING, F., RIGBY, P., MANZUR, M., MARTI, H. H., RABIE, T., KADEN, S., GRONE, H. J., HAMMERLING, G. J., ARNOLD, B. & GANSS, R. 2008. Vascular normalization in Rgs5-deficient tumours promotes immune destruction. *Nature,* 453**,** 410-4.

HAN, H. D., MANGALA, L. S., LEE, J. W., SHAHZAD, M. M., KIM, H. S., SHEN, D., NAM, E. J., MORA, E. M., STONE, R. L., LU, C., LEE, S. J., ROH, J. W., NICK, A. M., LOPEZ-BERESTEIN, G. & SOOD, A. K. 2010. Targeted gene silencing using RGD-labeled chitosan nanoparticles. *Clin Cancer Res,* 16**,** 3910-22.

HANAHAN, D. & FOLKMAN, J. 1996. Patterns and emerging mechanisms of the angiogenic switch during tumorigenesis. *Cell,* 86**,** 353-64.

HANAHAN, D. & WEINBERG, R. A. 2000. The hallmarks of cancer. *Cell,* 100**,** 57-70.

HANAHAN, D. & WEINBERG, R. A. 2011. Hallmarks of cancer: the next generation. *Cell,* 144**,** 646-74.

HASHIZUME, H., BALUK, P., MORIKAWA, S., MCLEAN, J. W., THURSTON, G., ROBERGE, S., JAIN, R. K. & MCDONALD, D. M. 2000. Openings between defective endothelial cells explain tumor vessel leakiness. *Am J Pathol,* 156**,** 1363-80.

HATAKEYAMA, H., AKITA, H., ITO, E., HAYASHI, Y., OISHI, M., NAGASAKI, Y., DANEV, R., NAGAYAMA, K., KAJI, N., KIKUCHI, H., BABA, Y. & HARASHIMA, H. 2011. Systemic delivery of siRNA to tumors using a lipid nanoparticle containing a tumor-specific cleavable PEG-lipid. *Biomaterials,* 32**,** 4306-16.

HELLBERG, C., OSTMAN, A. & HELDIN, C. H. 2010. PDGF and vessel maturation. *Recent Results Cancer Res,* 180**,** 103-14.

HELLSTROM, M., PHNG, L. K., HOFMANN, J. J., WALLGARD, E., COULTAS, L., LINDBLOM, P., ALVA, J., NILSSON, A. K., KARLSSON, L., GAIANO, N., YOON, K., ROSSANT, J., IRUELA-ARISPE, M. L., KALEN, M., GERHARDT, H. & BETSHOLTZ, C. 2007. Dll4 signalling through Notch1 regulates formation of tip cells during angiogenesis. *Nature,* 445**,** 776-80.

HERBERT, J. M., STEKEL, D., SANDERSON, S., HEATH, V. L. & BICKNELL, R. 2008. A novel method of differential gene expression analysis using multiple cDNA libraries applied to the identification of tumour endothelial genes. *BMC Genomics,* 9**,** 153.

HERRIN, B. R., ALDER, M. N., ROUX, K. H., SINA, C., EHRHARDT, G. R., BOYDSTON, J. A., TURNBOUGH, C. L., JR. & COOPER, M. D. 2008. Structure and specificity of lamprey monoclonal antibodies. *Proc Natl Acad Sci U S A,* 105**,** 2040-5.

HERZENBERG, L. A. & TOKUHISA, T. 1982. Epitope-specific regulation. I. Carrier-specific induction of suppression for IgG anti-hapten antibody responses. *J Exp Med,* 155**,** 1730-40.

HERZENBERG, L. A., TOKUHISA, T., PARKS, D. R. & HERZENBERG, L. A. 1982. Epitope-specific regulation. II. A bistable, Igh-restricted regulatory mechanism central to immunologic memory. *J Exp Med,* 155**,** 1741-53.

HETZ, C. 2012. The unfolded protein response: controlling cell fate decisions under ER stress and beyond. *Nat Rev Mol Cell Biol,* 13**,** 89-102.

HIRANO, M., DAS, S., GUO, P. & COOPER, M. D. 2011. The evolution of adaptive immunity in vertebrates. *Adv Immunol,* 109**,** 125-57.

HO, E. A., OSOOLY, M., STRUTT, D., MASIN, D., YANG, Y., YAN, H. & BALLY, M. 2013. Characterization of long-circulating cationic nanoparticle formulations consisting of a two-stage PEGylation step for the delivery of siRNA in a breast cancer tumor model. *J Pharm Sci,* 102**,** 227-36.

HO, M., YANG, E., MATCUK, G., DENG, D., SAMPAS, N., TSALENKO, A., TABIBIAZAR, R., ZHANG, Y., CHEN, M., TALBI, S., HO, Y. D., WANG, J., TSAO, P. S., BEN-DOR, A., YAKHINI, Z., BRUHN, L. & QUERTERMOUS, T. 2003. Identification of endothelial cell genes by combined database mining and microarray analysis. *Physiol Genomics,* 13**,** 249-62.

HODI, F. S., LAWRENCE, D., LEZCANO, C., WU, X., ZHOU, J., SASADA, T., ZENG, W., GIOBBIE-HURDER, A., ATKINS, M. B., IBRAHIM, N., FRIEDLANDER, P., FLAHERTY, K. T., MURPHY, G. F., RODIG, S., VELAZQUEZ, E. F., MIHM, M. C., JR., RUSSELL, S., DIPIRO, P. J., YAP, J. T., RAMAIYA, N., VAN DEN ABBEELE, A. D., GARGANO, M. & MCDERMOTT, D. 2014. Bevacizumab plus ipilimumab in patients with metastatic melanoma. *Cancer Immunol Res,* 2**,** 632-42.

HOM, C., LU, J., LIONG, M., LUO, H., LI, Z., ZINK, J. I. & TAMANOI, F. 2010. Mesoporous silica nanoparticles facilitate delivery of siRNA to shutdown signaling pathways in mammalian cells. *Small,* 6**,** 1185-90.

11

HORNUNG, V., GUENTHNER-BILLER, M., BOURQUIN, C., ABLASSER, A., SCHLEE, M., UEMATSU, S., NORONHA, A., MANOHARAN, M., AKIRA, S., DE FOUGEROLLES, A., ENDRES, S. & HARTMANN, G. 2005. Sequence-specific potent induction of IFN-alpha by short interfering RNA in plasmacytoid dendritic cells through TLR7. *Nat Med,* 11**,** 263-70.

HOWARD, K. A., RAHBEK, U. L., LIU, X., DAMGAARD, C. K., GLUD, S. Z., ANDERSEN, M. O., HOVGAARD, M. B., SCHMITZ, A., NYENGAARD, J. R., BESENBACHER, F. & KJEMS, J. 2006. RNA interference in vitro and in vivo using a novel chitosan/siRNA nanoparticle system. *Mol Ther,* 14**,** 476-84.

HUEICHEN, M. L. W. 2008a. Cavitation effects versus stretch effects resulted in different size and polydispersity of ionotropic gelation chitosan–sodium tripolyphosphate nanoparticle. *Carbohydrate Polymers,* 71**,** 448-457.

HUEICHEN, M. L. W. 2008b. Cavitation effects versus stretch effects resulted in different size and polydispersity of ionotropic gelation chitosan–sodium tripolyphosphate nanoparticle. *Carbohydrate Polymers,,* 71**,** p. 448-457.

.

HUIJBERS, E. J., RINGVALL, M., FEMEL, J., KALAMAJSKI, S., LUKINIUS, A., ABRINK, M., HELLMAN, L. & OLSSON, A. K. 2010. Vaccination against the extra domain-B of fibronectin as a novel tumor therapy. *FASEB J,* 24**,** 4535-44.

HUO, Y., IADEVAIA, V. & PROUD, C. G. 2011. Differing effects of rapamycin and mTOR kinase inhibitors on protein synthesis. *Biochem Soc Trans,* 39**,** 446-50.

HURWITZ, H., FEHRENBACHER, L., NOVOTNY, W., CARTWRIGHT, T., HAINSWORTH, J., HEIM, W., BERLIN, J., BARON, A., GRIFFING, S., HOLMGREN, E., FERRARA, N., FYFE, G., ROGERS, B., ROSS, R. & KABBINAVAR, F. 2004. Bevacizumab plus irinotecan, fluorouracil, and leucovorin for metastatic colorectal cancer. *N Engl J Med,* 350**,** 2335-42.

IADEVAIA, V., HUO, Y., ZHANG, Z., FOSTER, L. J. & PROUD, C. G. 2012. Roles of the mammalian target of rapamycin, mTOR, in controlling ribosome biogenesis and protein synthesis. *Biochem Soc Trans,* 40**,** 168-72.

INFANTE, J. C. 2018. Nanoparticle-Based Systems for Delivery of Protein Therapeutics to the Spinal Cord. *Front Neurosci,* 12**,** 484.

IZUMI, Y., XU, L., DI TOMASO, E., FUKUMURA, D. & JAIN, R. K. 2002. Tumour biology: herceptin acts as an anti-angiogenic cocktail. *Nature,* 416**,** 279-80.

JAKOBSSON, L., FRANCO, C. A., BENTLEY, K., COLLINS, R. T., PONSIOEN, B., ASPALTER, I. M., ROSEWELL, I., BUSSE, M., THURSTON, G., MEDVINSKY, A., SCHULTE-MERKER, S. & GERHARDT, H. 2010. Endothelial cells dynamically compete for the tip cell position during angiogenic sprouting. *Nat Cell Biol,* 12**,** 943-53.

JEGERLEHNER, A., WIESEL, M., DIETMEIER, K., ZABEL, F., GATTO, D., SAUDAN, P. & BACHMANN, M. F. 2010. Carrier induced epitopic suppression of antibody responses induced by virus-like particles is a dynamic phenomenon caused by carrier-specific antibodies. *Vaccine,* 28**,** 5503-12.

JIANG, L. Q., WANG, T. Y., WEBSTER, T. J., DUAN, H. J., QIU, J. Y., ZHAO, Z. M., YIN, X. X. & ZHENG, C. L. 2017. Intracellular disposition of chitosan nanoparticles in macrophages: intracellular uptake, exocytosis, and intercellular transport. *Int J Nanomedicine,* 12**,** 6383-6398.

JUDGE, A. D., SOOD, V., SHAW, J. R., FANG, D., MCCLINTOCK, K. & MACLACHLAN, I. 2005. Sequence-dependent stimulation of the mammalian innate immune response by synthetic siRNA. *Nat Biotechnol,* 23**,** 457-62.

KASAHARA, M. & SUTOH, Y. 2014. Two forms of adaptive immunity in vertebrates: similarities and differences. *Adv Immunol,* 122**,** 59-90.

KATAS, H., RAJA, M. A. & LAM, K. L. 2013. Development of Chitosan Nanoparticles as a Stable Drug Delivery System for Protein/siRNA. *Int J Biomater,* 2013**,** 146320.

KAWAI, T. & AKIRA, S. 2010. The role of pattern-recognition receptors in innate immunity: update on Toll-like receptors. *Nat Immunol,* 11**,** 373-84.

KELLY, C., JEFFERIES, C. & CRYAN, S. A. 2011. Targeted liposomal drug delivery to monocytes and macrophages. *J Drug Deliv,* 2011**,** 727241.

KENNEDY, B. K. & LAMMING, D. W. 2016. The Mechanistic Target of Rapamycin: The Grand ConducTOR of Metabolism and Aging. *Cell Metab,* 23**,** 990-1003.

KERBEL, R. S. 2008. Tumor angiogenesis. *N Engl J Med,* 358**,** 2039-49.

KHAN, K. A. 2016. Investigating the extracellular interactions of the tumour endothelial marker CLEC14A. *University of Birmingham. Ph.D.*

KHANBABAIE, R. & JAHANSHAHI, M. 2012. Revolutionary impact of nanodrug delivery on neuroscience. *Curr Neuropharmacol,* 10**,** 370-92.

KHASHAYAR, P., AMOABEDINY, G., LARIJANI, B., HOSSEINI, M. & VANFLETEREN, J. 2017. Fabrication and Verification of Conjugated AuNP-Antibody Nanoprobe for Sensitivity Improvement in Electrochemical Biosensors. *Sci Rep,* 7**,** 16070.

KI, M. K., JEOUNG, M. H., CHOI, J. R., RHO, S. S., KWON, Y. G., SHIM, H., CHUNG, J., HONG, H. J., SONG, B. D. & LEE, S. 2013. Human antibodies targeting the C-type lectin-like domain of the tumor endothelial cell marker clec14a regulate angiogenic properties in vitro. *Oncogene,* 32**,** 5449-57.

KIM, Y. C. & GUAN, K. L. 2015. mTOR: a pharmacologic target for autophagy regulation. *J Clin Invest,* 125**,** 25-32.

KISHIMOTO, T. K. & MALDONADO, R. A. 2018. Nanoparticles for the Induction of Antigen-Specific Immunological Tolerance. *Front Immunol,* 9**,** 230.

KOHANE, D. S. 2007. Microparticles and nanoparticles for drug delivery. *Biotechnol Bioeng,* 96**,** 203-9.

KOKKINOPOULOU, M., SIMON, J., LANDFESTER, K., MAILANDER, V. & LIEBERWIRTH, I. 2017. Visualization of the protein corona: towards a biomolecular understanding of nanoparticle-cell-interactions. *Nanoscale,* 9**,** 8858-8870.

KOU L., S. J. 2013. The endocytosis and intracellular fate of nanomedicines: implication for rational design. *Asian J. Pharm. Sci. ,* 8:1–10.

LAMMERT, E., CLEAVER, O. & MELTON, D. 2001. Induction of pancreatic differentiation by signals from blood vessels. *Science,* 294**,** 564-7.

LEE, J., YUN, K. S., CHOI, C. S., SHIN, S. H., BAN, H. S., RHIM, T., LEE, S. K. & LEE, K. Y. 2012. T cell-specific siRNA delivery using antibody-conjugated chitosan nanoparticles. *Bioconjug Chem,* 23**,** 1174-80.

LEE K. Y., H. W. S., PARK W. H 1995. *Biomaterials,* 16**,** 1211—1216

LI, D. & KANER, R. B. 2006. Shape and aggregation control of nanoparticles: not shaken, not stirred. *J Am Chem Soc,* 128**,** 968-75.

LI, W., PRABAKARAN, P., CHEN, W., ZHU, Z., FENG, Y. & DIMITROV, D. S. 2016a. Antibody Aggregation: Insights from Sequence and Structure. *Antibodies (Basel),* 5.

LI, X. W., LEE, D. K., CHAN, A. S. & ALPAR, H. O. 2003. Sustained expression in mammalian cells with DNA complexed with chitosan nanoparticles. *Biochim Biophys Acta,* 1630**,** 7-18.

LI, Y., WU, Y., HUANG, L., MIAO, L., ZHOU, J., SATTERLEE, A. B. & YAO, J. 2016b. Sigma receptor-mediated targeted delivery of anti-angiogenic multifunctional nanodrugs for combination tumor therapy. *J Control Release,* 228**,** 107-119.

LING, S., HU, Z., YANG, Z., YANG, F., LI, Y., LIN, P., CHEN, K., DONG, L., CAO, L., TAO, Y., HAO, L., CHEN, Q., GONG, Q., WU, D., LI, W., ZHAO, W., TIAN, X., HAO, C., HUNGATE, E. A., CATENACCI, D. V., HUDSON, R. R., LI, W. H., LU, X. & WU, C. I. 2015. Extremely high genetic diversity in a single tumor points to prevalence of non-Darwinian cell evolution. *Proc Natl Acad Sci U S A,* 112**,** E6496-505.

LU, C., HAN, H. D., MANGALA, L. S., ALI-FEHMI, R., NEWTON, C. S., OZBUN, L., ARMAIZ-PENA, G. N., HU, W., STONE, R. L., MUNKARAH, A., RAVOORI, M. K., SHAHZAD, M. M., LEE, J. W., MORA, E., LANGLEY, R. R., CARROLL, A. R., MATSUO, K., SPANNUTH, W. A., SCHMANDT, R., JENNINGS, N. B., GOODMAN, B. W., JAFFE, R. B., NICK, A. M., KIM, H. S., GUVEN, E. O., CHEN, Y. H., LI, L. Y., HSU, M. C., COLEMAN, R. L., CALIN, G. A., DENKBAS, E. B., LIM, J. Y., LEE, J. S., KUNDRA, V., BIRRER, M. J., HUNG, M. C., LOPEZ-BERESTEIN, G. & SOOD, A. K. 2010. Regulation of tumor angiogenesis by EZH2. *Cancer Cell,* 18**,** 185-97.

LUNDQVIST, M., STIGLER, J., CEDERVALL, T., BERGGARD, T., FLANAGAN, M. B., LYNCH, I., ELIA, G. & DAWSON, K. 2011. The evolution of the protein corona around nanoparticles: a test study. *ACS Nano,* 5**,** 7503-9.

LUO, T., HUANG, P., GAO, G., SHEN, G., FU, S., CUI, D., ZHOU, C. & REN, Q. 2011. Mesoporous silica-coated gold nanorods with embedded indocyanine green for dual mode X-ray CT and NIR fluorescence imaging. *Opt Express,* 19**,** 17030-9.

LYNCH, M. 2010. Rate, molecular spectrum, and consequences of human mutation. *Proc Natl Acad Sci U S A,* 107**,** 961-8.

MAAS, C., HERMELING, S., BOUMA, B., JISKOOT, W. & GEBBINK, M. F. 2007. A role for protein misfolding in immunogenicity of biopharmaceuticals. *J Biol Chem,* 282**,** 2229-36.

MAENG, Y. S., CHOI, H. J., KWON, J. Y., PARK, Y. W., CHOI, K. S., MIN, J. K., KIM, Y. H., SUH, P. G., KANG, K. S., WON, M. H., KIM, Y. M. & KWON, Y. G. 2009. Endothelial progenitor cell homing: prominent role of the IGF2-IGF2R-PLCbeta2 axis. *Blood,* 113**,** 233-43.

MANCUSO, P., CALLERI, A., GREGATO, G., LABANCA, V., QUARNA, J., ANTONIOTTI, P., CUPPINI, L., FINOCCHIARO, G., EOLI, M., ROSTI, V. & BERTOLINI, F. 2014. A subpopulation of circulating endothelial cells express CD109 and is enriched in the blood of cancer patients. *PLoS One,* 9**,** e114713.

MASIERO, M., SIMOES, F. C., HAN, H. D., SNELL, C., PETERKIN, T., BRIDGES, E., MANGALA, L. S., WU, S. Y., PRADEEP, S., LI, D., HAN, C., DALTON, H., LOPEZ-BERESTEIN, G., TUYNMAN, J. B., MORTENSEN, N., LI, J. L., PATIENT, R., SOOD, A. K., BANHAM, A. H., HARRIS, A. L. & BUFFA, F. M. 2013. A core human primary tumor angiogenesis signature identifies the endothelial orphan receptor ELTD1 as a key regulator of angiogenesis. *Cancer Cell,* 24**,** 229-41.

MCCLUSKIE, M. J., EVANS, D. M., ZHANG, N., BENOIT, M., MCELHINEY, S. P., UNNITHAN, M., DEMARCO, S. C., CLAY, B., HUBER, C., DEORA, A., THORN, J. M., STEAD, D. R., MERSON, J. R. & DAVIS, H. L. 2016. The effect of preexisting anti-carrier immunity on subsequent responses to CRM197 or Qb-VLP conjugate vaccines. *Immunopharmacol Immunotoxicol,* 38**,** 184-96.

MCMILLAN, J., BATRAKOVA, E. & GENDELMAN, H. E. 2011. Cell delivery of therapeutic nanoparticles. *Prog Mol Biol Transl Sci,* 104**,** 563-601.

MEIJER, L. A., ZHOU, H., CHAN, O. Y., ALTELAAR, A. F., HENNRICH, M. L., MOHAMMED, S., BOS, J. L. & HECK, A. J. 2013. Quantitative global phosphoproteomics of human umbilical vein endothelial cells after activation of the Rap signaling pathway. *Mol Biosyst,* 9**,** 732-49.

MOODY, P. R., SAYERS, E. J., MAGNUSSON, J. P., ALEXANDER, C., BORRI, P., WATSON, P. & JONES, A. T. 2015. Receptor Crosslinking: A General Method to Trigger

Internalization and Lysosomal Targeting of Therapeutic Receptor:Ligand Complexes. *Mol Ther,* 23**,** 1888-98.

MORA-HUERTAS, C. E., FESSI, H. & ELAISSARI, A. 2010. Polymer-based nanocapsules for drug delivery. *Int J Pharm,* 385**,** 113-42.

MU, Q., JIANG, G., CHEN, L., ZHOU, H., FOURCHES, D., TROPSHA, A. & YAN, B. 2014. Chemical basis of interactions between engineered nanoparticles and biological systems. *Chem Rev,* 114**,** 7740-81.

MURA, M., SWAIN, R. K., ZHUANG, X., VORSCHMITT, H., REYNOLDS, G., DURANT, S., BEESLEY, J. F., HERBERT, J. M., SHELDON, H., ANDRE, M., SANDERSON, S., GLEN, K., LUU, N. T., MCGETTRICK, H. M., ANTCZAK, P., FALCIANI, F., NASH, G. B., NAGY, Z. S. & BICKNELL, R. 2012. Identification and angiogenic role of the novel tumor endothelial marker CLEC14A. *Oncogene,* 31**,** 293-305.

MUZARELLI R. A. A. 1996. *Carbohydr. Polym,* 29**,** 309—316

NAGPAL, K., SINGH, S. K. & MISHRA, D. N. 2010. Chitosan nanoparticles: a promising system in novel drug delivery. *Chem Pharm Bull (Tokyo),* 58**,** 1423-30.

NAKAJIMA, N. & IKADA, Y. 1995. Mechanism of amide formation by carbodiimide for bioconjugation in aqueous media. *Bioconjug Chem,* 6**,** 123-30.

NAUMOV, G. N., FOLKMAN, J., STRAUME, O. & AKSLEN, L. A. 2008. Tumor-vascular interactions and tumor dormancy. *APMIS,* 116**,** 569-85.

NERI, D. & BICKNELL, R. 2005. Tumour vascular targeting. *Nat Rev Cancer,* 5**,** 436-46.

NOTHAFT, H. & SZYMANSKI, C. M. 2013. Bacterial protein N-glycosylation: new perspectives and applications. *J Biol Chem,* 288**,** 6912-20.

NOY, P. J., LODHIA, P., KHAN, K., ZHUANG, X., WARD, D. G., VERISSIMO, A. R., BACON, A. & BICKNELL, R. 2015. Blocking CLEC14A-MMRN2 binding inhibits sprouting angiogenesis and tumour growth. *Oncogene,* 34**,** 5821-31.

O'NEAL, C. M., CRAWFORD, S. E., ESTES, M. K. & CONNER, M. E. 1997. Rotavirus virus-like particles administered mucosally induce protective immunity. *J Virol,* 71**,** 8707-17.

OH, J. Y., KIM, H. S., PALANIKUMAR, L., GO, E. M., JANA, B., PARK, S. A., KIM, H. Y., KIM, K., SEO, J. K., KWAK, S. K., KIM, C., KANG, S. & RYU, J. H. 2018. Cloaking nanoparticles with protein corona shield for targeted drug delivery. *Nat Commun,* 9**,** 4548.

PADMA, V. V. 2015. An overview of targeted cancer therapy. *Biomedicine (Taipei),* 5**,** 19.

PAEZ-RIBES, M., ALLEN, E., HUDOCK, J., TAKEDA, T., OKUYAMA, H., VINALS, F., INOUE, M., BERGERS, G., HANAHAN, D. & CASANOVAS, O. 2009. Antiangiogenic therapy elicits malignant progression of tumors to increased local invasion and distant metastasis. *Cancer Cell,* 15**,** 220-31.

PATI, R., SHEVTSOV, M. & SONAWANE, A. 2018. Nanoparticle Vaccines Against Infectious Diseases. *Front Immunol,* 9**,** 2224.

PAUL W., G. C. P. 2000. *STP Pharma Sci,* 10**,** 5-22.

PENG, H., ZHOU, S., GUO, T., LI, Y., LI, X., WANG, J. & WENG, J. 2008. In vitro degradation and release profiles for electrospun polymeric fibers containing paracetanol. *Colloids Surf B Biointerfaces,* 66**,** 206-12.

PERRINO, E., STEINER, M., KRALL, N., BERNARDES, G. J., PRETTO, F., CASI, G. & NERI, D. 2014. Curative properties of noninternalizing antibody-drug conjugates based on maytansinoids. *Cancer Res,* 74**,** 2569-78.

PIRCHER, A., FIEGL, M., UNTERGASSER, G., HEIDEGGER, I., MEDINGER, M., KERN, J. & HILBE, W. 2013. Favorable prognosis of operable non-small cell lung cancer (NSCLC) patients harboring an increased expression of tumor endothelial markers (TEMs). *Lung Cancer,* 81**,** 252-8.

POCIUTE, K., SCHUMACHER, J. A. & SUMANAS, S. 2019. Clec14a genetically interacts with Etv2 and Vegf signaling during vasculogenesis and angiogenesis in zebrafish. *BMC Dev Biol,* 19**,** 6.

PODESTA, J. E. & KOSTARELOS, K. 2009. Chapter 17 - Engineering cationic liposome siRNA complexes for in vitro and in vivo delivery. *Methods Enzymol,* 464**,** 343-54.

PRADO-GOTOR, R. & GRUESO, E. 2011. A kinetic study of the interaction of DNA with gold nanoparticles: mechanistic aspects of the interaction. *Phys Chem Chem Phys,* 13**,** 1479-89.

PRAMANIK, A. K., SIDDIKUZZAMAN, PALANIMUTHU, D., SOMASUNDARAM, K. & SAMUELSON, A. G. 2016. Biotin Decorated Gold Nanoparticles for Targeted Delivery of a Smart-Linked Anticancer Active Copper Complex: In Vitro and In Vivo Studies. *Bioconjug Chem,* 27**,** 2874-2885.

PROKOP, A. & DAVIDSON, J. M. 2008. Nanovehicular intracellular delivery systems. *J Pharm Sci,* 97**,** 3518-90.

PUSIC, K., AGUILAR, Z., MCLOUGHLIN, J., KOBUCH, S., XU, H., TSANG, M., WANG, A. & HUI, G. 2013. Iron oxide nanoparticles as a clinically acceptable delivery platform for a recombinant blood-stage human malaria vaccine. *FASEB J,* 27**,** 1153-66.

QUINONES, J. P., PENICHE, H. & PENICHE, C. 2018. Chitosan Based Self-Assembled Nanoparticles in Drug Delivery. *Polymers (Basel),* 10.

RAGHUVANSHI, R. S., KATARE, Y. K., LALWANI, K., ALI, M. M., SINGH, O. & PANDA, A. K. 2002. Improved immune response from biodegradable polymer particles entrapping tetanus toxoid by use of different immunization protocol and adjuvants. *Int J Pharm,* 245**,** 109-21.

RAJA, M. A., KATAS, H. & JING WEN, T. 2015. Stability, Intracellular Delivery, and Release of siRNA from Chitosan Nanoparticles Using Different Cross-Linkers. *PLoS One,* 10**,** e0128963.

RAPISARDA, A. & MELILLO, G. 2009. Role of the hypoxic tumor microenvironment in the resistance to anti-angiogenic therapies. *Drug Resist Updat,* 12**,** 74-80.

RHO, S. S., CHOI, H. J., MIN, J. K., LEE, H. W., PARK, H., PARK, H., KIM, Y. M. & KWON, Y. G. 2011. Clec14a is specifically expressed in endothelial cells and mediates cell to cell adhesion. *Biochem Biophys Res Commun,* 404**,** 103-8.

RIHE LIU, B. K. K., SHAOYI JIANG AND SHENGFU CHEN 2009. Nanoparticle delivery: targeting and nonspecific binding

MRS Bull., 34 pp. 432-440.

ROSKOSKI, R., JR. 2007. Sunitinib: a VEGF and PDGF receptor protein kinase and angiogenesis inhibitor. *Biochem Biophys Res Commun,* 356**,** 323-8.

RYDSTROM, A., DESHAYES, S., KONATE, K., CROMBEZ, L., PADARI, K., BOUKHADDAOUI, H., ALDRIAN, G., POOGA, M. & DIVITA, G. 2011. Direct translocation as major cellular uptake for CADY self-assembling peptide-based nanoparticles. *PLoS One,* 6**,** e25924.

S. ZENG, K.-T. Y., I. ROY, X.-Q. DINH, X. YU, F. LUAN 2011. A review on functionalized gold nanoparticles for biosensing applications

Plasmonics, 6**,** p. 491.

SAGIV-BARFI, I., CZERWINSKI, D. K., LEVY, S., ALAM, I. S., MAYER, A. T., GAMBHIR, S. S. & LEVY, R. 2018. Eradication of spontaneous malignancy by local immunotherapy. *Sci Transl Med,* 10.

SALEM, A. K. 2015. Nanoparticles in vaccine delivery. *AAPS J,* 17**,** 289-91.

SANTEL, A., ALEKU, M., KEIL, O., ENDRUSCHAT, J., ESCHE, V., FISCH, G., DAMES, S., LOFFLER, K., FECHTNER, M., ARNOLD, W., GIESE, K., KLIPPEL, A. & KAUFMANN, J. 2006. A novel siRNA-lipoplex technology for RNA interference in the mouse vascular endothelium. *Gene Ther,* 13**,** 1222-34.

SATO, A., TAKAGI, M., SHIMAMOTO, A., KAWAKAMI, S. & HASHIDA, M. 2007. Small interfering RNA delivery to the liver by intravenous administration of galactosylated cationic liposomes in mice. *Biomaterials,* 28**,** 1434-42.

SAUPE, F., REICHEL, M., HUIJBERS, E. J., FEMEL, J., MARKGREN, P. O., ANDERSSON, C. E., DEINDL, S., DANIELSON, U. H., HELLMAN, L. T. & OLSSON, A. K. 2017. Development of a novel therapeutic vaccine carrier that sustains high antibody titers against several targets simultaneously. *FASEB J,* 31**,** 1204-1214.

SAWAENGSAK, C., MORI, Y., YAMANISHI, K., MITREVEJ, A. & SINCHAIPANID, N. 2014. Chitosan nanoparticle encapsulated hemagglutinin-split influenza virus mucosal vaccine. *AAPS PharmSciTech,* 15**,** 317-25.

SCHIPPER N. G., V. K. M., ARTURSSON P., 1996. *Pharm. Res,* 13**,** 1686— 1692

SCHNEIDER, B., GROTE, M., JOHN, M., HAAS, A., BRAMLAGE, B., ICKENSTEIN, L. M., JAHN-HOFMANN, K., BAUSS, F., CHENG, W., CROASDALE, R., DAUB, K., DILL, S., HOFFMANN, E., LAU, W., BURTSCHER, H., LUDTKE, J. L., METZ, S., MUNDIGL, O., NEAL, Z. C., SCHEUER, W., STRACKE, J., HERWEIJER, H. & BRINKMANN, U. 2012. Targeted siRNA Delivery and mRNA Knockdown Mediated by Bispecific Digoxigenin-binding Antibodies. *Mol Ther Nucleic Acids,* 1**,** e46.

SHERIDAN, W. F. & BARRNETT, R. J. 1969. Cytochemical studies on chromosome ultrastructure. *J Ultrastruct Res,* 27**,** 216-29.

SIEPMANN, J. & GOPFERICH, A. 2001. Mathematical modeling of bioerodible, polymeric drug delivery systems. *Adv Drug Deliv Rev,* 48**,** 229-47.

SINGH, R. & LILLARD, J. W., JR. 2009. Nanoparticle-based targeted drug delivery. *Exp Mol Pathol,* 86**,** 215-23.

SINGH, S. D. A. N. 2018. Probing the nanoparticle–AGO2 interaction for enhanced gene knockdown   *Royal Society of Chemistry*.

SON G.H., L. B. J. 2017. Mechanisms of drug release from advanced drug formulations such as polymeric-based drug-delivery systems and lipid nanoparticles. . *J. Pharmaceut. Invest.* .

SONAJE, K., CHUANG, E. Y., LIN, K. J., YEN, T. C., SU, F. Y., TSENG, M. T. & SUNG, H. W. 2012. Opening of epithelial tight junctions and enhancement of paracellular permeation by chitosan: microscopic, ultrastructural, and computed-tomographic observations. *Mol Pharm,* 9**,** 1271-9.

SPAETH, N., WYSS, M. T., PAHNKE, J., BIOLLAZ, G., TRACHSEL, E., DRANDAROV, K., TREYER, V., WEBER, B., NERI, D. & BUCK, A. 2006. Radioimmunotherapy targeting the extra domain B of fibronectin in C6 rat gliomas: a preliminary study about the therapeutic efficacy of iodine-131-labeled SIP(L19). *Nucl Med Biol,* 33**,** 661-6.

TATIPARTI, K., SAU, S., KASHAW, S. K. & IYER, A. K. 2017. siRNA Delivery Strategies: A Comprehensive Review of Recent Developments. *Nanomaterials (Basel),* 7.

TESNIERE, A., PANARETAKIS, T., KEPP, O., APETOH, L., GHIRINGHELLI, F., ZITVOGEL, L. & KROEMER, G. 2008. Molecular characteristics of immunogenic cancer cell death. *Cell Death Differ,* 15**,** 3-12.

TIYABOONCHAI W. 2003. *Naresuan University Journal,* 11**,** 51—66.

TOMARI, Y. & ZAMORE, P. D. 2005. Perspective: machines for RNAi. *Genes Dev,* 19**,** 517-29.

TREDAN, O., GALMARINI, C. M., PATEL, K. & TANNOCK, I. F. 2007. Drug resistance and the solid tumor microenvironment. *J Natl Cancer Inst,* 99**,** 1441-54.

ULLRICH, E., BONMORT, M., MIGNOT, G., KROEMER, G. & ZITVOGEL, L. 2008. Tumor stress, cell death and the ensuing immune response. *Cell Death Differ,* 15**,** 21-8.

UTO, T., AKAGI, T., HAMASAKI, T., AKASHI, M. & BABA, M. 2009. Modulation of innate and adaptive immunity by biodegradable nanoparticles. *Immunol Lett,* 125**,** 46-52.

VAN DEN BIGGELAAR, M., HERNANDEZ-FERNAUD, J. R., VAN DEN ESHOF, B. L., NEILSON, L. J., MEIJER, A. B., MERTENS, K. & ZANIVAN, S. 2014. Quantitative phosphoproteomics unveils temporal dynamics of thrombin signaling in human endothelial cells. *Blood,* 123**,** e22-36.

VAN DER LUBBEN, I. M., VERHOEF, J. C., VAN AELST, A. C., BORCHARD, G. & JUNGINGER, H. E. 2001. Chitosan microparticles for oral vaccination: preparation, characterization and preliminary in vivo uptake studies in murine Peyer's patches. *Biomaterials,* 22**,** 687-94.

VAN DER MOST, R. G., CURRIE, A. J., ROBINSON, B. W. & LAKE, R. A. 2008. Decoding dangerous death: how cytotoxic chemotherapy invokes inflammation, immunity or nothing at all. *Cell Death Differ,* 15**,** 13-20.

VARSHOSAZ, J. & FARZAN, M. 2015. Nanoparticles for targeted delivery of therapeutics and small interfering RNAs in hepatocellular carcinoma. *World J Gastroenterol,* 21**,** 12022-41.

VETRO, M., SAFARI, D., FALLARINI, S., SALSABILA, K., LAHMANN, M., PENADES, S., LAY, L., MARRADI, M. & COMPOSTELLA, F. 2017. Preparation and immunogenicity of gold glyco-nanoparticles as antipneumococcal vaccine model. *Nanomedicine (Lond),* 12**,** 13-23.

VO, T. N., KASPER, F. K. & MIKOS, A. G. 2012. Strategies for controlled delivery of growth factors and cells for bone regeneration. *Adv Drug Deliv Rev,* 64**,** 1292-309.

WANG, J., LU, Z., WIENTJES, M. G. & AU, J. L. 2010a. Delivery of siRNA therapeutics: barriers and carriers. *AAPS J,* 12**,** 492-503.

WANG, W., NEMA, S. & TEAGARDEN, D. 2010b. Protein aggregation--pathways and influencing factors. *Int J Pharm,* 390**,** 89-99.

WILHELM, S. M., ADNANE, L., NEWELL, P., VILLANUEVA, A., LLOVET, J. M. & LYNCH, M. 2008. Preclinical overview of sorafenib, a multikinase inhibitor that targets both Raf and VEGF and PDGF receptor tyrosine kinase signaling. *Mol Cancer Ther,* 7**,** 3129-40.

WRAGG, J. W., DURANT, S., MCGETTRICK, H. M., SAMPLE, K. M., EGGINTON, S. & BICKNELL, R. 2014. Shear stress regulated gene expression and angiogenesis in vascular endothelium. *Microcirculation,* 21**,** 290-300.

XIE, X., LIAO, J., SHAO, X., LI, Q. & LIN, Y. 2017. The Effect of shape on Cellular Uptake of Gold Nanoparticles in the forms of Stars, Rods, and Triangles. *Sci Rep,* 7**,** 3827.

Y. ZHOU, C. Y. W., Y.R. ZHU, Z.Y. CHEN 1999. A novel ultraviolet irradiation technique for shape-controlled synthesis of gold nanoparticles at room temperature

Chem. Mater.,, 11**,** p. 2310-2312.

YOUSSEF, A. M., ABDEL-AZIZ, M. S. & EL-SAYED, S. M. 2014. Chitosan nanocomposite films based on Ag-NP and Au-NP biosynthesis by Bacillus Subtilis as packaging materials. *Int J Biol Macromol,* 69**,** 185-91.

YUN, S., DARDIK, A., HAGA, M., YAMASHITA, A., YAMAGUCHI, S., KOH, Y., MADRI, J. A. & SUMPIO, B. E. 2002. Transcription factor Sp1 phosphorylation induced by shear stress inhibits membrane type 1-matrix metalloproteinase expression in endothelium. *J Biol Chem,* 277**,** 34808-14.

ZANIVAN, S., MAIONE, F., HEIN, M. Y., HERNANDEZ-FERNAUD, J. R., OSTASIEWICZ, P., GIRAUDO, E. & MANN, M. 2013. SILAC-based proteomics of human primary endothelial cell morphogenesis unveils tumor angiogenic markers. *Mol Cell Proteomics,* 12**,** 3599-611.

ZHANG, J. & SALTZMAN, M. 2013. Engineering biodegradable nanoparticles for drug and gene delivery. *Chem Eng Prog,* 109**,** 25-30.

ZHANG, X. Q., LAM, R., XU, X., CHOW, E. K., KIM, H. J. & HO, D. 2011. Multimodal nanodiamond drug delivery carriers for selective targeting, imaging, and enhanced chemotherapeutic efficacy. *Adv Mater,* 23**,** 4770-5.

ZHANG, Y., CHU, W., FOROUSHANI, A. D., WANG, H., LI, D., LIU, J., BARROW, C. J., WANG, X. & YANG, W. 2014a. New Gold Nanostructures for Sensor Applications: A Review. *Materials (Basel),* 7**,** 5169-5201.

ZHANG, Y., QIAN, J., WANG, D., WANG, Y. & HE, S. 2013. Multifunctional gold nanorods with ultrahigh stability and tunability for in vivo fluorescence imaging, SERS detection, and photodynamic therapy. *Angew Chem Int Ed Engl,* 52**,** 1148-51.

ZHANG, Z., WANG, J., NIE, X., WEN, T., JI, Y., WU, X., ZHAO, Y. & CHEN, C. 2014b. Near infrared laser-induced targeted cancer therapy using thermoresponsive polymer encapsulated gold nanorods. *J Am Chem Soc,* 136**,** 7317-26.

ZHAO, X., LI, H. & LEE, R. J. 2008. Targeted drug delivery via folate receptors. *Expert Opin Drug Deliv,* 5**,** 309-19.

ZHU, R., ZHANG, C. G., LIU, Y., YUAN, Z. Q., CHEN, W. L., YANG, S. D., LI, J. Z., ZHU, W. J., ZHOU, X. F., YOU, B. G. & ZHANG, X. N. 2015. CD147 monoclonal antibody mediated by chitosan nanoparticles loaded with alpha-hederin enhances antineoplastic activity and cellular uptake in liver cancer cells. *Sci Rep,* 5**,** 17904.

ZHUANG, X., AHMED, F., ZHANG, Y., FERGUSON, H. J., STEELE, J. C., STEVEN, N. M., NAGY, Z., HEATH, V. L., TOELLNER, K. M. & BICKNELL, R. 2015. Robo4 vaccines induce antibodies that retard tumor growth. *Angiogenesis,* 18**,** 83-95.

Appendix 1.

Nanoparticle Sizing MatLab Code:

```
clc

close all

ImageFile=imread('Nanoparticle2.jpg');

[IG]=ReadImage(ImageFile);

I=IG;figure;imshow(I);


T=FindThreshold(I);

BW = im2bw(I, T);

figure;imshow(BW);


MF=MorphFilter(BW);

figure;imshow(MF);


Diameter=DiameterMeasure(MF);
```

ReadImage

This section of code reads the image file and converts it to a matrix of pixel values (0-256).

FindThreshold:

Image is converted to black and white.

MorphFilter:

The image is filled out with the MorphFilter function and is now ready to be measured.

DiameterMeasure:

The longest diameter is measured and compared to the scale bar at the bottom of the image.

```
function [IG] = ReadImage(ImageFile)

I=imread('Nanoparticle2.jpg');

figure; imshow (I,[]);

IG=I(:,:,1);
```

ReadImage

This section of code reads the image file, separates it into each 3 RGB layers and converts them to a matrix of pixel values (0-256).

```
end


function [T] = FindThreshold(I)

maxI=max(I(:));

binSize=0.002;

nBins=256; %nBins=maxI/binSize

h=(hist(double(I(:)),nBins))';

L=length(h);

M=find(h==max(h));


for k=M+1:L

    x=(M:k)';

    X=[x [ones(size(x))]];

    y=h(x);

    P=X\y; %This is the same as P=(X'*X)^-1 *X'*y;

    Y=X*P;

    R1(k)=sum( (h(x)-Y).^2 );


    clear x

    x=(k:L-1)';

    X=[x [ones(size(x))]];

    y=h(x);

    P=X\y; %This is the same as P=(X'*X)^-1 *X'*y;

    Y=X*P;

    R2(k)=sum( (h(x)-Y).^2 );


    R(k)=R1(k)+R2(k);

end
```

FindThreshold:

To convert the image into black and white a threshold pixel value is needed. The FindThreshold function takes the pixel value matrix previously generated and plots a histogram which is analysed toto identify the ideal pixel value for the cut off. Anything above this value is made white; anything below is black.

```matlab
eps=R(M+1:L);

index=M+1+find(eps==min(eps));


figure; hold on

plot(h)

plot(index,h(index),'or');


% For illustration compute and display the linear fits

x=(M:index)';

X=[x [ones(size(x))]];

y=h(x);

P=X\y; %This is the same as P=(X'*X)^-1 *X'*y;

Y=X*P;

plot(x,Y,'--c');


clear x

x=(index:L-1)';

X=[x [ones(size(x))]];

y=h(x);

P=(X'*X)^-1 *X'*y;

Y=X*P;

plot(x,Y,'--c');


% Threshold image

T=index*binSize


end
```

```
function [ MF ] = MorphFilter(BW)

BWO = bwareaopen(BW, 5);

figure;imshow(BWO);

%Fills in holes in binary images

BWI=imcomplement(BWO);

figure;imshow(BWI)


X = imfill(BWI,26,'holes');

figure;imshow(X);


%Forms filter disk for erosion and dilation

SE = strel('disk', 5:5);

%Dilation

Di = imdilate(X,SE);


X=double(Di);

MF=bwlabel (X);


end
```

MorphFilter:

Once the image is converted to black and white there are often holes left in solid structures due to an imperfect threshold value (it is almost impossible to get a perfect value as solid structures are never binary in colour).

The MorphFilter function passes over the black and white image filling in any holes that are smaller than 26 pixels. Next a disk that is 5x5 pixels is passed over the matrix to smooth any edges and fill in any extra gaps left in solid structures.

```
function [WMF] = DiameterMeasure(MF)


rp = regionprops(MF,'All');
```

```matlab
ObjDI=zeros(size(rp,1),1);

CenterX=zeros(size(rp,1),1);

CenterY=zeros(size(rp,1),1);

for i=1:size(rp,1)

    ObjDI(i)=rp(i).MajorAxisLength;

    CenterX (i)= rp(i).Centroid(1);

    CenterY (i)= rp(i).Centroid(2);

end


Final=[ObjDI CenterX CenterY];

WMF=imcomplement(MF);

imshow(WMF);

hold on

for i=1:size(Final,1)

    text(Final(i,2),Final(i,3),num2str(Final(i,1)),'Color',
'red'),...

    'HorizontalAlignment'; 'center';

    'VerticalAlignment';  'middle';


end

title('Diameter of Particles');
```

DiameterMeasure:

This function creates a database of information about the image and defines the shapes within the image to be analysed. "Centroids" or spheres, as well as the scale bar, are identified and measured for the number of pixels on their longest axis.

The data is superimposed on the image over the relevant "centroids" and the error bar so that the data can be compared, and size calculated.

Appendix 2.

CLEC14A-FrC Plasmid Construct:
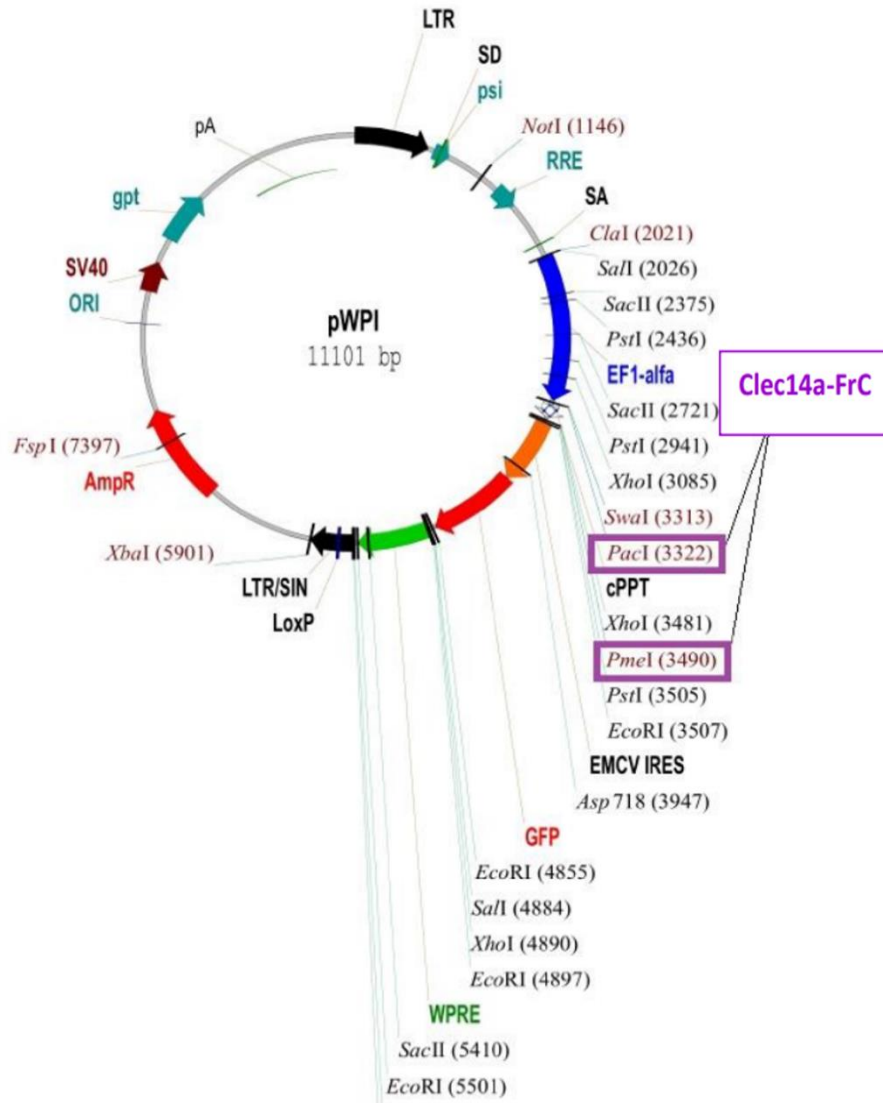
CLEC14A-FrC Plasmid Construct:

A diagrammatic representation of the structure of the pWPI plasmid used to synthesise the CLEC14A-FrC fusion protein. As can be seen, the fusion protein is inserted between the PacI and Pmel restriction sites. A GFP IRES site is placed after the fusion protein to give visual confirmation of gene transfection.

Appendix 3.

CLEC14A-FrC Plasmid Sequence:

Sequencing results of CLEC-FrC construct

Primer: EF-1a promotor region Forwards, AGTTCGGAGTCTGTCACCAAG

```
ACACGGGGGSTYTAAATTACATCATAGTTTATTCTMTAAGWTCTGGCCTCGGCCAGGGAA
TGGGGAGCATCCCACGGCCGATCSCSCAKCTTGTTCGGCCTCGGGGGCTTGCTACAGCCT
TCACCACGCTACCTTCAARAGAAGGGCGGCGGAGGAGGCCTGCAGCCTAAGGGGCGGGAC
TCTCAGCMCCGTGCMCTCAGGCTCGGAGTTTCAAGCTGTGCTCCTGCTCTTGCGTGCAGG
TCCCGGGCCTGGCGGAGGCTCCAAAGATCTTCTGTTCTGGGTGGCTCTGGAACGCAGCAT
CTCACAGTGCACTCAGGAGAAAGAGCCTTTAAGGGGTTTCTCCTGGTTGCACCCGGACTC
ARAARACTCARAGGACAGCCCACTACCGKGGGTGGAAGAGCCACAACGTTCCTGTACAGT
GAGAAAGTGCGCTGCGCTCCAGGCCACCAGGGGAGTGGAGCCTGCTGGTTGGAAGGAGAT
GCGCTGTCATCTGCGCGCCGATGGCTACCTATGCAAGTACCAGTTTGAGGTTCTGTGCCC
TGCACCTCGCCCAGGAGCCGCCTCTAATTTGAGTTTCCAAGCTCCCTTCCGGCTGAGCAG
CTCCGCGCTGGACTTCAGCCCTCCTGGGACAGAGGTGAGTGCGATGTGTCCCGGGGACCT
CTCTGTTTCGTCCACCTGCATCCAGGAAGAGACAAGCGCACACTGGGACGGGCTTTTCCC
TGGGACAGTGCTCTGCCCCTGTTCCGGGAGGTMCCTCYTTGCTGGCAAGTGTGTGGAGCT
CCCTGAYTGTCTAGATCACTTGGGARACTTCACCCTGCGAATGTGCAGTGGGCYTTGAGC
TGGGGAAGGAMGGACGTTTCTTGTGAGAMCAAAKTGGAAGAACAGCTAWCCCTYGAGGGG
ACCAAKTTGCCYCMCAGGAWTGWAAYAKCCCTCACRCAGGGGYGGTAYAACAKAT
```

Primer for IRES region Reverse, CCTCACATTGCCAAAAGACG

```
GAGGGGGTCGGGACGAAGTACCAGTCGCAACCCAGGATTTTGTCTTTCAGGTGGTTGAAG
TACCAGTTAGAAGCGATCAGGATGTCACGGTTCGGGTCGTTACCGATCTGACCGTTGTGG
GTACCAACCAGACCCAGAGAAGCGTTTTTGTCGTCSTACAGTTTCAGCTGAACAGAGTAG
GTTTTCAGGTCACGCAGTTTAACAGCTTCCATTTTTTTGTACAGCGGGATACCCGGAGCG
TTGTAACCAACACGCAGAATTCTGTCCAGGTTGTTGAAAGCGTTACCGTCTTTCGGGTAA
CCAACGATGTGTTCGTTGTTGTTGTAAGAAACGTACAGTTTGATGAAGTCACCAGATTTA
ACGAAAGAATCGATTTCGTTGTTCGGAGTGTAGCGTTTGATGATGAATTTCAGGCCGTTG
TACAGACGTCGGTAGTAGATGTTCAGTTTACCGTTAGTGTAGGACGGCGCGTTGGTCAGG
TACATGTAGTCAGTGATGTTTTTCAGCTGAACGTCTTTAGAGCTAGAAGCTACCGGGATC
AGGTAATATTCGGTGTCGTAACGCAGCGGGTTACCCCAGAAGTCACGCAGGAAGGTGATA
GACAGGTAGCTGGTATACAGTTTTTCGATCTCYTTTCGGGTTCAGTGCTTTGCRAAGAAC
GGAAYTTGTCCATGGATACGTACTGTTTGTTGTTWTGCAACCKYCCCCCTWRTAKTGAKC
TTC
```

CLEC14A-FrC Sequencing Results:

Presented here are the results from the CLEC14A-FrC sequencing. The fusion protein failed to be excreted in any significant concentration, so the plasmid was sequenced to check for any mutations preventing synthesis or secretion.

It was later decided that glycosylation issues resulted in incorrect folding and a therefor a failure to be excreted.

Appendix 4.

VLRB Fusion Plasmid Sequences:

His-CLEC14a fragment-VLRBv1

Nde1, His-tag (6xHis), GS-linker, Clec14a fragment, GS-linker, VLRBv1, Stop, Xho1)

Nucleotide sequence (234 nt):

CAT ATG CAC CAT CAC CAT CAC CAT GGT TCT GGT TCT GAA CGC AGC ATC TCA CAG TGC ACT
CAG GAG AAA GAG GGT TCT GGT TCT GGT AGC GGA TCC ACC TCA ATT CAG GAG AGG AAG
AAC AGC GGT GGC GAC TGC GGA AAG CCC GCC TGC ACA ACT CTC CTG AAC TGC GCG AAT
TTC CTC AGC TGC CTC TGC TCG ACC TGC GCC CTC TGC AGG AAA CGT TGA TAG TAA CTC GAG

Translated amino acid sequence of interest:

H M H H H H H H G S G S E R S I S Q C T Q E K E G S G S G S G S T S I Q E R K N S G G D C G K P
A C T T L L N C A N F L S C L C S T C A L C R K R - - - L E

> **His-CLEC14A-Fragment:**
> Presented here are the domains, nucleotide sequence and translated amino acid sequence for the F-VLRB fusion protein that was produced in SHuffle® T7 Express lysY Competent *E. coli*.

His-CLEC-lectin domain-VLRBv1

Nde1, His-tag (6xHis), GS-linker, Clec-Lectin domain, GS-linker, VLRBv1, Stop, Xho1)

Nucleotide sequence (627 nt):

CAT ATG CAC CAT CAC CAT CAC CAT GGT TCT GGT TCT TGT TCG GCC TCG GGG GCT TGC TAC
AGC CTT CAC CAC GCT ACC TTC AAG AGA AGG GCG GCG GAG GAG GCC TGC AGC CTA AGG
GGC GGG ACT CTC AGC ACC GTG CAC TCA GGC TCG GAG TTT CAA GCT GTG CTC CTG CTC
TTG CGT GCA GGT CCC GGG CCT GGC GGA GGC TCC AAA GAT CTT CTG TTC TGG GTG GCT
CTG GAA CGC AGC ATC TCA CAG TGC ACT CAG GAG AAA GAG CCT TTA AGG GGT TTC TCC
TGG TTG CAC CCG GAC TCA GAA GAC TCA GAG GAC AGC CCA CTA CCG TGG GTG GAA GAG
CCA CAA CGT TCC TGT ACA GTG AGA AAG TGC GCT GCG CTC CAG GCC ACC AGG GGA GTG
GAG CCT GCT GGT TGG AAG GAG ATG CGC TGT CAT CTG CGC ACC GAT GGC TAC CTA TGC
AAG TAC GGT TCT GGT TCT GGT AGC GGA TCC ACC TCA ATT CAG GAG AGG AAG AAC AGC
GGT GGC GAC TGC GGA AAG CCC GCC TGC ACA ACT CTC CTG AAC TGC GCG AAT TTC CTC
AGC TGC CTC TGC TCG ACC TGC GCC CTC TGC AGG AAA CGT TGA TAG TAA CTC GAG

Translated amino acid sequence of interest:

H M H H H H H H G S G S C S A S G A C Y S L H H A T F K R R A A E E A C S L R G G T L S T V H S
G S E F Q A V L L L L R A G P G P G G G S K D L L F W V A L E R S I S Q C T Q E K E P L R G F S W
L H P D S E D S E D S P L P W V E E P Q R S C T V R K C A A L Q A T R G V E P A G W K E M R C H
L R T D G Y L C K Y G S G S G S G S T S I Q E R K N S G G D C G K P A C T T L L N C A N F L S C L C
S T C A L C R K R - - - L E

His-CLEC14A-Lectin:

Presented here are the domains, nucleotide sequence and translated amino acid sequence for the L-VLRB fusion protein that was produced in SHuffle® T7 Express lysY Competent *E. coli*.

The size of this protein caused issues in protein synthesis. As a result, only the fragment fusion was carried forward for purification.

Appendix 5.

ChNP CLEC14A Knockdown in HUVEC

Microarray Data:

The complete Microarray data from the ChNP CLEC14A knockdown in HUVEC can be found in the University Birmingham E-Data storage:

Pearce, Jack (2019) *Jack Pearce Chitosan Nanoparticle (CLEC14A siRNA) Knockdown in HUVEC: Microarray analysis.*